交通大學

機械工程學系

博士論文

平行化三維 DSMC-NS 偶合數值方法之發展及驗證

Development and Verification of a Parallel Coupled DSMC-NS

Scheme Using A Three-dimensional Unstructured Grid

學生 連又永

指導教授 吳宗信 博士

民國九十五年七月

平行化三維 DSMC-NS 偶合數值方法之發展及驗證

Development and Verification of a Parallel Coupled DSMC-NS Scheme
Using A Three-dimensional Unstructured Grid

研 究 生：連又永　　　　　　Student：Yu-Yung Lian
指導教授：吳宗信 博士　　　　Advisor：Dr. Jong-Shinn Wu

國 立 交 通 大 學
機 械 工 程 學 系
博 士 論 文

A Thesis
Submitted to Institute of Mechanical Engineering Collage of Engineering
National Chiao Tung University
in Partial Fulfillment of the Requirements
for the Degree of
Doctor of Philosophy
in
Mechanical Engineering
July 2006

Hsinchu, Taiwan

中華民國九十五年七月

Development and Verification of a Parallel Coupled DSMC-NS Scheme
Using A Three-dimensional Unstructured Grid

Student：Yu-Yung Lian　　　　　　Advisors：Dr. Jong-Shinn Wu

Department of Mechanical Engineering
National Chiao Tung University

Abstract

In this thesis, an efficient and accurate parallel coupled DSMC-NS method using three-dimensional unstructured grid topology is proposed and verified for the simulation of high-speed gas flows involving continuum and rarefied regimes. In addition, breakdown parameters near the solid wall are reinvestigated by a detailed kinetic study and a new criterion of breakdown parameter is proposed. Research in this thesis is divided into two phases, which are described in the following in turn.

In the first phase, a parallel coupled DSMC-NS method using three-dimensional unstructured grid topology is proposed and verified. A domain overlapping strategy, taking advantage of unstructured data format, with Dirichlet-Dirichlet type boundary conditions based on two breakdown parameters is used iteratively to determine the choice of solvers in the spatial domain. The selected breakdown parameters for this study include: 1) a local maximum Knudsen number defined as the ratio of the local mean free path and local

characteristic length based on property gradient and 2) a thermal non-equilibrium indicator

defined as the ratio of the difference between translational and rotational temperatures to the

translational temperature.   A supersonic flow (M_∞=4) over a quasi-2-D 25° wedge is

employed as the first step in verifying the present coupled method.   The results of simulation

using the coupled method are in excellent agreement with those of the pure DSMC method,

which is taken as the benchmark solution. Effects of the size of overlapping regions and the

choice of breakdown parameters on the convergence history are discussed. Results show that

the proposed iteratively coupled method predicts the results more accurately as compared to

the "one-shot" coupled method, which has been often used in practice. Further, two realistic

3-D nitrogen flows are simulated using the developed coupled DSMC-NS scheme. The first

one is a flow, which consists of two near-continuum parallel orifice jets underexpanding into

a near-vacuum environment. The second one is a flow issuing from a typical RCS (Reaction

Control System) thruster. Results are compared with experimental data wherever is available.

In the second phase, a detailed kinetic investigation using the DSMC method is used to

re-examine previous proposed criteria of continuum breakdown parameters by studying the

supersonic flow past a finite-size wedge flow. Choice of this particular flow for kinetic study

lies in the fact that it includes a leading edge, a boundary layer, an oblique shock and an

expanding fan, which covers most critical flow phenomena for the present hybrid DSMC0-NS

method. Velocities of three Cartesian directions at various critical locations in the flow field

are sampled and compared with the corresponding local Maxwell-Boltzmann distribution. In addition, degree of thermal non-equilibrium among various degrees of freedoms is computed at these locations. To efficiently indicate the degree of thermal non-equilibrium among various degrees of freedoms, a general indicator of thermal non-equilibrium, with its threshold value 0.03, is used with the consideration of temperature deviations among different temperature modes, including translational temperatures in the three Cartesian directions, rotational temperature and vibrational temperature. From the results, it is found that the degree of the continuum breakdown in the boundary-lay region is overestimated with the previously recommended threshold value of $Kn_{max}^{Thr.}$ 0.05. Revised criterion near the isothermal solid wall is proposed as 0.8 in the present study.
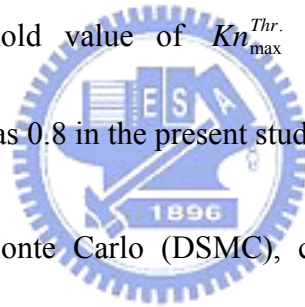
Key words: direct simulation Monte Carlo (DSMC), coupled method, rarefied gas flow, Navier-Stokes solver, supersonic flows

平行化三維 DSMC-NS 偶合數值方法之發展及驗證

學生：連又永　　　　　　　　　　　　指導教授：吳宗信 博士

國立交通大學機械工程學系博士班

中文摘要

　　本論文提出一個兼顧效率及準確度的平行化三維非結構性網格之直接蒙地卡羅法與 Navier-Stokes 偶合數值方法。本文中針對幾個同時涉及連續體及稀薄流域之高速氣流場進行模擬，以驗證該偶合數值方法之正確性。藉由使用直接蒙地卡羅法進行詳盡的分子動力學研究重新檢視，在靠近固體邊界區連續流假設失效參數的使用，並且提出新的連續體假設失效與否的新標準。以下，將本論文的工作分成兩個階段分別來介紹。

　　第一階段，本論文先提出一個平行化、使用三維非結構性網格的直接蒙地卡羅法與 Navier-Stokes 偶合數值方法。本方法是反覆地根據兩個連續體失效參數來決定在空間上各個區域其數值方法的選擇。利用非結構性網格的優點，採用數值方法區域重疊 (Domain Overlapping) 策略，流場性質在邊界上的交換則採用固定式的邊界交換形式 (Dirichlet-Dirichle type)。在本論文中所採用的兩個連續體失效參數包括: 1)區域性最大紐森數(local maximum Knudsen number)，其定義為，氣體分子平均自由徑除以流體性質梯度所定義之特徵長度，以及 2)熱力平衡指標數，其定義為: 移動動能分布溫度與旋轉動能分布溫度的差值除以移動動能分布溫度。為了驗證本論文所提出來之偶合方法，首先

我們針對超音速($M_\infty=4$)氣流流過一個近似二維的 25° 之楔形體作為驗證的第一個算例。在這個驗證算例中，未經偶合的直接蒙地卡羅法視為是對照用的正確解。利用本文提出之偶合方法跟未經偶合的直接蒙地卡羅法的比較結果極為吻合。關於數值方法重疊區域 (Overlapping Region) 的大小以及連續體失效參數標準大小的選用，對於這個偶合方法收斂性的影響也在本論文有所討論。這個算例結果顯示，相較於實務上常被使用的一次交換邊界的偶合 (One-shot coupled) 方法，目前本論文提出的反覆進行數值方法疊代之偶合數值方法可以更正確地預測流場結果。更進一步，將使用本論文目前所提的偶合數值方法，針對兩個真實三維氮氣場算例進行模擬：第一個是擴散到幾乎真空的環境的平行雙孔噴流，第二個則是衛星姿態控制器(Reaction control system)的噴嘴形成的氣流場，而模擬結果將與現有的實驗結果進行比較。

為了重新檢驗過去研究工作所建議的連續體失效參數的判斷標準，本論文的第二階段將以直接蒙地卡羅法，針對超音速氣流流經一個有限長度的楔形體的算例，進行詳盡的分子動力學研究。選用該流場作為分子動力學分析的原因是本算例的流場同時存在銳緣區(leading edge)、邊界層區、斜震波區以及扇形擴散區(expanding fan)，這些流場區域涵蓋了對於目前直接蒙地卡羅法與 Navier-Stokes 偶合數值方法模擬所遭遇的大多數關鍵性之流場現象。文中在流場各個不同特定位置上，針對卡氏坐標系之三個方向速度進行採樣，並與該位置所對應的馬斯威爾-波茲曼速度分布進行分析比較。此外，亦計算在這些位置上的各個不同溫度自由度之間熱力不平衡的程度。為了有效定義各種不同溫度自由度(這包括卡氏座標三個不同方向上的移動動能分布溫度、旋轉動能溫度以及振

動動能溫度)之間熱力不平衡的程度，本文進一步重新定義一個更具一般性的熱力平衡指標數，並提出以 0.03 為其對應之熱力平衡臨界值。據結果顯示可發現，使用過去相關研究所建議的區域性最大紐森數 0.05 作為判定是否連續體失效標準，對於在邊界層區域裡連續體失效程度的判斷可能會過於高估。本論文提出針對於靠近固體邊界區域，採用與其他區域不同的區域性最大紐森數判斷標準 0.8，作為該區域是否發生連續體失效之判定。

關鍵字: 直接蒙地卡羅法、偶合數值方法、稀薄氣流場、Navier-Stokes 數值解法、超音速流場

誌 謝

在論文付梓之際，心中滿是感謝。感謝上天的安排，讓我在交通大學度過美好與充實的歲月，匯聚如此之因緣。

本論文得以順利之完成，首先要感謝指導教授 吳宗信教授在論文撰寫期間之督促與悉心指導，在遭遇瓶頸時總是幫我渡過難關，解決心中的疑問。恩師在研究工作上的積極與執著態度，是我學習的榜樣。感謝美國阿拉巴馬州大學伯明罕分校 Gary Cheng教授促成這次出訪研究合作的機會，以及對我在美國時的種種照顧及指導，同時也感謝伯明罕分校的Roy Koomullil教授在本研究發展初期的協助。特別感謝國家太空中心的陳彥升博士撥冗協助學生之論文研究，並提供許多寶貴意見，特此致上由衷謝忱。

在這段學習成長的期間，感謝所有陪伴我同甘共苦的夥伴，感謝學長 坤樟、佑霖、雲龍及學弟妹 桂雄、允民、欣芸、捷粲，以及學弟 維呈、志偉、育進、凱文在論文口試期間的協助。特別感謝難兄難弟國賢：我們終於畢業了!!

研究工作得以順利進行，特別感謝國家太空中心「衛星推進器引致污染及衝擊影響分析軟體發展計畫」(93-NSPO(A)-PC-FA04-01）、美國太空總署(NASA)之大學研究工程及技術機構計畫URETI(NCC3-994)提供相關研究論文補助。

最後，更要感謝永遠默默付出的家人之關懷與鼓勵，特別是我的父母，對我的包容，讓我得以無憂無慮的求學。要感謝的人實在太多太多，無法一一致謝，僅將此論文獻給我的家人、師長以及所有關心我的朋友。

連又永 謹誌于
交大風城
中華民國九十五年七月

Table of Contents

List of Algorithms

List of Tables

List of Figures

Nomenclature

λ	mean free path
ρ	density
σ	the differential cross section
ω	viscosity temperature exponent
Ω	: space domain
ε_{rot}	rotational energy
ε_{v}	vibrational energy
ζ_{rot}	rotational degree of freedom
ζ_{v}	vibrational degree of freedom
$\triangle t$	time-step
σ_T	the total cross section
c	the total velocity
c'	random velocity
c_o	mean velocity
c_r	relative speed
d	molecular diameter
D	the throat diameter of the twin-jet interaction
d_{ref}	reference diameter
E	energy
k	the Boltzmann constant
Kn	Knudsen number
Kn_{max}	: continuum breakdown parameter
$Kn_{max}^{Thr.}$	: the threshold value of continuum breakdown parameter
Kn_Q	: local Knudsen numbers based on flow property Q
L	characteristic length;
m	molecule mass
M_{∞}	free-stream mach number
n	number density

P_{Tne} : thermal non-equilibrium indicator

$P_{Tne}^{Thr.}$: the threshold value of thermal non-equilibrium indicator

Re   Reynolds number

T_o stagnation temperature

T_∞ free-stream temperature

T_{ref} reference temperature

T_{rot} rotational temperature

T_{tot} total temperature

T_{tr} translational temperature

T_v vibrational temperature

T_w wall temperature

Chapter 1   Introduction

1.1   Background

Fluid dynamics is one of fields in which computer simulation shows a great deal of promise, and interest in the development of better algorithms is strong.   In a broad sense, there are two methods by which fluid flows are simulated: continuum methods and particle method.   The former relies on the numerical solution of a set of partial differential equations, for example Navier-Stokes equations, describing the fluid flow, with proper boundary conditions applied.   On the other hand, particle method is the other way to attempts to model a fluid flow by simulating the interactions of particles themselves and the interactions between particles and body boundaries. Despite of its requirement of tremendous computational effort, particle-based method can handle gas flows involving rarefaction and non-equilibrium phenomena, while the generally more efficient continuum method like Navier-Stokes solver becomes invalid.   The understanding of rarefied gas dynamics (high-Knudsen number flows) plays an important role in several research disciplines, e.g. space flight research and semiconductor processing, and many related important flow problems of interest often are involving both of continuum and rarefied regions.

Several important flow problems often involve continuum and rarefied regions in the

flow fields. Examples include, but are not limited to, expanding reaction control system plumes [Taniguchi *et al.*, 2004 and Ivanov *et al.*, 2004], expanding plumes from a flying projectile at high altitude [Wilmoth *et al.*, 2004], spiral-grooved turbo booster pump with high compression ratio [Cheng *et al.*, 1999] and jet-type (Chemical Vapor Deposition) [Versteeg *et al.*, 1994] and will be introduced in the following. Fig. 1.1 is the sketch of expanding reaction control system plumes. When spacecraft or satellite flies through an altitude of near vacuum environment, the RCS thrusts are used to provide the power and control the spacecraft or satellite. In this flow field, the flow is continuum flow from the throat and becomes transition flow and rarefied as the flow pass through the nozzle to the space. Usually, the thrusters are made up by a lot of small nozzles. Exhaust jets issuing from thrusts of spacecraft produce a huge jet plume. Various jet plumes cause many types of plume impingement on the associated or neighboring surfaces. When any part of surface suffers impingement of the plume, undesirable effects such as contamination, heating, disturbance torque and erosion will damage to the safety of spacemen and cause an anomalous behavior of the instruments. Thus, simulation of the plume impingement is very important.

The second example is expanding plumes from a flying projectile at high altitude shown in Fig. 1.2. There are many complicating phenomena in the upper continuum boost phase regime between 40 and 70 km the including turbulent transition onset, body flow separation,

body heating, angle of attack effects, thermal non-equilibrium, dispersion of particulates and flow interactions from complex flying object geometries. The more important thing is plumes issuing from those flying objects usually are high temperature gases, thus, reversed flow with radiation effect may damage the tail of those high speed objects at high altitude. Accurate predictive tools for the modeling of flying object exhausting plume flows are critical to the development of high speed flying object related technologies.

Fig. 1.3 shows a sketch of spiral-grooved turbo booster pump (TBP). Spiral-grooved turbo booster pump has both volume type and momentum transfer type vacuum pump functions, and is capable of operating at optimum discharge under pressures from approximately 1000 Pa to a high vacuum. Pumping performance is usually predicted and examined via traditional CFD methods. However, such the numerical tools are unsuitable for calculating such rarefied gas region in the highly vacuum chamber. Meanwhile the computational cost by using a DSMC method in the operation condition with high foreline pressure (1000 Pa) will be extremely high. Only a hybrid particle-continuum method could meet both of the above issues with computational efficiency and physical accuracy in both of the continuum and rarefied gas region.

Configuration of a jet-type CVD reactor is shown in Fig. 1.4. Pulsed Pressure CVD (PP-CVD) is one of jet-type CVD technique that has demonstrated improved performance

over traditional CVD technologies and the precursor is delivered in timed pulses into a continuously evacuated reactor volume. Experimental studies and a phenomenological model of PP-CVD have shown that during the deposition of titania, the conversion efficiency of the TTIP precursor into solid film with highly uniform thicknesses exceeds 90% under certain operational conditions. The unsteady under-expanded jet which forms during the injection phase contains high property gradients in the shock structure. Consequently during a pulse cycle the flow contains regions in the continuum, transition and rarefied regimes. This makes modelling the process extremely challenging, since the validity of continuum techniques is questionable and particle based techniques such as DSMC are extremely computationally expensive. In order to continue to develop this promising technology, a greater understanding of the flow dynamics of the unsteady pulsed pressure regime in PP-CVD is required.

These above problems can not solved only by either particle method or continuum method. Thus, it is necessary to develop a proper simulation tool or practical strategy while considering both of solution accuracy and computational efficiency while involving continuum and rarefied regions.

1.1.1 Classification of Gas flows

Knudsen number (Kn=λ/L) is usually used to denote the degree of rarefaction where λ is

the mean free path traveled by molecules before collision and L is the flow characteristic

length. Flows are divided into four regimes as follows in general: Kn <0.01 (continuum),

0.01<Kn<0.1 (slip flow), 0.1<Kn<3 (transitional flow) and Kn>3 (free molecular flow).

Figure 1.5 shows the various flow regions based on Knudsen number and their corresponding

solution methods in a dilute gas.   The local Kn number is defined with L as the scale length

of the macroscopic gradient; that is, $L = \dfrac{\rho}{d\rho/dx}$.   As shown in the lower bar, when the local

Kn number approaches zero, the flow reaches inviscid limit and can be solved by Euler

equation.   Molecular nature of the gas becomes dominated in the flow of interest with the

increase of local Kn increases.   When the Kn larger than 0.1, continuum assumption begins

to break down and the particle-based method is necessary.   That's why that the Navier-Stoke

equation based computational fluid dynamics (CFD) techniques will not be adopted while the

Kn are greater that 0.1.   The top bar in this figure also shows the validity of the molecular

modeling in the microscopic formulation. It indicates the Boltzmann equation is valid for all

flow regimes.   It is well known that Boltzmann equation is more appropriate for all flow

regimes; it is, however, rarely used to numerically solve the practical problems because of

two major difficulties: 1) Higher dimensionality (up to seven) of the Boltzmann equation and

2) difficulties of modeling the integral collision term.

    Direct Simulation Monte Carlo (DSMC), proposed by Bird, is an alternative method to

solve the Boltzmann equation using direct simulation of particle collision kinetics, and the

associated monograph was published in [Bird, 1976] and [Bird, 1994]. It is demonstrated

that the DSMC method is equivalent to solving the Boltzmann equation as the simulated

particle numbers become large by both Nanbu [1986] and Wagner [1992]. This method has

been widely used for gas flow simulations in which molecular effects become important.

The advantage of using particle method under these circumstances is that molecular model

can be implemented directly to the calculation of particle collisions without the macroscopic

continuum assumption. Most importantly, DSMC is the only practical way to deal with flows

in the transitional regime, without resorting to the difficult Boltzmann equation, which

requires modeling an integral-differential (collision) term.

1.1.2 Challenge to Particle-Continuum Flow Simulation

For the realistic flows of interest having continuum and continuum breakdown regions,

the direct simulation Monte Carlo (DSMC) method can provide more physically accurate

results in flows having rarefied and non-equilibrium regions than continuum flow models.

However, the DSMC method is extremely computational expensive especially in the

near-continuum region, which prohibits its applications to practical problems with complex

geometries and large domains. In contrast, the computational fluid dynamics (CFD) method,

employed to solve the Navier-Stokes (NS) or Euler equation for continuum flows, is

computationally efficient in simulating a wide variety of flow problems. But the use of

continuum theories for the flow problems involving the rarefied gas or very small length

scales (equivalently large Knudsen numbers) can produce inaccurate results due to the breakdown of continuum assumption or thermal equilibrium. A practical approach for solving the flow fields having near-continuum to rarefied gas is to develop a numerical model combining the CFD method for the continuum regime with the DSMC method for the rarefied and thermal non-equilibrium regime. A well-designed hybrid scheme is expected to take advantage of both the computational efficiency and accuracy of the NS solver in the continuum regime and the physical accuracy of the DSMC method in the rarefied or thermal non-equilibrium regime.

1.2 Literature Reviews

Aktas and Aluru [2002] proposed a multi-scale method that combines the Stokes equation solver with the DSMC method, which was used for the analysis of micro-fluidic filters. The continuum regions were governed by Stokes equations solved by a scattered point finite cloud method. The continuum and DSMC regions were coupled through an overlapped Schwarz alternating method with Dirichlet-Dirichlet type boundary conditions. However, the interface location between two solvers was specified in advance. Garcia *et al.* [1999] constructed a hybrid particle/continuum algorithm with an adaptive mesh and algorithm refinement, which was designed to treat multi-scale flow problems. The DSMC method was used as a particle method embedded within a Godunov-type compressible

Navier-Stokes solver. This methodology is especially useful when local mesh refinement for the continuum solver becomes inappropriate as the grid size approaches the molecular scales. Glass and Gnoffo [2000] proposed "one-shot" coupled 3-D CFD-DSMC method for the simulation of highly blunt bodies using the structured grid under steady-state conditions. CFD is used to solve the high-density blunt forebody flow defining an inflow boundary condition for a DSMC solution of the afterbody wake flow. Interfacial location between the CFD and DSMC zones was identified manually after one-shot CFD simulation. Results of CFD simulation at this interface were then used as the inflow boundary conditions (Dirichlet type) for the DSMC method in the rarefied regions. Wang *et al.* [2002] proposed a hybrid information preservation/Navier-Stokes (IP-NS) method to reduce statistical uncertainties during the process of coupling. The spatial domain decomposition to both of the particle and continuum domains is based on the continuum breakdown parameter proposed by Wang and Boyd [2003]. Since the IP method provides the macroscopic information in each time step, determination of the continuum fluxes across the interface between the particle and continuum domains becomes straightforward. This method is potentially suitable for simulating unsteady flows. However, the advantage of particle method in the regions involving non-equilibrium disappears because the IP method assumes the simulated flow field is equilibrium thermally. Furthermore, the breakdown parameter proposed by Wang and Boyd [2003] may overestimate the degree of the continuum breakdown near the solid wall

due to the effect of high velocity gradient in the boundary layer regions.   Roveda *et al.* [1998]

also proposed a hybrid Euler-DSMC approach for unsteady flow simulations.   Two special

approaches were designed to reduce statistical uncertainties at the interface during the

coupling procedures: 1) use of an overlapped region between the DSMC and Euler zones

and   2) use of a "ghost level structure" to reduce statistical uncertainties.   However, cloning

of particles is required in this approach and may be problematic in a particle method such as

DSMC.   At present, only one-dimensional and two-dimensional flows were demonstrated in

the literature and extension to parallel or three-dimensional simulation has not been reported

to the best knowledge of the authors.

1.3   Motivation

1.3.1   Key Factors of Hybrid DSMC-NS Scheme

As well-known, rarefaction or thermal non-equilibrium can be correctly modeled by the

DSMC method, while CFD (NS, Euler or Stokes) solver can provide a more efficiently

solution for the computational domain.   Thus, a hybrid DSMC-NS method can apply the

concept of spatial domain decomposition to distinguish the computational domain of

rarefaction or thermal non-equilibrium to be modeled by the DSMC method, and the

computational domain of continuum to be solved by the CFD (NS, Euler or Stokes) solver.

Success of such hybrid numerical method relies upon three important factors: 1) Proper

breakdown criteria in detecting precisely the degree of continuum breakdown in the whole computational domain. Correct detection of breakdown regions not only guarantees a physically correct simulation but also prevents the unnecessary computational waste (using DSMC method in continuum flow regions). It is expected to design some criteria that can be used to efficiently and accurately identify the breakdown regions and be easily evaluated during runtime; 2) Comeliness in locating spatial domain boundaries for either DSMC or continuum method during computation. The location of domain boundaries for DSMC and continuum domains are identified based on the breakdown regions of the whole computational domain considering the boundary iterative efficiency during the coupling process. Coupling strategies, e.g. overlapping region between the continuum and particle domains, should be used to help the convergence on the hybrid interface for a efficient simulation; 3) Properly and efficiently exchanging interfacial information (or flow properties) during runtime. In practice, one side of the interface is the DSMC method with accuracy strongly depending upon the sampling statistics. The computational efficiency and accuracy of the continuum solver can be potentially jeopardized by the possibly noisy boundary conditions if the uncertainty of statistical sampling is large; 4) The effect of steadiness of the flow solution on designing data exchange at the interface. In the case of unsteady simulations, the algorithm for data exchange can be very complicated in order to keep the statistical uncertainties of the particle method as low as possible.
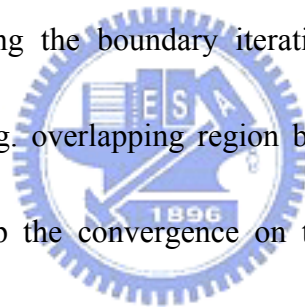
1.3.2 Continuum Breakdown Parameter

In prior works of continuum breakdown, Bird proposed a semiempirical parameter for steady-state expanding flows [Bird, 1970]

$$P = Ma \sqrt{\frac{\pi\gamma}{8}} \frac{\lambda}{\rho} \left| \frac{d\rho}{ds} \right|$$
(1.1)

where *Ma* is the local march number, γ is the ratio of specific heats and *s* is the distance along a streamline. Although it is indicated that the value of *P* 0.05 is a good criterion for detecting continuum breakdown in steady flow, the evaluation of the gradient in the stream-wise direction involves the velocity components to calculate the breakdown parameter *P*, it is generally a problem at stagnation points. Furthermore, it is believed that in complicated flows density is not the only flow property needed to be taken into account. Wang and Boyd [2003] proposed a new breakdown parameter, which will be introduced particularly in Chapter 2, to address these issues through the extensive numerical study. It should be pointed out that the zone of boundary layer is usually indicated as the continuum breakdown due to the high velocity gradient near the solid wall boundary. However, molecules which collide on the solid wall with fixed temperature should be thermalized with the wall temperature based on Maxiwell-Boltzmann distribution. The above concern motivate us to ponder if the threshold value of continuum breakdown parameter near the solid wall could be revised to a higher value, which can thus reduce the size of DSMC

simulation domain accordingly and possibly speed up the convergence of a hybrid method

by not including the boundary layers as part of the continuum breakdown regions. This

necessitates a detailed kinetic study of a well-designed flow problem, in which we can

investigate the continuum breakdown criterion in a more rigorous way.

1.4　Objectives of the Thesis

Based on previous reviews, the objectives of the current study are summarized as

follows.

1) To develop a coupled parallel DSMC-NS method using three-dimensional tetrahedral
   or hexahedral unstructured mesh, capable of efficiently and correctly simulating steady
   flow.

2) To evaluate and validate the proposed coupled method with supersonic flow over
   two-dimension wedge and three-dimensional parallel twin-jets.

3) To revise the continuum breakdown parameter near the solid wall through studying a
   kinetic study.

4) To apply the proposed coupled DSMC-NS method to a realistic case which is the study
   of plume phenomena from RCS thrusters.

1.5　Organization of the Thesis

In the thesis, a parallel coupled DSMC-NS method using three-dimensional unstructured

mesh, capable of efficiently and correctly simulating steady flows, consisting of both continuum and rarefied regions is proposed and verified. Steady-state simulations were performed to reduce the complexity in the coupling process and to verify the present coupled DSMC-NS method. Possible issues related to the extension of the present approach to unsteady flows are addressed at the end of the paper.

The present thesis is organized as follows. The particle method (PDSC), the continuum flow solvers (HYB3D and UNIC-UNS) are introduced in Chapter 2. Details of the proposed coupled DSMC-NS method are also described in Chapter 2. In Chapter 3, a supersonic nitrogen flow past a quasi-2-D wedge is chosen as 2-D validation cases for the proposed coupled method while another realistic 3-D nitrogen flow, which two near-continuum parallel orifice jets underexpand into a near-vacuum environment, is simulated using the present coupled method to demonstrate its superior capability. The results and discussions of both the simulations also summarized. An application of the coupled method that is a study of plume phenomena of RCS (Rotation Control System) thruster is also simulated by the coupled method in Chapter 3. By a kinetic study of analyzing the cell velocity samplings, the continuum breakdown parameter proposed by Wang and Boyd [2003] is reinvestigated and a new threshold value of the continuum breakdown parameter near the solid wall is also suggested in Chapter 4. The conclusions and future work of the current study are summarized in Chapter 5.

Chapter 2   Numerical Methods

2.1   Direct Simulation Monte Carlo

The direct simulation Monte Carlo method (DSMC) [Bird, 1976 and Bird, 1994] is a

particle method for the simulation of gas flows.   The gas is modeled at the microscopic level

using simulated particles, which each represents a large number of physical molecules or

atoms.   The physics of the gas are modeled through the motion of particles and collisions

between them.   Mass, momentum and energy transports between particles are considered at

the particle level.   The method is statistical in nature and depends heavily upon

pseudo-random number sequences for simulation.   Physical events such as collisions are

handled probabilistically using largely phenomenological models, which are designed to

reproduce real fluid behavior when examined at the macroscopic level.   General procedures

of the DSMC method consist of four major steps: moving, indexing, collision and sampling.

In the current study, we use VHS molecular model [Bird, 1976 and Bird, 1994] to reproduce

real fluid behavior as well as no time counter (NTC) [Bird, 1994] for the collision mechanics.

Details of the procedures and the consequences of the computational approximations

regarding DSMC can be found in Bird [Bird, 1976 and Bird, 1994].   In addition, cells in

DSMC are mainly used for particle collision and sampling.   Hence, adoption of different

grid system will definitely affect the practical DSMC implementation, especially the method

of particle tracking.   A special three-dimensional particle ray-tracing technique has to be designed to efficiently track the particle movement for the special grid system (unstructured) we use in the current study.   The details of the DSMC method and the important features of PDSC, the parallel generalized three-dimensional DSMC code in the proposed method, will be introduced later.

2.1.1   General Description of DSMC

Due to the expected rarefaction caused by the very small size of micro-scale devices or the rarefied gas flows, the current research is performed using the DSMC [Bird, 1976 and Bird, 1994] method, which is a particle-based method.   The basic idea of DSMC is to calculate practical gas flows through the use of a method that has a physical rather than a mathematical foundation, although it has been proved that the DSMC method is equivalent to solving the Boltzmann equation [Nanbu, 1986 and Wagner, 1992].   The assumptions of molecular chaos and a dilute gas are required by both the Boltzmann formulation and the DSMC method [Bird, 1976 and Bird, 1994].   The molecules move in the simulated physical domain so that the physical time is a parameter in the simulation and all flows are computed as unsteady flows.   An important feature of DSMC is that the molecular motion and the intermolecular collisions are uncoupled over the time intervals that are much smaller than the mean collision time.   Both the collision between molecules and the interaction between molecules and solid boundaries are computed on a probabilistic basis and, hence, this method

makes extensive use of random numbers. In most practical applications, the number of simulated molecules is extremely small compared with the number of real molecules. The general procedures of the DSMC method are described in the next section, and the consequences of the computational approximations can be found in Bird [Bird, 1976 and Bird, 1994].

In the current study, the Variable Hard Sphere (VHS) molecular model [Bird, 1994] and the No Time Counter (NTC) [Bird, 1994] collision sampling technique are used to simulate the molecular collision kinetics. Note that the corresponding molecular data including reference diameter (d_{ref}), reference temperature (T_{ref}), and the viscosity temperature exponent (ω) for each species are taken from those listed in Ref. [Bird, 1994]. Solid walls for all cases considered in this study are assumed to be fully diffusive (100% thermal accommodation), unless otherwise specified.

2.1.2 The DSMC Procedures

Fig. 2.1 is a general flowchart of the DSMC method. Important steps of the DSMC method include setting up the initial conditions, moving all the simulated particles, indexing (or sorting) all the particles, colliding between particles and sampling the molecules within cells to determine the macroscopic quantities. The details of each step will be described in the following subsections.

Initialization

The first step to use the DSMC method in simulating flows is to set up the geometry and flow conditions. A physical space is discredited into a network of cells and the domain boundaries have to be assigned according to the flow conditions. A point has to be noted is the cell dimension should be smaller than the mean free path, and the distance of the molecular movement per time step should be smaller than the cell dimension. After the data of geometry and flow conditions have been read in the code, the numbers of each cell is calculated according to the free-stream number density and the current cell volume. The initial particle velocities are assigned to each particle based on the Maxwell-Boltzmann distribution according to the free-stream velocities and temperature, and the positions of each particle are randomly allocated within the cells.
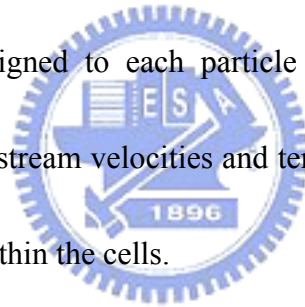
Molecular Movement

After initialization process, the molecules begin move one by one, and the molecules move in a straight line over the time step. A special particle ray-tracing technique has to be designed to efficiently track the particle movement for the special grid system, unstructured grid, which we use in the current study. The particle ray-tracing technique of three-dimensional domain is described in the following, respectively.

3-D Particle Ray-Tracing in Unstructured Mesh

Fig 2.2 is the sketch of the particle movement in three-dimensional unstructured mesh. The details are described in the following:

Without considering the external force effects, free-flying position of traced particle at $t + \Delta t$ can be written as, on one hand,

$$\overline{P}_f(t) = \overline{P}_i + \overline{V} \cdot \Delta t \qquad (2.1)$$

where

$$\overline{P}_f(t) = \begin{pmatrix} x_f \\ y_f \\ z_f \end{pmatrix} = \text{final particle position column vector} \qquad (2.1a)$$

$$\overline{P}_i(t) = \begin{pmatrix} x_i \\ y_i \\ z_i \end{pmatrix} = \text{initial particle position column vector} \qquad (2.1b)$$

$$\overline{V} = \begin{pmatrix} u \\ v \\ w \end{pmatrix} = \text{particle velocity column vector} \qquad (2.1c)$$

On the other hand, cell face can simply be represented as a planar equation as

$$\overline{n} \cdot \overline{p} + d = 0 \qquad (2.2)$$

where $\overline{n} = [a,b,c]$ is the normal unit vector of the face and $\overline{P} = [x,y,z]$ is the position vector on the plane. By solving Eqs. (2.1) and (2.2), we have

$$\Delta t' = \frac{-(ax_i + by_i + cz_i + d)}{(au + bv + cw)} \tag{2.3}$$

By computing in turn Eq. (2.3) of each face in the current cell, the correct intersecting

face number can be identified by finding the minimum positive $\Delta t'$. The intersecting

coordinate can be found by substituting $\Delta t'$ into Eq. (2.1). If the intersecting face is a

normal face between cells, then the particle will continue its trajectory until it stops.

If the intersecting face is a solid face, the particle will be reflected in a special way (e.g.,

diffusively or secularly) according to the specified boundary condition. These are related by

the coordinate transformation matrix between the local coordinate system (on the face) and

the absolute coordinate system for both types of conditions. First, a unit vector $\overline{x}'$ along

the face is chosen, then $\overline{y}'$ is the cross product of $\overline{x}'$ and $\overline{z}'$ (the normal unit vector of the

face)

$$\overline{y}' = \overline{z}' \times \overline{x}' \tag{2.4}$$

The coordination transformation matrix $\overline{\overline{H}}$, is

$$\overline{\overline{H}} = \begin{bmatrix} \overline{x}' \\ \overline{y}' \\ \overline{z}' \end{bmatrix} \tag{2.5}$$

Furthermore, due to the orthonormal set of $\overline{x}'$, $\overline{y}'$ and $\overline{z}'$, so the inverse

19

transformation $\overline{\overline{H}}^{-1}$ can be easily written as

$$\overline{\overline{H}}^{-1} = \overline{\overline{H}}^{T} \tag{2.6}$$

where $\overline{\overline{H}}^{T}$ is the transpose matrix of $\overline{\overline{H}}$.

Now, the particle velocity can be transformed from the velocity in absolute coordinate system ($\overline{V}_{abs}$) to the velocity in local coordinate system ($\overline{V}_{loc}$) before the reflection by using $\overline{\overline{H}}$.

$$\overline{V}_{loc} = \overline{\overline{H}}\overline{V}_{abs} \tag{2.7}$$

After the reflection of the particle, the new local coordinate system velocity ($\overline{V}_{loc}{}'$) can be written as

$$\overline{V}_{loc}{}' = \mathrm{F}(\overline{V}_{loc}, \text{ wall condition}) \tag{2.8}$$

where $\mathrm{F}(\overline{V}_{loc}, \text{ wall condition})$ is a kernel function, depending upon the wall condition and velocity before reflection.

Finally, the absolute velocity after the reflection ($\overline{V}_{abs}{}'$) will be obtained by using the inverse transformer as

$$\overline{V}_{abs}{}' = \overline{\overline{H}}^{-1}\overline{V}_{loc}{}' = \overline{\overline{H}}^{T}\overline{V}_{loc}{}' \tag{2.9}$$

Then, the particle continues its journey with its new absolute velocity until it stops.

20

Indexing

The location of the particle after movement with respect to the cell is important information for particle collisions. The relations between particles and cells are reordered according to the order of the number of particles and cells. Before the collision process, the collision partner will be chosen by a random method in the current cell. And the number of the collision partner can be easy determined according to this numbering system.

Gas Phase Collisions

The other most important phase of the DSMC method is gas phase collision. The current DSMC method uses the no time counter (NTC) method to determine the correct collision rate in the collision cells. The number of collision pairs within a cell of volume Vc over a time interval Δt is calculated by the following equation;

$$\frac{1}{2} N \overline{N} F_N (\sigma_T c_r)_{max} \Delta t / V_c \qquad (2.10)$$

N and $\overline{N}$ are fluctuating and average number of simulated particles, respectively. F_N is the particle weight, which is the number of real particles that a simulated particle represents. σ_T and c_r are the cross section and the relative speed, respectively. The collision for each pair is computed with probability

21

$$(\sigma_T c_r)/(\sigma_T c_r)_{\max} \qquad\qquad (2.11)$$

The collision is accepted if the above value for the pair is greater than a random fraction. Each cell is treated independently and the collision partners for interactions are chosen at random, regardless of their positions within the cells. The collision process is described sequentially as follows:

1. The number of collision pairs is calculated according to the NTC method, Eq. (2.10), for each cell.

2. The first particle is chosen randomly from the list of particles within a collision cell.

3. The other collision partner is also chosen at random within the same cell.

4. The collision is accepted if the computed probability, Eq. (2.11), is greater than a random number.

5. If the collision pair is accepted then the post-collision velocities are calculated using the mechanics of elastic collision. If the collision pair is not to collide, continue choosing the next collision pair.

6. If the collision pair is polyatomic gas, the translational and internal energy can be redistributed by the Larsen-Borgnakke model [1975], which assumes in equilibrium.

The collision process will be finished until all the collision pairs are handled for all cells and then progress to the next step.

<u>Sampling</u>

After the particle movement and collision process finish, the particle has updated positions and velocities.   The macroscopic flow properties in each cell are assumed to be constant over the cell volume and are sampled from the microscopic properties of each particle within the cell.   The macroscopic properties, including density, velocities and temperatures, are calculated in the following equations [Bird, 1976 and Bird, 1994];

$$\rho = nm \tag{2.12a}$$

$$c_o = \bar{c} = \bar{c_o} + \bar{c'} \tag{2.12b}$$

$$\frac{3}{2} k T_{tr} = \frac{1}{2} m (\overline{u'^2} + \overline{v'^2} + \overline{w'^2}) \tag{2.12c}$$

$$T_{rot} = \frac{2}{k} (\varepsilon_{rot} / \zeta_r) \tag{2.12d}$$

$$T_v = \frac{2}{k} (\varepsilon_v / \zeta_v) \tag{2.12e}$$

$$T_{tot} = (3T_{tr} + \zeta_{rot} T_{rot} + \zeta_v T_v) / (3 + \zeta_{rot} + \zeta_v) \tag{2.12f}$$

n, m are the number density and molecule mass, receptively. c, c_o, and c' are the total velocity, mean velocity, and random velocity, respectively.   In addition, T_{tr}, T_{rot}, T_v and T_{tot} are translational, rotational, vibrational and total temperature, respectively. ε_{rot} and ε_v are

the rotational and vibrational energy, respectively. ζ_{rot} and ζ_v are the number of degree of freedom of rotation and vibration, respectively. If the simulated particle is monatomic gas, the translational temperature is regarded simply as the total temperature. Vibrational effect can be neglect if the temperature of the flow is low enough.

The flow will be monitored if steady state is reached. If the flow is under unsteady situation, the sampling of the properties should be reset until the flow reaches steady state. As a rule of thumb, the sampling of particles starts when the number of molecules in the calculation domain becomes approximately constant.

2.1.3 Parallel DSMC Code PDSC

In the proposed coupled DSMC-NS method, PDSC (Parallel Direct Simulation Monte Carlo Code), developed by Wu's group [Wu and Tseng, 2005, Wu and Lian, 2003, Wu et al., 2004a and Wu et al., 2004b], is the 3-D DSMC code used for rarefied and thermally non-equilibrium regions. Important features of the PDSC code can be found in the references [Wu and Tseng, 2005, Wu and Lian, 2003, Wu et al., 2004a and Wu et al., 2004b] and are briefly described in the following.

3-D unstructured-grid topology

PDSC can accept either tetrahedral, hexahedral or hybrid tetrahedral-hexahedral mesh.

Computational cost of particle tracking for the unstructured mesh is generally higher than that for the structured mesh. However, the use of the unstructured mesh, which provides excellent flexibility of handling complicated boundary conditions (geometries and varieties) and of parallel computing using dynamic domain decomposition based on load balancing, is highly justified.

Parallel computing using dynamic domain decomposition

Load balancing of PDSC is achieved by repeatedly repartitioning the computational domain using a multi-level graph-partitioning tool, METIS [Karypis and Kumar, 1998 and Karypis and Kumar, 2003], by taking advantage of the unstructured mesh topology employed in the code. A decision policy for repartition with a concept of Stop-At-Rise (SAR) [Nicol and Saltz, 1988] or constant period of time (fixed number of time steps) can be used to decide when to repartition the domain. Capability of repartitioning of the domain at constant or variable time interval is also provided in PDSC. Resulting parallel performance is excellent if the problem size is comparably large. Details can be found in Wu and Tseng [2005].

Variable time-step scheme

PDSC employs a variable time-step scheme (or equivalently a variable cell-weighting scheme) [Wu *et al.*, 2004a], based on particle flux (mass, momentum, energy) conservation when particles pass interface between cells. This strategy can greatly reduce both the

number of iterations towards the steady state, and the required number of simulated particles

for an acceptable statistical uncertainty.   Past experience shows this scheme is very effective

when coupled with an adaptive mesh refinement technique.

2.2   Navier-Stokes Method

Computational Fluid Dynamics have been well developed to numerically solve the

Navier-Stokes equations during the past few decades.   Unstructured grid methods are

characterized by their ease in handling completely unstructured meshes and have become

widely used in computational fluid dynamics.   The relative increase of computer memory

and CPU time with unstructured grid methods is not trivial, but can be offset by using parallel

techniques in which many processors are put together to work on the same problem.
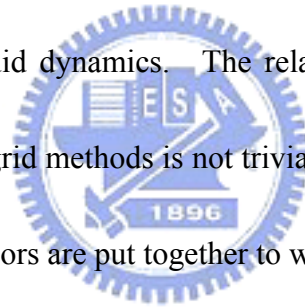
Traditionally, numerical methods developed for compressible flow simulations use an

unsteady form of the Navier-Stokes or Euler equations.   In general, either density or pressure

(density-based or pressure-based) is chosen as one of the primary variables when building up

the discretized governing equations.   However, the density-based method in cases of

incompressible or low Mach number flows is questionable, since in low compressibility limit,

and the pressure-density coupling becomes very weak.   For flows for all speed regimes,

there are some important researches reported by Hirt *et al.* [1989], Karki and Patankar [1989]

and Chen [1989].   The Navier-Stokes solvers, called HYB3D [Koomullil *et al.*, 1996a,

Koomullil *et al.*, 1996b, Koomullil *et al.*, 1996c, Koomullil and Soni, 1999], are used as flow

solver of continuum flow region in the first phase of developing a coupled method.   Then,

the UNIC-UNS code [Chen,1989, Shang *et al.*,1995a, Shang *et al.*, 1995b, Shang *et al.*, 1995c,

Shang *et al.*, 1997 and Zhang *et al.*, 2001] developed by Chen has been used as the continuum

domain solver in the current couple method instead of HYB3D code because of its powerful

capabilities in handling flows of interest involving low-speed (or incompressible) region, slip

boundary condition and chemical reactions.

2.2.1   General Description of Navier-Stokes Method

The continuum method, employed to solve the Navier-Stokes (NS) or Euler equation for

continuum flows, is computationally efficient in simulating a wide variety of flow problems.

In general, numerical methods developed for compressible flow simulations use an unsteady

form of the Navier-Stokes or Euler equations. The general form of mass conservation,

Navier-Stokes equation, energy conservation and other transport equations can be written in

Cartesian tensor form:
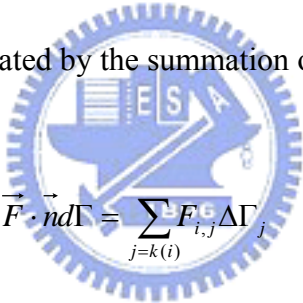
$$\frac{\partial(\rho\phi)}{\partial t} + \frac{\partial}{\partial x_j}(\rho U_j \phi) = \frac{\partial}{\partial x_j}(\mu_\phi \frac{\partial \phi}{\partial x_j}) + S_\phi \qquad (2.13)$$

where μ_ϕ is an effective diffusion coefficient, S_ϕ denotes the source term, ρ is the fluid

density and $\phi =$(1, *u, v, w, h, k, ε*) stands for the variables for the mass, momentum, total

energy and turbulence equations, respectively. Detailed expressions for the *k-ε* turbulence

models and wall functions can be found in [Launder and Spalding, 1974].   For spatial

discretization in cell-centered scheme, the transport equations can also be written in integral

form as

$$\frac{\partial}{\partial t}\int_{\Omega}\rho\phi d\Omega + \oint_{\Gamma}\vec{F}\cdot\vec{n}d\Gamma = \int_{\Omega}S_{\Omega}d\Omega \qquad (2.14)$$

where Ω is the domain, Γ is the domain surface, $\vec{n}$ is the unit normal in outward

direction and $\vec{F}$ is the flux function of the variables φ and ρ. The flux integral formulation in

finite volume scheme can be evaluated by the summation of the flux vectors over each face,

$$\oint_{\Gamma}\vec{F}\cdot\vec{n}d\Gamma = \sum_{j=k(i)}F_{i,j}\Delta\Gamma_{j} \qquad (2.15)$$

where k(i) is a list of faces of cell i , $F_{i,j}$ represents convection and diffusion fluxes

through the interface between cell i and j, and $\Delta\Gamma_{j}$ is the cell-face area.

In the present work, two cell-centered unstructured finite volume methods HYB3D

[Koomullil *et al.*, 1996a, Koomullil *et al.*, 1996b, Koomullil *et al.*, 1996c,   Koomullil and

Soni, 1999] and UNIC-UNS [Chen,1989, Shang *et al.*,1995a, Shang *et al.*, 1995b, Shang *et al.*,

1995c, Shang *et al.*, 1997 and Zhang *et al.*, 2001] are used as the continuum solver in the

proposed coupled DSMC-NS method and the general features of both Navier-Stokes solver

will be described in the following sections. General features of the HYB3D and UNIC-UNS

codes will be introduced briefly and interested readers are referred to Koomullil [Koomullil *et al.*, 1996a, Koomullil *et al.*, 1996b, Koomullil *et al.*, 1996c, Koomullil and Soni, 1999] and Chen [Chen,1989, Shang *et al.*,1995a, Shang *et al.*, 1995b, Shang *et al.*, 1995c, Shang *et al.*, 1997 and Zhang *et al.*, 2001] for the details.

2.2.2   Navier-Stokes Solvers: HYB3D and UNIC-UNS Code

HYB3D

The HYB3D is a Navier-Stokes solver using a generalized- or an unstructured- grid topology and has the following important features: 1) Cell-centered finite-volume upwind scheme for the numerical integration of governing equations, 2) Roe's approximate Riemann solver for convective flux evaluation, 3) Parallel computing using message passing interface (MPI), 4) Laminar or turbulent flow simulation capability with various turbulence models, and 5) Application of overset grid topology for flow simulation over moving or complex bodies.   Implicit time integration is used with local time stepping, where the maximum allowable time step in each cell is determined by the CFL condition constrained by advection and viscous stability criteria.   A second order spatial accuracy is achieved using Taylor's series expansion and the gradients of the flow properties are computed using a least-square method.   The creation of local extrema during the higher order linear reconstruction is eliminated by the application of Venkatakrishnan's type [Venkatakrishnan, 1995] limiter.

Parallel computing of the HYB3D also incorporates the graph-partition tool, METIS [Karypis and Kumar, 1998], which is the same as that in the PDSC. The dynamic domain decomposition in the current HYB3D computation is circumvented by not adaptively refining in this phase of computation. Details of the algorithms and numerical methods used in HYB3D are omitted here for brevity and interested readers are referred to Koomullil [Koomullil *et al.*, 1996a, Koomullil *et al.*, 1996b, Koomullil *et al.*, 1996c, Koomullil and Soni, 1999] for the details.

UNIC-UNS

In the thesis, UNIC-UNS is the Navier-Stokes solver using 3D hybrid unstructured- grid topology for the application of the thesis. Its importance features, which are similar to the HYB3D code, are list as follows: 1) Cell-centered upwind finite-volume scheme, 2) Roe's approximate Riemann solver for convective flux evaluation, 3) Parallel computing using message passing interface (MPI), 4) Capability of Laminar or turbulent flow simulation, and 5) the local extreme limiter of flux with data reconstruction proposed by Barth [1993] is employed in the UNIC-UNS. Implicit time integration is used. For general applications, a dual-time sub-iteration method is now used in the UNIC-UNS code for time accurate time-marching computations. A multi-dimensional linear reconstruction approach, proposed by Barth and Jespersen [1989], is used in the UNIC-UNS code with modifications for high order accurate estimation of flux at the cell faces. The most important specialties of

30

UNIC-UNS, different form HYB3D, are listed as follows: 1) Pressure-velocity-density

coupling. Unlike density-based method, SIMPLE [Karki and Patankar, 1989 and Chen, 1989]

family pressure correction equation, formulated using the perturbed equation of state,

momentum and continuity equations, can be applied for all-speed flow, even for low Mach

number or incompressible flow. 2) Automatics Slip boundary condition near the solid wall in

the flow region 0.01<Kn<0.1. 3) Capability of chemical reaction modeling. A general

chemical reacting flow module is included in the UNIC-UNS code for simulations such as

CVD reactor simulations or plume related study of flying object at high altitude issued from

combustion chamber. 4) Mesh adaptive refinement with handing nodes. Mesh adaptation with

refinement and coursing modules [Shang et al., 1997 and Zhang et al., 2001] in UNIC-UNS

code can maintain a smooth grid density variation required for solver to guarantee the stability

and accuracy. Details of the algorithms and numerical methods used in UNIC-UNS are

omitted here for brevity and interested readers are referred to Chen [Chen,1989, Shang et

al.,1995a, Shang et al., 1995b, Shang et al., 1995c, Shang et al., 1997 and Zhang et al., 2001]

for the details.

2.3   Hybrid DSMC-NS scheme

2.3.1   Breakdown Parameters

The first issue in developing the coupled DSMC-NS method is how to determine both

the appropriate computational domain for the DSMC and NS solvers, and the proper interface

boundary between these two solvers. A continuum breakdown parameter, proposed by

Wang and Boyd [2003] for hypersonic flows, is employed in the present coupled DSMC-NS

method as one of the criteria for selecting proper solvers. The continuum breakdown

parameter Kn_{max} is defined as [Wang and Boyd, 2003],

$$Kn_{max} = \max[Kn_D, Kn_V, Kn_T] \tag{2.16}$$

where Kn_D, Kn_V and Kn_T are the local Knudsen numbers based on density, velocity and

temperature, respectively. They can be calculated from the following general formula

[Wang and Boyd, 2003]

$$Kn_Q = \frac{\lambda}{Q}|\nabla Q| \tag{2.17}$$

where Q is the specific flow property (density, velocity and temperature) and λ is the local

mean free path. If the calculated value of the continuum breakdown parameter in a region

is larger than a preset threshold value, for example $Kn_{max}^{Thr.}$, then it cannot be modeled using

the NS equation. Instead, a particle solver like DSMC has to be used for that region.

In addition, another breakdown parameter is used to identify regions that exhibit thermal

non-equilibrium among various degrees of freedom. The breakdown parameter of thermal

equilibrium is proposed to be the ratio of the difference between translational and rotational

temperatures to translational temperature in the present study, if diatomic gas molecules at

moderate temperature are involved in the simulation. Indeed, the definition of this parameter for atomic gas can be easily changed to the ratio of the difference between two translational temperatures to any specific translational temperature. For high-temperature flows, vibrational degrees of freedom may be also used to define this thermal non-equilibrium indicator. In the current study, this thermal non-equilibrium indicator is defined as

$$P_{Tne} = \left| \frac{T_{Tr} - T_R}{T_{Tr}} \right| \tag{2.18}$$

where T_{Tr} and T_R are translational and rotational temperature, respectively. It is obvious that the nearer the value of P_{Tne} is zero, the closer the thermal equilibrium between translational and rotational degrees of freedom is. If the value of the computed thermal non-equilibrium indicator in a region is larger than some preset threshold value, for example $P_{Tne}^{Thr.}$ in the current study, then this flow region cannot be modeled correctly by the NS equation because it generally assumes thermal equilibrium among various degrees of freedom. Hence, the DSMC method has to be used for that region instead. Note the parameter P_{Tne} defined in Eq. (3) can be calculated only by DSMC, because HYB3D does not have the multi-temperature modelling capbability. This means it can only serve simultaneously with the Knudsen numbers (Eq. (1)) to control a potential switch back from DSMC to NS for those regions where the thermal non-equilibrium effect disappears after iterating between DSMC and NS methods.
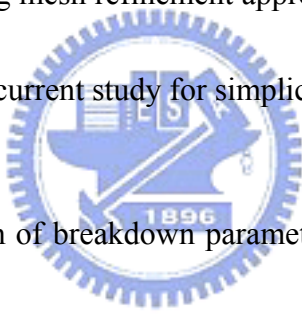
Some comments address the use of the single-temperature Maxwellian distribution function at the interface of DSMC and NS regions in the proposed coupled method as follows. Use of multiple-temperature NS equation solver could help to model the thermal non-equilibrium in much extended (into DSMC region) NS region; however, two or more energy (or temperature) equations have to be solved in all NS regions. In addition, extended NS region into DSMC region (larger property gradients or more rarefied) may further deteriorate the inherent assumption of Maxwellian distribution function in each degree of freedom in the multiple-temperature NS equation solver. Thus, use of two- or multiple-temperature NS solver may possibly benefit in reducing computational efforts, while it may introduce inaccuracy from physical point of view.
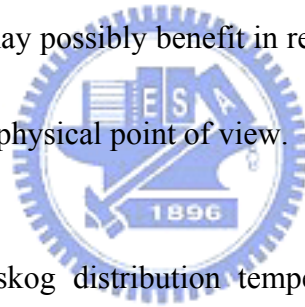
Furthermore, Chapmann-Enskog distribution temperature and density gradients may have to be used at the interface of DMSC and NS regions, where slight thermal non-equilibrium is considered. Its use would, however, greatly increase the computational cost as demonstrated in Garcia and Alder [1998] since more random number calls and computational operations are required. In practice, use of the single-temperature Maxwellian distribution function at the interface of DSMC and NS regions is much easier and with less computational cost. By taking the above intertwining factors into account, the proposed coupled DSMC-NS scheme simply utilizes Maxwellian distribution function at the DSMC-NS interface by properly controlling the magnitude of the breakdown parameters and

the appropriate overlapping regions that extends the DSMC region.

Based on the breakdown parameters, calculated from the preliminary simulation data using the continuum flow solver, and the criteria for the breakdowns of the continuum theory and thermal equilibrium, the domain for suitable DSMC simulation can be determined properly. Detailed procedures of determining the boundary (Boundary-I) between the DSMC and NS approaches and marking the breakdown domain $\overline{\Omega}_A$ are shown in Algorithm 2.1, which will be explained later. In addition, the mesh resolution across this region (e.g., shock layer) can be increased using mesh refinement approach [Wu *et al.*, 2004] in the PDSC, although it is not employed in the current study for simplicity.

In Algorithm 2.1, distribution of breakdown parameters and the array of right-hand and left-hand cells for each cell interface are first read in. Note that the idea of right-hand and left-hand arrays of each cell interface is schematically shown in Algorithm 2.1. Then, all cells and cell faces are initialized, respectively, to be neither a continuum breakdown region ($\overline{\Omega}_A$) nor a Boundary-I face. Note that the notations used in the current study can be found in Fig 2.3 with explanation that will be introduced shortly. All cells and cell faces are then checked, respectively, to decide if they are part of $\overline{\Omega}_A$ and interface Boundary-I. Using this subroutine, breakdown ($\overline{\Omega}_A$) and non-breakdown regions ($\overline{\Omega}_B \bigcup \overline{\Omega}_C \bigcup \overline{\Omega}_D$), and Boundary-I can be properly identified for the entire computational domain.

2.3.2 Overlapping Regions Between DSMC and NS Domain

Fig 2.3 shows the sketch of overlapping regions and boundaries near the interface of the DSMC and NS solvers at an intermediate step (other than the first CFD simulation step for the whole domain). Related symbols and notation are listed and explained below the sketch in Fig. 2.3. The general iterative procedure of the present coupling framework is that running the DSMC solver first after the breakdown regions are identified, and then running the NS solver next with the boundary values calculated from DSMC simulations. We now focus on the overlapping regions and boundaries in Fig. 2.3, which is important in understanding the coupling procedures which will be explained later. Note that all domains mentioned in the following include the boundaries surrounding them. Domain $\overline{\Omega}_A \bigcup \overline{\Omega}_B \bigcup \overline{\Omega}_C$ represents the DSMC simulation region, while domain $\overline{\Omega}_B \bigcup \overline{\Omega}_C \bigcup \overline{\Omega}_D$ represents the NS simulation region; thus, domain $\overline{\Omega}_B \bigcup \overline{\Omega}_C$ is the designated overlapping region. Boundary conditions (Dirichlet-type) on Boundary-I ($= \overline{\Omega}_A \bigcap \overline{\Omega}_B$) for NS simulation come from part of the previous iterative DSMC simulation, while boundary conditions (Dirichlet-type) on Boundary-III ($= \overline{\Omega}_C \bigcap \overline{\Omega}_D$) for DSMC simulation come from part of the previous iterative NS solution. Location of Boundary-I is determined from strict comparison of breakdown parameters ($Kn_{\max}$ and P_{Tne}), computed based on previous iterative solution of domain $\overline{\Omega}_A \bigcup \overline{\Omega}_B \bigcup \overline{\Omega}_C \bigcup \overline{\Omega}_D$, with the preset criteria. Or, logically, it can be defined as

$$S(I) = \left\{ \; \partial\overline{\Omega}_{P_{Tne}} \cup \partial\overline{\Omega}_{Kn_{max}} \; \right\} \cup \left\{ \; \partial\overline{\Omega}^c_{P_{Tne}} \cup \partial\overline{\Omega}^c_{Kn_{max}} \; \right\} \tag{2.19}$$

where

$$\overline{\Omega}_{P_{Tne}} = \left\{ \; \vec{r} \in \overline{\Omega} \middle| P_{Tne}(\vec{r}) \geq P_{Tne}^{Thr.} \right\} \tag{2.20a}$$

$$\overline{\Omega}_{Kn_{max}} = \left\{ \; \vec{r} \in \overline{\Omega} \middle| Kn_{max}(\vec{r}) \geq Kn_{max}^{Thr.} \right\} \tag{2.20b}$$

$$\overline{\Omega}^c_{P_{Tne}} = \left\{ \; \vec{r} \in \overline{\Omega} \middle| P_{Tne}(\vec{r}) \leq P_{Tne}^{Thr.} \right\} \tag{2.20c}$$

$$\overline{\Omega}^c_{Kn_{max}} = \left\{ \; \vec{r} \in \overline{\Omega} \middle| Kn_{max}(\vec{r}) \leq Kn_{max}^{Thr.} \right\} \tag{2.20d}$$

$\vec{r}$ is the position vector (x,y,z), and the parameters with the superscript "*Thr.*" are the

preset threshold values for breakdown parameters. Location of Boundaries-II and -III are

then determined by extending from Boundary-I towards the neighboring continuum region.

In addition, the "thickness" (number of cell layers) of domains $\overline{\Omega}_B$ and $\overline{\Omega}_C$ can be

adjusted to achieve better convergence for the coupling procedure.

A typical example of the overlapping regions in practice is demonstrated in Fig. 2.4,

which results from the current test case described later. Regions across the oblique shock

layer and in the boundary layer along the wedge surface are shown with the details of cell

distribution. It shows $\overline{\Omega}_B$ is the extension of $\overline{\Omega}_A$ towards its neighboring continuum

regions with 4 cell layers, while $\overline{\Omega}_C$ is its further extension in the same direction with 2 cell

layers.   Obviously, the size of the overlapping regions can be adjusted depending upon the

numbers of cell layers for $\overline{\Omega}_B$ and $\overline{\Omega}_C$, respectively.   One last important thing we should

point out is that in designing the overlapping regions and boundaries the DSMC domain is in

general slightly larger than which is strictly determined based on the distribution of

breakdown parameters.   This is justified in physics because DSMC can intrinsically simulate

all regimes of gas flows if computational cost is not a concern.   In addition, the method of

introducing particles from the interface boundaries into the DSMC domain can be further

simplified by only using Maxwellian velocity distribution since the flow is very close to

equilibrium condition.   An algorithm for generating overlapping regions and locating

Boundary-III is also shown in Algorithm 2.2, which is explained briefly as follows.
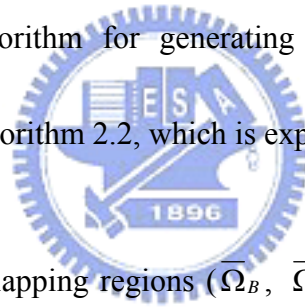
In Algorithm 2.2, only overlapping regions ($\overline{\Omega}_B$, $\overline{\Omega}_C$, and $\overline{\Omega}_D$) and Boundary-III are

identified, while Boundary-II is not identified specifically.   The reason is that only

Boundary-I and Boundary-III are the locations which require imposing boundary conditions

for NS and DSMC solvers, respectively, while Boundary-II only serves as the interface for

updating solutions.   Details of Algorithm 2.2 are skipped since it is rather self-explanatory.

The main idea of this algorithm is to keep track of the list of current interface nodes

originating from Boundary-I interface and to extend the necessary number of cell layers in the

direction of non-breakdown regions ($\overline{\Omega}_B \bigcup \overline{\Omega}_C \bigcup \overline{\Omega}_D$).   Also, the number of cell layers of

$\overline{\Omega}_B$ and $\overline{\Omega}_C$ can be adjusted in this subroutine (Algorithm 2.2), respectively.

Furthermore, in the current coupled DSMC-NS method the choice of solution update for each cell is based on its domain type. Domain $\overline{\Omega}_A \bigcup \overline{\Omega}_B$ is the region where the updated solution comes from the DSMC simulation, while domain $\overline{\Omega}_C \bigcup \overline{\Omega}_D$ is the region where the updated solution comes from the NS simulation.

2.3.3 Coupling Procedures

The second issue of the coupled method is the information exchange through the interface between the NS domain and the DSMC domain. Algorithm 2.3 summarizes general procedures of current coupled DSMC-NS method, which will be explained in detail shortly. In addition, Algorithm 2.4 describes the procedures about how the macroscopic flow properties at the Boundary-III, calculated from the previous NS simulation, are used as the new Dirichlet-type boundary conditions and fed into the DSMC solver for domain $\overline{\Omega}_A \bigcup \overline{\Omega}_B \bigcup \overline{\Omega}_C$. Flow properties on both sides of Boundary-III, calculated from NS simulation, are averaged as the boundary conditions for the DSMC solver. From the DSMC simulation, the macroscopic flow properties at Boundary-I are employed as the Dirichlet-type boundary conditions and fed back to the NS solver for domain $\overline{\Omega}_B \bigcup \overline{\Omega}_C \bigcup \overline{\Omega}_D$. Detailed procedures of extracting data on Boundary-I are presented in Algorithm 2.5, which is similar to Algorithm 2.4. Since steady flow is assumed, coupling between the DSMC and NS solvers at each integration time step is not necessary. Statistical uncertainty from the DSMC simulation can thus be minimized if enough sampling at each iteration step is accumulated.

Generally, less than ten couplings are good enough to achieve converged solution, which will be shown in Section 3.

In brief summary, major procedures of the present coupled DSMC-NS method are listed as follows (Algorithm 2.3):

1. Apply the NS solver (HYB3D or UNIC-UNS) to simulate the whole flow field as continuum;

2. Determine the locations of Boundary-I and -III and, thus, the DSMC simulation domain ($\overline{\Omega}_A \bigcup \overline{\Omega}_B \bigcup \overline{\Omega}_C$).

3. Impose Dirichlet-type boundary conditions (velocities, temperature and number density) on Boundary-III, obtained from latest NS simulation, for the next DSMC simulation domain ($\overline{\Omega}_A \bigcup \overline{\Omega}_B \bigcup \overline{\Omega}_C$).

4. Simulate and sample the flow field in the DSMC domain ($\overline{\Omega}_A \bigcup \overline{\Omega}_B \bigcup \overline{\Omega}_C$), using the PDSC code, until acceptable statistical uncertainties are reached.

5. Impose Dirichlet-type boundary conditions (velocities, temperature and density) on Boundary-I, obtained from latest DSMC simulation, for the next NS simulation domain ($\overline{\Omega}_B \bigcup \overline{\Omega}_C \bigcup \overline{\Omega}_D$).

6. Conduct flow simulation in the NS domain ($\overline{\Omega}_B \bigcup \overline{\Omega}_C \bigcup \overline{\Omega}_D$), using the NS solver, to obtain a converged steady-state solution.

7. Update solution of the whole computational domain.

8. Repeat from Steps 2 to 7 until the maximum number of coupling iterations is exceeded or the preset convergence criterion is reached.

Some specific details in the above procedures are described as follows. In **Procedure 1**, we need to have the most updated solution in the whole domain for determining overlapping regions and interface boundaries between the NS and DSMC solvers. Such solution of the whole domain comes from the "one-shot" NS simulation. Extension of the overlapping regions in **Procedure 2** from Boundary-I towards Boundary-III can slightly increase the computational time in DSMC simulation; however, it may reduce the overall number of coupling iterations required to reach the converged solution according to our numerical experience. Up to four layers of cells in domain $\overline{\Omega}_B$ and two layers of cells in domain $\overline{\Omega}_C$ in the overlapping regions are adopted in the current implementation. The effect of varying the size of overlapping region is reported in Section 3. In **Procedure 4**, the Dirichlet boundary conditions on Boundary-III for the PDSC code are treated according to the Maxwell-Boltzmann velocity distribution assuming that local flow is very close to thermal equilibrium. In **Procedure 7**, the solution of the whole domain is updated as a combination of previous NS solver (HYB3D or UNIC-UNS) and PDSC calculations, with Boundary-II acting as the interface for the solution. In addition, the use of the unstructured mesh is highly justified since the locations of the Boundary-I and -III may not be smooth and have irregular shapes. This often occurs in multi-dimensional flows.

2.3.4 Practical Implementation

Numerical simulations with the coupled DSMC-NS code are conducted on a memory-distributed PC cluster system (64 Nodes, dual processors, 2GB RAM per node, GB switching hub) running under a Linux operating system.   32 processors are used throughout this study, unless otherwise specified.   The PDSC and NS solver (HYB3D or UNIC-UNS) are coupled through a simple shell script (Algorithm2.3), which is a standard in the Linux or equivalent system.   This approach has three advantages: 1) to avoid unnecessary human errors in modifying the source code,   2) to provide the flexibility of replacing either solver with an improved one under the present hybrid framework, and   3) to eliminate the concern about arranging memory allocation in both codes during the coupling process, which may further constrain the size of physical problem the coupled solver can simulate.   Thus, the coupled DSMC-NS code is expected to be highly portable among parallel machines with distributed memory.   Most importantly, our experience shows that the I/O time related to the switching of solver and read/write files is negligible comparing to the simulation time used by each solver.

Chapter 3   Benchmark tests and verifications

In the chapter, we use two test cases to verify and to validate the proposed coupled DSMC-NS method.   The first test case is a supersonic flow past 25° wedge for the validation of the proposed coupled method. To demonstrate the present coupled DSMC-NS method in dealing with realistic 3-D flows, a nitrogen flow with two parallel near-continuum orifice jets issuing into a near-vacuum environment is simulated. This flow is in generally very difficult to simulate alone using either the DSMC or NS solver.

3.1   Supersonic Nitrogen Flow over a Two-Dimensional Wedge

3.1.1   Flow and Simulation Conditions

Flow Conditions

A supersonic flow past a 2-D half-angle with a length of 60.69mm, the same as that in Wang *et al.* [2002], is chosen as the test case to validate the present coupled DSMC-NS method.   An equivalent quasi-2-D DSMC simulation is performed with the PDSC code by imposing the Neumann boundary conditions in the span-wise direction (z-coordinate), which is normal to the 2-D wedge.   Tests show that 3-4 cells in the z-direction are generally enough to mimic the 2-D flow.   The numerical results of the 2-D DSMC simulation is taken as the benchmark values for the validation of the proposed DSMC-NS method.   Also, the quasi

2-D simulation requires less computational resource than the 3-D simulation. Extension to

3-D flows is straightforward since the PDSC and HYB3D are both three-dimensional codes.

Sketch of the current benchmark test is shown in Fig. 3.1 Free-stream conditions for this test

case include: gaseous nitrogen as the flowing fluid, a Mach number (M_∞) of 4, a velocity (U_∞)

of 1111.1m/s, a density (ρ_∞) of 6.545E-4kg/m^3 and a temperature (T_∞) of 185.6K. The

wedge has a wall temperature (T_w) of 293.3K and a length of 60.69mm. The Knudsen

number based on the length of the wedge and the free-stream conditions is 0.0017.

Simulation Conditions

In the pure DSMC simulation and the DSMC part of the coupled method, variable hard

sphere (VHS) [Bird, 1994] model is used to simulate molecular collisions. A constant

rotational collision number of 5 [Bird, 1994] is used in the Larsen-Borgne model [Borgnakke

and Larsen, 1970] for simulating energy exchange between translational and rotational

degrees of freedom. In the NS simulation (pure CFD or part of the coupled method), a CFL

number of 100 and a threshold parameter of 0.5 in the limiter function proposed by

Venkatakrishnan [1995] are used throughout this study, unless otherwise specified. The

same mesh (180,000 hexahedrons) is used for the three numerical approaches (pure DSMC,

pure CFD, and the coupled methods) detailed in the current study. Pure DSMC simulation

using the PDSC code is taken as the benchmark result for comparison hereafter in the current

test case, since it intrinsically solves the Boltzmann equation that governs the gas flows in all

regimes.   There are four sets of simulation conditions tested in the current study, which are

shown in Table 3.1.   Among those, **Set 1** is taken as the baseline case for future discussions,

unless otherwise specified.   Also, the parametric details about the different numerical

approaches that are used in the current study are present below.

This simulation is performed on a PC-cluster system, termed as "Cahaba", at University

of Alabama, Birmingham. This system is configured in master-slave network architecture

with the following features: 64 dual-processor nodes, 2.4 GHz Xeons for each processor, 2GB

RAM at least for each node and GB-ethernet for networking. The proposed coupled

DSMC-NS method is expected to have high portability across various parallel machines if

they are memory-distributed and using MPI as the communication protocol. Totally 32

processors are used in this benchmark test unless otherwise specified.

Pure DSMC simulation and DSMC simulation in the coupled method

Note that the number appearing in parenthesis in the following description represents the

value corresponding to the PDSC simulation in the coupled method. Approximately 3.1

million (0.7 million) particles are used for the pure DSMC simulation. The number of

computational cells that are used for PDSC in the coupled method is in the range of

64,000~85,000 (Table 3.2), which is about 1/3~1/2 of the total number of cells of 180,000 for

the pure DSMC method. A number of sampling time steps for the pure DSMC simulation of

35,000 (10,000), and a corresponding number of transient time steps of 30,000 (15,000) are employed to make sure the transient period does not affect the sampling result. The total number of sampling time steps for pure DSMC simulation is much larger than that of DSMC simulation in the coupled method at each iteration step to ensure low statistical uncertainties in the pure DSMC simulation. The reference (or smallest) time step of 8.71E-9 seconds is used for both DSMC simulations with the variable time-step approach. The number of particles per cell in the DSMC simulation is generally kept greater than 10 throughout the DSMC simulation domain. Resulting total computational time for the pure DSMC method and DSMC simulation in the coupled method is approximately 16.3 hours and 12.2 hours (for 10 coupled iterations), respectively. Related timing data are also shown in Table 3.3 for reference.
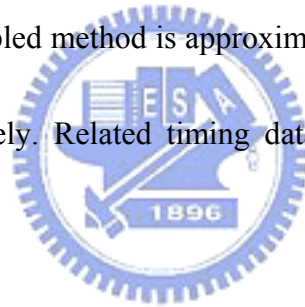
Pure NS simulation and NS simulation in the coupled method

In both NS simulations, an implicit scheme with a local time stepping and a CFL number of 100 is used for the time iterations. Iteration numbers of 7000 and 2000 are used for pure NS simulation and NS simulation in the coupled method respectively. In addition, grid convergence of the NS code is demonstrated in Fig. 3.2, where the simulated data using fewer cells (120,000 cells) are essentially the same as those by (180,000 cells) as used in the verification of the coupled method with the quasi-2-D wedge flow. In the current study,

46

180,000 cells are used throughout the study, unless otherwise specified. The number of

computational cells for HYB3D in the coupled method is about 1/2~2/3 of the total number of

cells used for pure NS simulation. Total HYB3D computational time is approximately 2.8

hours and 9.2 hours (for 10 coupling iterations), respectively, for the pure NS simulation and

the NS simulation in the coupled method. Furthermore, the total computational time in the

coupled method is about 24.2 hours (Table 3.3). For other sets of simulation, the total

computational time of the coupled method is within ±20% difference from that of Set-1

simulation.

Distribution of Breakdown Parameters

The distributions of breakdown parameters of test case Set 1 (initial values of Kn_{max}, and

Kn_{max} and P_{Tne} at the end of 15th coupled iteration) along the normal direction from the wedge

surface at x= 0.5, 5 and 50mm are illustrated in Fig. 3.3a-3.3c, respectively. As discussed

before, only the DSMC method is able to produce P_{Tne}; hence, there is no corresponding

distribution of the thermal non-equilibrium indicator after the initial HYB3D simulation. Two

horizontal lines showing the threshold values (0.02 for Kn_{max} and 0.03 for P_{Tne}) become the

borderlines that continuum breaks down or thermal non-equilibrium exists, in which the NS

solver cannot be used. General trend of the Kn_{max} distribution along the normal direction from

the wedge surface shows that the value is rather large (up to 0.4 or larger) near the surface

(x=0.5, 5mm) due to large property gradients in the viscous boundary layer, and then

decreases to a much smaller value in the region between the boundary layer and the oblique

shock, and finally becomes large again across the oblique shock (slightly larger than 0.2 or

less). As for the P_{Tne} distribution, high value (up to 0.4) can be found only at the location

across the oblique shock at all surface locations. Noticeably, a comparably broader region for

P_{Tne} than Kn_{max} can be found in Figs. 3.3a-3.3b, which justifies the use of the thermal

non-equilibrium indicator, P_{Tne}, in the current study. In addition, the maximum value of Kn_{max}

across the oblique shock decreases slightly with increasing distance from the leading edge.

This is understandable since the property gradient near the leading edge is very large. Another

important finding is that the initial distribution of Kn_{max}, computed from the initial HYB3D

simulation, differs to a great extent from that after the final (15th) coupling iteration. This

shows that previous "one-shot" CFD simulation, which provides the Dirichlet-type boundary

conditions for the DSMC simulation, is problematic for an accurate simulation. Also, the

maximum values of Kn_{max}, predicted by the latest PDSC simulation, are generally lower than

those predicted by the initial HYB3D simulation except the leading edge region. Based on the

distribution of breakdown parameters calculated at each iteration step, the threshold value of

breakdown parameters and the concept of overlapping regions mentioned earlier, we can thus

properly determine the computational domain for the DSMC and NS solvers, respectively.

3.1.2   Evolution of DSMC and NS Domains

Fig. 3.4a and Fig. 3.4b, respectively, show the initial distribution of continuum (NS)

breakdown regions ($\overline{\Omega}_A$) and DSMC simulation domains ($\overline{\Omega}_A \cup \overline{\Omega}_B \cup \overline{\Omega}_C$) in the coupled

method, while Fig. 3.5a and Fig. 3.5b, respectively, show the corresponding distribution after

the 15th coupled iteration. Note that the initial distribution of NS breakdown regions is solely

determined by the HYB3D computation for the whole domain, while the later distribution is

updated from the solutions of both PDSC and HYB3D simulations. In Fig. 3.5a, the

continuum breakdown regions are rather scattered, especially near the leading-edge region,

while in Fig. 3.5b the DSMC simulation domains that are originally disconnected spatially

becomes connected due to the current strategy of overlapping regions. In the current test case,

there are two major DSMC simulation domains: one is across the oblique shock and the other

is near the boundary layer of the wedge surface. In addition, the region in front of the leading

edge is also identified as the DSMC simulation domain due to large gradient of the flow

properties. To be numerically accurate, a threshold value of Kn_{max} in the current study is

chosen conservatively as 0.02, which guarantees that even minor deviation from the

continuum theory can be captured. Note that Wang *et al.* [2002] used the same value,

although Wang and Boyd [2003] previously recommended 0.05 as the threshold value instead.

Consideration of another breakdown parameter P_{Tne} (0.03 in the current study) further extends

the possible DSMC simulation region, especially in the region near the leading edge and

across the oblique shock, as can be seen in Figs. 3.3a-3.3c. Thus, we can expect a larger

DSMC domain exists, which increases the computational time accordingly, should this

threshold value decrease even more. Of course, both Kn_{max} and P_{Tne} can be adjusted based on numerical experience. Comparing Fig. 3.4 with Fig. 3.5, we can find that the DSMC simulation domain expands with increasing number of coupled iteration, which justifies the necessity of repeated coupling between two solvers as proposed in the current study. Nevertheless, the DSMC simulation region ceases to expand as the converged solution is reached.

3.1.3 Verification of the Coupled DSMC-NS Scheme

Fig. 3.6a and Fig. 3.6b compare contour distributions of density and translational temperature, respectively, obtained from the pure DSMC simulation and the coupled DSMC-NS method. The results of the present coupled DSMC-NS method are in excellent agreement with those of pure DSMC simulation except the unexpected density profile behind the oblique shock near the downstream end. Note that the wiggle appearing in Fig. 3.6a (density contour) may be misleading at first glance since the density values in the region between the oblique shock and the wedge surface is actually almost uniform. Obviously, the oblique shock originating from the leading edge is well captured by both pure DSMC simulation and the coupled method. Detailed comparisons of density and temperature profiles obtained from the present coupled DSMC-NS, pure DSMC and pure NS solvers are introduced next to further demonstrate the validity of the current proposed coupled DSMC-NS method.

Figs. 3.7a-3.7c show the comparison of density, temperature and velocity contour, respectively, obtained from these three numerical methods, along a line normal to the wedge surface (δn direction) at x=0.5mm. Horizontal dash-dot line represents the boundary between the NS solution domain (above) and the DSMC solution domain (below). In addition, the data of the coupled method represent the results after the 15th coupled iteration. Due to rarefaction of the free stream and the shock forming near the leading edge region, as shown in those figures, the majority portion normal to the wedge surface at this location belongs to the DSMC simulation domain except for the region far away from the wedge surface (large δn). Results of the coupled method are in excellent agreement with those of pure DSMC simulation at all δn of x=0.5mm. Because the HYB3D code only solves the thermal-equilibrium and continuum-based governing equations, the results of HYB3D are different to a large extent from other two methods due to the combined effect of large Kn_{man} (low density and large gradient of properties) and large P_{Tne} (highly thermal non-equilibrium) near the leading edge. Observation from Figs. 3.7a-3.7c shows that overlapping regions may be shrunk to further reduce the computational time. Effects of reducing the overlapping regions are discussed later.

Figs. 3.8a-3.8c show the similar comparison among the three numerical approaches at x=5mm. Based on the calculated breakdown parameters (Kn_{max} and P_{Tne}) and the selected threshold values, the flow region is divided into four sub-domains along the δn direction, as

shown in Fig. 3.8: Zone I (δn < 0.74 mm) and Zone III (1.71mm< δn < 2.61mm) are the

DSMC solution domains, while the other two regions, Zone II (0.74mm < δn < 1.71mm) and

Zone IV (δn > 2.61mm), are the NS solution domains. At this location, the results of the NS

solver deviate appreciably from those of both pure DSMC simulation and the coupled method.

This deviation occurs even in the region between the shock and the boundary layer, where it

is identified as the NS solution domain. This large deviation is reasonable since the boundary

conditions for the NS solution domain (Zone II) can only be accurately obtained from DSMC

simulation domains (Zone I and III). Results of the present coupled method are still in

excellent agreement with those of pure DSMC simulation for the entire domain.
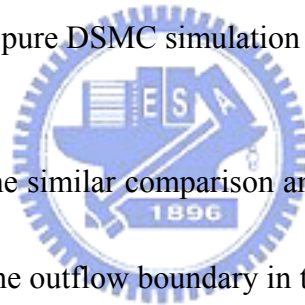
Figs. 3.9a-3.9c also show the similar comparison among the three numerical methods at

x=50mm, which is very close to the outflow boundary in the current test case. The flow region

is again divided into four sub-domains along the δn direction. Two zones (I and III) are the

DSMC simulation domains, while the other two zones (II and IV) are the NS simulation

domains. In general, similar trends to Fig. 3.8 can still be found in Fig. 3.9 except that there is

a slight discrepancy between the coupled method and pure DSMC simulation. This could be

possibly due to the problematic treatment of outflow boundary conditions in the DSMC

simulation. In the NS simulation, supersonic outflow boundary conditions assuming no

information is passed back to the computational domain from the outside, while in DSMC

simulation, fixed outflow boundary conditions based on free-stream supersonic flow

conditions are used, which are obviously incorrect. Indeed, further detailed study regarding this matter is required to resolve the discrepancy.

3.1.4 Effect of the Varying Simulation Parameters on Convergence

As mentioned earlier, varying the size of the overlapping regions and the criteria of breakdown parameters may have an impact on the convergence rate, computational cost and accuracy of solutions. Figs. 3.10 and 3.11 illustrate the convergence history of L2-norm deviation of density and total temperature, respectively, with different simulation parameters. This L2-norm deviation for i^{th} iteration is defined as the root mean square of flow properties between the $(i$-$1)^{th}$ and the ith iteration in the whole simulation domain. There are 4 test sets of simulation conditions listed in Table 3.2. Note that the L2-norm deviations level off within less than 10 coupled iterations for all the test sets. Indeed, the converged deviation of flow properties depends upon the statistical uncertainties of the DSMC solver. However, the effect of the number of sampling used in the PDSC code is not pursued in the current study. As compared with the baseline case (Set 1), decreasing the size of overlapping regions (Set 2) or increasing the threshold values of $Kn_{max}^{Thr.}$ (Set 3) and $P_{Tne}^{Thr.}$ (Set 4) does not clearly change the convergence behavior of the coupled method as shown in Fig. 3.10 and Fig. 3.11. In addition, varying the simulation parameters (Set 1 ~ Set 4 in Table 3.2) does not alter the accuracy of the solution. Typical examples are shown in Fig. 3.12a and Fig. 3.12b (x=0.5mm), whereas the profiles of flow properties at other positions show a similar trend. However, the

choice of simulation parameters slightly changes the resulting number of cells for DSMC

simulation (Table 3.2), which in turn may change the total computational time slightly. In

addition, this slightly large number of coupled iterations required for convergence will be

discussed in detail next along with the results by applying the coupled method in computing a

3-D realistic flow.

3.2 Three-Dimensional Parallel Twin-Jets

3.2.1 Flow and Simulation Conditions
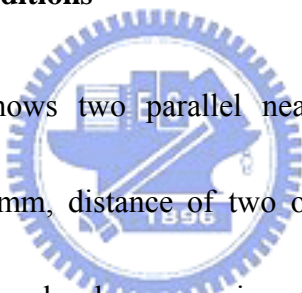
Fig. 3.13 schematically shows two parallel near-continuum thin orifice free jets

(nitrogen gas, orifice diameter=3mm, distance of two orifice centers=9mm) issuing into a

near-vacuum environment. This flow has been experimentally measured by Soga *et al.* [1984]

with background pressure ~3.7Pa. Since only limited computational domain is utilized,

vacuum boundary conditions are employed at all outer boundaries for simplicity. In addition,

only 1/4 of the whole physical domain is simulated due to the geometrical symmetry. Inflow

conditions at the thin orifices, as summarized in Table 3.4, are assumed to be sonic with flow

data obtained from 1-D inviscid flow analysis. Indeed, this restriction can be relieved if a

pressure-based NS solver, unlike the current HYB3D code, is selected that can be used to

simulate starting from the stagnation reservoir. Clearly, this flow is too dense for a meaningful

DSMC simulation based on the flow conditions at the orifices (Kn_{throat}=0.00385), while it is

too rarefied for a correct NS simulation due to the near-vacuum ambient environment.

Fig. 3.14 shows the global surface mesh distribution, which is used for the coupled method, along with an exploded view of the surface mesh distribution near the orifice. Note only tetrahedral mesh is used in this simulation. Computational domain extends up to 20D, 10D and 10D, respectively, in the direction of x- (streamwise), y- (crosstreamwise) and z-coordinate (crosstreamwise). Mesh near the orifice lip is intentionally refined considering the large gradient of flow properties in this region. Resulting number of cells is approximately 0.52 million, while other simulation conditions are summarized in Table 3.5. Among these, $Kn_{max}^{Thr.}$ and $P_{Tne}^{Thr.}$ are chosen as 0.05 and 0.1, respectively. One cell layer is used for $\overline{\Omega}_B$, and none for $\overline{\Omega}_C$. In addition, at all outer boundaries supersonic flow boundary conditions and vacuum boundary conditions are assumed, respectively, in the NS and DSMC solver. Fig. 3.15 illustrates the exploded view of the surface mesh distribution of DSMC domain (breakdown region) in the coupled method after 2nd iteration. Related timing data are also shown in Table 3.6 for reference.
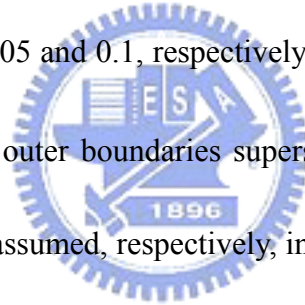
3.2.2 Distributions of Flow Properties

Fig. 3.16 illustrates the density contour distribution at the symmetric and orifice planes. In each orifice jet, the flow expands very quickly into the near-vacuum environment, while at the symmetric line between two orifice jets a secondary jet is clearly formed due to the

expanding molecules from both jets. Fig. 3.17a illustrates the contour distribution of thermal

non-equilibrium ($P_{Tne}^{\cdot}$) at the symmetric and orifice planes, while Fig. 3.17b shows the contour

distribution of thermal non-equilibrium near the orifice with the surface of the breakdown

domain in the enlarged view. It clearly shows that except near the entrance of the orifice jet

most regions are highly non-equilibrium, which necessitates the use of DSMC solver. The

region simulated by the NS solver is considerably small; however, it becomes a formidable

task using the DSMC solver alone at this low Knudsen number (0.00385).

3.2.3 Profile along Center Line between Parallel Twin-Jets

Fig. 3.18 and Fig. 3.19, respectively, illustrate the simulated profile of density and

rotational temperature along the symmetric line between the two jets, along with pure NS data

and experimental data [Soga *et al.*, 1984]. Note both the predicted normalized densities

(hybrid and pure NS), with respect to their peak value, are shown along with the normalized

measured density data in Fig. 3.18a since only relative experimental density data were

provided [Soga *et al.*, 1984], while only absolute predicted ones are illustrated in Fig. 3.18b

for comparison. Thus, Fig. 3.18a only serves to demonstrate the general trend of both

predictions (hybrid and pure NS) coincide with the measurements, except in the near-wall

region. However, Fig. 3.18b clearly shows large discrepancy between the results obtained by

the coupled and NS methods, since the values of continuum breakdown parameters are large

(>0.05) along this symmetric line due to large gradients of flow properties in the near field and

strong rarefaction in the far field. Results show that density first increases very rapidly with increasing x/D, then reaches a maximal value near x/D=2 due to the collisions of gas molecules from both jets and finally decreases rapidly towards ambient value. In contrast, temperature decreases continuously from ~200K at x/D=0 with increasing x/D. Note only the total temperature obtained in the pure NS method is presented due to the assumption of thermal-equilibrium in the NS solver (HYB3D). In this highly rarefied region, the simulated temperature data using coupled method agree reasonably well with experimental data within experimental uncertainties, while the temperature data by NS solver deviate greatly from experimental data as expected. In addition, the simulation data of the coupled method deviate relatively large from the experimental data near the wall region (x/D≤1), which requires further investigation. There are two possible reasons of this large deviation. One is that it might originate from the errors introduced by reflection of light from the wall in Soga's study using fluorescence technique [Soga *et al.*, 1984]. Another possible reason is the inlet flow data assuming 1-D inviscid flow conditions.

3.2.4 Convergence History of Parallel Twin-Jets

Fig. 3.20 and Fig. 3.21 show the convergence history of the L2-norm deviation of density and temperature, respectively. The density deviation decreases from 1.1E-4 kg/m^3 down to 1.3E-5 kg/m^3 and levels off quickly after two coupling iterations, while the temperature deviation shows similar trend decreasing from 30K down to ~1.5K. This fast

57

convergence of the deviation as compared to the case of quasi-2-D wedge flow can be clearly

explained by Fig. 3.22, which shows the Mach number contour distribution near the

breakdown interface for both cases of quasi-2-D wedge flow and of two parallel jets. In Fig.

3.22a subsonic flow dominates in the regions near the breakdown interface above the

boundary layer along the wedge wall that necessitates more number of couplings to exchange

the information between two solvers, although supersonic flow dominates in the regions near

the breakdown interface around the oblique shock. However, in Fig. 3.22b, supersonic flow

dominates near the breakdown interface around entrance regime of orifice jets, which greatly

reduces the number of couplings required for convergence as seen from the simulation. The

above observation is very important from the viewpoints of practical implementation. For

example, in the early stage of simulation we can determine the number of couplings required

for convergence by simply monitoring to which the flow regime near the breakdown interface

belongs. If most flows near the breakdown interface are supersonic, then two coupling

iterations should be enough for convergence. If not, more coupling iterations are required to

have a converged solution. Further investigation in determining the optimum number of

coupling iterations is required in practical applications of the current coupled method.

3.3　Application: Plume Analysis of RCS thrusters

The proposed coupled DSMC-NS method has been verified by the previous two test

cases. To demonstrate its applicability, we apply it to simulate a plume issuing from a RCS thruster, which is a very challenging and important problem in designing the Attitude Determination Control System (ADCS) on a spacecraft.

3.3.1 Flow and Simulation Conditions

Sketch of the plume simulation in the near-field region is shown in Fig. 3.23. Corresponding flow conditions represent a challenging problem since it involves flow regimes from continuum at the nozzle inlet of the thruster to continuum breakdown at downstream, where the DSMC method may be the only available tool for analyzing this problem. Related flow conditions are summarized in Table 3.7 and are listed as follows: nitrogen gas; stagnation pressure P_o=0.1 bar; stagnation temperature T_o= 300 K; nozzle wall temperature of 300K, area ratio of 60 and throat diameter of 4.36 mm. Estimated Reynolds number at the throat using inviscid theory is about 6,200, which is suitable the use of turbulence model in the NS solver. In this study we have used standard $k-\varepsilon$ model unless otherwise specified. Background pressure assumed as vacuum condition (for PDSC) and supersonic flow conditions (for NS solver). In this simulation, the UNIC-UNS code, the NS solver developed by Chen's group [Chen,1989, Shang *et al.*,1995a, Shang *et al.*, 1995b, Shang *et al.*, 1995c, Shang *et al.*, 1997 and Zhang *et al.*, 2001], is used instead of HYB3D. Simulation conditions of the PDSC for coupled method for the RCS thruster plume are summarized in Table 3.8 and are listed as follows: ~210,000-250,000 cells, 2.2-2.5 million

particles, reference timestep size 6.8E-08 seconds and number of sampling timestep 8000.

$Kn_{max}^{Thr.}$ and $P_{Tne}^{Thr.}$ is set as 0.03 and 0.03, respectively. Note the total number of hexahedral

cells is 380,100.

Three-dimensional mesh distribution is shown in Fig. 3.24. The three-dimensional rather

than the axisymmetric mesh is used since we are interested in simulating the far-field plume

interaction with the spacecraft in the future. With the present mesh, we can simply add extra

grid which includes the spacecraft body to the original 3D mesh. Fig. 3.25 shows the

distribution of DSMC and NS domains at 6th iterative step. Note most of the regions inside the

nozzle are NS domain, while DSMC domain dominates outside the nozzle exit with intrusion

along the nozzle wall from the lip to the mid of divergent part of the nozzle. Fig. 3.26 shows

the domain decomposition of NS solver (Fig. 3.26a) and DSMC solver (Fig. 3.26b and 3.26c)

for 6 processors. Since the NS solver does not apply dynamic domain decomposition, the

decomposition remains intact during the runtime, while decomposition of the DSMC solver

adapts during the runtime with dynamic domain decomposition.

3.3.2 Properties Contour

Fig. 3.27 shows the continuum breakdown distribution, while Fig. 3.28 illustrates the

thermal non-equilibrium ratio between translational and rotational degree of freedom. The

continuum breakdown parameter generally increases along the streamlines from the nozzle

and becomes very large due to rapid expansion outside the nozzle. Thermal non-equilibrium ratio shows a similar trend. Fig. 3.29 shows the distribution of the particles per cell in the DSMC domain at the 6th coupling step. It is clearly that in the major portion of the plume the particles per cell is larger than 10, which is generally an acceptable number in DMSC simulation. In addition, it also shows that in the back flow region behind the nozzle outer wall the number of particles per cell is very small, which causes the large scattering of the temperature data which will be presented later.

Fig. 3.30a and Fig. 30b illustrate the density distribution obtained from one-shot NS method and coupled DSMC-NS method at 6th coupling step, respectively. Results clearly demonstrate that with one-shot NS method the density distribution near the edge of the plume is very different, although the core of the plume shows a similar trend. In generally, with the coupled method, the plume expands more as compared to that obtained from one-shot NS method.

Fig. 31a and Fig. 31b show the corresponding distribution of the total temperature obtained from one-shot NS method and coupled DSMC-NS method at 6th coupling step, respectively. Similarly, the temperature contour obtained from the coupled method expands more due to the highly vacuum ambient. Note the highly scattered temperature data in the backflow region originate from the fact that very few or even no particles enter this region,

which was mentioned earlier. Expansion of the flow, similar to a point source, outside the nozzle exit can be clearly seen from Fig. 3.32b, where the flow near the lip of nozzle flows back due to the vacuum ambient. However, this cannot be observed using one-shot NS method, which justifies the use of the coupled method in this problem.

Fig. 3.33a and Fig. 33b illustrate the distribution of Mach number obtained from one-shot NS method and coupled DSMC-NS method at 6th coupling step, respectively. Results obtained from the one-shot NS method are clearly very different from those from coupled method, especially in the core of the plume. With coupled method at the nozzle exit, flow is accelerated up to Mach number of 5-6 (Fig. 33b) with a very thick boundary layer along the nozzle wall. Flow is generally accelerated along the core of the plume obtained from the coupled method, while it is first accelerated and then decelerated along the core of the plume using one-shot NS method, which is not correct due to the breakdown of continuum assumption in this region.

Fig. 3.34 and Fig. 3.35 show the convergence history of L2 norm of density and temperature of the coupled method in the RCS plume simulation, respectively. It is clearly that the L2 norm of density decreases up to 1-2 orders of magnitude within 6-8 couplings, while L2 norm of temperature drops to 1-2 K for the same number of couplings.

In brief summary, we have applied the coupled DSMC-NS scheme to simulate a very

challenging RCS plume in the near-field. The magnitude of stagnation pressure and temperature is not realistic from a practical viewpoint; nevertheless, it represents the first simulation using coupled method to the best knowledge of the author. More realistic operating conditions (~10bar, ~1000K) will be tested in the future by combining the results from the kinetic study which will be presented in Chapter 4.

Chapter 4   Revisit to the Continuum Breakdown

Previously, Wang and Boyd [2003] have proposed a continuum breakdown parameter Kn_{max} based on the maximum value of Knudsen number defined using property gradients, including density, velocity magnitude and temperature. With detailed comparison of solutions between the DSMC and NS solvers [Wang and Boyd, 2003], criterion of Kn_{max} was proposed as 0.05, above which the domain is identified as a continuum breakdown region. With this criterion ($Kn_{max}^{Thr.}$=0.05), the regions across shock waves, expansion waves, leading edges and high shear-rate boundary layers are often identified as continuum breakdown regions in a practical hybrid DSMC-NS simulation.

However, two problems arise using the above-mentioned continuum breakdown criterion proposed by Wang and Boyd [2003]. *Firstly*, detection of the continuum breakdown in the region of high-shear boundary layers necessitates the use of a particle solver, e.g., DSMC method, which is comparatively expensive with respect to the continuum solver, e.g., NS method. *Secondly*, the flow speed normal to the continuum breakdown interface (often approximately parallel to the solid wall) near the boundary layer is very low subsonic since the flow in the boundary layer is largely parallel to the solid wall [Wang *et al.*, 2002, Wu and Lian, 2006]. This causes the slow convergence of coupling between the DSMC and NS solvers if the boundary layer region represents a large portion of the continuum breakdown

region [Wu and Lian, 2006]. The above concerns motivate us to ponder if the value of $Kn_{max}^{Thr.}$

near the solid wall could be revised to a higher value, which can thus reduce the size of

DSMC simulation domain accordingly and possibly speed up the convergence of a hybrid

method by not including the boundary layers as part of the continuum breakdown regions.

However, this can only be justified by if the flow is in thermal equilibrium state in the

boundary layer, even with very large properties gradient. This necessitates a detailed kinetic

study of a well-designed flow problem, in which we can investigate the continuum breakdown

criterion in a more rigorous way.

4.1   Generally Thermal Non-Equilibrium Indicator

In the first phase of the thesis, thermal non-equilibrium indicator is defined only

considering the deviation between translational and rotational temperature for simplicity. To

further efficiently indicate degree of thermal non-equilibrium among various degrees of

freedom, a general thermal non-equilibrium indicator P_{Tne}^{*} is defined as the L2 norm

deviation of different temperature modes shown as follows:

$$P_{Tne}^{*} = \sqrt{\frac{(\frac{T_x}{T_{tot}} - 1)^2 + (\frac{T_y}{T_{tot}} - 1)^2 + (\frac{T_z}{T_{tot}} - 1)^2 + \zeta_{rot}(\frac{T_{rot}}{T_{tot}} - 1)^2 + \zeta_v(\frac{T_v}{T_{tot}} - 1)^2}{(3 + \zeta_{rot} + \zeta_v)}} \quad (4.1)$$

where T_x, T_y and T_z are translational temperature in the x-, y-, z-direction, respectively. T_{rot},

T_v and T_{tot} are rotational, vibrational and total temperature, respectively. ζ_{rot} and ζ_v are the number of degree of freedom of rotation and vibration, respectively. If flow temperature is cold enough, the vibrational effect can be neglected, which is assumed in the following test case. Criterion of this indicator is critical in determining the thermal equilibrium breakdown region, which is major focus in this chapter. The general thermal non-equilibrium indicator P_{Tne}^* is used throughout this chapter unless otherwise specified.

4.2 Kinetic Study with a 2-D Wedge Supersonic Flow

In the present section we conduct a detailed kinetic study for a two-dimensional supersonic nitrogen flow past a 25° finite wedge to investigate if previously defined breakdown criterion in Ref. [Wang and Boyd, 2003] is appropriate or not, especially near an isothermal solid wall, by employing the DSMC method. This test problem represents an idealistic flow for studying the continuum and thermal breakdown parameter since it includes a leading edge near the tip of the wedge surface, an oblique shock wave originating from the leading edge, a boundary layer along the wedge surface and an expanding fan starting at the end of wedge surface.

4.2.1 Flow and Simulation Conditions

A supersonic flow past a 2-D wedge, similar to the first benchmark test in Chapter 3 but

with an extending computational domain to the downstream region, is chosen as the test case

for a detailed kinetic study. Free-stream conditions for this test case, which is the same as

previous test case in Chapter 3, include: gaseous nitrogen as the flowing fluid, a Mach

number (M_∞) of 4, a velocity (U_∞) of 1111.1m/s, a density (ρ_∞) of 6.545E-4kg/m^3 and a

temperature (T_∞) of 185.6K.   The wedge has a wall temperature (T_w) of 293.3K and a length

of 60.69mm.

Fig. 4.1 shows the surface mesh distribution, which is used for the current kinetic study.

Note only hexahedral mesh is used in this simulation. 103,520 DSMC cells and about 8

millions of simulation particles are used for this kinetic test. Fig. 4.2 illustrates the

distribution of continuum breakdown parameter Kn_{max} and the locations of random velocity

sampling in this kinetic study. Totally 52 points in the regions, including near leading edge,

oblique shock, boundary layer and expanding fan, are selected. Velocity distributions of three

Cartesian directions at each selected point are sampled for particles up to at least 0.3 million,

and then are compared with the corresponding local Maxwell-Boltzmann velocity

distributions to understand the degree of continuum breakdown in these representative points.

In addition, the thermal non-equilibrium indicator P_{Tne}^{*} is also calculated at each selected

point from the DSMC simulation. Fig. 4.3 shows the domain distributions of the maximum

local Knudsen number based on the local gradient of the specific flow property according to

eqns. (2.16) and (2.17). In general, the Kn_D and Kn_T dominates the most part of the

67

computational domain and across the oblique shock, respectively, while Kn_V dominates near

the solid wall due to the high velocity gradient in the boundary layer and wake regions.

Results of the kinetic study in each specific region are described in the following in turn.

4.2.2   Region near the Leading Edge

Fig. 4.4a shows the locations of the sampling points 3-7, while Figs. 4.4b-f illustrate

three corresponding Cartesian random velocity distributions at each point, respectively. In Figs.

4.4b-4.4f, the Maxwell-Boltzmann distribution represents the equilibrium state of flow in each

translational degree of freedom, respectively, and temperature ratios in different degrees of

freedom are also listed in these figures. Note the temperatures in each degree of freedom are

normalized to the averaged temperature throughout the study unless otherwise specified.

Firstly, the flows are in continuum (Kn_{max}<0.02 in Fig. 4.2) and in thermal equilibrium state in

each degree of freedom and among all degrees of freedom at Point 3 (Fig. 4b) and 4 (Fig. 4c)

in free stream due to very small property gradients. Secondly, the flow continuum breakdowns

(Kn_{max}>>0.02 in Fig. 4.2) and the flow deviates greatly from the equilibrium state at Point 5

(Fig. 4d), Point 6 (Fig. 4e) and Point 7 (Fig. 4f) very near the leading edge due to very large

property gradients. For better understanding, more quantitative description all probing points

(Figs. 4b-4f) will be stated in the following in turn.

Because the locations of Points 3 and 4 are close to the free stream region, the random

velocity distributions agree very well with the Maxwell-Boltzmann distribution in Figs. 4.4b

and 4.4c. In addition, the maximum temperature deviation to average temperature is lower

than 1% (normalized to T_{tot}) and general thermal non-equilibrium indicator P_{Tne}^*, as defined

in eqn. (4.1), is lower than 0.0021 at both Points 3 and 4. Thus, in the free stream region such

as Points 3 and 4 the flows can be assumed to be in continuum and thermal equilibrium state,

in which the NS equations are valid. As stated earlier, Fig. 4.2 shows the continuum

breakdown parameter Kn_{max} at both Points 3 and 4 is lower than 0.02. Based on the threshold

value $Kn_{max}^{Thr.}$=0.05 proposed previously by Wang and Boyd [2003], locations of Point 3 and 4

shall be assigned as the continuum domain, which is consistent with the above observation by

the present kinetic study.
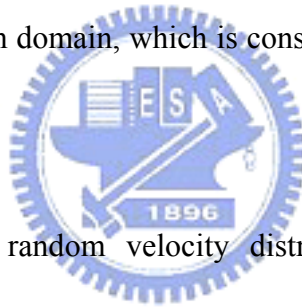
Figs. 4.4d-4.4f show the random velocity distributions deviate greatly from the

Maxwell-Boltzmann distribution, in addition to the large discrepancy of temperatures existing

among the various degrees of freedom. For example, the temperature at Point 6 (very near the

leading edge as shown in Fig. 4e) in the x-direction deviates from the average temperature up

to 87% more. Resulting P_{Tne} and Kn_{max} is approximately 0.45 and 0.8, respectively. Thus, the

use of DSMC method is necessary for such strong non-equilibrium and large deviation from

Maxwell-Boltzmann distribution.

4.2.3 Region near the Oblique Shock

Fig. 4.5a shows the locations of the sampling points 14-19, while Figs. 4.5b-f illustrate three corresponding Cartesian random velocity distributions at each point, respectively. The random velocity distributions in each direction at Points 14 (pre-shock, Fig. 5b) and 19 (post-shock, Fig. 5c) agree very well with the Maxwell-Boltzmann distribution, respectively, because the property gradients are small at Points 14 and 19 which are distant from the oblique shock. The maximum deviation of the temperature from the average temperature is less than 3%, while P_{Tne} and Kn_{max} (Fig. 4.2) is lower than 0.03 and 0.04, respectively. As the locations are close to the oblique shock region, such as Points 15-18, either the random velocity begins to deviate from the Maxwell-Boltzmann distribution (Point 15), the temperature in some degree of freedom begins to deviate from the average temperature (Point 18) or show very large discrepancies of both velocity distribution and thermal non-equilibrium among various degrees of freedom (Points 16 and 17).

For example, temperature in the y-direction at Point 17 can deviate greatly from the average temperature up to 27% more, which results in the P_{Tne} and Kn_{max} approximately as 0.223 and 0.424, respectively. This indicates the regions at Points 16 and 17 near the oblique shock are in continuum breakdown and strong non-equilibrium among various degrees of freedom and should be treated using the DSMC method. In addition, even the random velocity distributions agrees very well to the Maxwell-Boltzmann distribution at Point 18 in

Fig. 4.5f, strong thermal non-equilibrium among various degrees of freedom exists (P_{Tne}=0.101 and $Kn_{\max}$=0.155).

From the above observation of the kinetic study, continuum breakdown parameter $Kn_{\max}$, as defined in eqn. (2.16), with a threshold value $K_{\max}^{Thr.}$=0.05 and previously proposed thermal non-equilibrium indicator, as defined in eqn. (2.18), with a threshold value 0.03 can successfully predict the breakdown of the flow in the leading edge and oblique shock regions. In the next section, the continuum breakdown will be reinvestigated in the regions near the boundary layer and near the expanding fan.

4.2.4 Region near the Boundary Layer
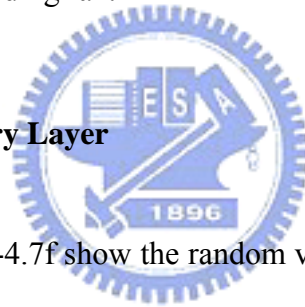
Figs. 4.6b-4.6f and Fig. 4.7b-4.7f show the random velocity distributions at Points 26-30 and Points 31-35 near the boundary layer, respectively, along with the local Maxwell-Boltzmann distribution. Note that Points 26-30, as compared to Points 31-35, are at locations closer to the leading edge, which are expected to have larger property gradients. As shown in Fig. 4.2 in both regions in the boundary layer, very large breakdown parameter Kn_{max} occurs due to the large velocity gradient (Fig. 4.3), especially near the solid wall (Kn_{max}>0.4). Normally these two regions in the boundary layer would be considered as continuum breakdown domains based on previously proposed criterion of $Kn_{\max}$.

Astonishingly at first, at Points 31-35 the velocity distributions are in very good

71

agreement with the local Maxwell-Boltzmann distribution and the temperature variation among different degrees of freedom is very small, even with very large value of Kn_{max} (all higher than 0.05 as shown in Fig. 4.2). At Points 26-30 that are closer to the leading edge, the velocity distributions are also in excellent agreement with the local Maxwell-Boltzmann distribution, although the temperature in both x- and y-direction begins to deviate from the average temperature. Even at Point 30, which is very near the solid wall, the maximum temperature deviation to the average temperature is less than 5-6% (P_{Tne}^{*}=0.034). In addition, at Points 31-35, which is further downstream in the boundary layer, not only the velocity distribution agrees very well with the local Maxwell-Boltzmann distribution, but also the temperature deviation among the various degrees of freedom is very small. Even at Point 35 that is very close to the solid wall, the maximum temperature deviation is less than 3% (P_{Tne}^{*}=0.018). The reason of being capable of maintaining the continuum condition and thermal equilibrium among various degrees of freedom lies in the fact that the particles collide with the isothermal solid wall and are thermalized to the wall temperature before emitting into the region near the wall.

In Fig. 4.2, the continuum breakdown parameter Kn_{max} in the boundary layer region is higher than $K_{max}^{Thr.}$=0.05 recommended by Wang and Boyd [2003]. That means the boundary layer regions would be assigned as the breakdown regions. However, it can be found the random velocity distributions in the x-, y-, z-direction agree excellently with the

72

Maxwell-Boltzmann distribution, respectively, in Figs. 4.7. Furthermore, the value of P_{Tne}

are lower than 0.0185 for all of the Point 31-35. Thus, we can conclude that the degree of the

continuum breakdown in the locations, such as Point 31-35, is overestimated based on the

previous criterion of Kn_{max}. The above kinetic studies indicate that it is not necessary to utilize

the DSMC method in the whole boundary-layer region, even the continuum breakdown

parameter Kn_{max} is very large. This observation is critical in improving the efficiency of a

coupled DSMC-NS scheme presented in Chapter 3.

4.2.5 Region near the Expanding Fan
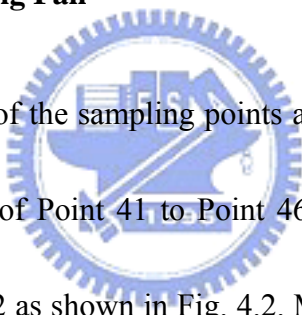
Fig. 4.8 shows the locations of the sampling points and random velocity distributions of

Point 41-46. Along the direction of Point 41 to Point 46, the value of Kn_{max} increase from

0.021 to the maximum value 1.182 as shown in Fig. 4.2. Most of the Points 41-46 are located

in the breakdown domain based on the previous recommended criterion of Kn_{max}, except

Point 41. In Figs. 4.8b-4.8d, random velocity distribution in each direction agrees well with

Maxwell-Boltzmann distribution at Point 41 to 43, while the values of P_{Tne} are higher than

0.03 except at Point 41 (<0.001). In addition, velocity distributions at Points 44 to 46 disagree

appreciably with the local Maxwell-Boltzmann distribution with very high values of Kn_{max}

(>0.2 as shown in Fig. 4.2). Thus, previously proposed criterion of Kn_{max} can correctly predict

the breakdown domain in the expanding fan region.

4.3   Revised Criterion of Continuum Breakdown Parameter

All previous kinetic studies indicate that previously recommended value of continuum breakdown parameter $K_{max}^{Thr.}=0.05$ [Wang and Boyd, 2003] needs to be modified in the boundary layer region. Figs. 4.9-4.12 show the dependence of the L2 norm deviation of random velocity distribution (compared with Maxwell-Boltzmann distribution) and the general thermal non-equilibrium indicator P_{Tne}^{*} with the continuum breakdown parameter Kn_{max} sampled at regions, including leading edge, oblique shock, expanding fan and boundary layer. Note previous proposed criterion of continuum breakdown parameter $K_{max}^{Thr.}=0.05$ and $P_{Tne}^{*}=0.03$ are shown in Figs. 4.9-4.12, while an additional suggested criterion of velocity deviation (0.005) are also shown in these figures. As the velocity deviation is less than 0.005, we define that the velocity distribution coincides with the corresponding local Maxwell-Boltzmann distribution.

In the regions of leading edge, oblique shock and expanding fan (Figs. 4.9-4.11), as Kn_{max} is less than 0.05, velocity deviations of all data points are below 0.005, which demonstrates that breakdown of the flow near the leading edge can be predicted correctly using previously proposed criterion $K_{max}^{Thr.}=0.05$, although several points exhibit higher values of P_{Tne} due to strong thermal non-equilibrium among various degrees of freedom. Interestingly and importantly, in the region of boundary layer along the isothermal solid wall (Fig. 4.12), as Kn_{max} is less than approximately 0.8, velocity deviations of all data points are

still below 0.005, which shows that the degree of continuum breakdown with previously

proposed criterion $K_{\max}^{Thr.}$=0.05 is overestimated in this region. In addition, P_{Tne}^{*} at most of the

data points in this region is below previously proposed $P_{Tne}^{Thr.}$=0.03. By taking these into

account, breakdown region near the boundary layer can be greatly reduced if a new criterion

of continuum breakdown parameter $K_{\max}^{Thr.}$ is adopted. We attribute the maintenance of nearly

equilibrium state to the existence of the isothermal solid wall. When the particles hit the solid

wall, they have to be thermalized with the wall temperature and then emit with Maxwellian

velocity distribution, which in turn enhances the thermal equilibrium of the gas particles near

the solid wall. Thus, with all the data presented in this kinetic study, we proposed this $K_{\max}^{Thr.}$

as 0.8 in the boundary layer region, while keeping the $K_{\max}^{Thr.}$=0.05 in other regions.
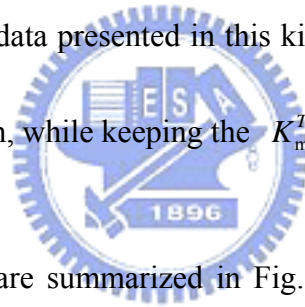
All the above observations are summarized in Fig. 4.12 for brevity, which shows the

distribution of proposed breakdown domains as a function of $Kn_{\max}$ and P_{Tne}. In brief

summary, $K_{\max}^{Thr.}$ is still kept as 0.05 except in the region of boundary layer, in which $K_{\max}^{Thr.}$

is set as 0.8. As for P_{Tne}^{*}, it is set as 0.03, which is the same as previous study [Wu and Lian,

2006].

As mentioned earlier, detection of the continuum breakdown in the region of high-shear

boundary layers necessitates the use of DSMC method, which is comparatively expensive

with respect to the continuum solver. Furthermore, the flow speed normal to the breakdown

interface is very low near the boundary layer, which causes the slow convergence of coupling between the DSMC and NS solvers. Thus, with the new value of $Kn_{max}^{Thr.}$ (=0.8) near the isothermal solid wall, we would expect much shorter runtime due to reduced size of the DSMC domain and fewer coupling required for convergence for our previously proposed coupled DSMC-NS scheme [Wu and Lian, 2006]. Testing of this new criterion of Kn_{max} is currently in progress and will be reported elsewhere.

Chapter 5   Conclusions

5.1   Summary

A coupled DSMC-NS approach using 3-D unstructured mesh is presented to combine the high computational efficiency of the NS solver in continuum and thermal-equilibrium regions with high fidelity of the DSMC method in "breakdown" regions. Furthermore, Breakdown parameters are reinvestigated by a detailed kinetic study and a new criterion of breakdown parameter only for the region near the solid wall is proposed. Studies in this dissertation are described in the following in turn.

In the first phase, flexible overlapping regions between DSMC and NS simulation domains are designed by taking advantage of the unstructured grid topology in both solvers. Two breakdown parameters, including a continuum breakdown parameter proposed by Wang and Boyd [2003] and a thermal non-equilibrium indicator, are employed to determine the DSMC simulation and NS simulation domains, in addition to the concept of overlapping regions. Two benchmark tests are used to verify and validate the proposed coupled DSMC-NS method in Chapter 3. The results from a pure DSMC simulation of a supersonic flow past a quasi-2-D wedge case is chosen as the benchmark data for evaluating and verifying the present coupled method. In addition, a realistic 3-D nitrogen flow, which two

parallel near-continuum orifice jets expands into a near-vacuum environment, is simulated to

demonstrate the capability of the current coupled method in dealing with practical problems.

Then, the present coupled method is also used to simulate a plume issuing from a RCS

thruster, which is a very challenging and important problem in designing the ADCS system

on a spacecraft. The present coupled DSMC-NS method is shown to be capable of accurately

simulating the characteristics of the continuum and thermal-equilibrium breakdown in the test

cases. It is argued that the present coupled approach using flexible overlapping regions can be

easily applied to any DSMC and NS solvers using the unstructured grid topology in general.

Nevertheless, the advantage of applying this coupled method to simulate flow, which is

predominantly continuum, can be highly expected since the computation with the pure DSMC

method is practically impossible and the pure NS solver is incorrect in rarefied regions.
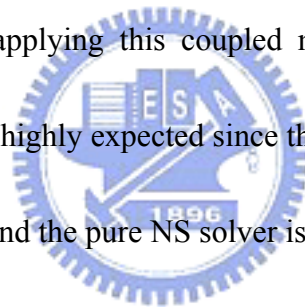
In the second phase, previously proposed continuum breakdown parameter criterion is

re-examined by a detailed kinetic study using the DSMC method in Chapter 4.

Two-dimensional nitrogen supersonic flows (M_∞=4) past a 25° finite wedge are simulated by

PDSC and velocity distributions are sampled at 52 various locations in the computational

domain. Results of the comparison show that thermal equilibrium among various degrees of

freedom near the leading edge, shock and expansion waves breaks down following the

previously proposed value of the $Kn_{\max}^{Thr.}$. However, thermal equilibrium exists in the

boundary layer near the solid wall even the value of the continuum breakdown parameter is

much larger than the previously proposed value of the $Kn_{\max}^{Thr.}$. With very detailed comparison, revised value of the $Kn_{\max}^{Thr.}$ near the solid wall is proposed as (0.8) in the present study.

Some comment about extending the current coupling method to unsteady flows is made as follows. An implicit scheme with a CFL number of 100 is used in the current NS solver while the time step of DSMC is constrained by the limit of a unity CFL number time step. Thus, it is highly possible that the coupling between DSMC and NS solvers can be made at each NS time step, over which DSMC data are accumulated for 100-1000 DSMC time steps. If a sufficiently large number of simulation particles in DSMC can be used along with possible "multilevel" cloning technique [Roveda *et al.*,1998], then a fairly low-noise coupling between DSMC and NS solver for unsteady flows may be performed, although its cost is expected to be high as compared to steady-flow simulation.

5.2   Recommendations for Future Work

Although we have made some progress in developing a coupled DSMC-NS scheme using unstructured mesh that is the first one in this community, there are several studies we would like to recommend in this thesis. Recommended tasks for the future work are briefly summarized in the following:

1.   To test the new criterion of continuum breakdown parameter near the solid wall.

2. To integrate a mesh refinement technique into the proposed coupled DSMC-NS method.

3. To apply this code to flow simulation of expanding plumes from a flying projectile at high altitude, high compression ratio turbomolecular pump and jet-type chemical vapor deposition, to name a few.

4. To extend the current coupling method to unsteady flows.

5. To implement the axisymmetric analysis modeling in the current coupled method.

References

1   Aktas, O. and Aluru, N. R., "A Combined Continuum/DSMC Technique for Multiscale Analysis of Microfluidic Filters", *Journal of Computational Physics*, Vol. 178, pp. 342-372 , 2002.

2   Barth, T. J., "Recent Development in High Order K-Exact Reconstruction on Unstructured Meshes," *AIAA Paper 93-0668*, 1993.

3   Barth, T. J. and Jespersen, D. C., "The Design and Application of Upwind Schemes on Unstructured meshes," *AIAA Paper 89-0366*, 1989.

4   Bird, G. A., *Molecular Gas Dynamics*, Oxford university Press, 1976.

5   Bird, G. A. *Molecular Gas Dynamics and the Direct Simulation of Gas Flows*, Oxford Univ. Press, 1994.

6   Bird, G. A., "Breakdown of Translational and Rotational Equilibrium in Gaseous Expansions," *AIAA Jounral*, Vol. 8, No. 11, pp.1998-2003, 1970.

7   Borgnakke, C., Larsen, P. S., "Statistical Collision Model for Monte Carlo Simulation of Polyatomic Gas Mixture", *Journal of Computational Physics*, Vol.18, 405-420, 1975.

8   Chen, Y.S., "An Unstructured Finite Volume Method for Viscous Flow Computations", *7th International Conference on Finite Element Methods in Flow Problems*, University of Alabama in Huntsville, Huntsville, Alabama, Feb. 3-7, 1989.

9   Cheng, H.-P., Jou, R.-Y., Chen, F.-Z., and Chang, Y.-W., "Three-Dimensional Flow Analysis of Spiral-Grooved Turbo Booster Pump in Slip and Continuum Flow," *Journal of Vacuum Science & Technology A: Vacuum, Surfaces, and Films*, Vol. 18, pp. 543-551, 1999.

10 Garcia, A. L., Bell, J. B., Crutchfield, W. Y. and Alder, B. J., "Adaptive Mesh and Algorithm Refinement Using Direct Simulation Monte Carlo," *Journal of Computational Physics*, Vol. 154, pp. 134-155, 1999.

11 Garcia A. and Alder, B., "Generation of the Chapman-Enskog Distribution," *Journal of Computational Physics*, Vol. 140, Issue 1**,** pp. 66-70, 1998.

12 Glass, C. E. and Gnoffo, P. A., "A 3-D Coupled CFD-DSMC Solution Method with Application to the Mars Sample Return Orbiter," *NASA report TM-2000-210322, 2000*.

13 Hirt, C.W., Amsden, A.A. and Cook, J.L., "An Arbitrary Lagrangean-Eulerian Computing Method for all Flow Speeds," *Journal of Computational Physics*, Vol. 14, pp.

226-253, 1974.

14 Ivanov, M. S., D. Khotyanovsky, V., Kudryavtsev, A. N., Vashchenkov, P. V., Markelov, G. N. and Schmidt, A. A., "Numerical Study of Backflow for Nozzle Plumes Expanding into Vacuum," *37th AIAA Thermophysics Conference*, *AIAA Paper 2004-2687*, 2004.

15 Karki, K.C. and Patankar, S.V., "Pressure Based Calculation Procedure for Viscous Flows at all Speeds in Arbitrary Configurations," *AIAA Journal*, Vol. 27, pp. 1167-1174, 1989.

16 Karypis, G. and Kumar, V., METIS: A Software Package for Partitioning Unstructured Graphs, Partitioning Meshes, and Computing Fill-Reducing Orderings of Sparse Matrices, 1998.

17 Karypis, G. and Kumar, V., *ParMETIS* 3.1: An MPI-based Parallel Library for Partitioning Unstructured Graphs, Meshes, and Computing Fill-Reducing Orderings of Sparse matrices, 2003.

18 Koomullil, R. P., Soni, B. K. and Huang, C.-T., "Navier-Stokes Simulation on Hybrid Grids," *34th Aerospace Sciences Meeting and Exhibit*, *AIAA 96-0768*, 1996.

19 Koomullil, R. P., Soni, B. K., Huang, C.-T., "Unsteady Flow Simulations on Hybrid Grids," in *Proc. First AFOSR Conference in Dynamic Motion CFD, Rutgers Unuversity, NJ, June 3-5, 1996*, edited by L. Sakell and D. D. Knight, pp. 427-434.

20 Koomullil, R. P., Soni, B. K. and Huang, C.-T., "Flow Simulations on Generalized Grids," in *Proc. 5th International Conference on Numerical Grid Generation in Computation Fluid Dynamics and Related Fields*, Mississippi State University, MS, April 1-5, 1996, edited by B. K. Soni, J. F. Thompson, J. Hauser and P. Eiseman, pp. 527-536.

21 Koomullil, R. P. and Soni, B. K., "Flow Simulation Using Generalized Static and Dynamics Grids," *AIAA Journal*, Vol. 37, pp. 1551-1557, 1999.

22 Launder, B.E. and Spalding, D.B., "The Numerical Calculation of Turbulent Flows," *Computer Methods in Applied Mechanics and Engineering*, Vol. 3, pp. 269-289, 1974.

23 Nanbu, K., "Theoretical Basis on the Direct Monte Carlo Method," *1th International Symposium on Rarefied Gas Dynamics*, Teubner, Stuttgart, 1986.

24 Nicol, D. M. and Saltz, J. H., "Dynamic Remapping of Parallel Computations with Varying Resource Demands", *IEEE Transactions on Computers*, Vol. 37, pp. 1073-1087, 1988.

25 Roveda, R. and Goldstein, D. B. and Varghese, P. L., "Hybrid Euler/Particle Approach

for Continuum/Rarefied flows," *Jounral of Spacecraft and Rockets*, Vol. 35, 258-265, 1998.

26   Shang, H.M., Chen, Y.S., Liaw, P., Shih, M.S. and Wang, T.S., "Numerical Modeling of Spray Combustion with an Unstructured Grid Method", *AIAA Paper 95-2781*,1995.

27   Shang, H.M., Chen, Y.S., Liaw, P. and Chen, C.P., "A Hybrid Unstructured Grid Method for Fluid Flow Computation", *Numerical Developments in CFD Symposium of the Joint ASME/JSME Fluids Engineering Conference*, Hilton Head Island, SC, August 13-18, 1995.

28   Shang, H.M., Shih, M.H., Chen, Y.S., and Liaw, P., "Flow Calculation on Unstructured Grids with a Pressure-Based Method", *Proceedings of 6th International Symposium on Computational Fluid Dynamics*, Lake Tahoe, NV, Sep. 4-8, 1995.

29   Shang, H.M. and Chen, Y.S., "Unstructured Adaptive Grid Method for Reacting Flow Computation", *AIAA Paper 97-3183,* July 1997.

30   Takanishi, T. M. and Yasuhara, M., "Experimental Study of Interation of Underexpended Jets," *14th International Symposium on Rarefied Gas Dynamics, Tsukuba Science City, Japan, 1984*, edited by H. Oguchi, pp. 485-493.

31   Taniguchi, M., Mori, H., Nishihira, R. and Niimi, T., "Experimental Analyses of Flow Field Structures around Clustered Linear Aerospike Nozzles," *24th International Symposium on Rarefied Gas Dynamics*, *AIP Conference Proceeding*, Vol. 762, pp. 349-354, 2005.

32   Venkatakrishnan,V., "Convergence to Steady State Solutions of the Euler Equations on Unstructured Grids with Limiters," *Journal of Computational Physics*, Vol. 118, pp. 120-130, 1995.

33   Versteeg, V., Avedisian, C. T. and Raj, R., "Method and Apparatus for CVD Using Liquid Delivery System with an Ultrasonic Nozzle," *U.S Patent Number: 5,451,260* (1994)

34   Wagner, W., "A Convergence Proof for Bird's Direct Simulation Monte Carlo method for the Boltzmann equation," *Journal of Statistical Physics*, Vol. 66 (3/4), pp. 1011-1044, 1992.

35   Wang, W.-L., Sun, Q.-H. and Boyd, I. D., "Towards Development of a Hybrid DSMC-CFD Method for Simulating Hypersonic Interacting Flows," *8th AIAA/ASME Joint Thermophysics and Heat Transfer Conference* , *AIAA Paper 2002-3099*, 2002.

36   Wang, W.-L. and Boyd, I. D., "Predicting Continuum Breakdown in Hypersonic Viscous

Flows," *Physics of Fluids*, Vol. 15, Issue 1, pp. 91-100, 2003.

37 Wilmoth, Richard G., Yellin, Keith A. and Papp, John L. "Continuum-DSMC Coupling Issues for Steady and Unsteady Two-Phase Plumes," *28th EPTS and 10th SPIRITS User Group Joint Meeting*, San Diego, CA, Nov. 1-5, 2004.

38 Wu, J.-S. and Tseng, K.-C., "Parallel DSMC Method Using Dynamic Domain Decomposition," *International Journal for Numerical Methods in Engineering*, Vol. 63, pp. 37-76, 2005.

39 Wu, J.-S. and Lian, Y.-Y., "Parallel Three-Dimensional Direct Simulation Monte Carlo Method and Its Applications," *Computers & Fluids*, Vol. 32, pp. 1133-1160, 2003.

40 Wu, J.-S., Tseng, K.-C. and Wu, F.-Y., "Parallel Three Dimensional Direct Simulation Monte Carlo Method Using Unstructured Adaptive Mesh and Variable Time Step," *Computer Physics Communications*, Vol. 162, 166-187, 2004.

41 Wu, J.-S. and Tseng, K.-C., Lee, U.-M. and Lian, Y.-Y., "Development of a General Parallel Three-Dimensional Direct Simulation Monte Carlo Code," *24th International Symposium on Rarefied Gas Dynamics, AIP Conference Proceedings*, Vol. 762, pp. 559-564, 2005.

42 Wu, J.-S., Lian, Y.-Y., Cheng, G. and Koomullil, R. P., "Validation of a Coupled DSMC-NS Scheme Using Unstructured Mesh," *Journal of Computational Physics*, 2006 (accepted).

43 Zhang, S.J., Liu, J., Chen, Y.-S. and Wang, T.-S., "Adaptation for Hybrid Unstructured Grid with Hanging Node Method," *AIAA Paper 2001-2657*, 2001.

Algorithm 2.1 Procedures of locating breakdown regions and Boundary-I.

Subroutine ***Set_Breakdown_domain_Boundary-I***

#

    Input both of the right- and the left-hand side cells for each cell interface.

    Input P_{Tne} and Kn_{max} of each cell from the last iterative solution.

D_j: identifier of the domain types for the specific cell j.

=0, for the breakdown domain $\overline{\Omega}_A$; =1, for the overlapping region $\overline{\Omega}_B$;

=2, for the overlapping region $\overline{\Omega}_C$; =3, for the rest of the region $\overline{\Omega}_D$

Initialize array domain type number.

    Set D = 3 for all cells.

Initialize array IBIF (*Indicator of Boundary-I faces*).

*Indicator of Boundary-I faces* array records if the specific cell interface k belongs to

one of the Boundary-I faces.

    Set IBIF = 0 for each cell interface.

Mark the cells of the breakdown domain $\overline{\Omega}_A$ as 0.

    for each cell i **do**

        if $((P_{Tne})_i \geq P_{Tne}^{Thr.}$ **OR** $(Kn_{max})_i \geq Kn_{max}^{Thr.})$ **then**

            Set D_i=0

        end if

    end for

Mark the faces of Boundary-I.

    for each cell interface k **do**

        iR = the right-side cell of cell interface k

        iL = the left-side cell of cell interface k

        if $(D_{iR} \backslash= D_{iL})$ **then**

            $IBIF_k$ = 1

        end if

    end for
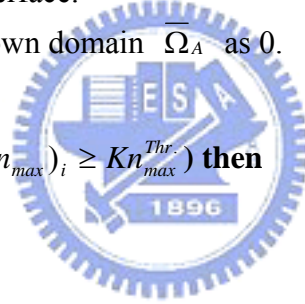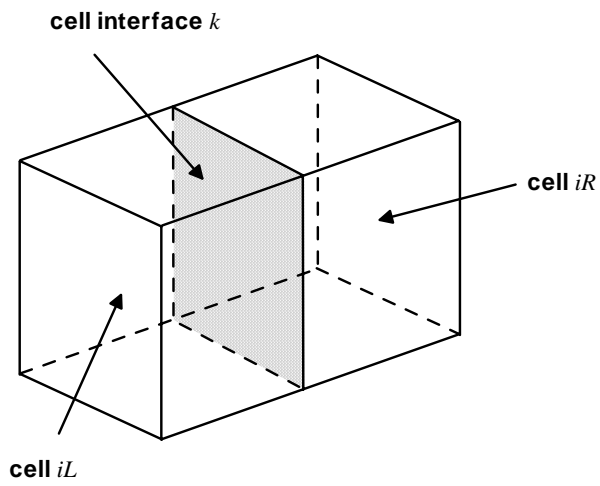
(a) Hexahedral cell type   (b) Tetrahedral cell type
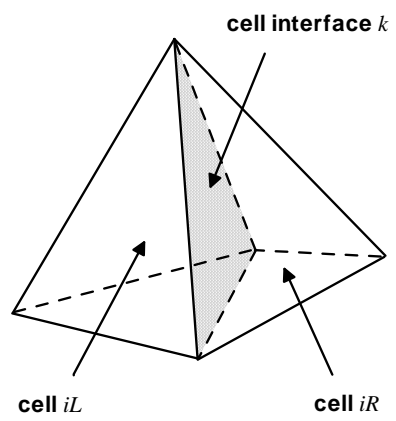
The right-side cell *iR* and left-side cells *iL* for the specific cell interface *k*

Algorithm 2.2 Procedures of locating overlapping regions and Boundary.

Subroutine *Set_overlapping_regions_and_Boundary*

\#

    Input the list of cells surrounding each node.

\#   Initialize array IBIN (*Indicator of Boundary-I nodes*)

\#   ICLN (*Indicator of current layer nodes*)

\#   INLN (*Indicator of next layer nodes*)

\#   Array of *Indicator of Boundary-I nodes* records if the specific node j belongs to one of

\#   the Boundary-III faces.

\#   *Current layer nodes* is a special node group which forms a close layer of the current

\#   extended overlapping regions and breakdown domains in each extension of

\#   overlapping regions layer-by-layer. Once each layer extension of overlapping is

\#   completed, nodes of *Current layer* will be updated with the *next layer nodes.*

    Set IBIN = 0, ICLN = 0 and INLN = 0 for each node.

\#   *Indicator of Boundary-III faces* array records if the specific cell interface k belongs to

\#   one of the Boundary-III faces.

\#   Initialize array IBIIIF (Recorder of Boundary-III faces)

    Set IBIIIF = 0 for each cell interface.

\#   Preset the numbers of cell layers for each overlapping domain $\overline{\Omega}_B$ and $\overline{\Omega}_C$.

    Set No_layers(1) = 4

    Set No_layers(2) = 2

\#   Mark the nodes on Boundary-I

    for each cell interface k such that IBIF $_k$ == 1 **do**

        for each node j of cell interface k **do**

            IBIN$_j$ = 1

        end for

    end for

\#   Nodes on the on Boundary-I is the first close node layer of the breakdown domains.

\#   Mark all the nodes on Boundary-I as the nodes of currently searched node layer.

    ICLN(:) = IBIN (:)

\#   Mark cells of domain $\overline{\Omega}_B$ ($R = 1$) and $\overline{\Omega}_C$ ($R = 2$) by searching layer-by-layer

\#   extension.

    for overlapping region $R = 1, 2$ **do**

        Set $n = 1$

        while (n No_layers(R)) **do**

            for each node j such that ICLN$_j$ == 1 **do**

$\quad$**for** each cell i surrounding node j such that $D_i == 3$ **do**

$\qquad$ Set $D_i = R$

$\qquad$**for** each node k of cell i such that $ICLN_k == 0$ **do**

$\qquad\quad$**if** $(INLN_k == 0)$ **then**

$\qquad\qquad INLN_k == 1$

$\qquad\quad$**end if**

$\qquad$**end for**

$\quad$**end for**

end for

$ICLN(:) = INLN(:)$

$INLN = 0$

$n = n + 1$

end while

end for

\#$\quad$Mark the faces of Boundary-III

$FBIII = 0$

\#$\quad$Remark: $D_i = 3$ means the cell i belong to $\overline{\Omega_D}$ in NS domain

for each cell interface k **do**

$\quad iR =$ the right-side cell of cell interface k

$\quad iL =$ the left-side cell of cell interface k

$\quad$**if** $((D_{iR} == 3 \text{ } \mathbf{AND} \text{ } D_{iL} == 2) \text{ } \mathbf{OR} \text{ } (D_{iR} == 2 \text{ } \mathbf{AND} \text{ } D_{iL} == 3))$ **then**

$\qquad FBIII_k = 1$

$\quad$**end if**

end for
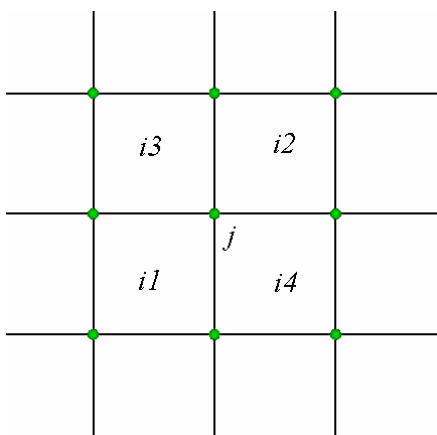
(a) Quadrilateral cell type $\qquad\qquad\qquad$ (b) Triangular cell type
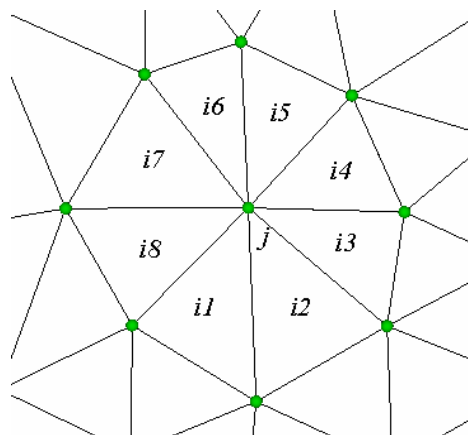
The list of cells surrounding the specific node j

Algorithm 2.3 General procedures of the proposed coupled DSMC-NS method.

Main loop

\#

    Set MCI = maximum number of coupling iterations

\#   Initial "one-shot" NS simulation for whole domain

    call NS solver (HYB3D or UNIC-UNS) (for the whole simulation domain)

\#   Coupling Iterations

    loop = 1

    while (*loop*   MCI **) do**

        call Subroutine *Set_breakdown_domai_and_Boundary-I*

        call Subroutine *Set_overlapping_regions_and_Boundary-III*

        call Subroutine *Extract_Boundary-III_data_for_DSMC_solver*

\#   For domain $\overline{\Omega}_A \bigcup \overline{\Omega}_B \bigcup \overline{\Omega}_C$

        call DSMC code *PDSC*

        call Subroutine *Extract_Boundary-I_data_for_NS_solver*

\#   For domain $\overline{\Omega}_B \bigcup \overline{\Omega}_C \bigcup \overline{\Omega}_D$

        call NS solver

        call Subroutine *Solution_update*

        loop = *loop* + 1

    end do
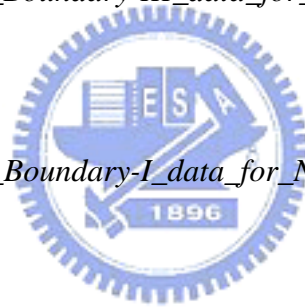
Algorithm 2.4 Procedures of extracting Boundary-III data for DSMC solver.

Subroutine ***Extract_Boundary-III_data_for_DSMC_solver***

$n=0$

for each cell interface k such that $\text{FBIII}_k = 1$ **do**

$n=n+1$

iR = the right-hand side cell of cell interface k

iL = the left-hand side cell of cell interface k

average flow properties of both cell iR and iL as flow data of the *n-th* face of

DSMC hybrid boundary

end for

Algorithm 2.5 Procedures of extracting Boundary-I data for NS solver.

Subroutine *Extract_Boundary-I_data_for_NS_solver*

#

    for each cell interface k such that $FBI_k = 1$ **do**

        iR = the right-hand side cell of cell interface k

        iL = the left-hand side cell of cell interface k

        if ($D_{iR} = 0$) **then**

            set flow data of cell interface k with flow properties of cell iR from DSMC domain

        else

            set flow data of cell interface k with flow properties of cell iL from DSMC domain

        end if

    end for

Table 3.1   Free-stream conditions in supersonic flow over quasi-2-D 25o wedge.

Gas	ρ_∞	U_∞	T_∞	M_∞
N_2	6.545E-4kg/m^3	1111m/s	185.6K	4

Table 3.2   Four simulation sets with various parameters in supersonic flow over quasi-2-D 25° wedge.

Set No.	1	2	3	4
Cell layer No. of $\overline{\Omega}_B$	4	2	4	4
Cell layer No. of $\overline{\Omega}_C$	2	1	2	2
$Kn_{max}^{Thr.}$	0.02	0.02	0.04	0.02
$P_{Tne}^{Thr.}$	0.03	0.03	0.03	0.06
Final DSMC cells	~85,000	~71,000	~64,000	~84,000
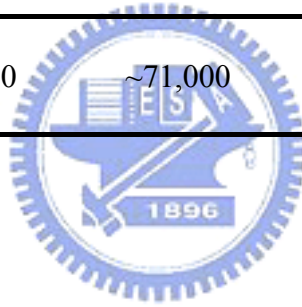
Table 3.3   Total computational time (hours) with pure NS solver, pure DSMC and coupled method in supersonic flow over quasi-2-D 25° wedge.

	Pure NS	Pure DSMC	Coupled DSMC-NS method[*]		
			One-shot NS	DSMC	NS
			2.8	12.2	9.2
Total time	2.8	16.3		24.2	

[*]10 coupling iterations are used in the coupled method for 2-D 25° wedge flow.

Table 3.4   Sonic conditions at the orifice exiting plane in two parallel near-continuum orifice free jets flow.

Gas	ρ_{throat}	U_{throat}	T_{throat}	Re_{throat}
N_2	6.52E-3 kg/m^3	314 m/s	237.5 K	401

Table 3.5   Simulational conditions of two parallel near-continuum orifice free jets flow.

Method	DSMC for coupled method
Cell No.	~470,000
Sim. Particle No.	~6,200,000
Reference Δt (sec)	3.01E-09
Sampling time steps	13,500
Cell layer No. of $\overline{\Omega}_B$	1
Cell layer No. of $\overline{\Omega}_C$	0
$Kn_{max}^{Thr.}$	0.05
$P_{Tne}^{Thr.}$	0.1

* Total cell No. of computational domain for coupled DSMC-NS method is 520,830

Table 3.6   Total computational time (hours) with pure NS solver and coupled method in two parallel near-continuum orifice free jets flow.

	Pure NS	Coupled DSMC-NS method[*]		
		One-shot NS	DSMC	NS
		2.5	22.2	4.1
Total time	2.5		30.8	

[*]3 coupling iterations are used for a converged solution in the coupled method.

Table 3.7   Flow conditions of the plume simulation issuing from RCS thruster

Gas	P_o	T_o	T_w	D_{throat}	Re_{throat}	Area ratio
N_2	0.1 bar	300K	300K	4.36mm	6,256	60

Table 3.8   Simulation conditions of the plume simulation issuing from RCS thruster.

Method	DSMC for coupled method
Cell No.	210,000~250,000
Sim. Particle No.	2,200,000~2,500,000
Reference Δt (sec)	6.9E-08
Sampling time steps	8,000
Cell layer No. of $\overline{\Omega}_B$	2
Cell layer No. of $\overline{\Omega}_C$	1
$Kn_{max}^{Thr.}$	0.03
$P_{Tne}^{Thr.}$	0.03

* Total number of the hexahedral cells for coupled DSMC-NS method is 380,100.
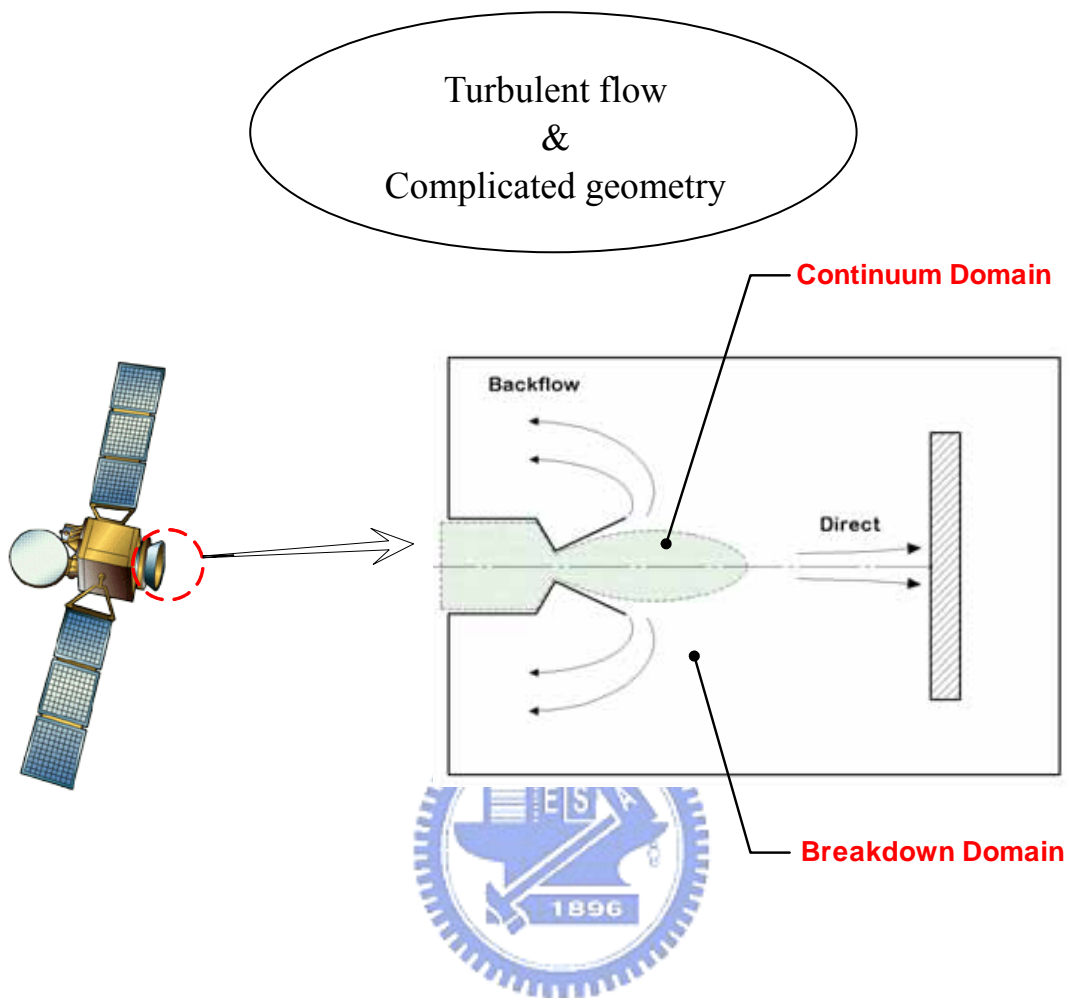
Fig. 1.1   Sketch of expanding reaction control system plumes.
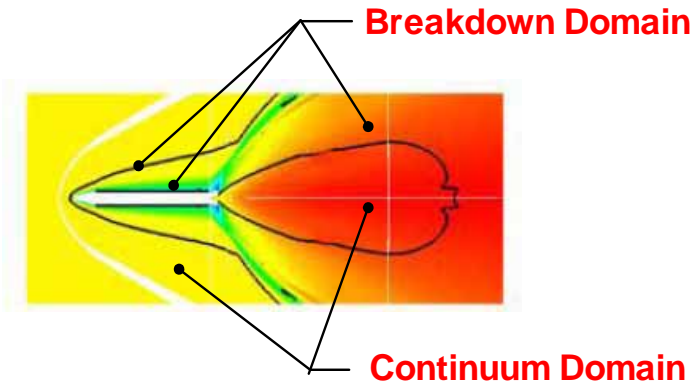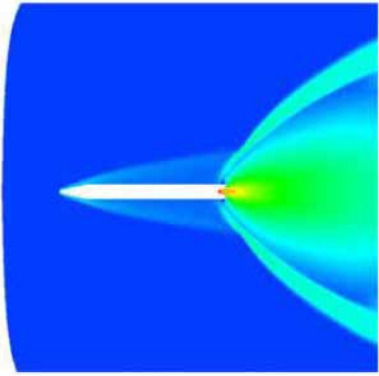
Fig. 1.2   Sketch of expanding flying object plume at high altitude.
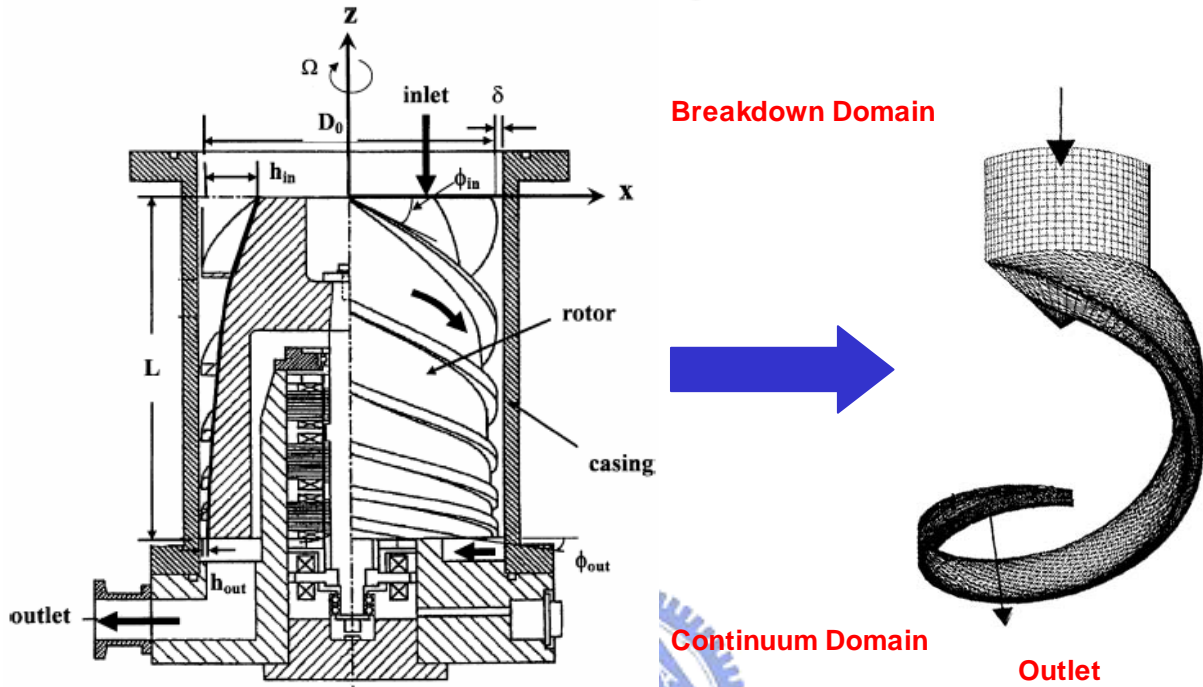
Fig. 1.3   Sketch of a sketch of spiral-grooved turbo booster pump.
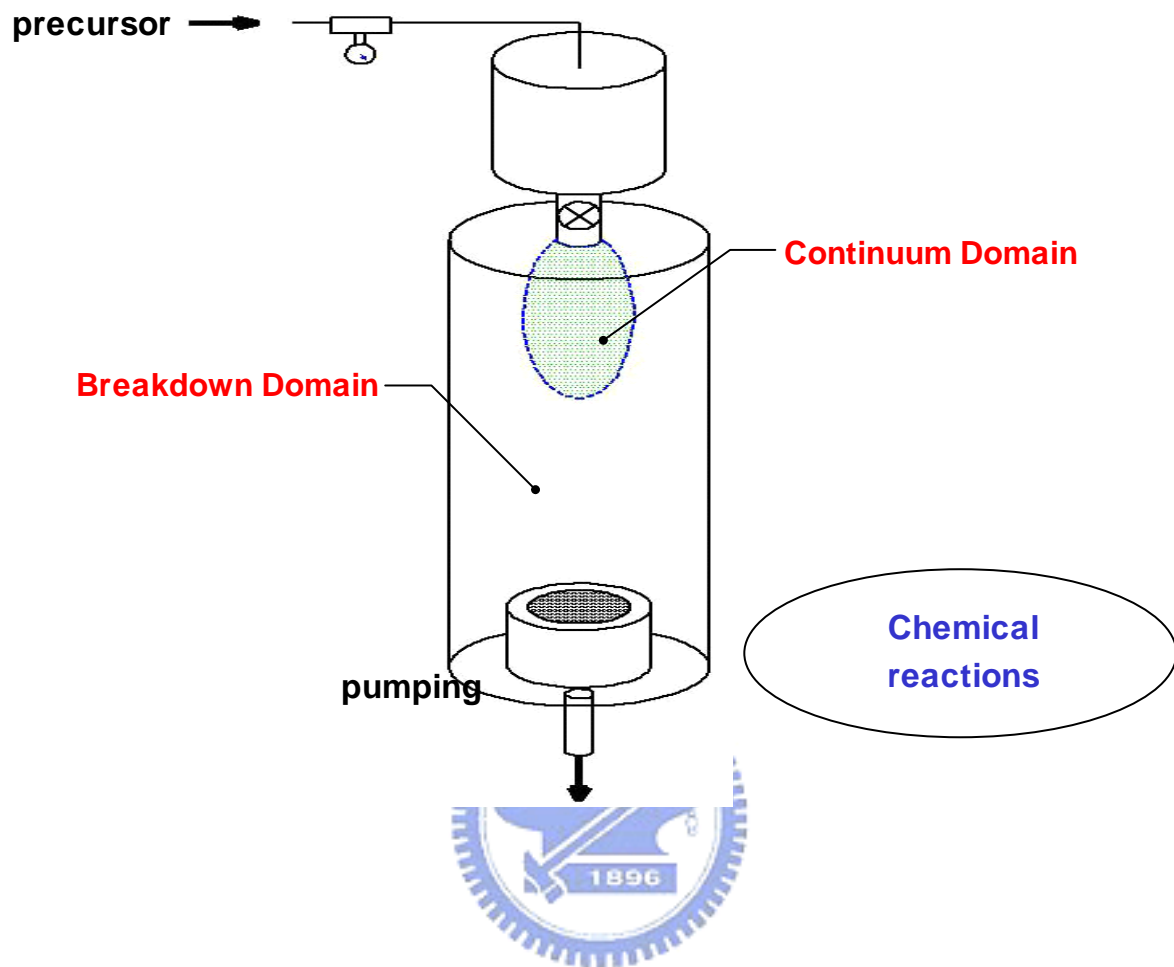
Fig. 1.4   Configuration of a jet-type CVD reactor.
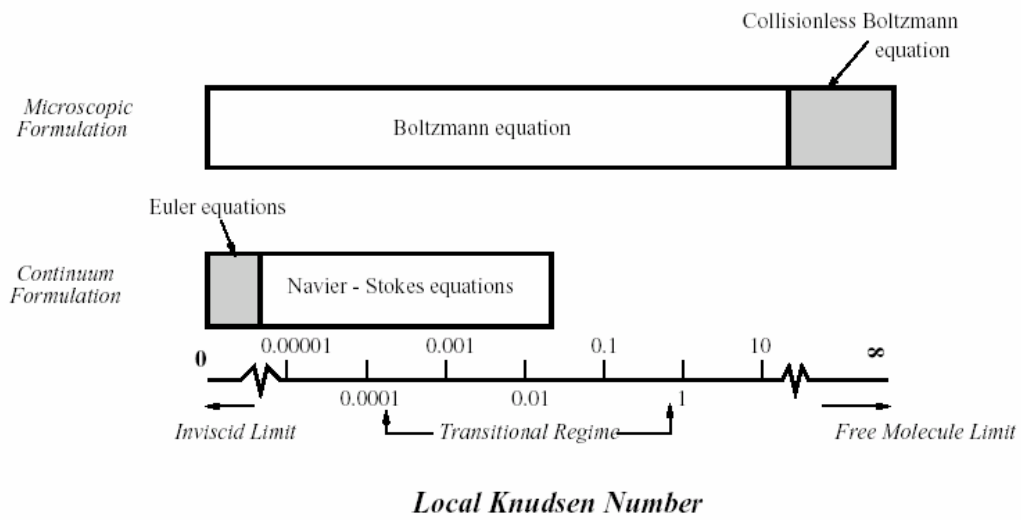
Fig. 1.5   Schematic sketch of solution method applicability in a dilute gas.
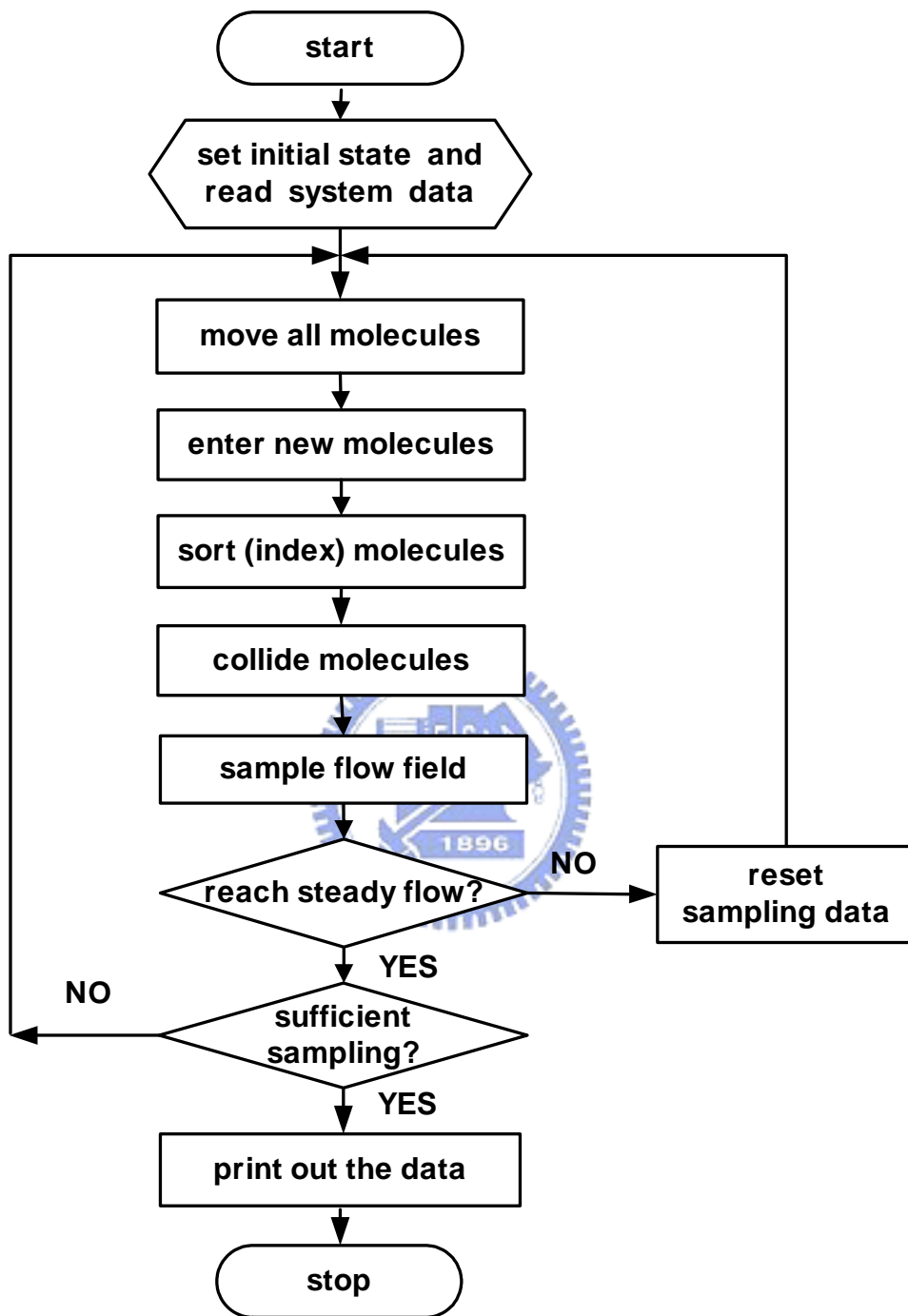
Fig. 2.1   Flow chart of the DSMC method.

105

$\bar{n}=(a,b,c)$

(x_f, y_f)

(x_i, y_i)

$\Delta t'$
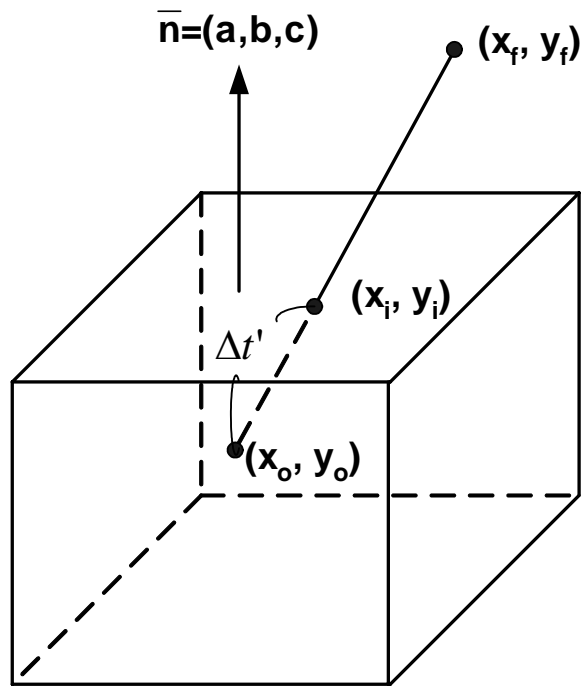
(x_o, y_o)

(x_o, y_o) : the initial position (x_f, y_f) : the final position

(x_i, y_i) : the intersection position $\Delta t'$: intersecting time

Fig. 2.2   Sketch of the particle movement in three-dimensional unstructured mesh.
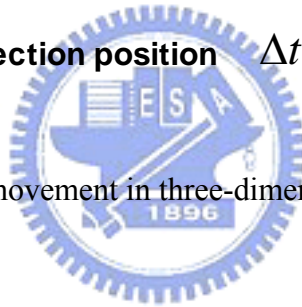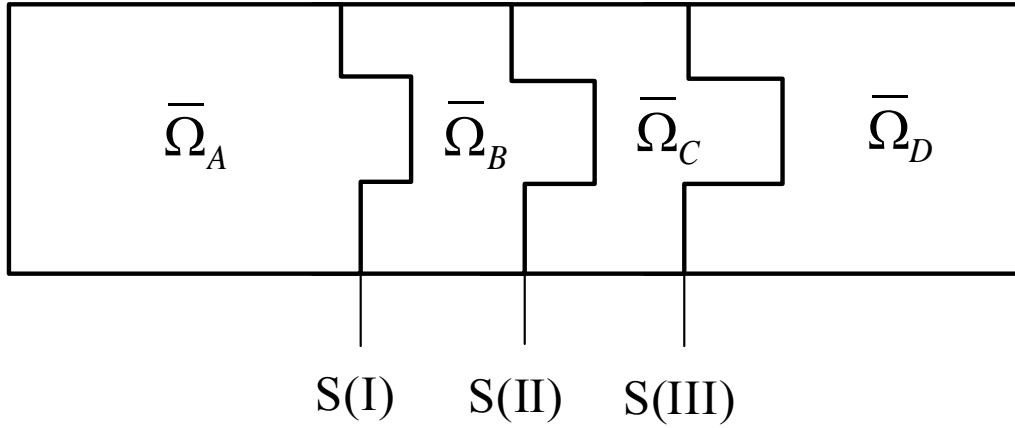
$\overline{\Omega}_A$: $\left\{ \overline{\Omega}_{P_{T_{ne}}} \bigcup \overline{\Omega}_{Kn_{max}} \right\}$ Union of continuum breakdown and thermal non-equilibrium regions

$\overline{\Omega}_B$: The extension of $\overline{\Omega}_A$ with some specified number of cell layers

$\overline{\Omega}_C$: The further extension of $\overline{\Omega}_B$ with some specified number of cell layers

$\overline{\Omega}_A \bigcup \overline{\Omega}_B \bigcup \overline{\Omega}_C$: DSMC simulation domain

$\overline{\Omega}_B \bigcup \overline{\Omega}_C \bigcup \overline{\Omega}_D$: NS solver simulation domain

$\overline{\Omega}_A \bigcup \overline{\Omega}_B$: Domain with flow properties updated from DSMC calculation

$\overline{\Omega}_C \bigcup \overline{\Omega}_D$: Domain with flow properties updated from NS calculation

$S(I) = \overline{\Omega}_A \bigcup \overline{\Omega}_B$:   Boundary-I (Dirichlet B.C.) for NS simulations

$S(II) = \overline{\Omega}_B \bigcup \overline{\Omega}_C$:   Boundary-II for updated solution using different solvers

$S(III) = \overline{\Omega}_C \bigcup \overline{\Omega}_D$: Boundary-III (Dirchlet B.C.) for DSMC simulations

Fig. 2.3   Sketch of domain distribution of the present coupled DSMC-NS method with overlapping regions and boundaries
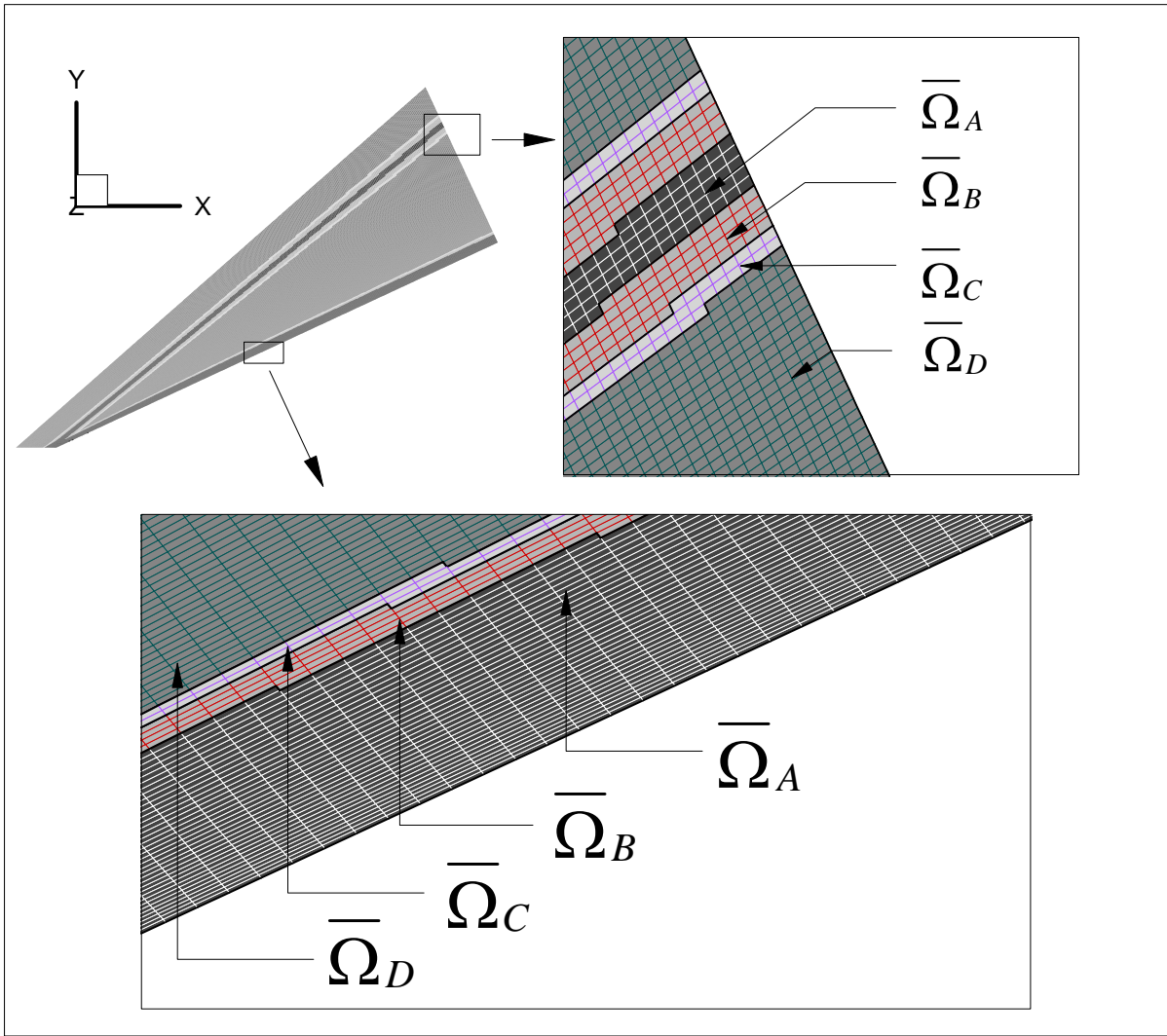
Fig. 2.4 A typical example of the overlapping regions between the particle and the continuum domains.

N$_2$, Ma=4
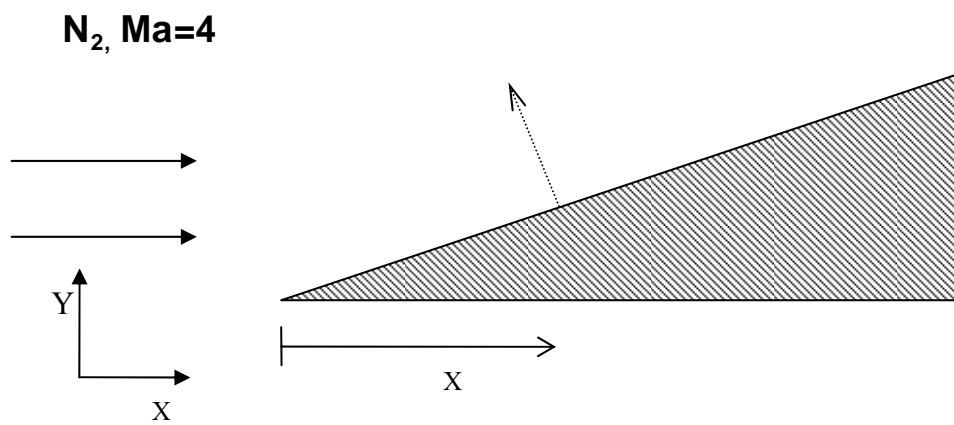
Fig. 3.1　　Sketch of a hypersonic flow over 25° 2-D wedge

Level D (kg/m^3)

Level	D (kg/m^3)
6	3.0E-03
5	2.5E-03
4	1.0E-03
3	9.6E-04
2	7.9E-04
1	6.5E-04

Fined Grid (180,000 cells)

Coarse Grid (120,000 cells)

Grid Sensitivity Test
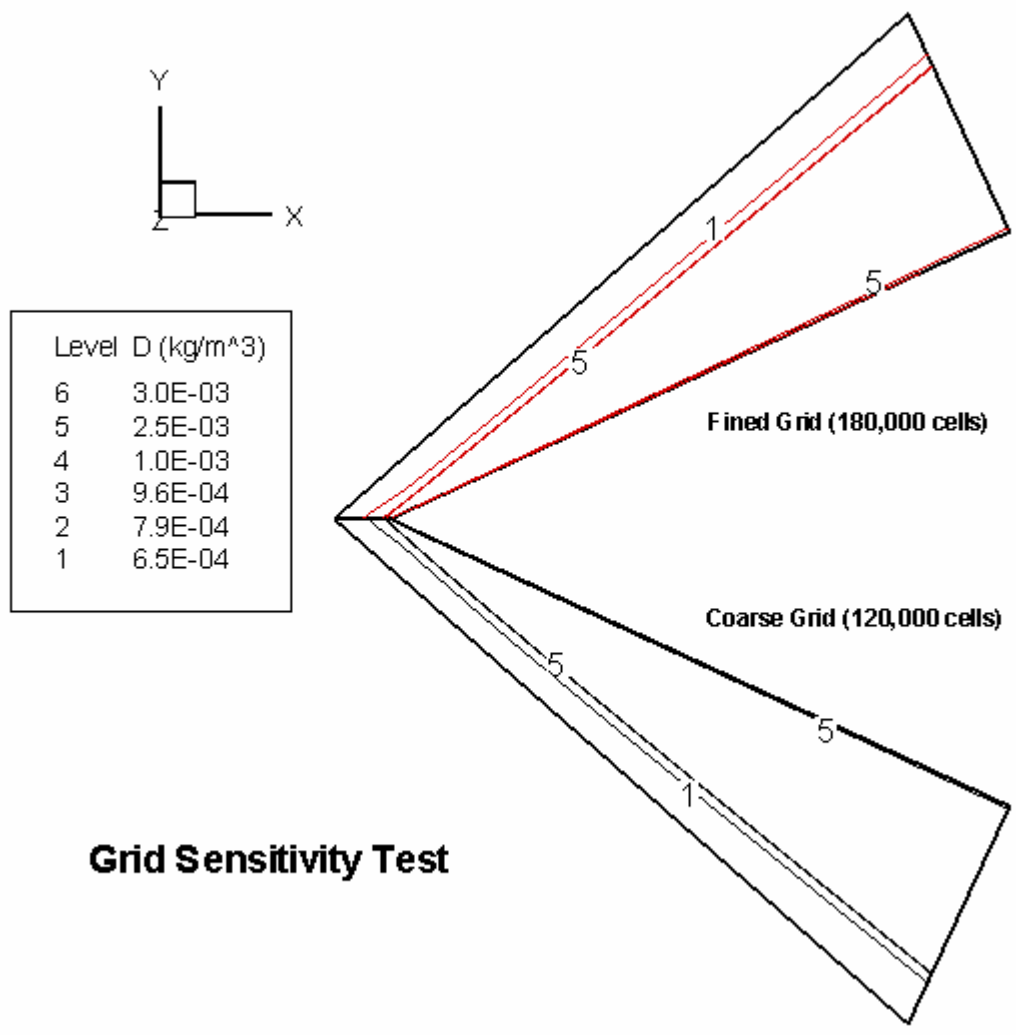
Fig. 3.2a   Grid sensitivity test of HYB3D on quasi-2-D 25° wedge flow (Density).
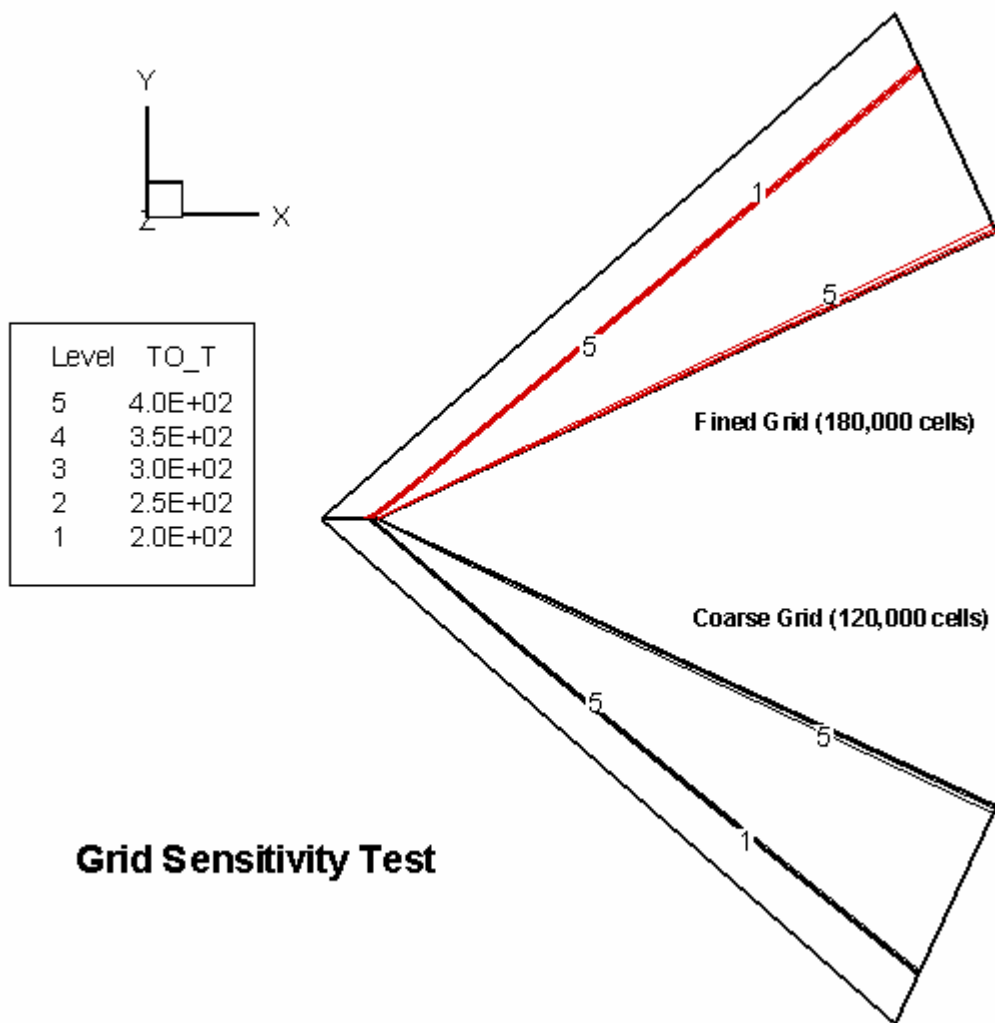
Fig. 3.2b   Grid sensitivity test of HYB3D on quasi-2-D 25° wedge flow (Total temperature).
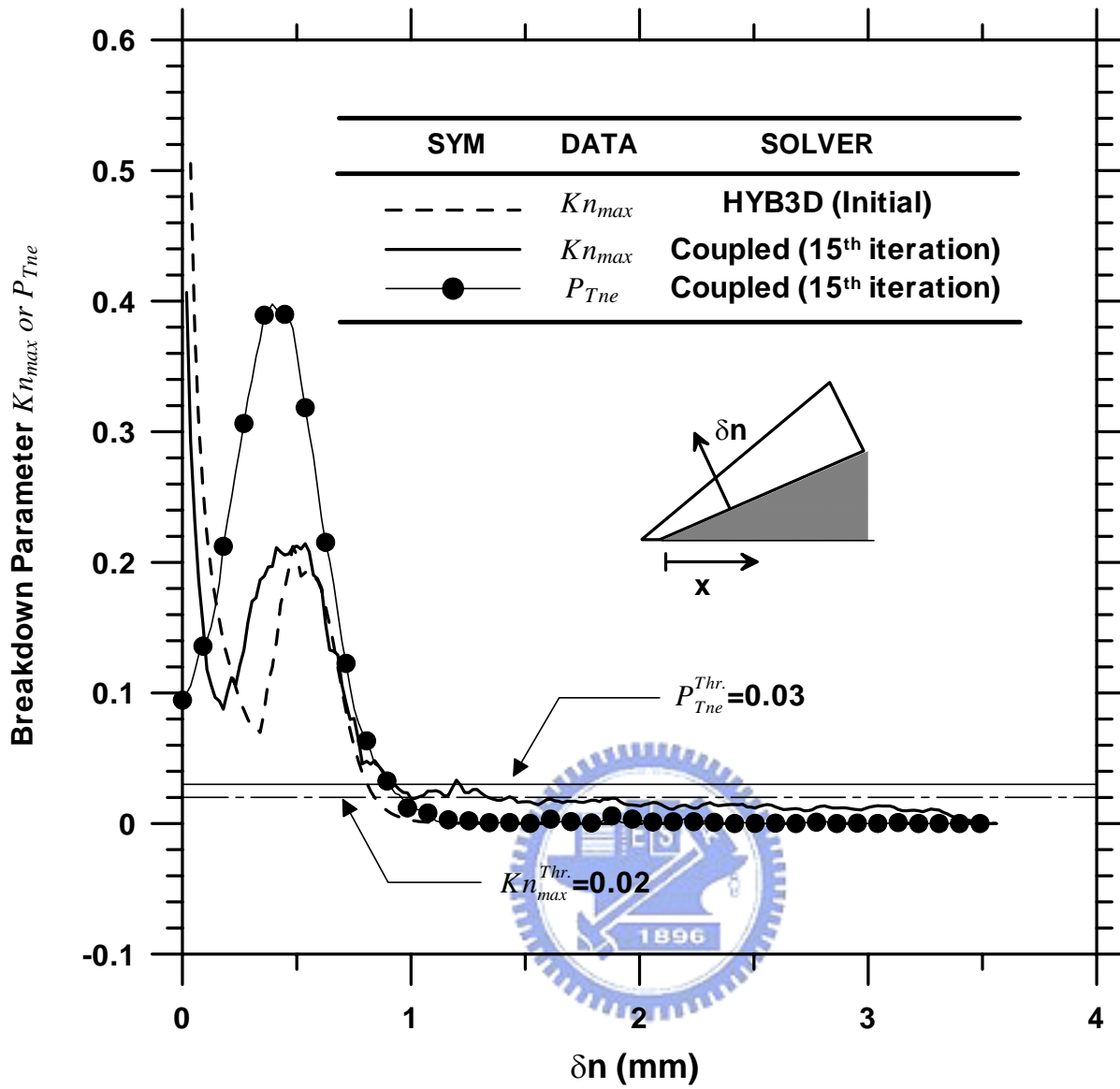
Fig. 3.3a   Breakdown parameters along the line normal to the wedge at x=0.5mm.
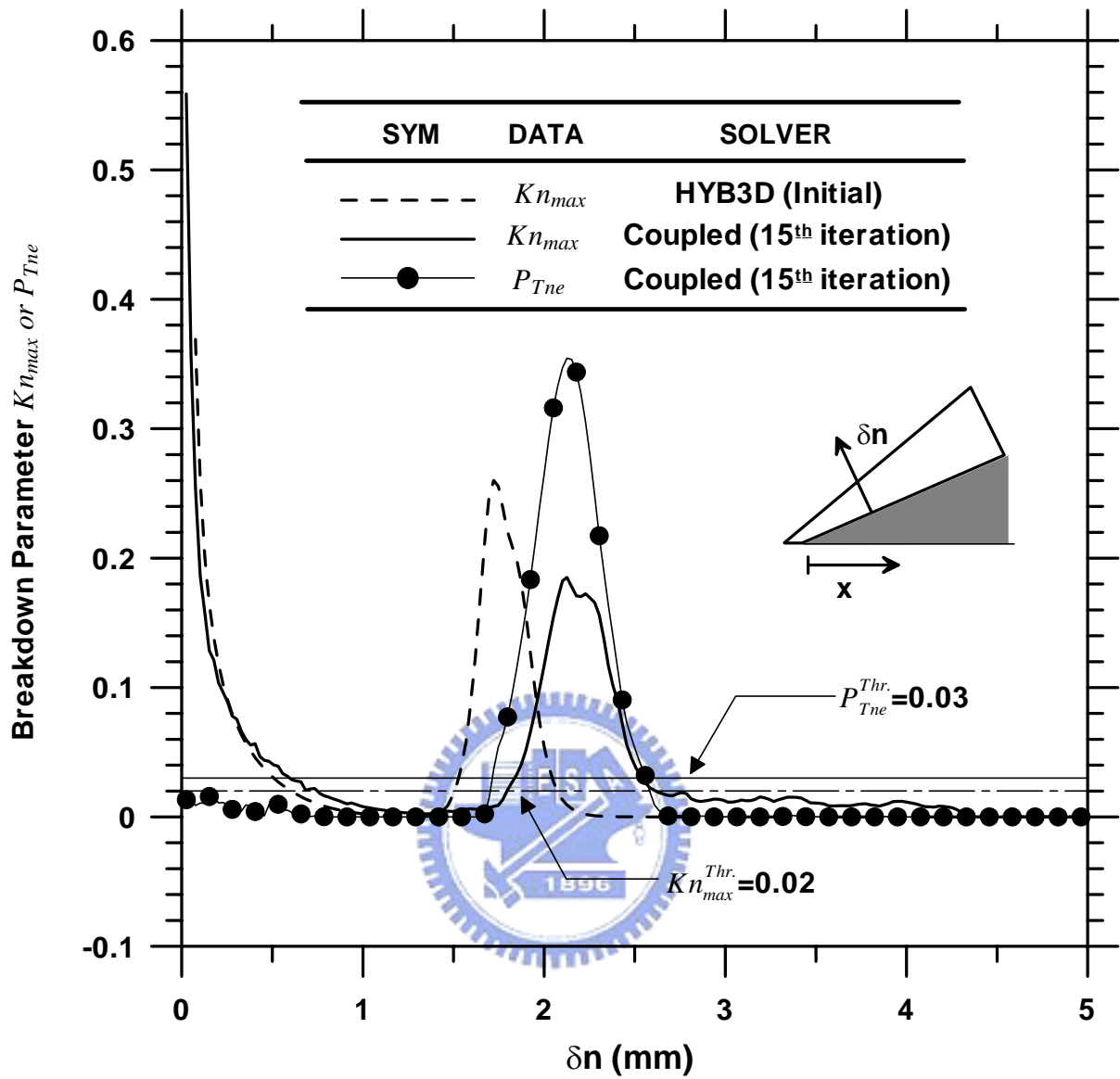
Fig. 3.3b   Breakdown parameters along the line normal to the wedge at x=5mm.
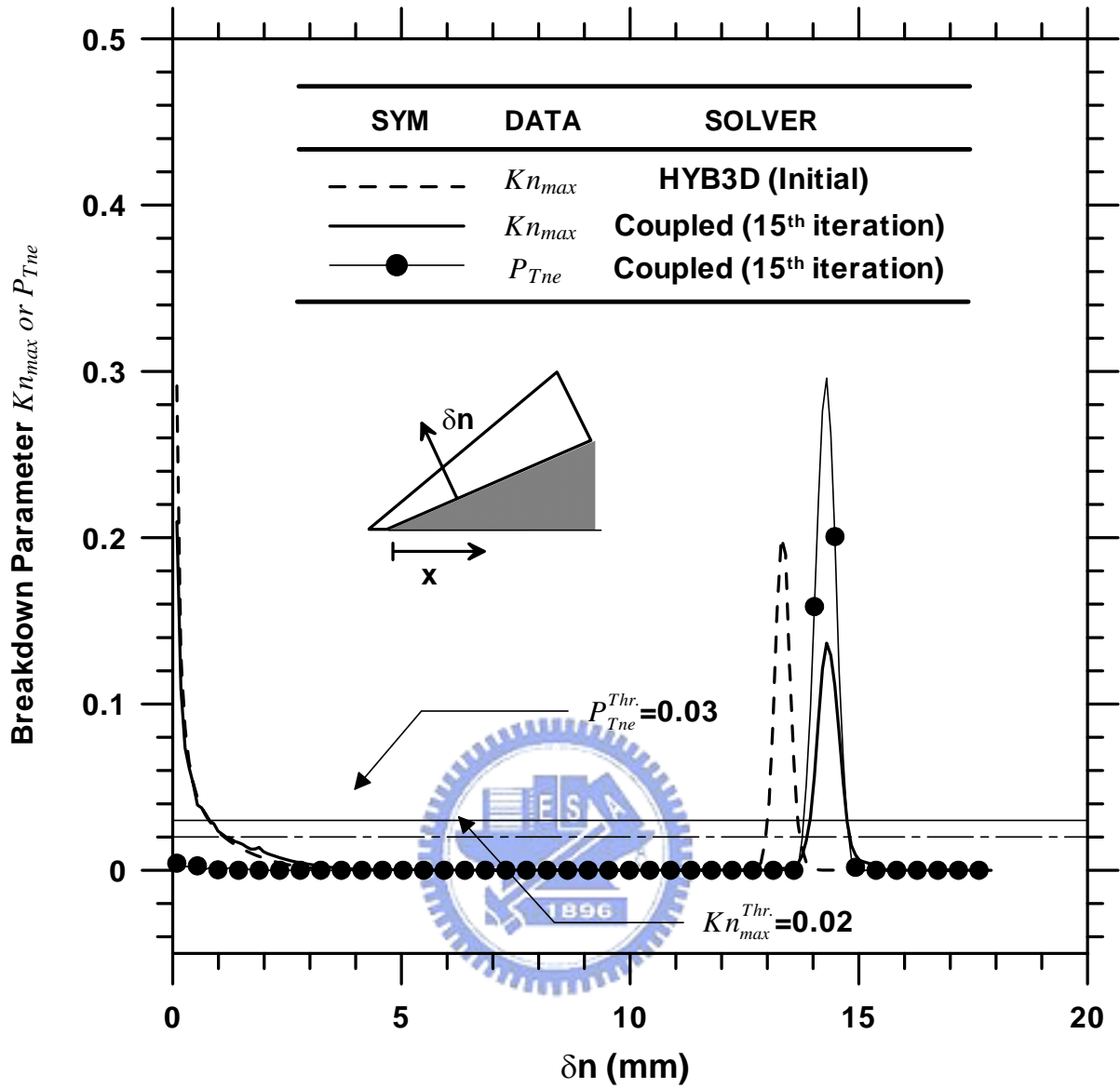
Fig. 3.3c   Breakdown parameters along the line normal to the wedge at x=50mm.

114
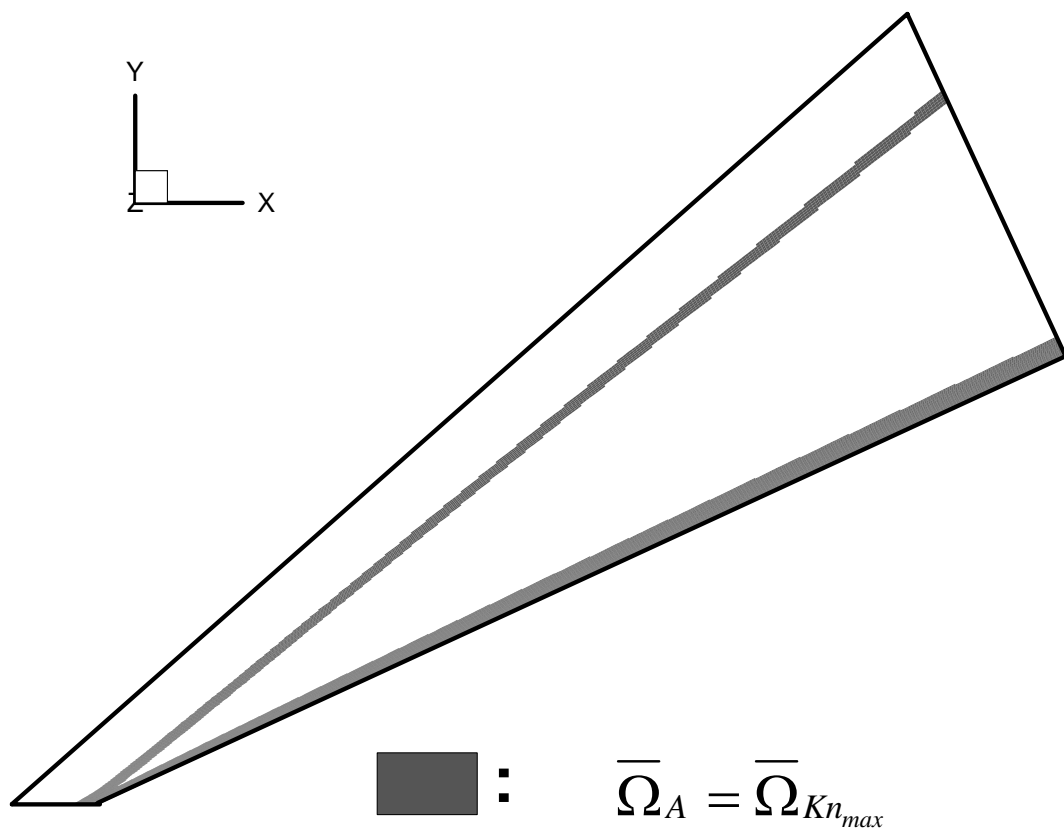
Fig. 3.4a   Initial continuum breakdown (NS) domain distribution in quasi-2-D 25° wedge flow.
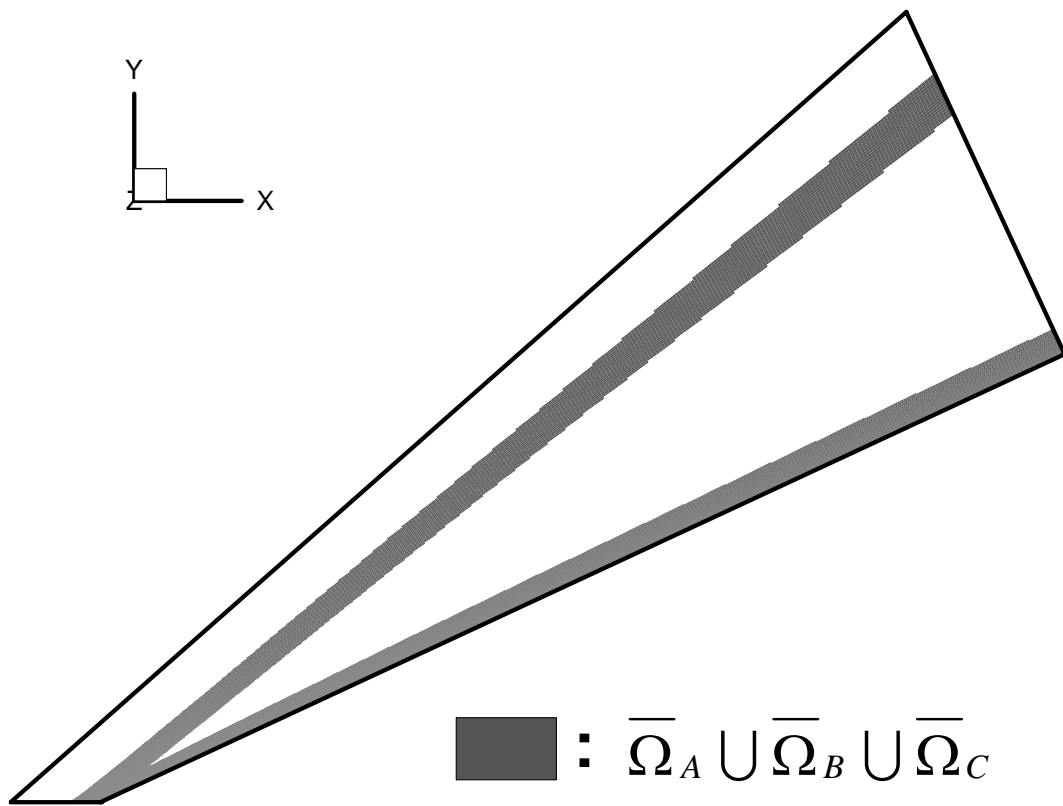
Fig. 3.4b   Initial DSMC domain including the overlapping regions in quasi-2-D 25$^\text{o}$ wedge flow.
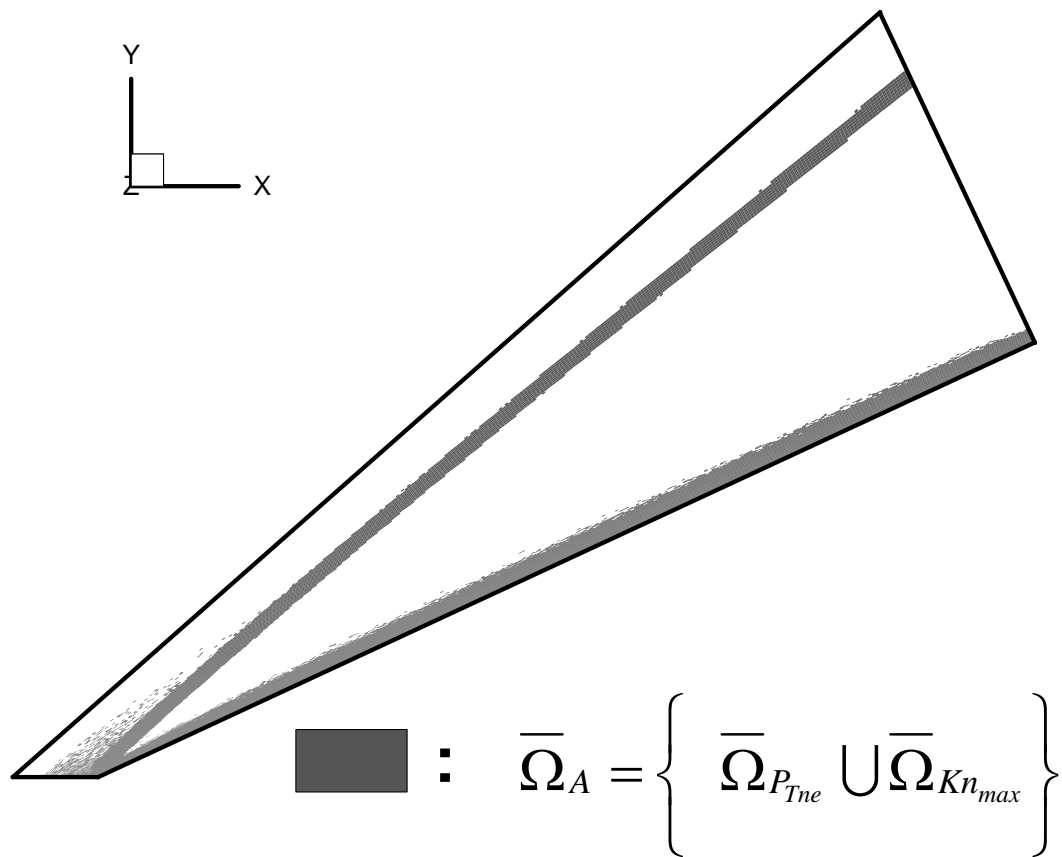
Fig. 3.5a   Breakdown domain distribution at 15th coupling iteration in quasi-2-D 25° wedge flow.

The figure contains the legend:

$$\blacksquare \; : \; \overline{\Omega}_A = \left\{ \overline{\Omega}_{P_{Tne}} \bigcup \overline{\Omega}_{Kn_{max}} \right\}$$
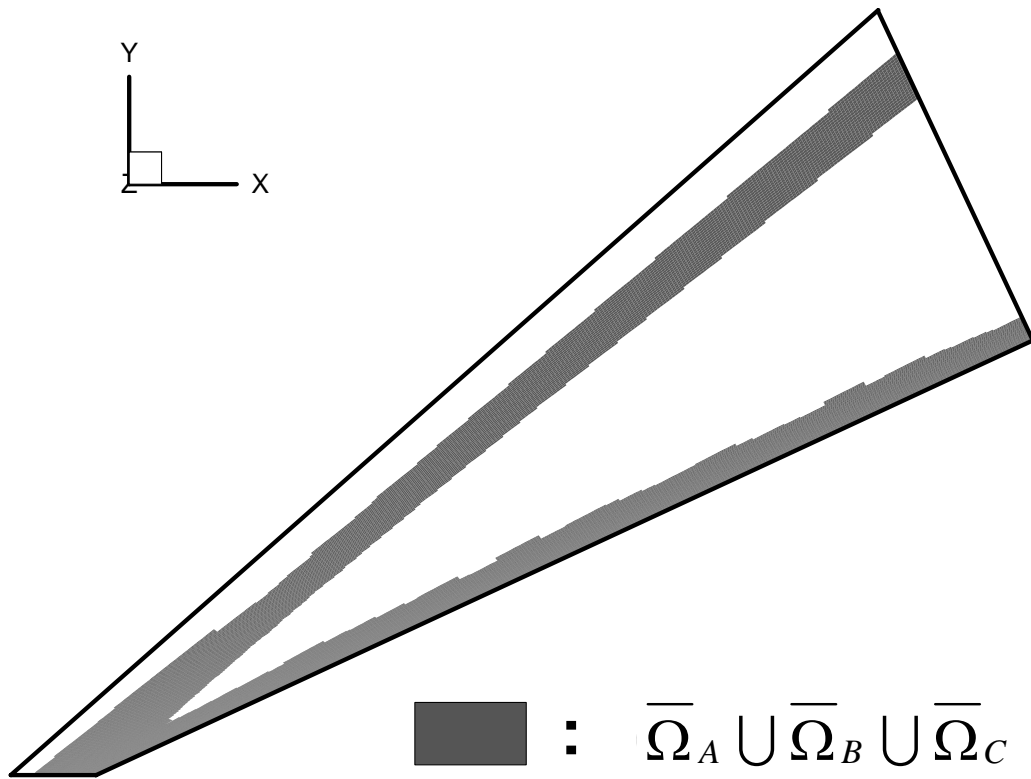
Fig. 3.5a DSMC domain including the overlapping regions at 15th coupling iteration in quasi-2-D 25° wedge flow.
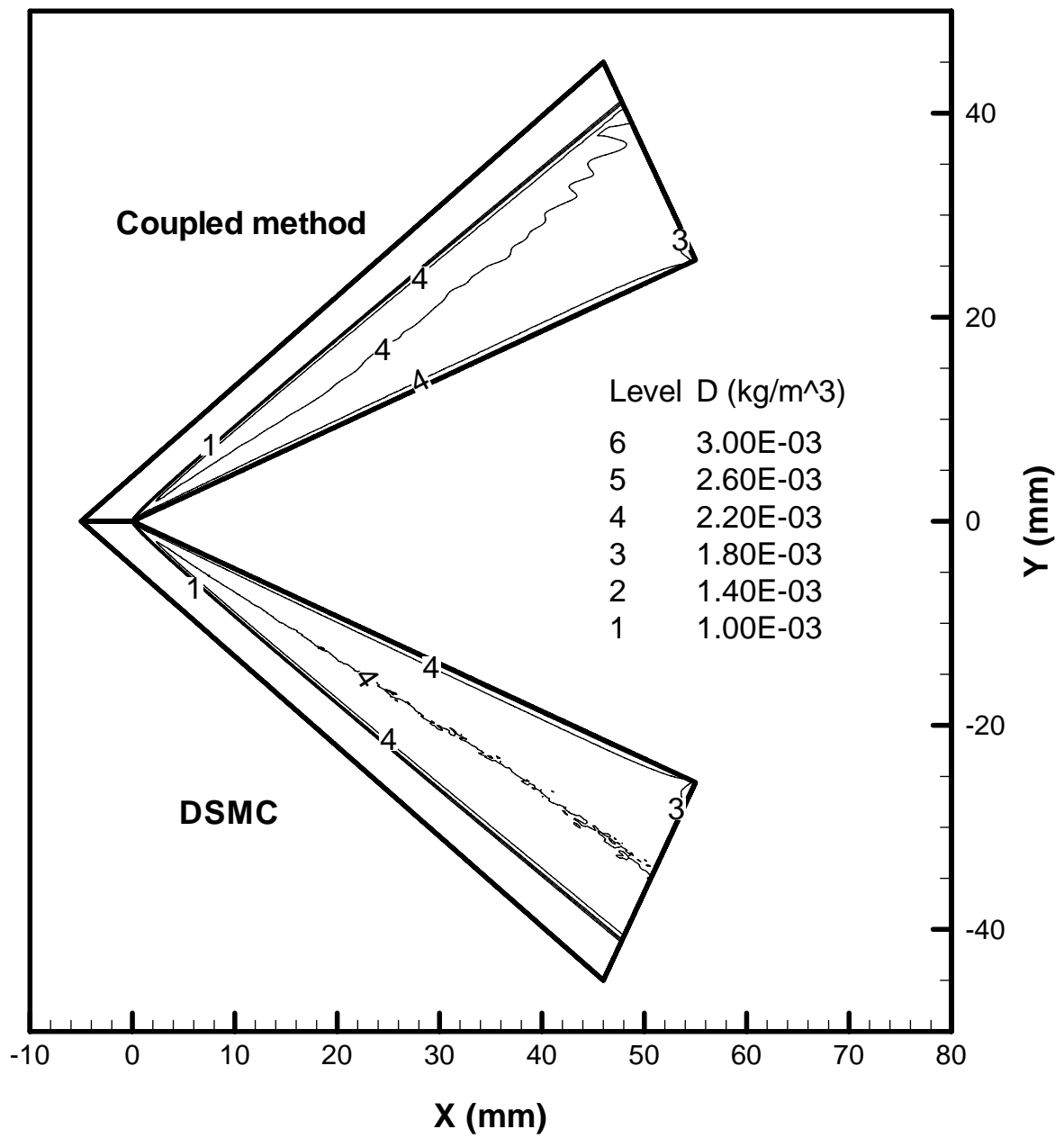
Fig. 3.6a Density comparison between the DSMC method and the present coupled DSMC-NS method in quasi-2-D 25° wedge flow.
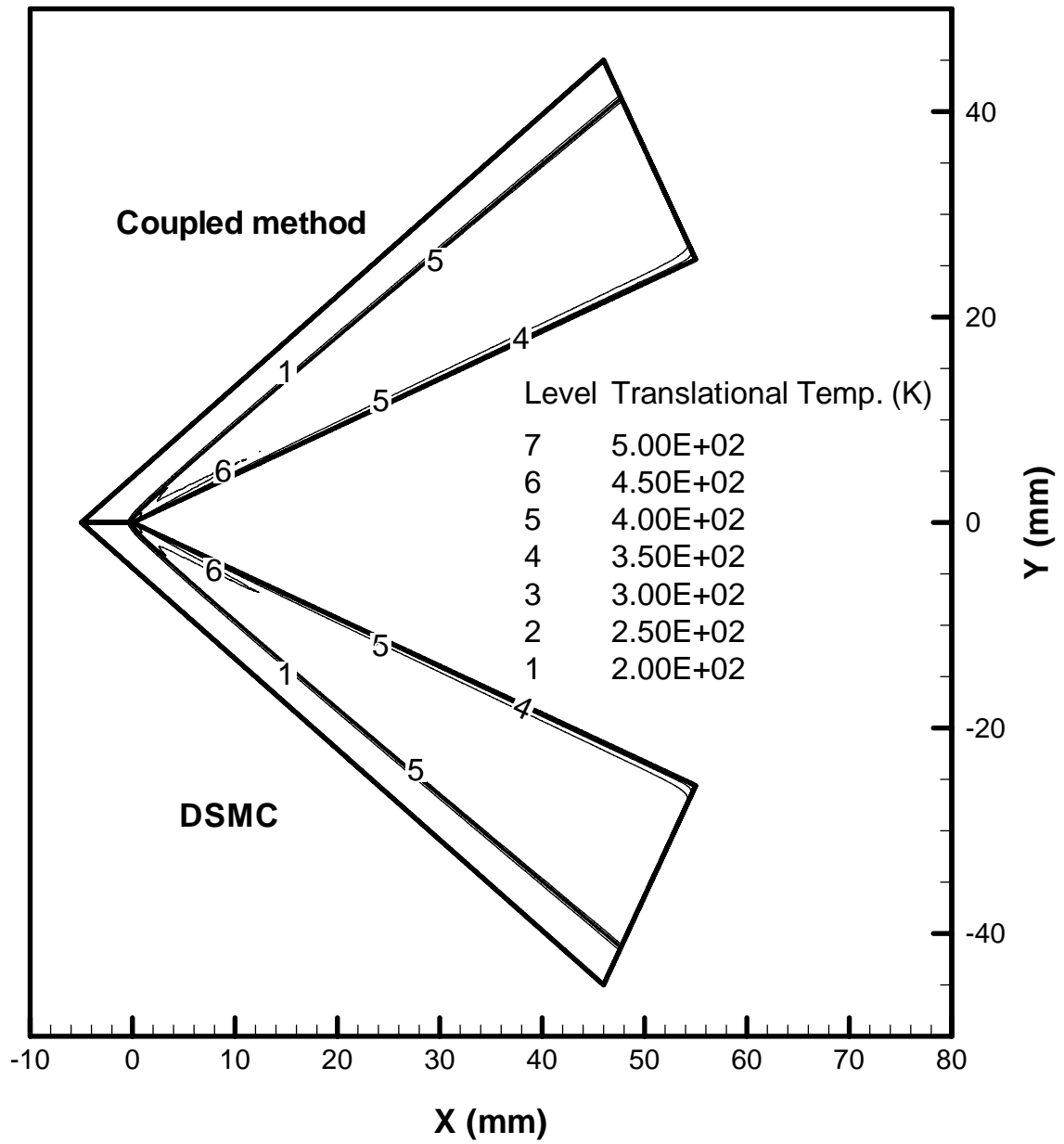
Fig. 3.6b   Translation temperature comparison between the DSMC method and the present coupled DSMC-NS method in quasi-2-D 25° wedge flow.
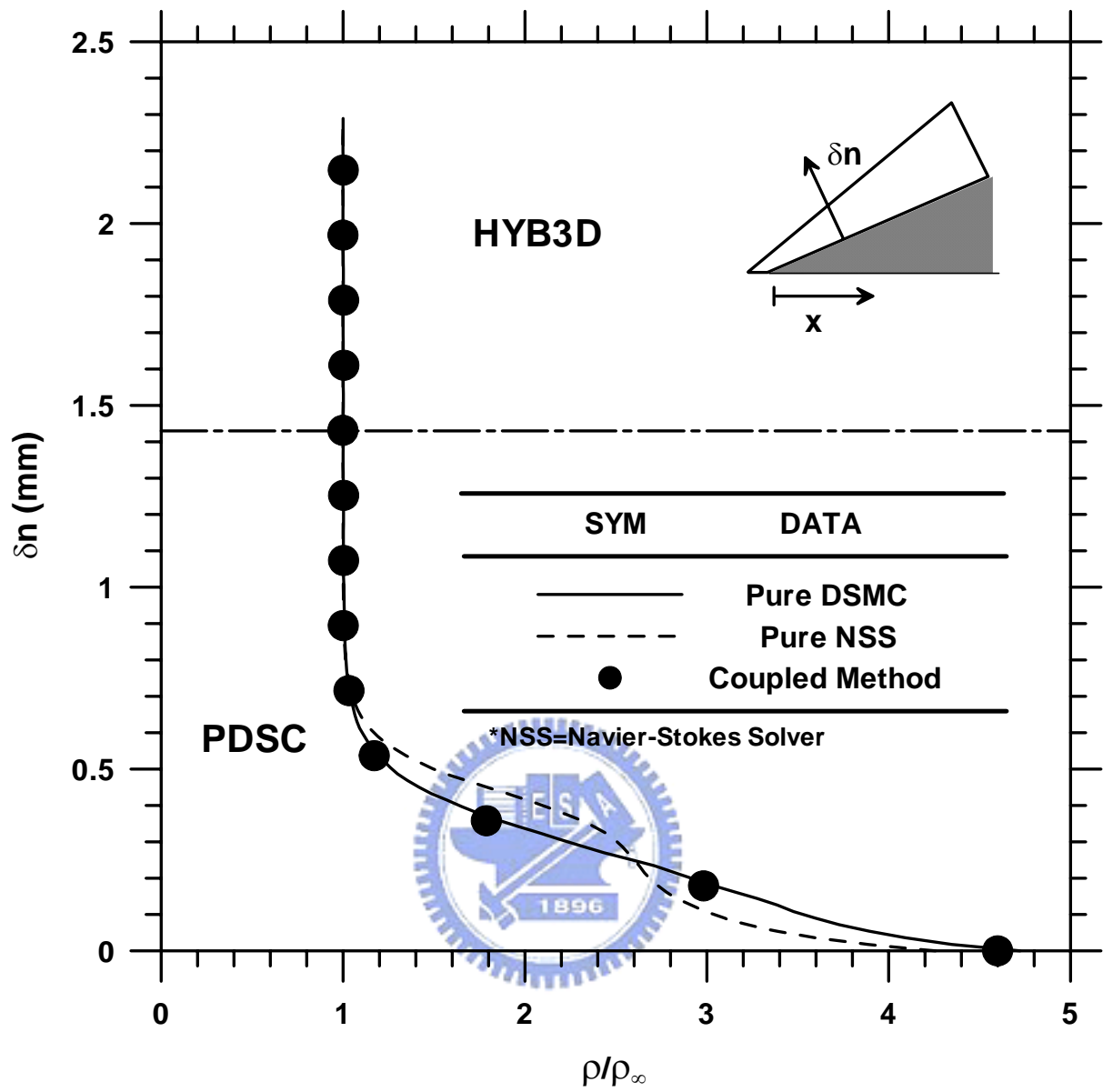
Fig. 3.7a   Density profile along a line normal to the wedge at x=0.5mm.
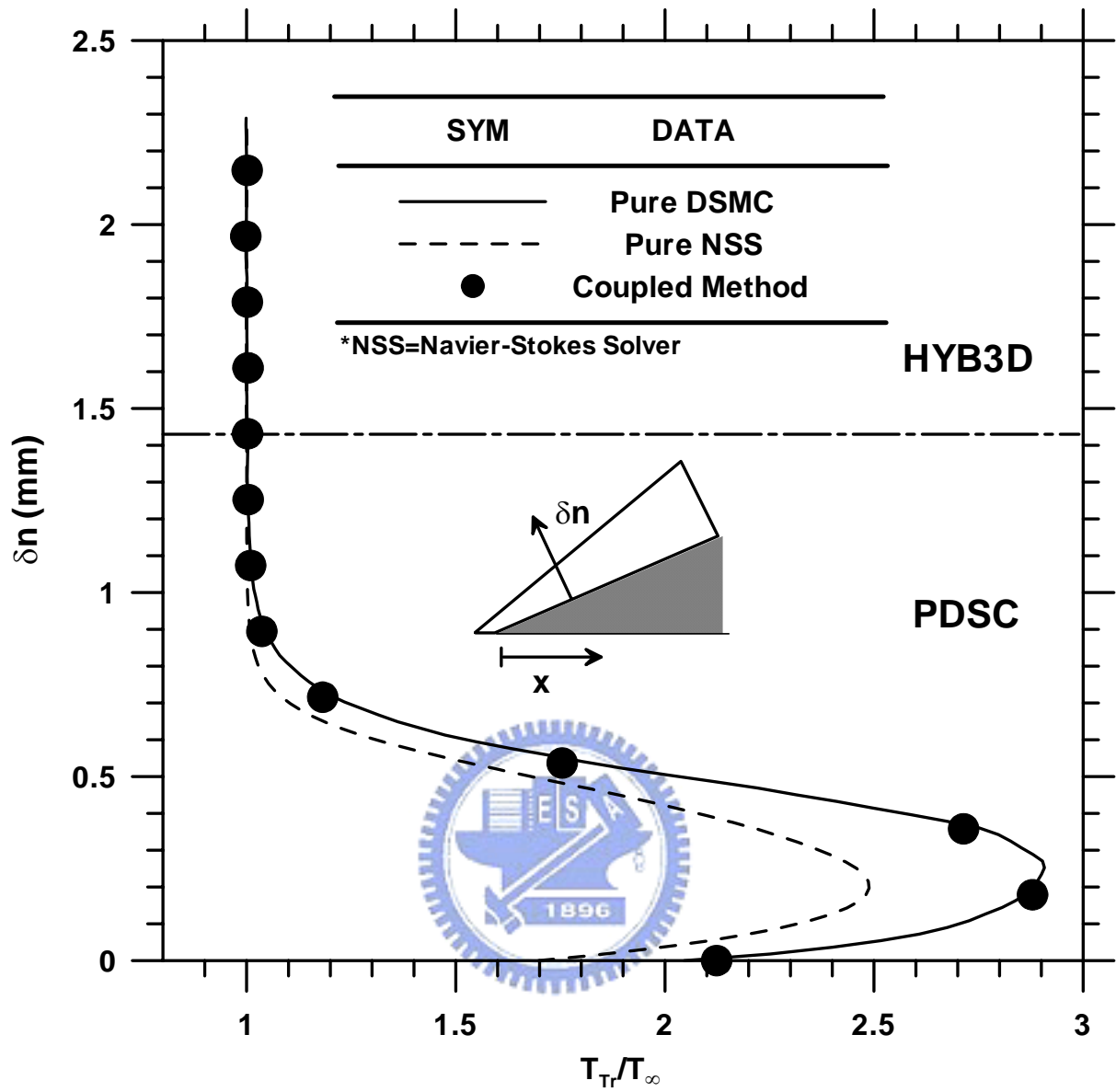
Fig. 3.7b   Translational temperature profile along a line normal to the wedge at x=0.5mm.
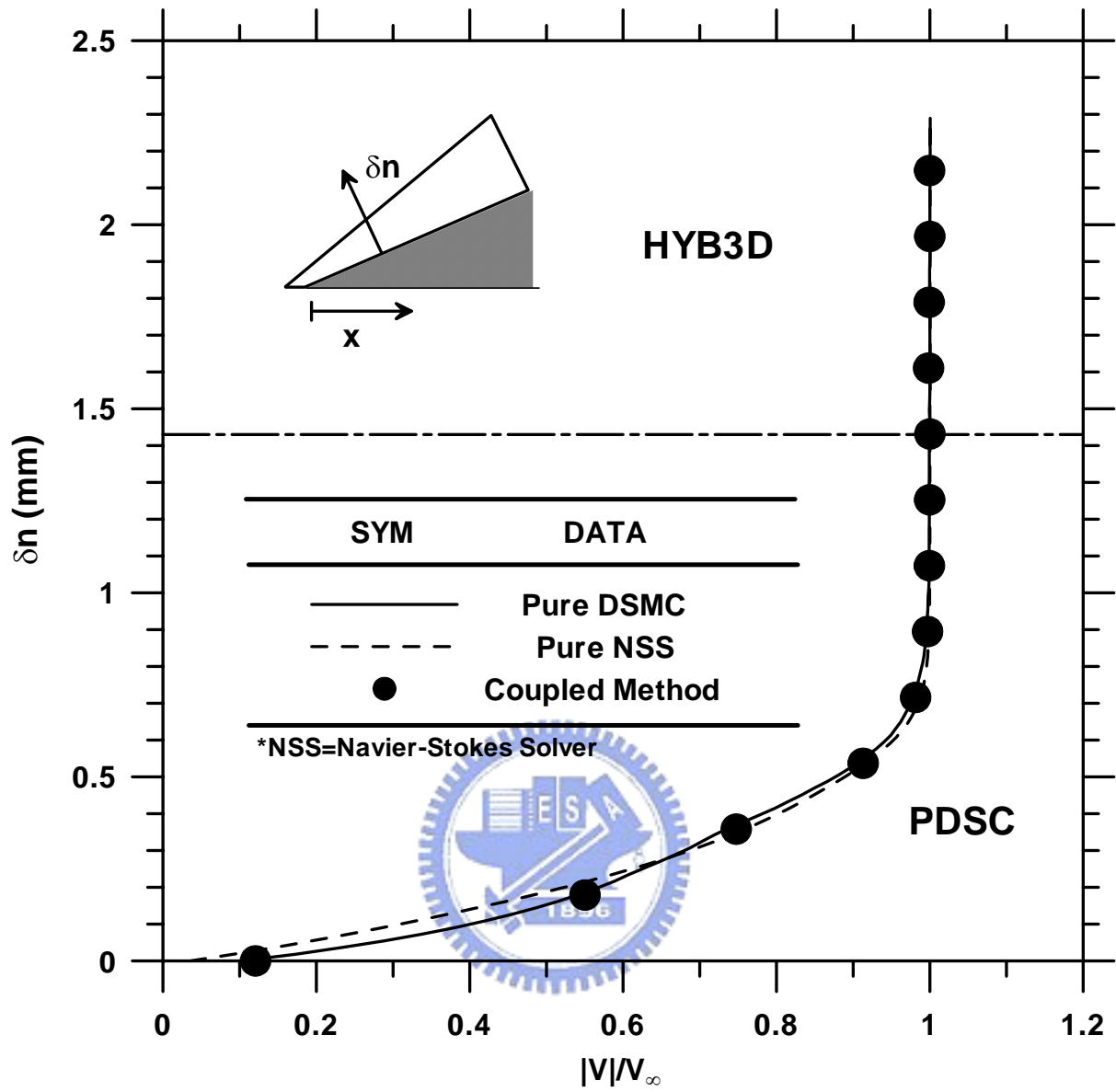
Fig. 3.7c   Velocity profile along a line normal to the wedge at x=0.5mm.
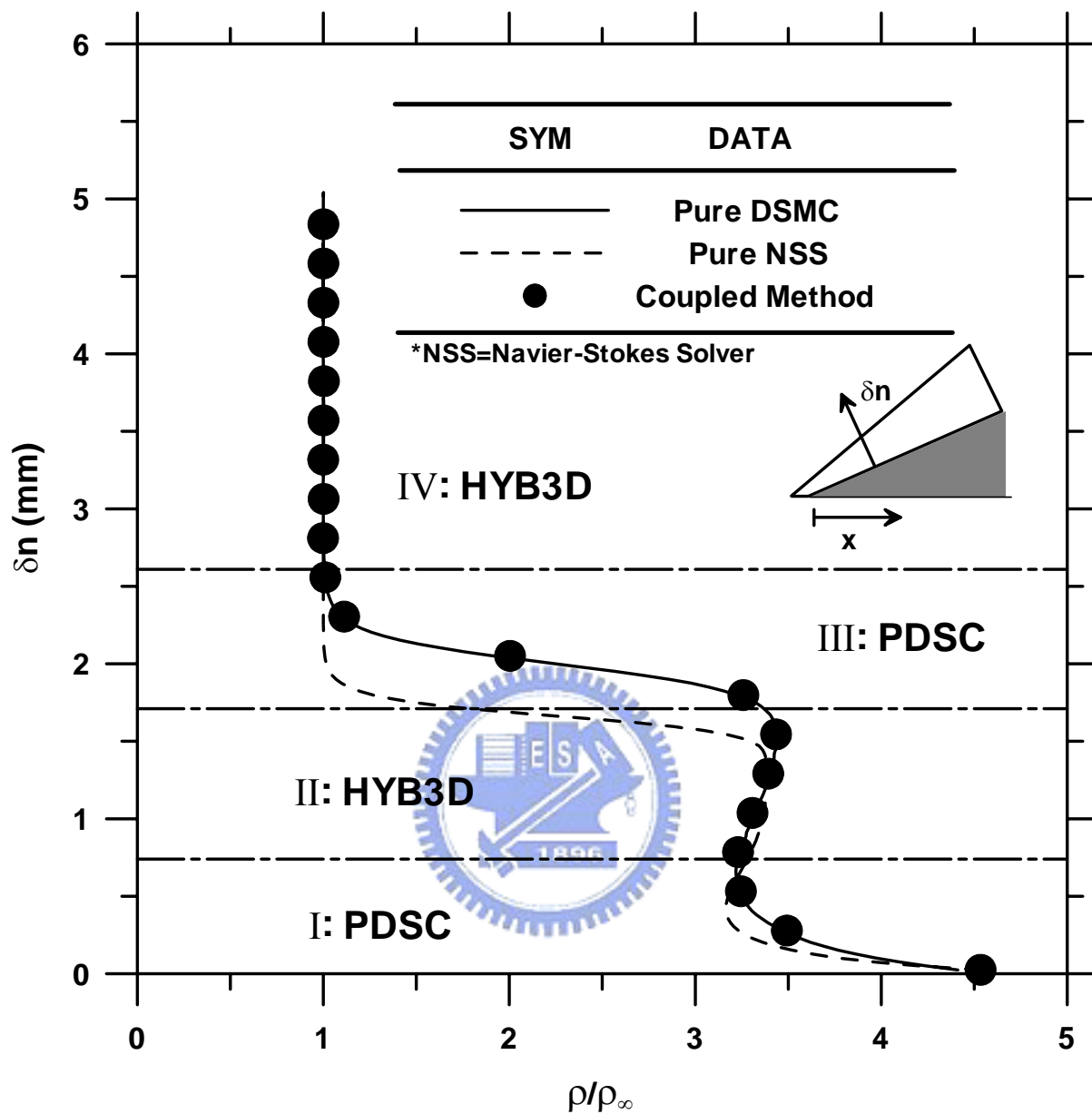
Fig. 3.8a   Density profile along a line normal to the wedge at x=5mm.
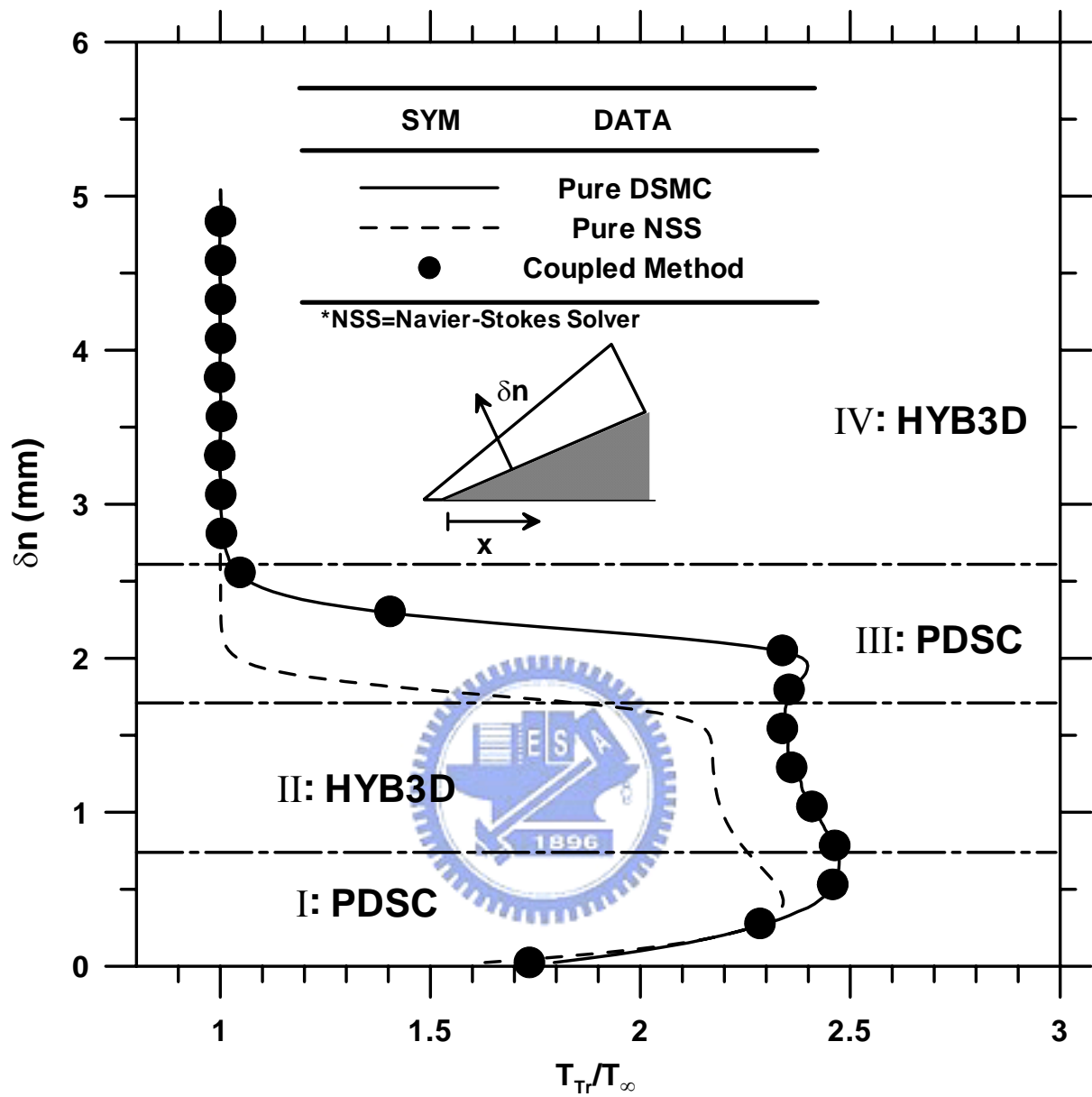
Fig. 3.8b   Translational temperature profile along a line normal to the wedge at x=5mm.
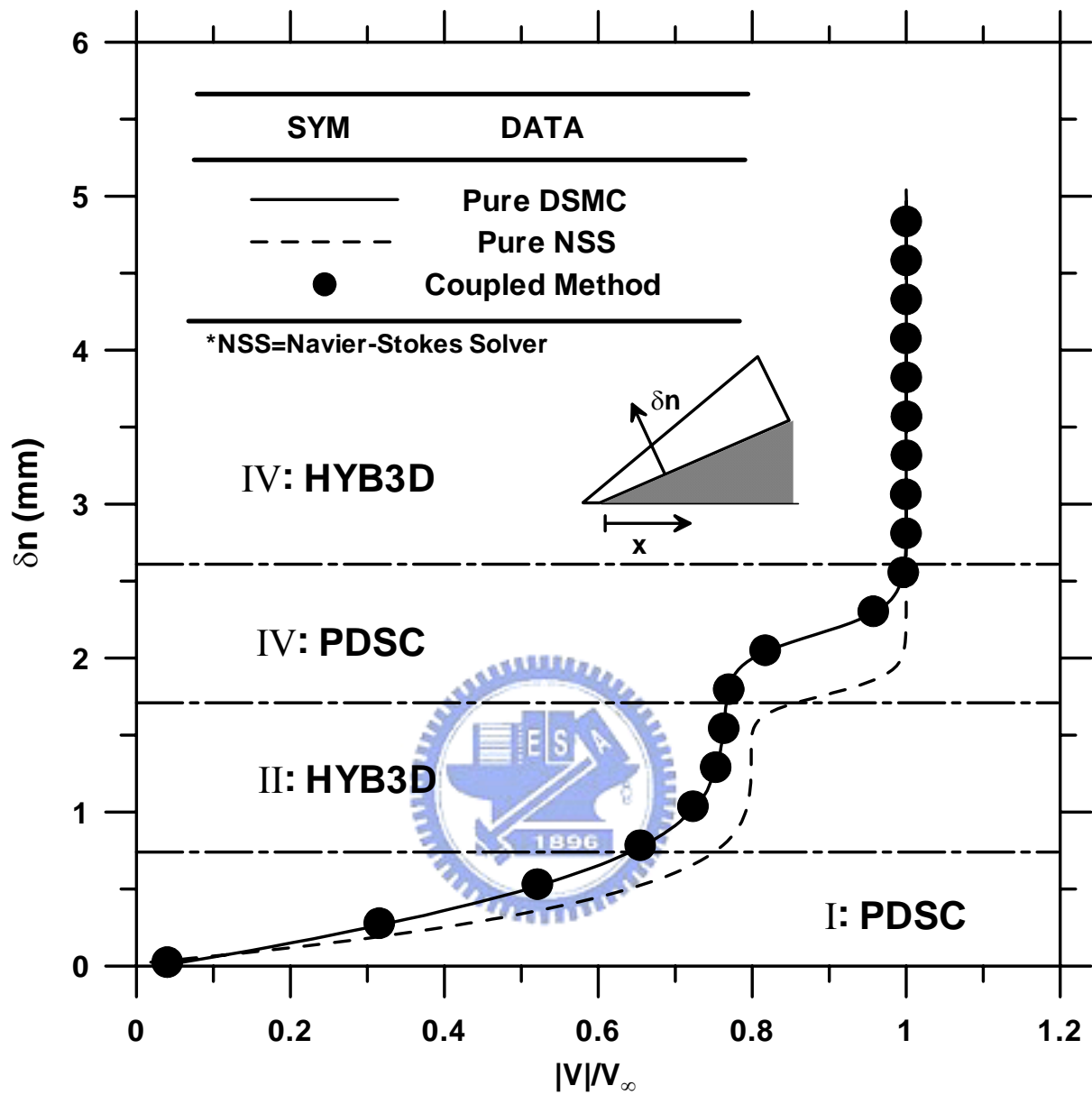
Fig. 3.8c   Velocity profile along a line normal to the wedge at x=5mm.
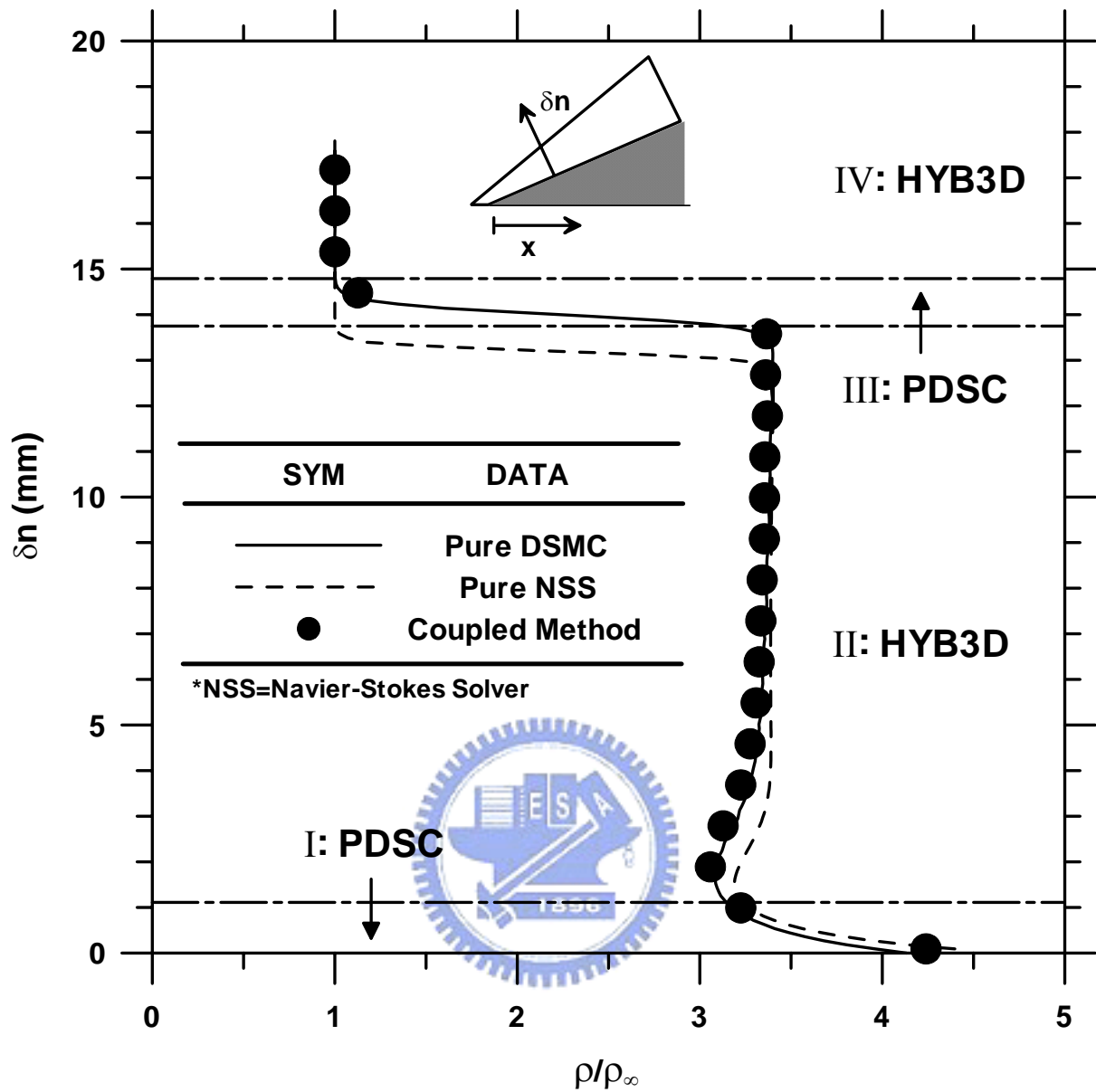
Fig. 3.9a   Density profile along a line normal to the wedge at x=50mm.
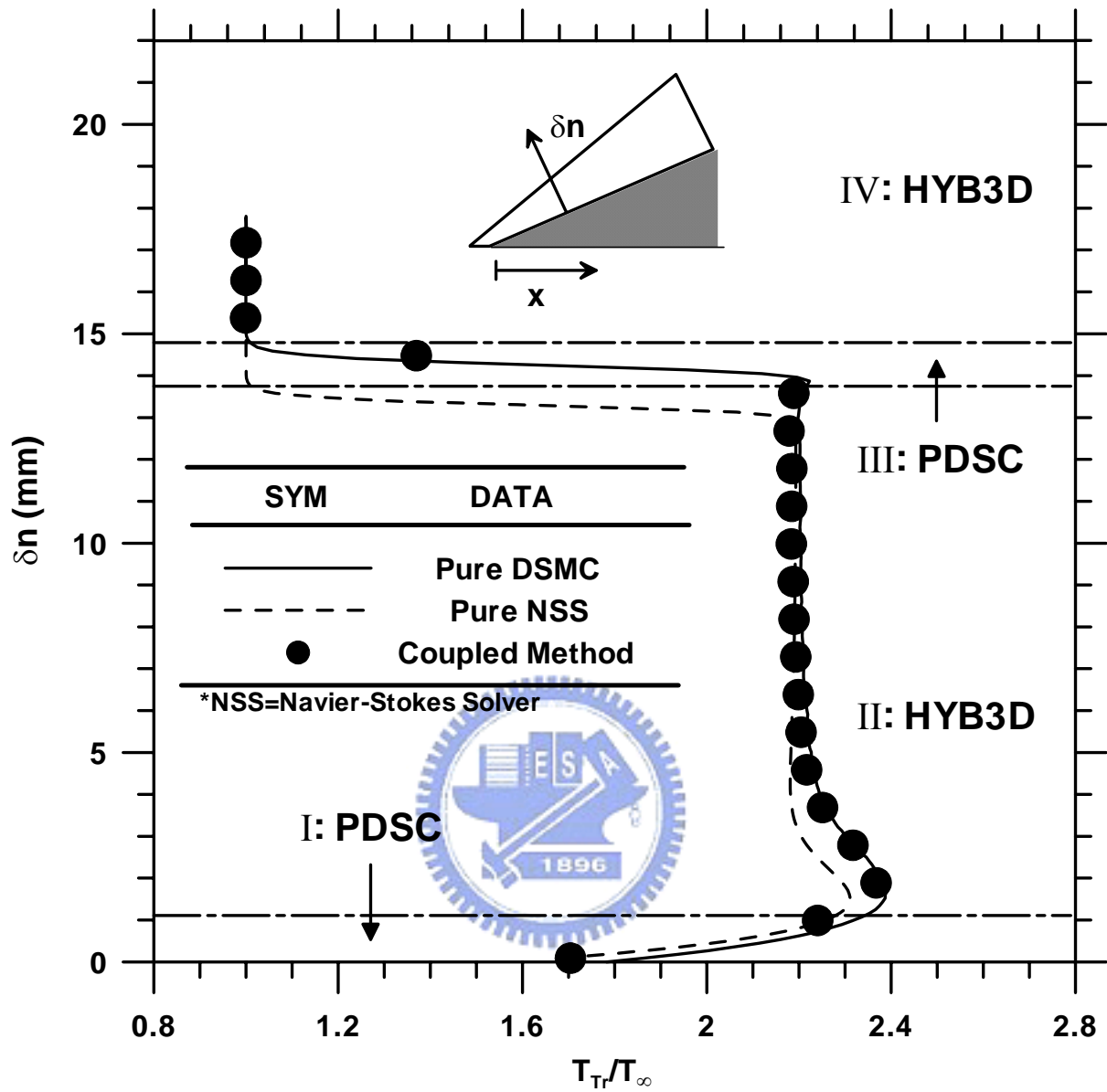
Fig. 3.9b   Translational temperature profile along a line normal to the wedge at x=50mm.
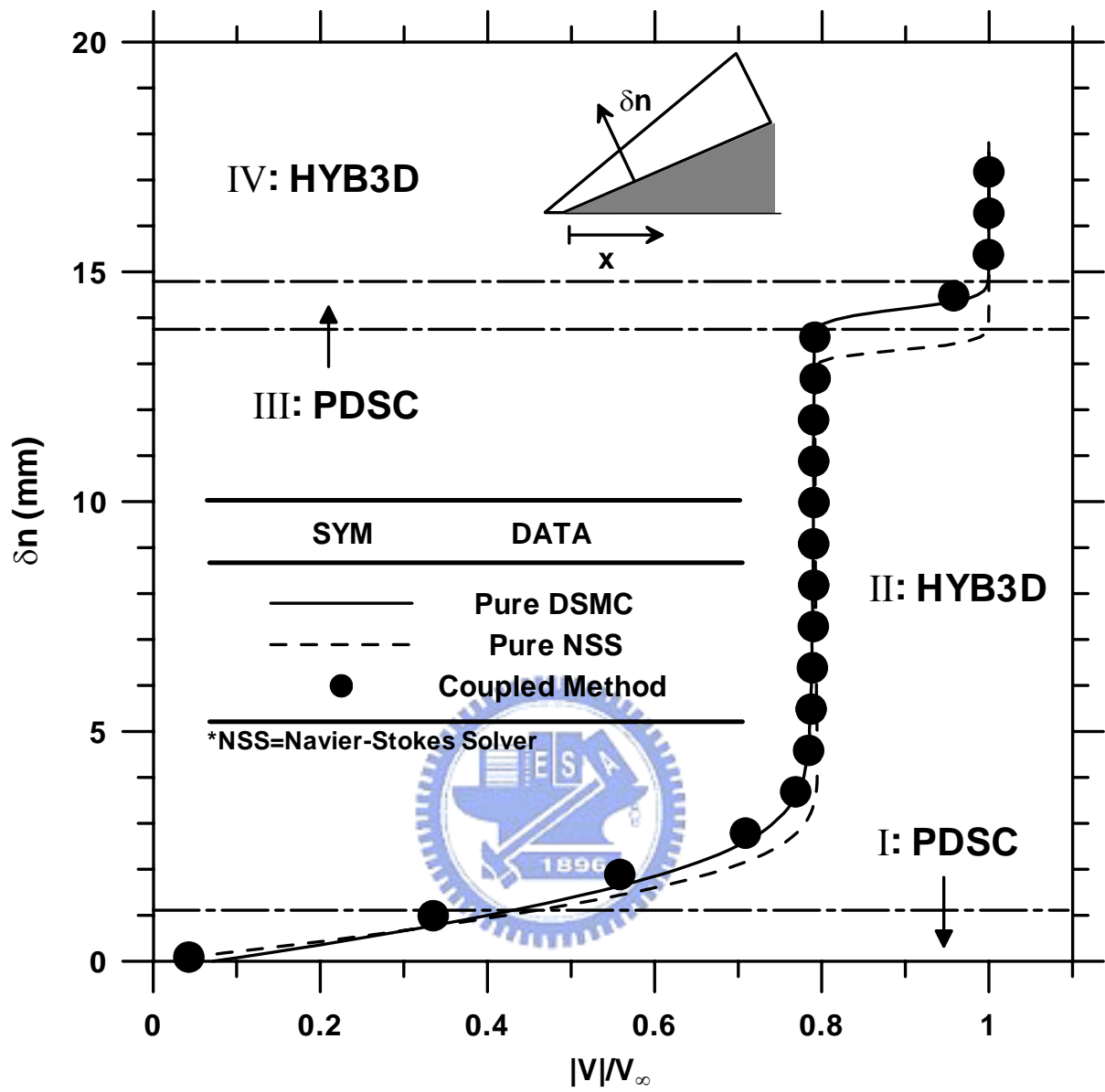
Fig. 3.9c   Velocity profile along a line normal to the wedge at x=50mm.
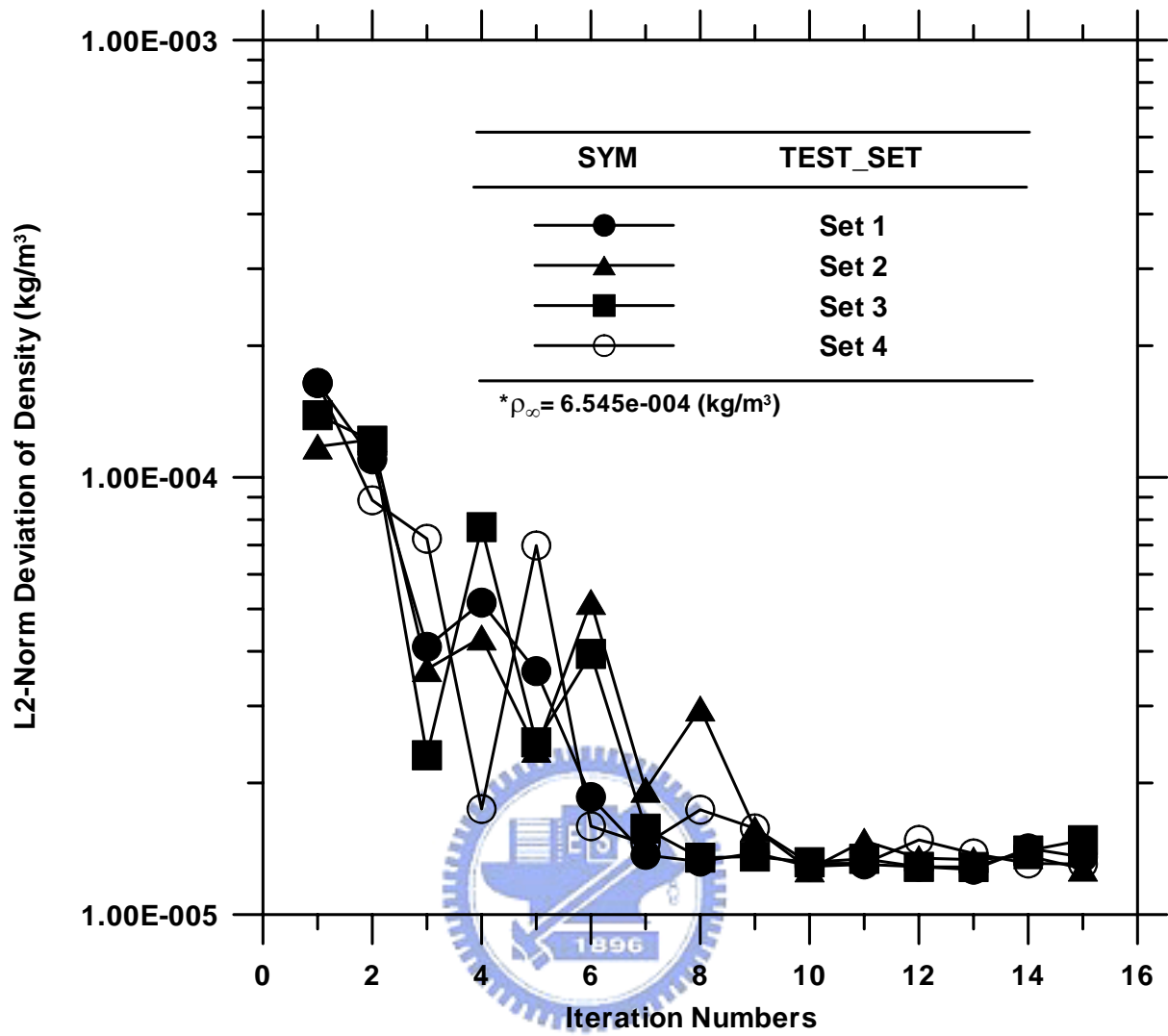
Fig. 3.10   Convergence history of L2-norm deviation of density among the four simulation
sets in quasi-2-D 25° wedge flow.
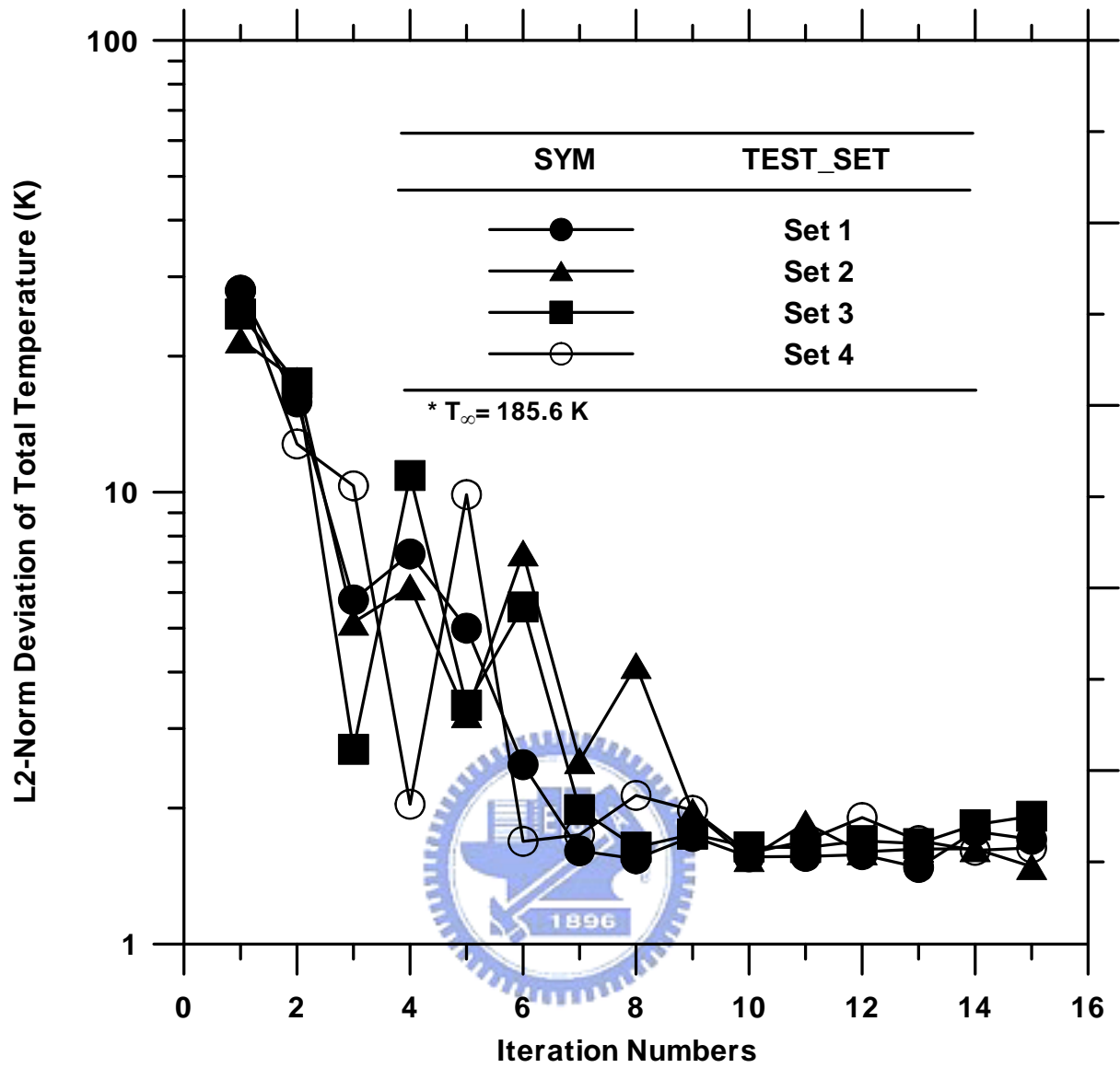
Fig. 3.11 Convergence history of L2-norm deviation of total temperature among the four simulation sets in quasi-2-D 25° wedge flow.
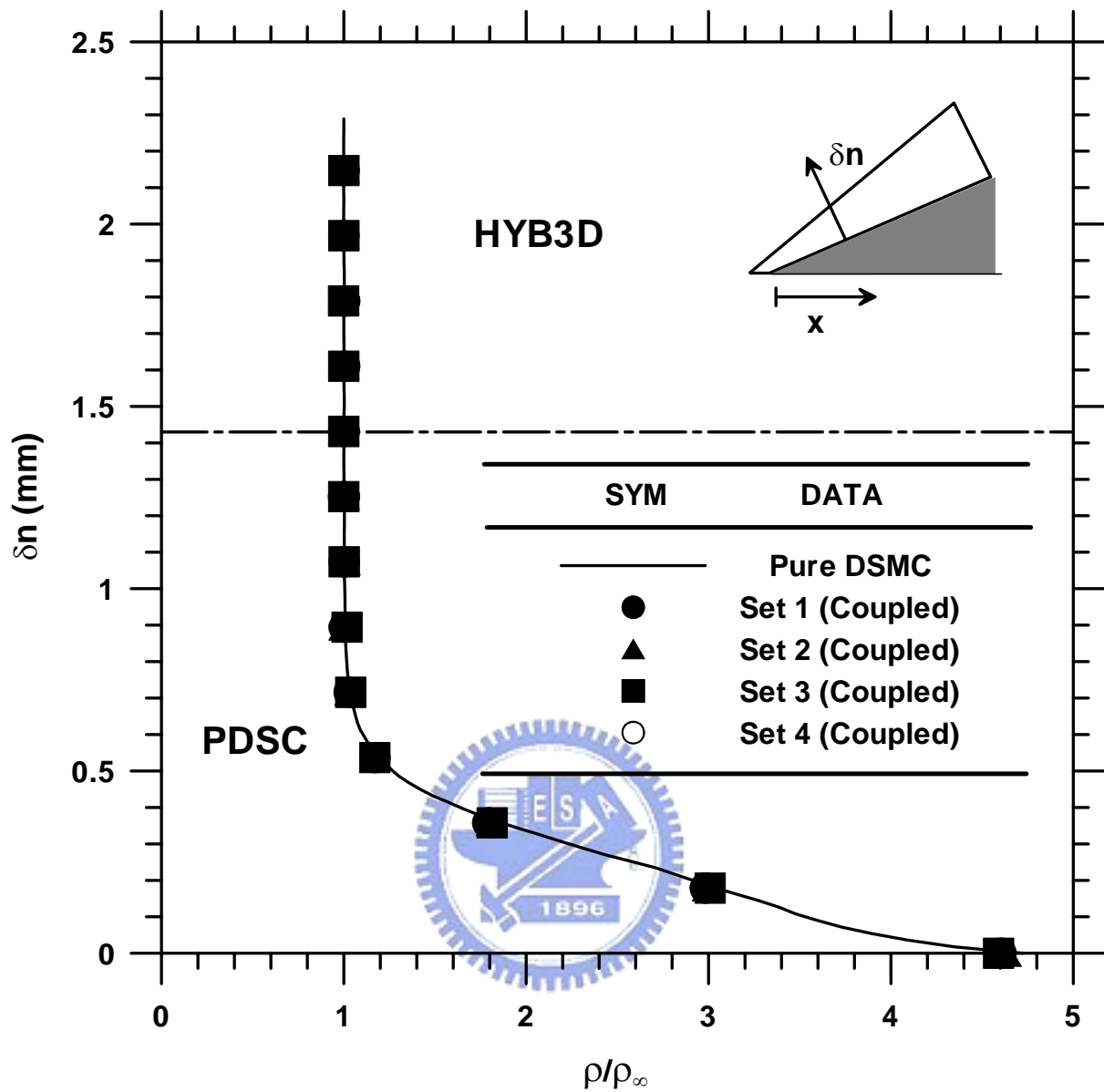
Fig. 3.12a Comparison of density along a line normal to the wedge at x=0.5mm among the four simulation sets.
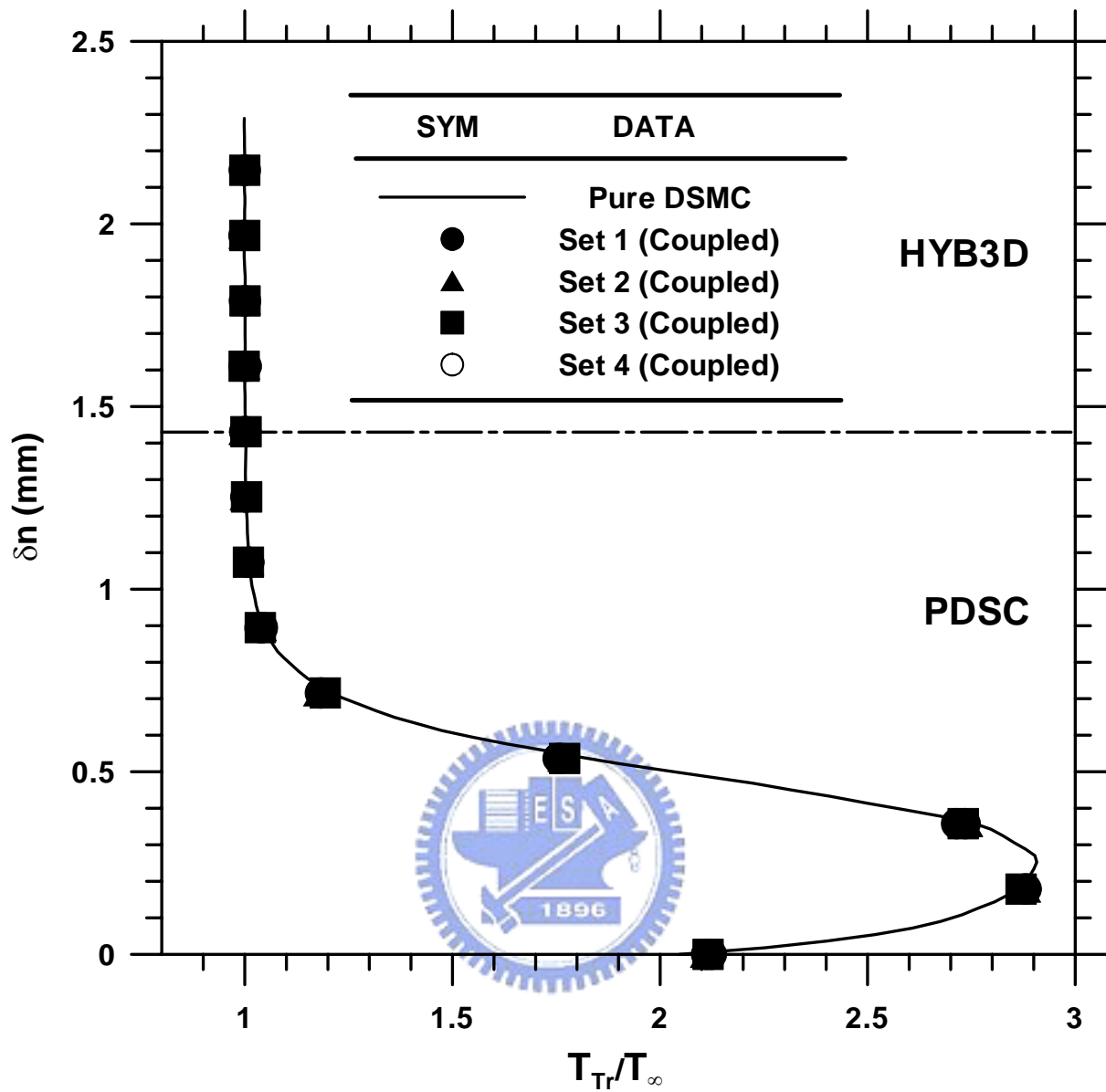
Fig. 3.12b Comparison of translational temperature along a line normal to the wedge at x=0.5mm among the four simulation sets.
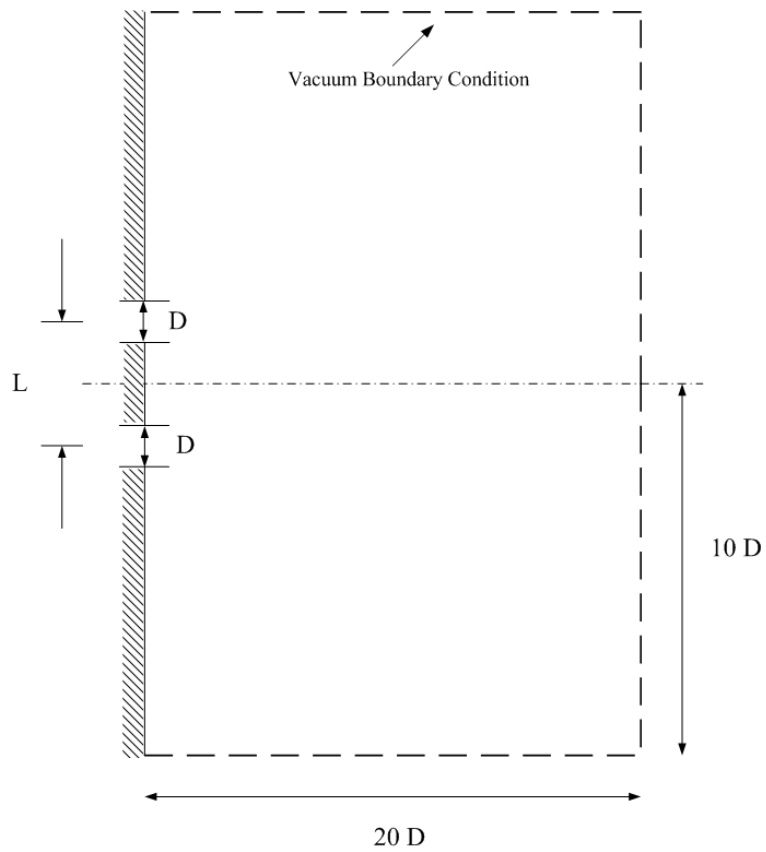
Fig. 3.13   Sketch of two parallel near-continuum orifice free jets flow.
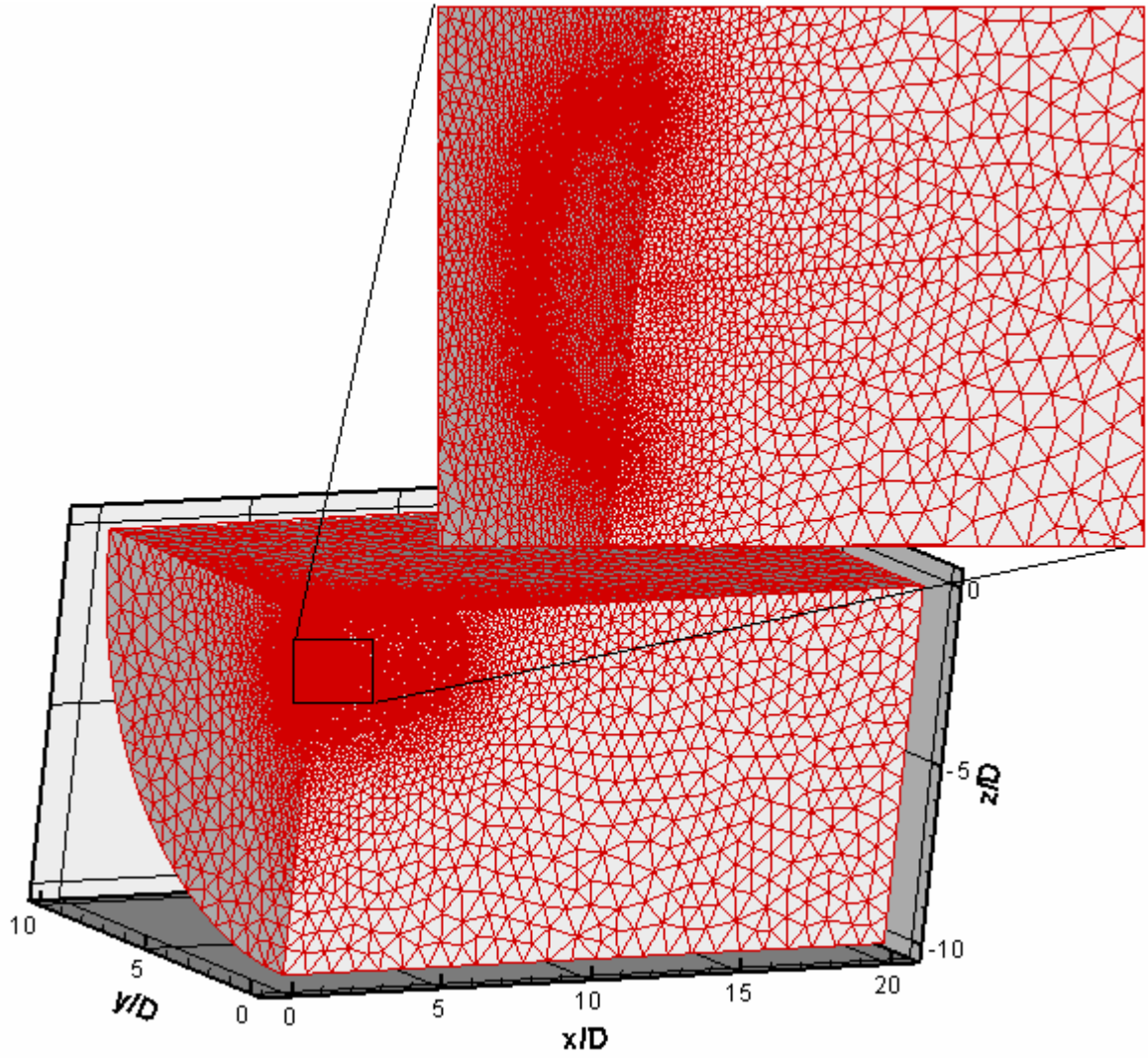
Fig. 3.14   Mesh distribution of two parallel near-continuum orifice free jets flow simulation.
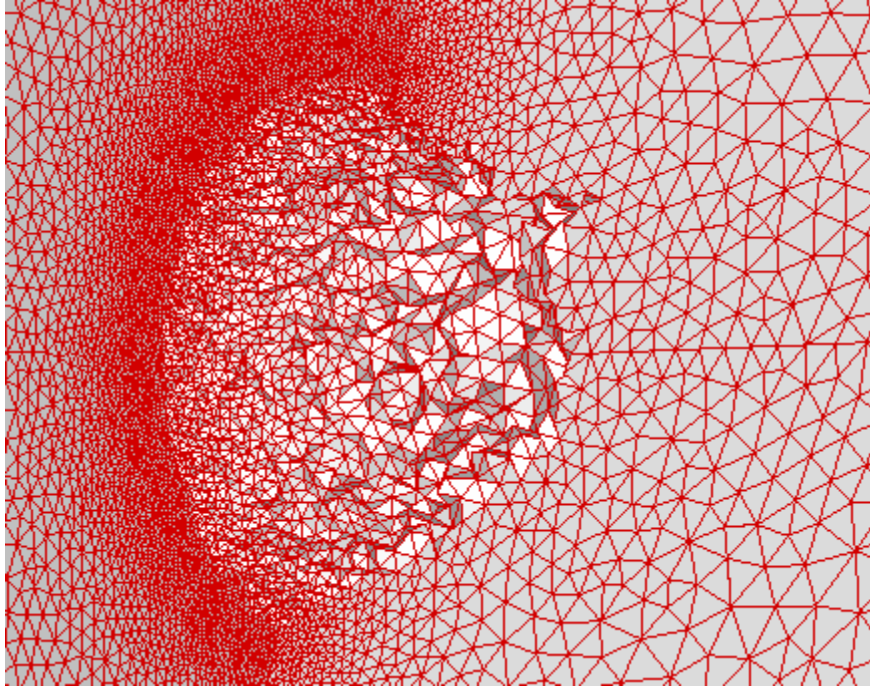
Fig. 3.15 Surface mesh distribution of breakdown domain (DSMC domain) of two parallel near-continuum orifice free jets flow simulation with an exploded view (after 2 coupled iterations).
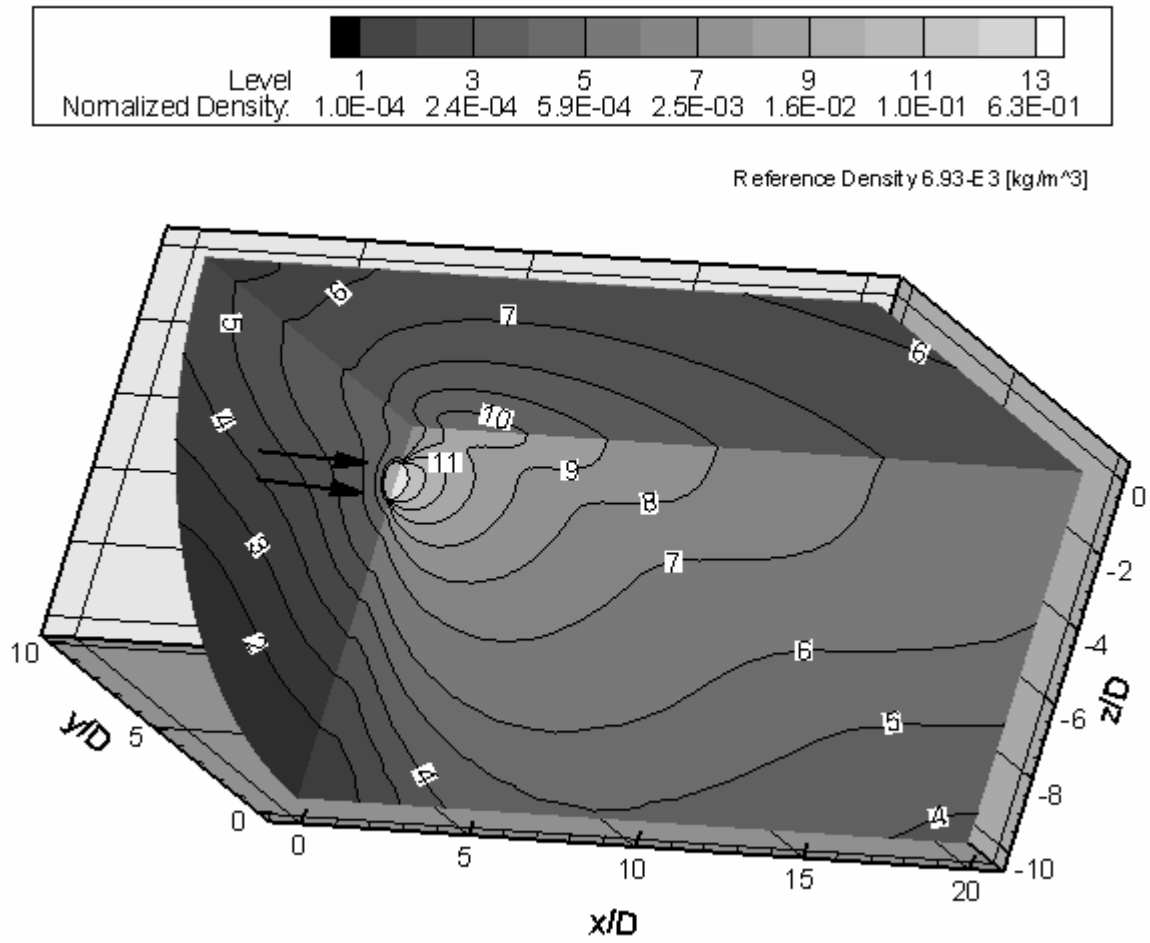
Fig. 3.16   Density contours of two parallel near-continuum orifice free jets flow.
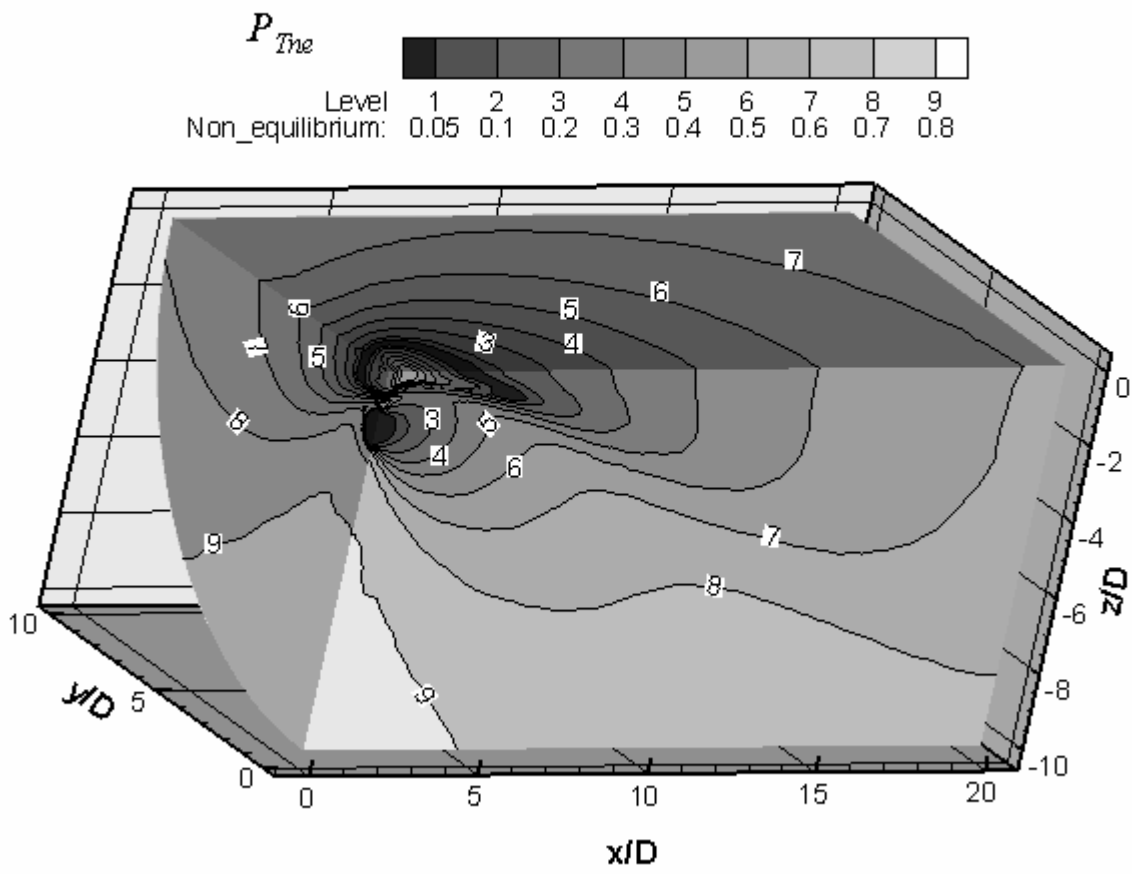
Fig. 3.17a Thermal non-equilibrium contours of two parallel near-continuum orifice free jets flow.
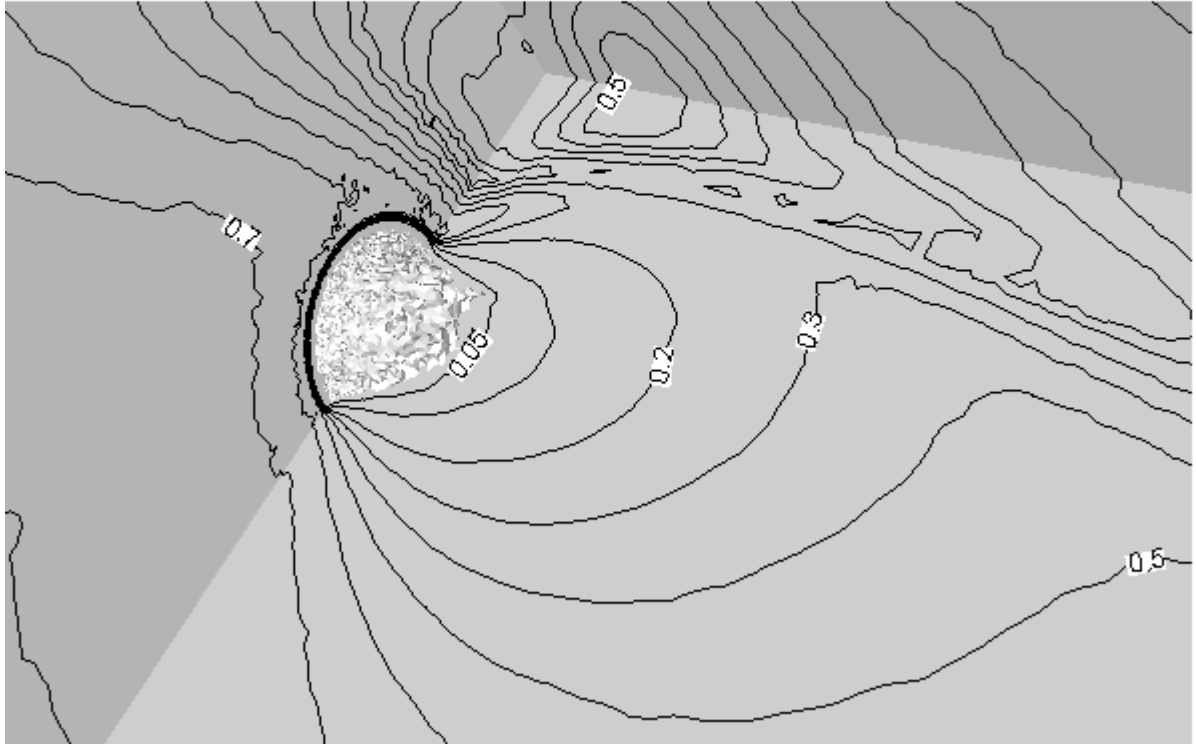
Fig. 3.17b Thermal non-equilibrium contours near the orifice.
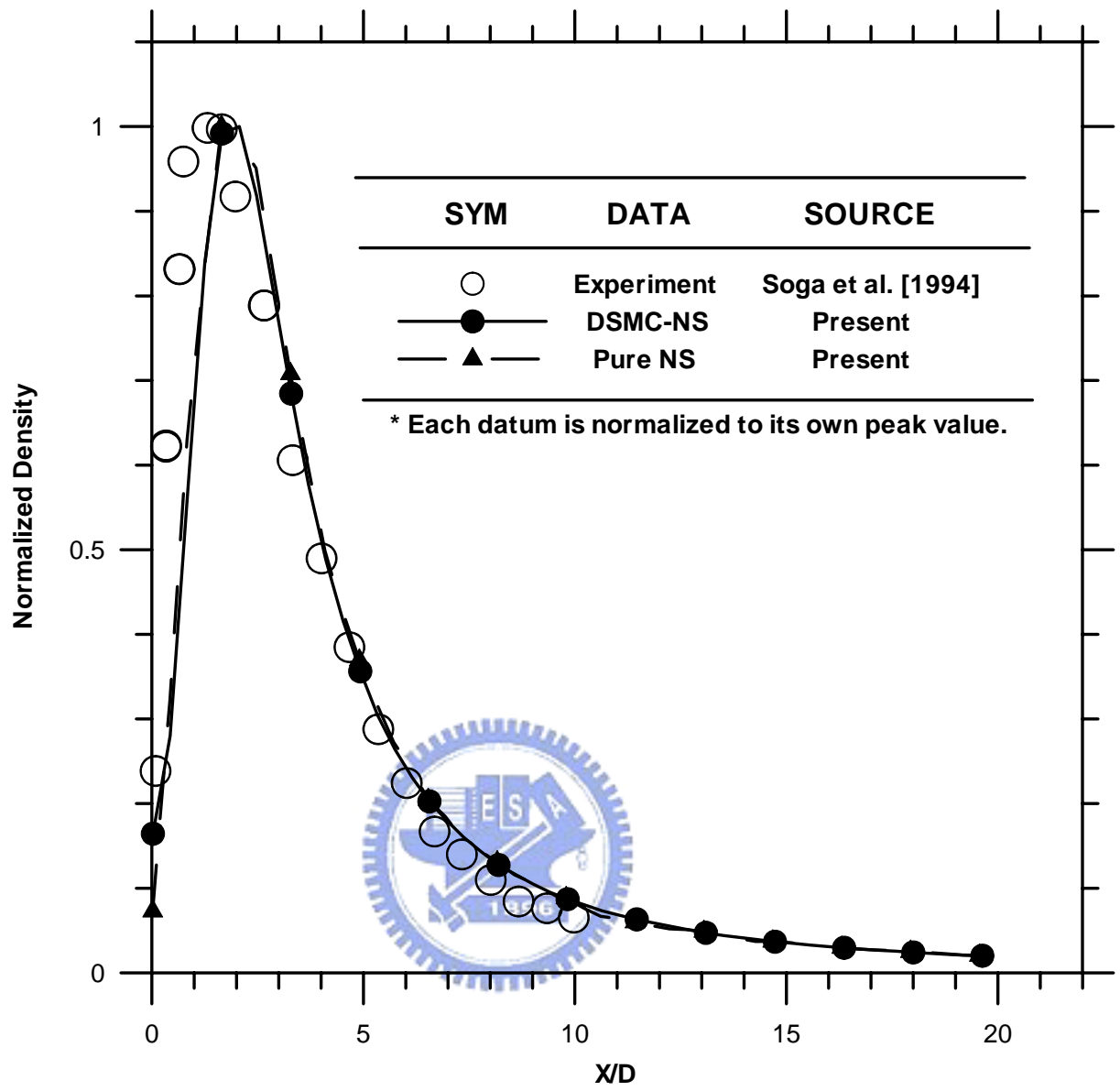
Fig. 3.18a Normalized density distribution along the symmetric line of two parallel near-continuum orifice free jets flow.
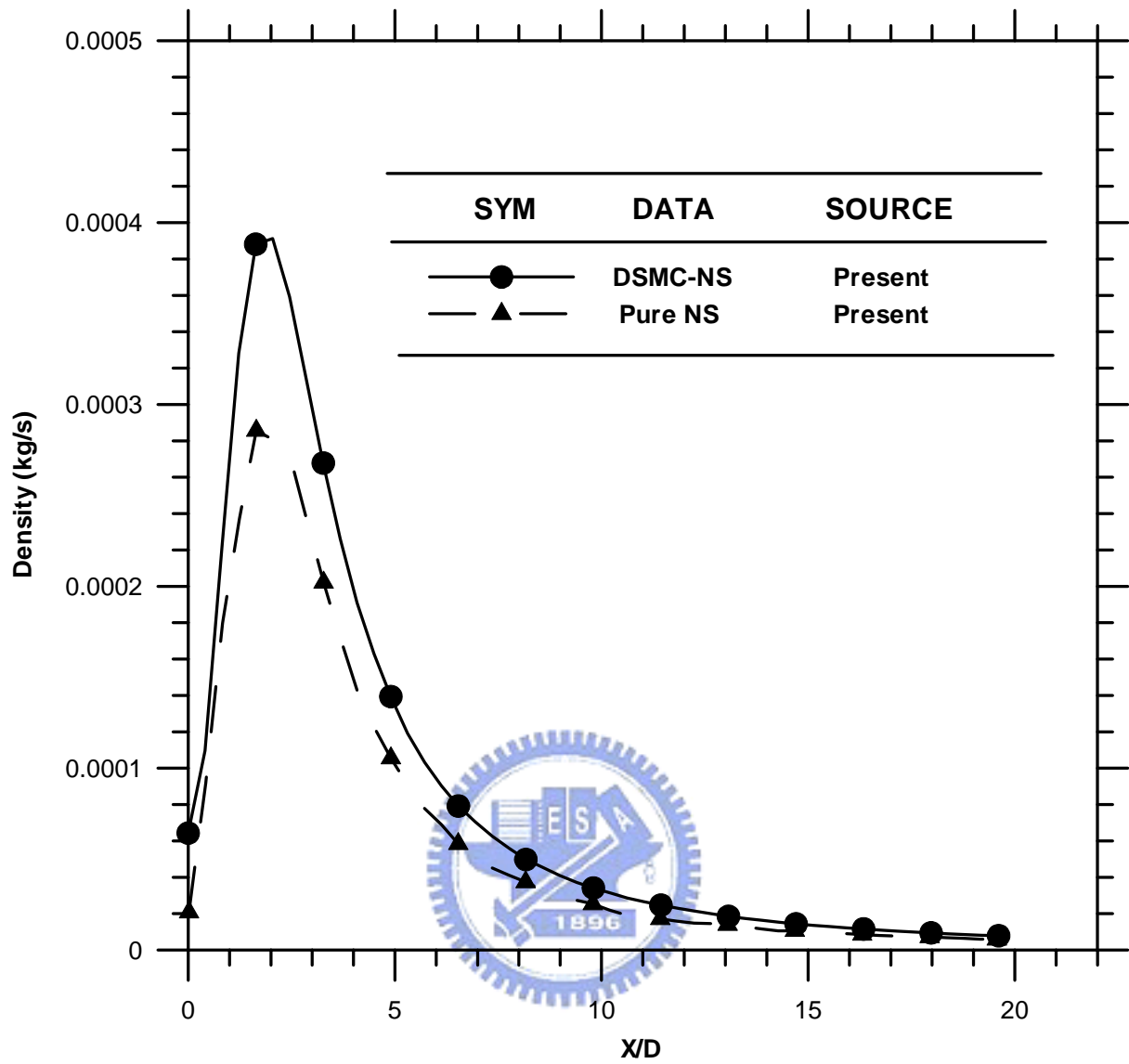
Fig. 3.18b Density distribution along the symmetric line of two parallel near-continuum orifice free jets flow.
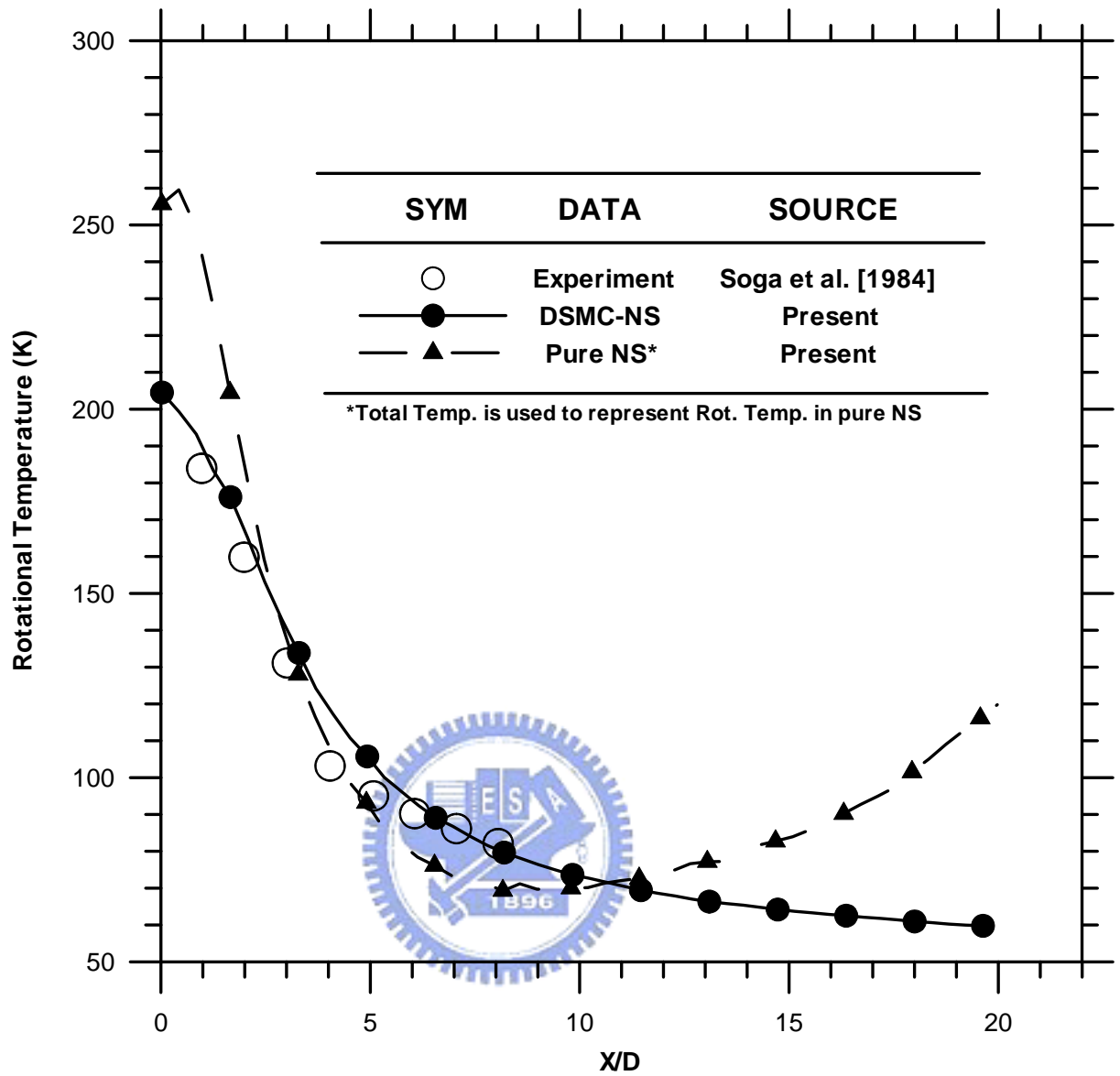
Fig. 3.19 Rotational temperature distribution along the symmetric line of two parallel near-continuum orifice free jets flow.
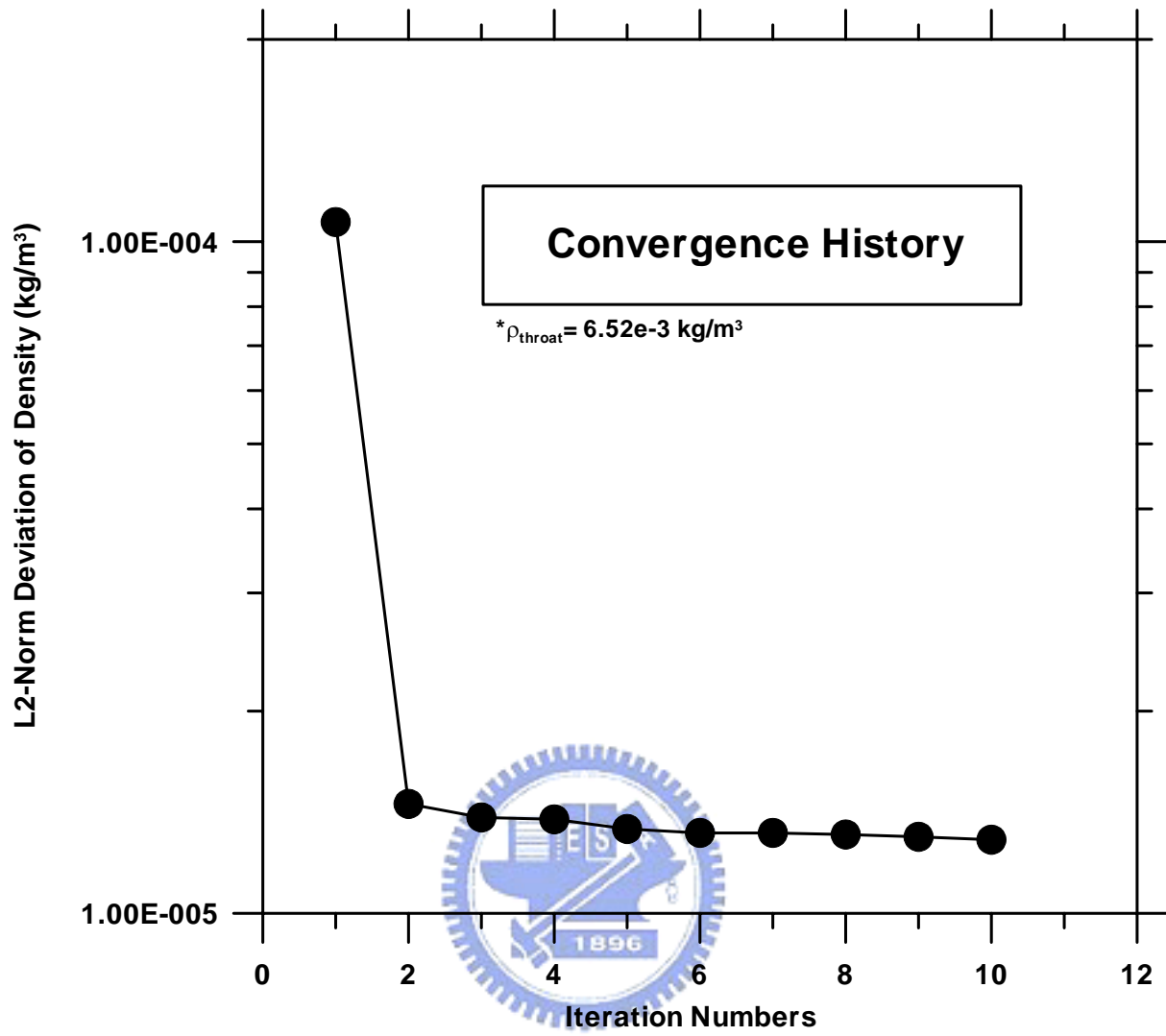
Fig. 3.20 Convergence history of density for two parallel near-continuum orifice free jets flow.
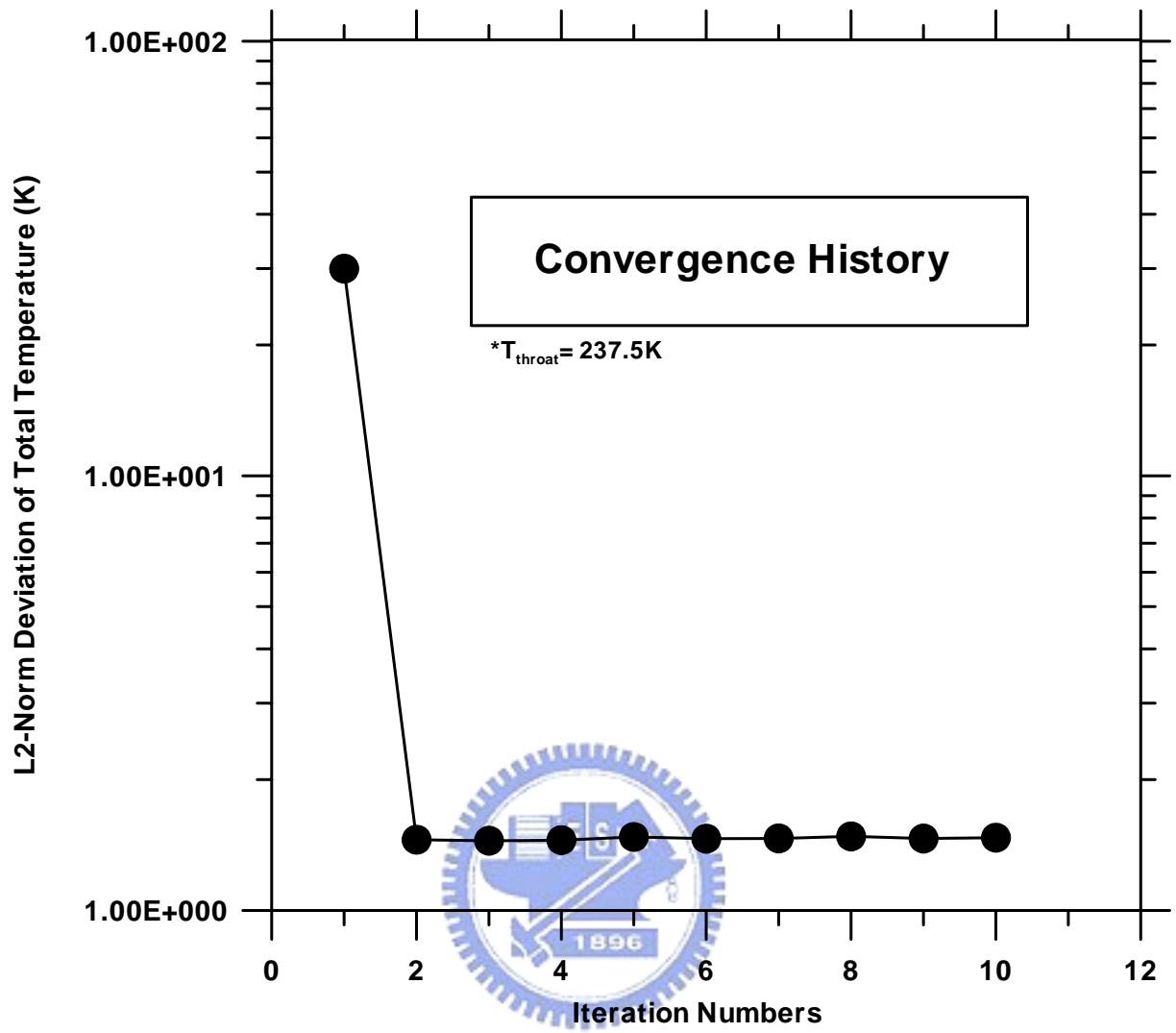
Fig. 3.21 Convergence history of total temperature for two parallel near-continuum orifice free jets flow.

Mach Number Distribution & Breakdown Domains
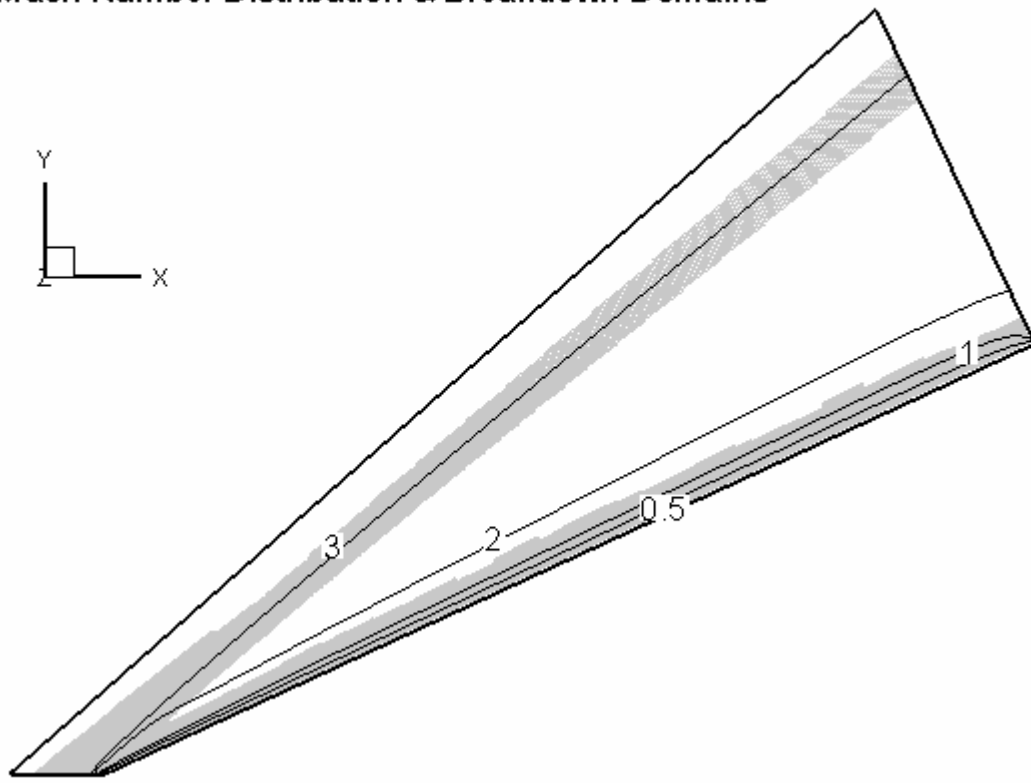
Fig. 3.22a Mach number distribution of quasi-2-D supersonic wedge flow (gray areas: DSMC domain; others: NS domain).

Mach Number Distribution near the Orifice
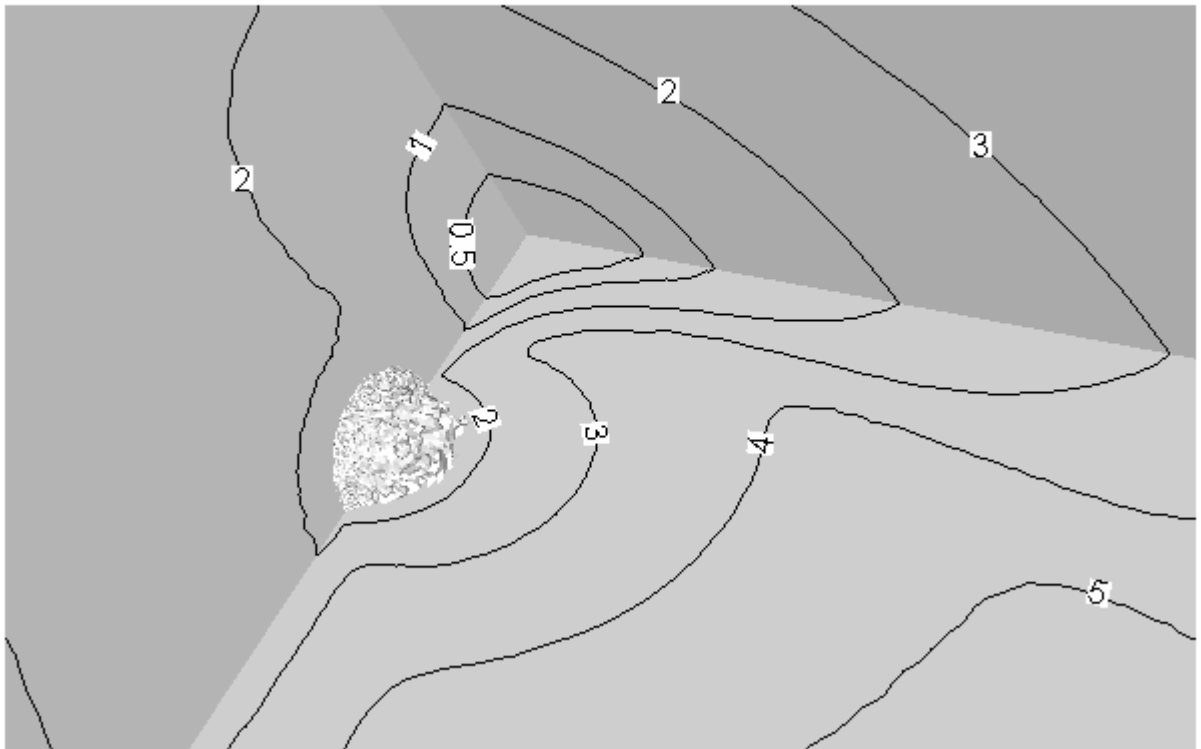
Fig. 3.22b Mach number distribution of two parallel near-continuum free jets near orifice (white region: breakdown interface).

N₂

P_o= 0.1bar
T_o=300K

AR=60

Isothermal wall (300K)

Vacuum Boundary conditions   (For DSMC)
Supersonic Boundary conditions   (For NS solver)
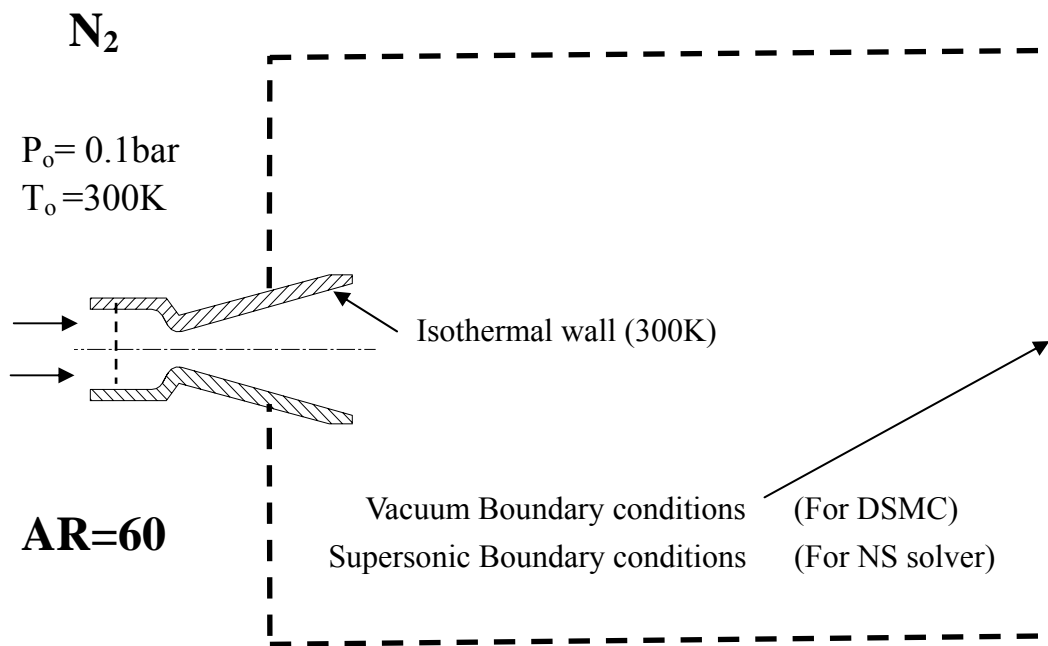
Fig. 3.23   Sketch of the plume simulation issuing from RCS thruster.
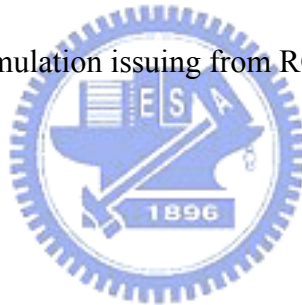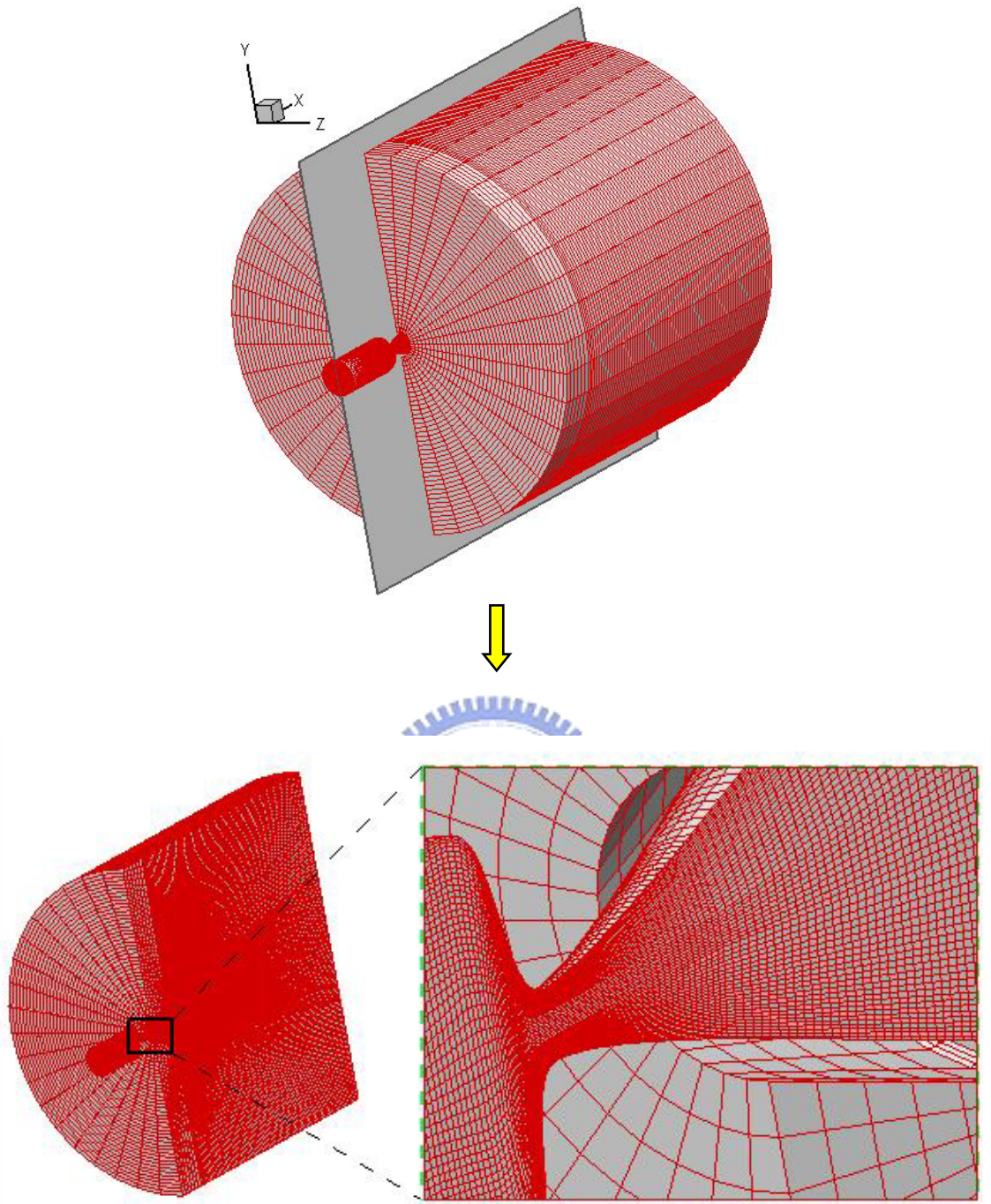
Fig. 3.24　Mesh distribution of the plume simulation issuing from RCS thruster.
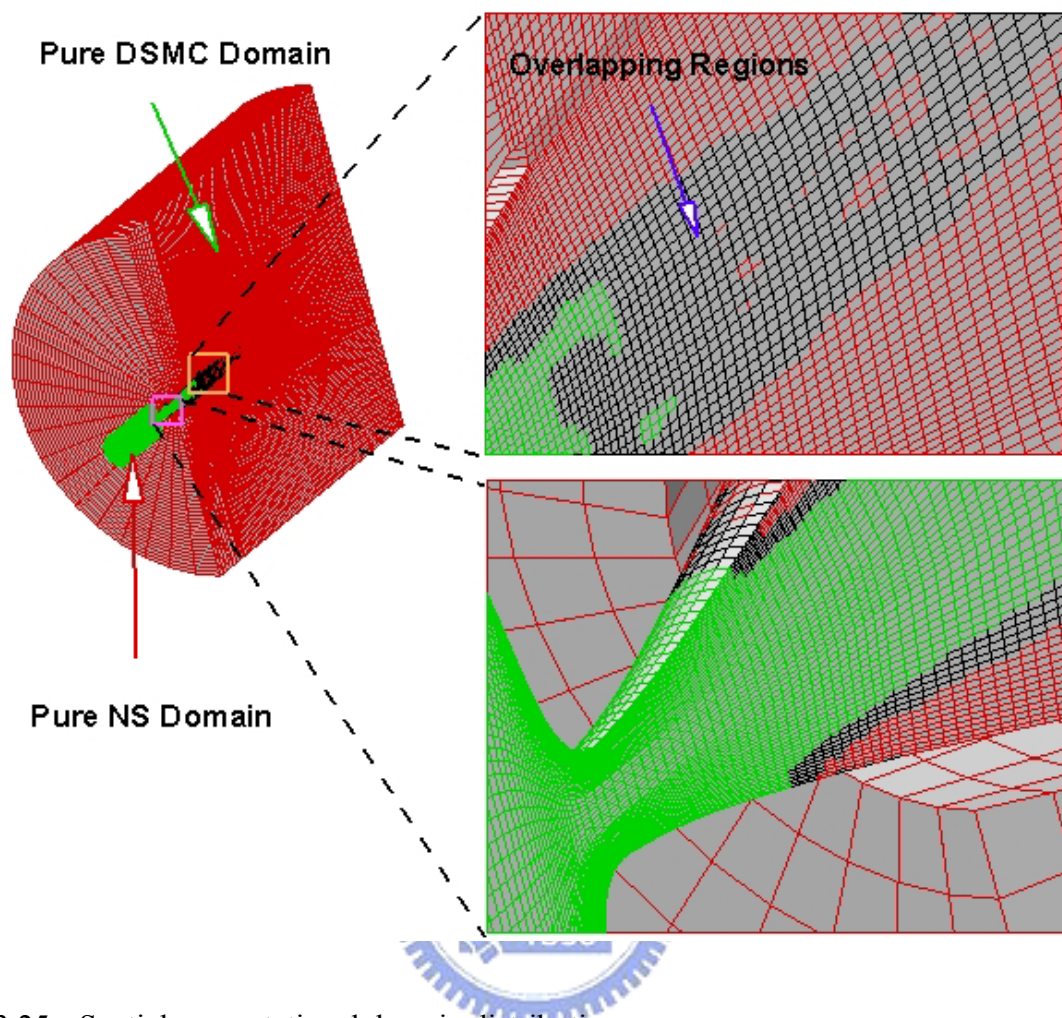
Fig. 3.25   Spatial computational domain distributions.

149
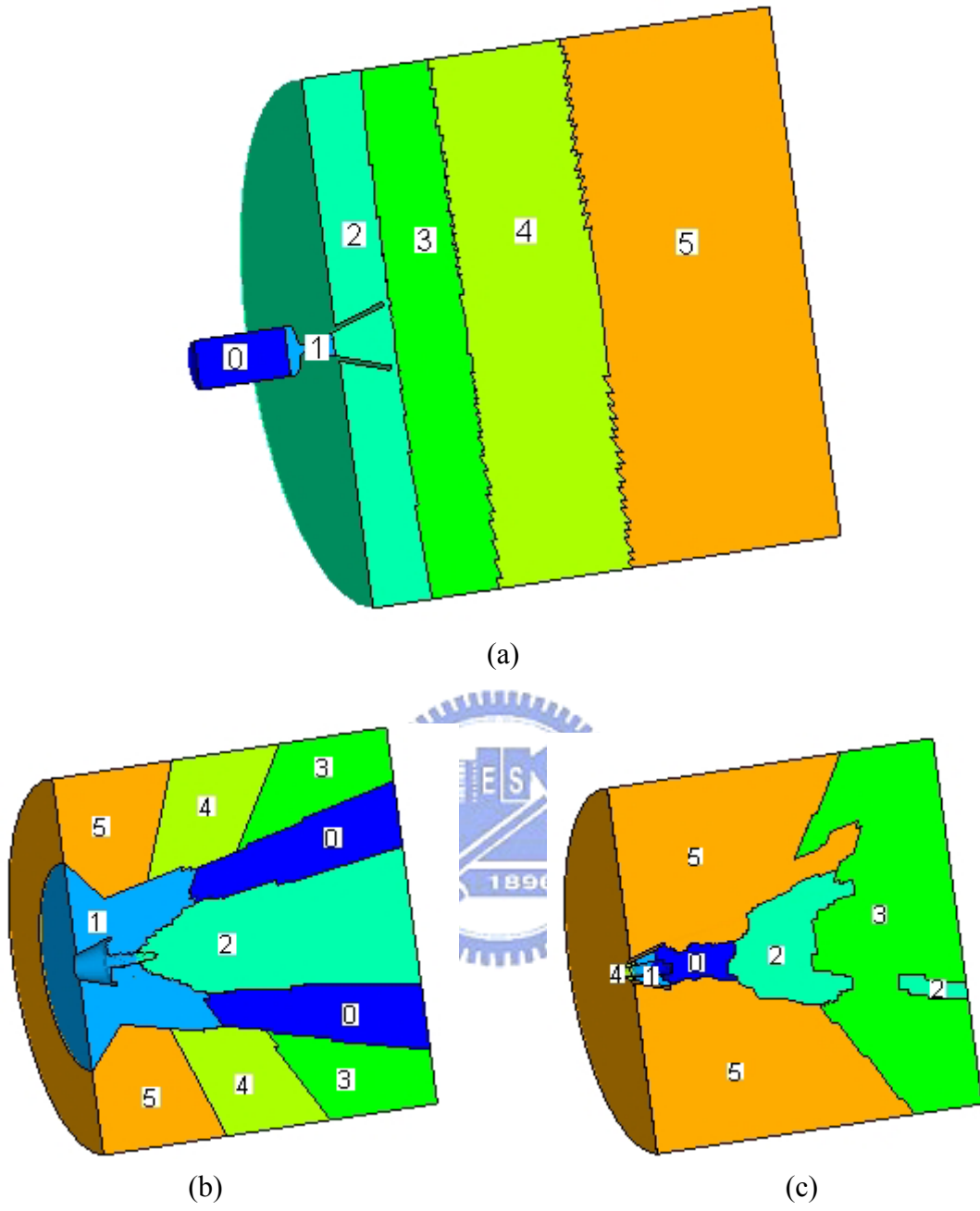
Fig. 3.26 Domain decomposition for 6 processors (a) NS CPU domain; (b) Initial DSMC CPU domain; (c) Final DSMC CPU domain (6th iteration).
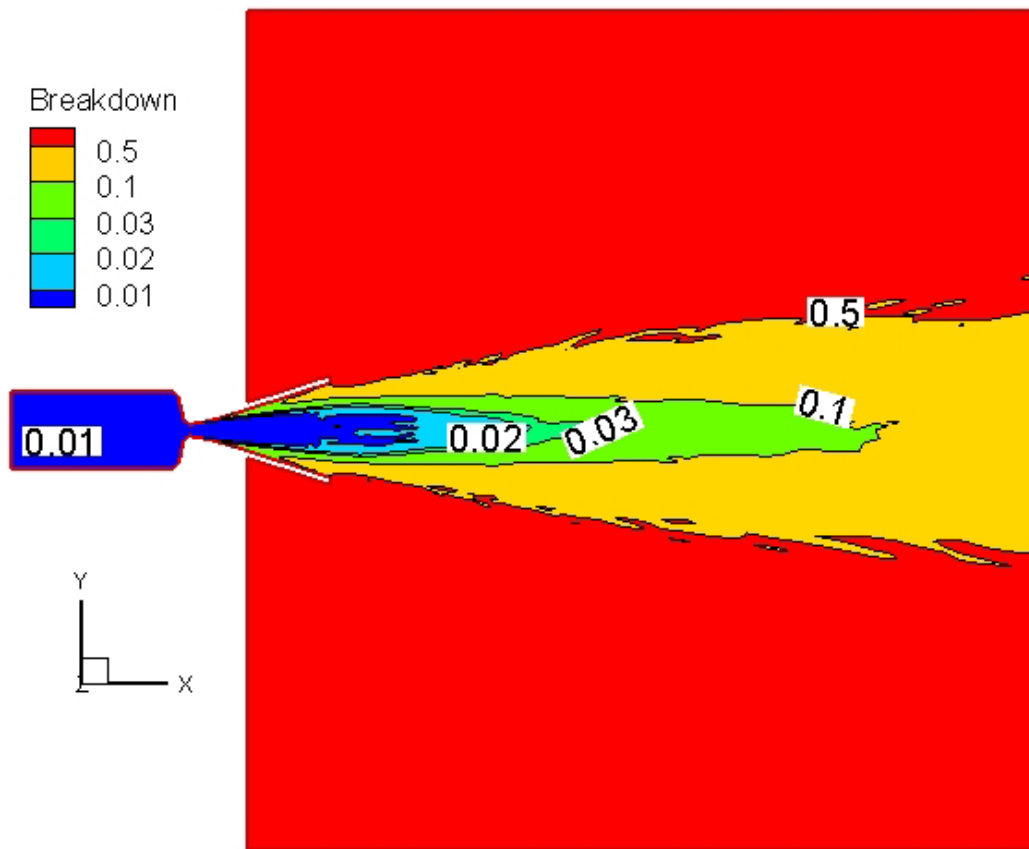
Fig. 3.27   Continuum breakdown distribution of the plume simulation issuing from RCS thruster.
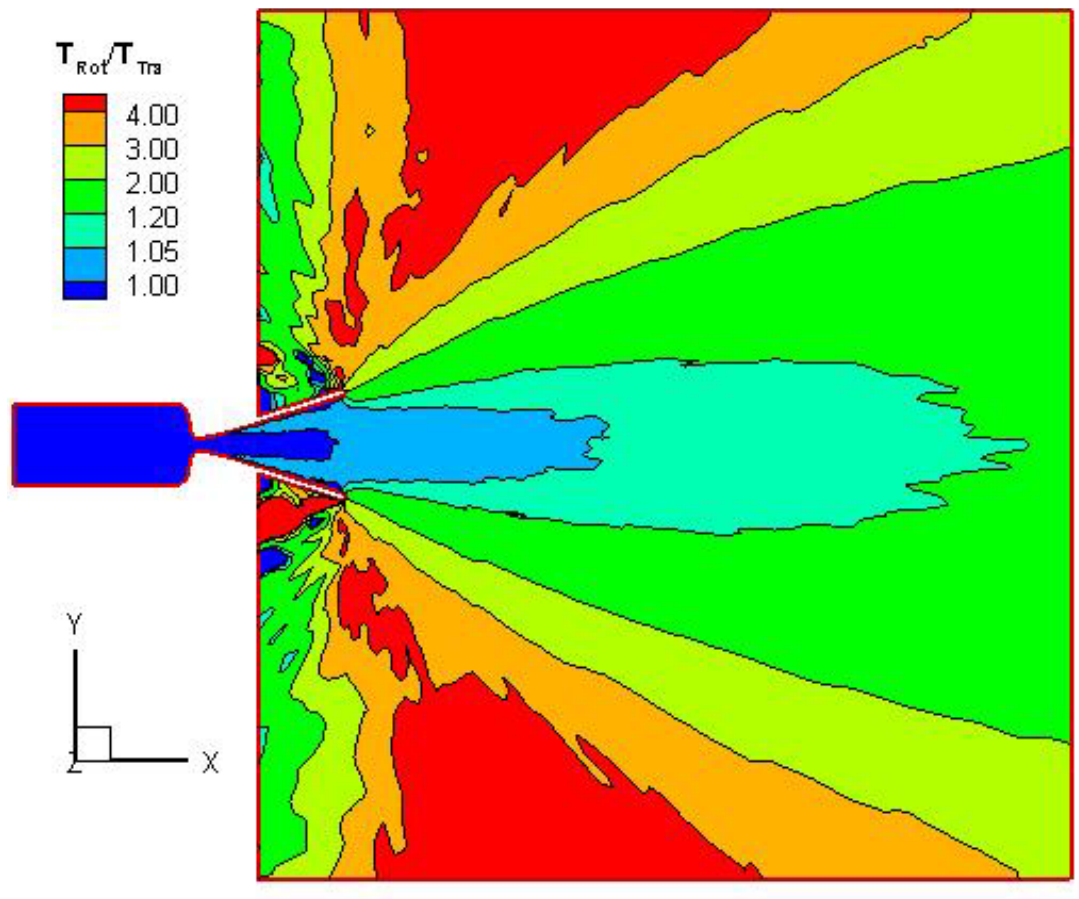
Fig. 3.28   Distribution of non-equilibrium ratio in the RCS plume simulation.
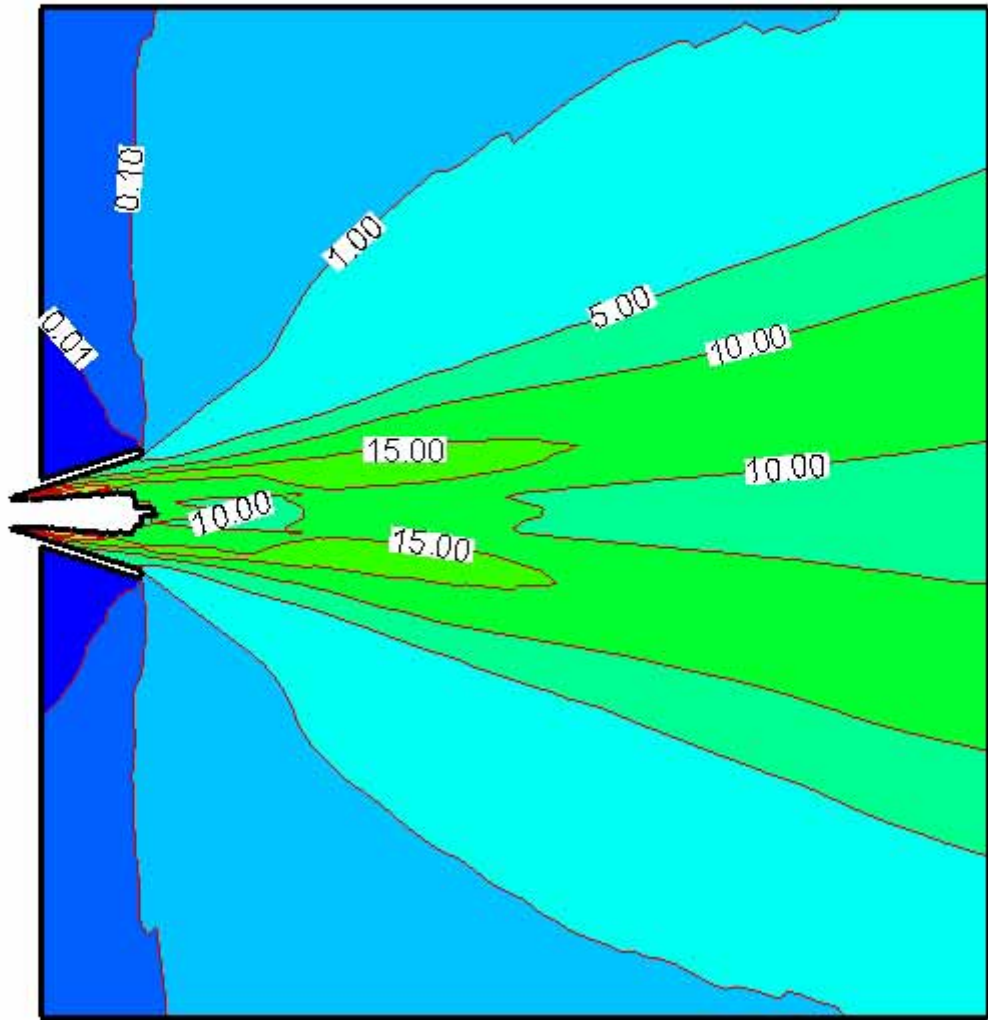
Fig. 3.29　Particle per cell in the RCS plume simulation.
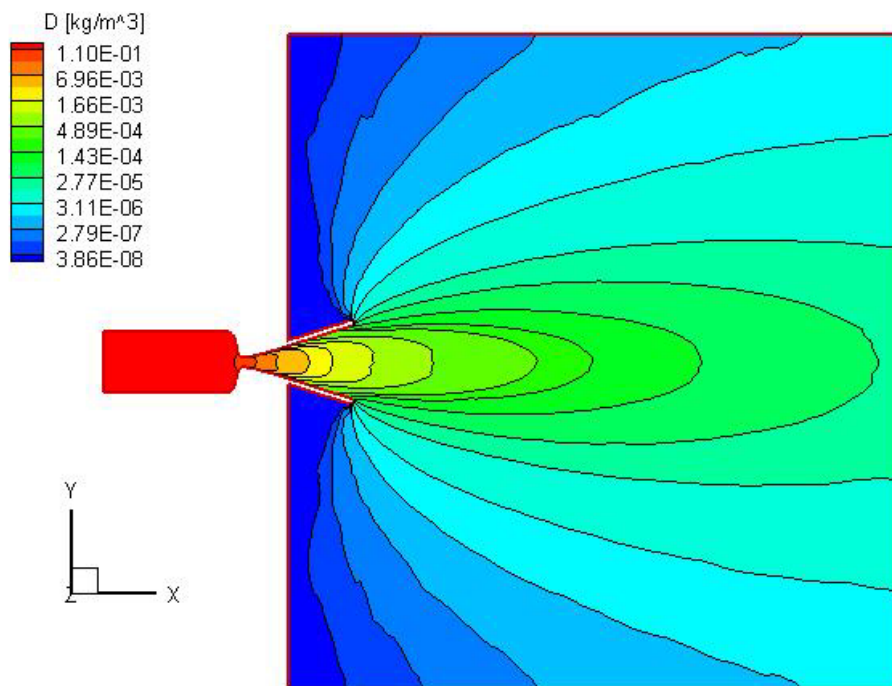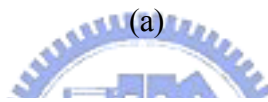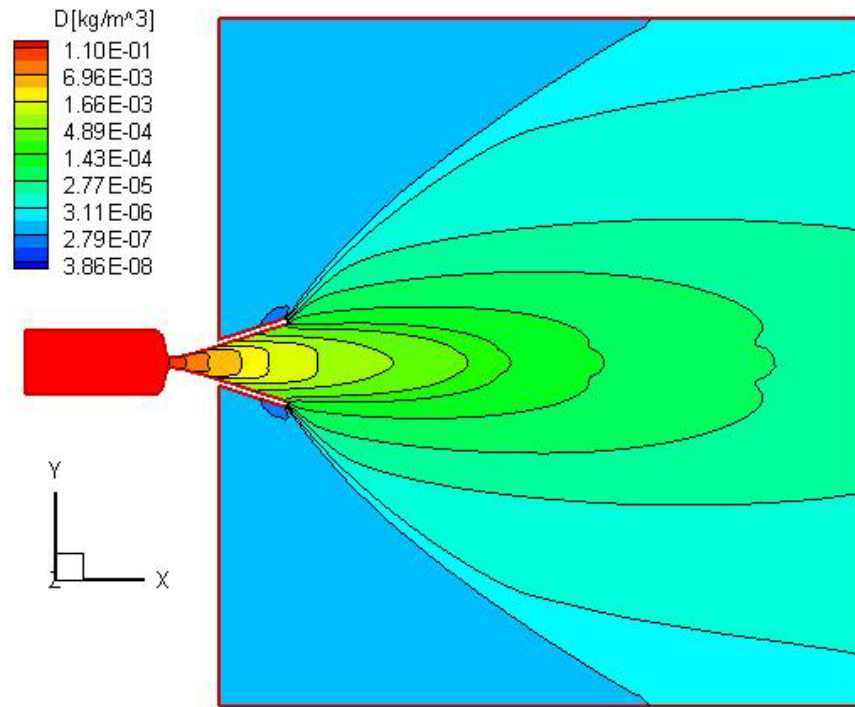
Fig. 3.30 Density distribution of the plume simulation issuing from RCS thruster (a) One-shot NS method; (b) Coupled DSMC-NS method (6th iteration).

154
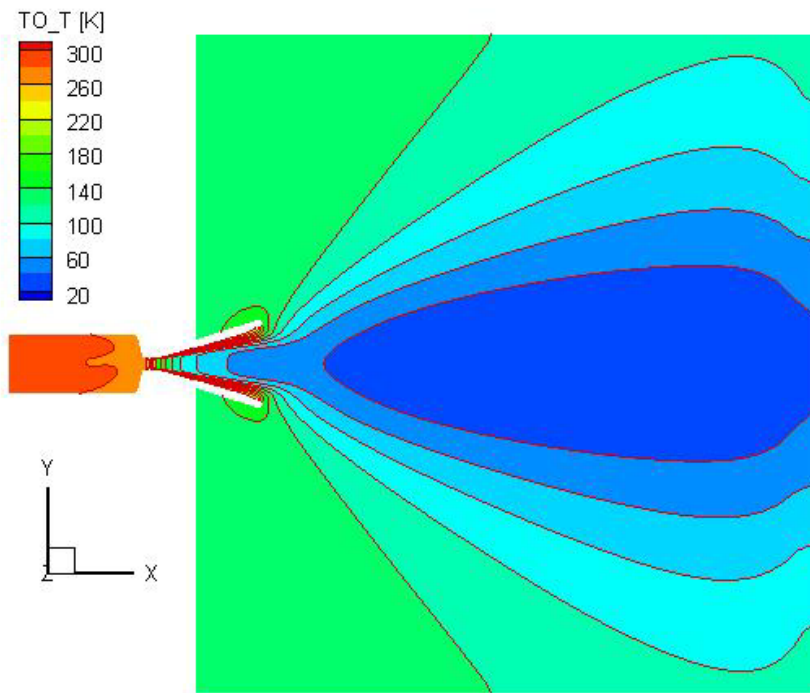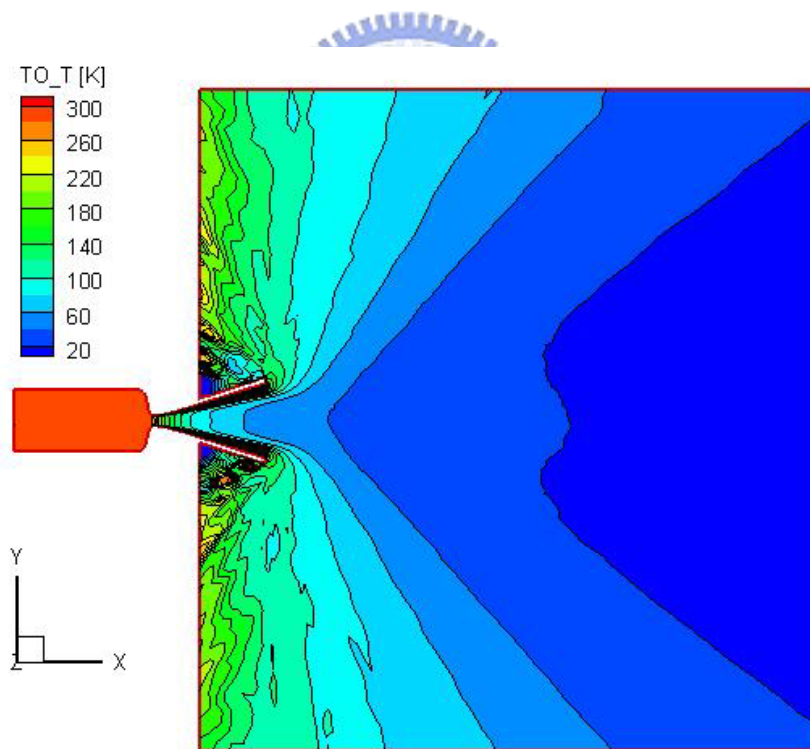
Fig. 3.31 Temperature distribution of the plume simulation issuing from RCS thruster (a) One-shot NS method; (b) Coupled DSMC-NS method (6th iteration).
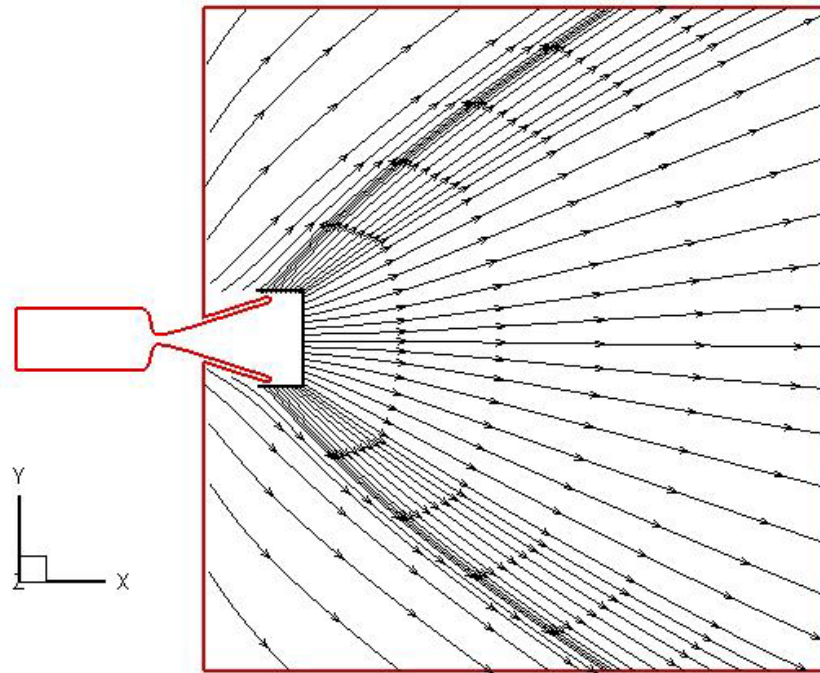
(a)
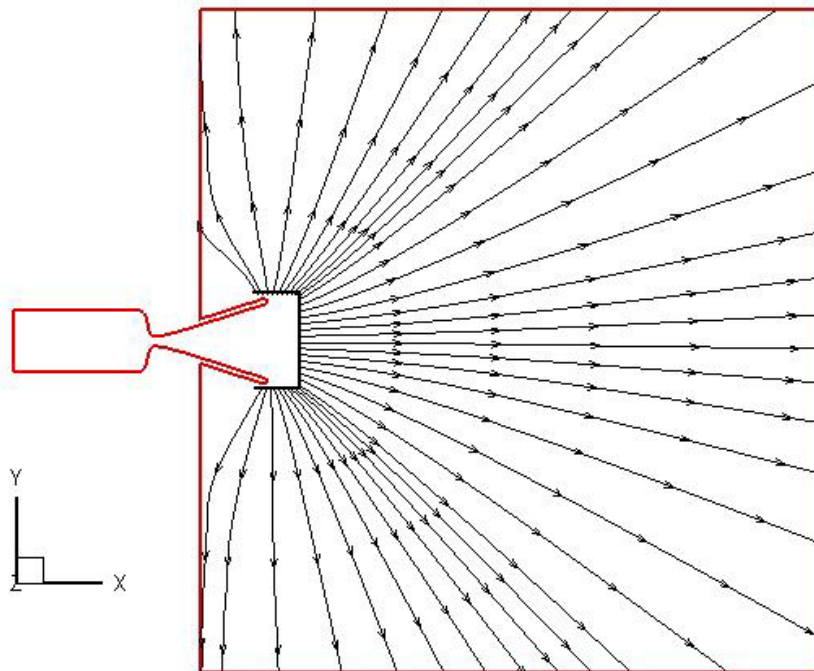
(b)

Fig. 3.32   Stream lines of the plume simulation issuing from RCS thruster (a) One-shot NS method; (b) Coupled DSMC-NS method (6th iteration).
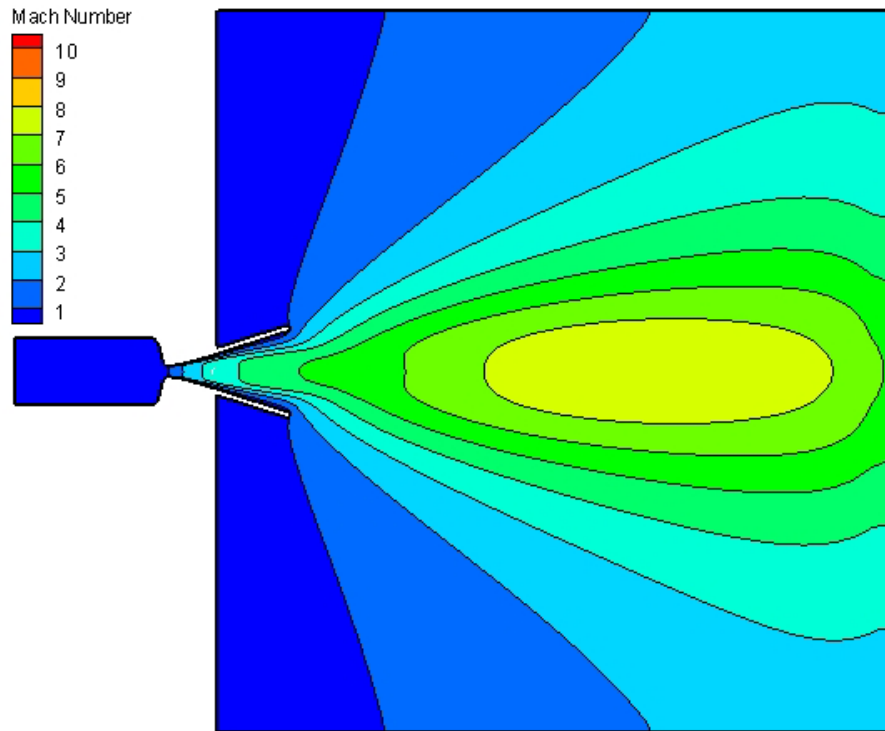
(a)
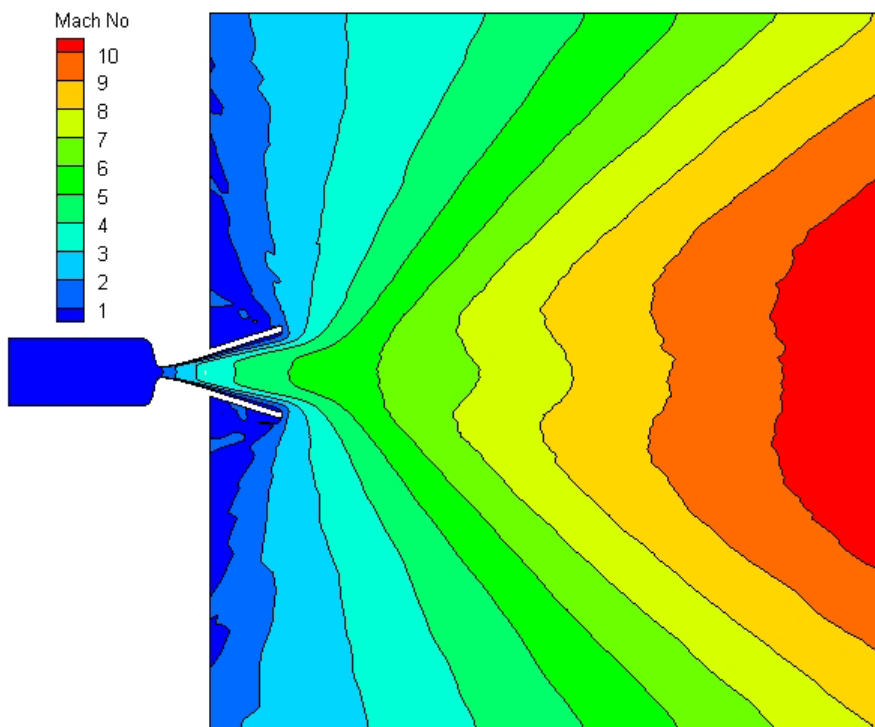
(b)

Fig. 3.33   Mach number distribution of the plume simulation issuing from RCS thruster (a)
One-shot NS method; (b) Coupled DSMC-NS method (6th iteration).
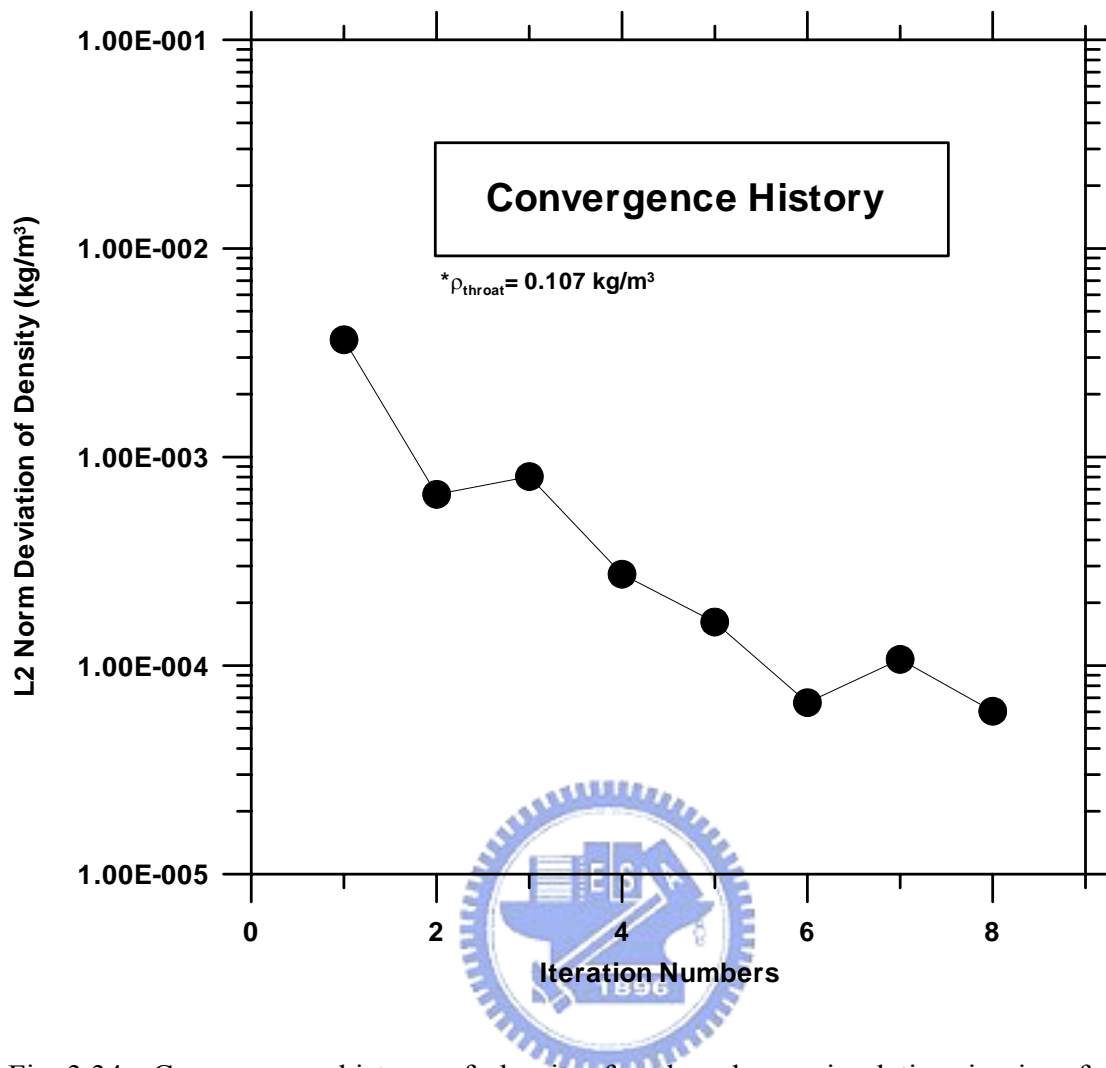
Fig. 3.34   Convergence history of density for the plume simulation issuing from RCS
thruster.
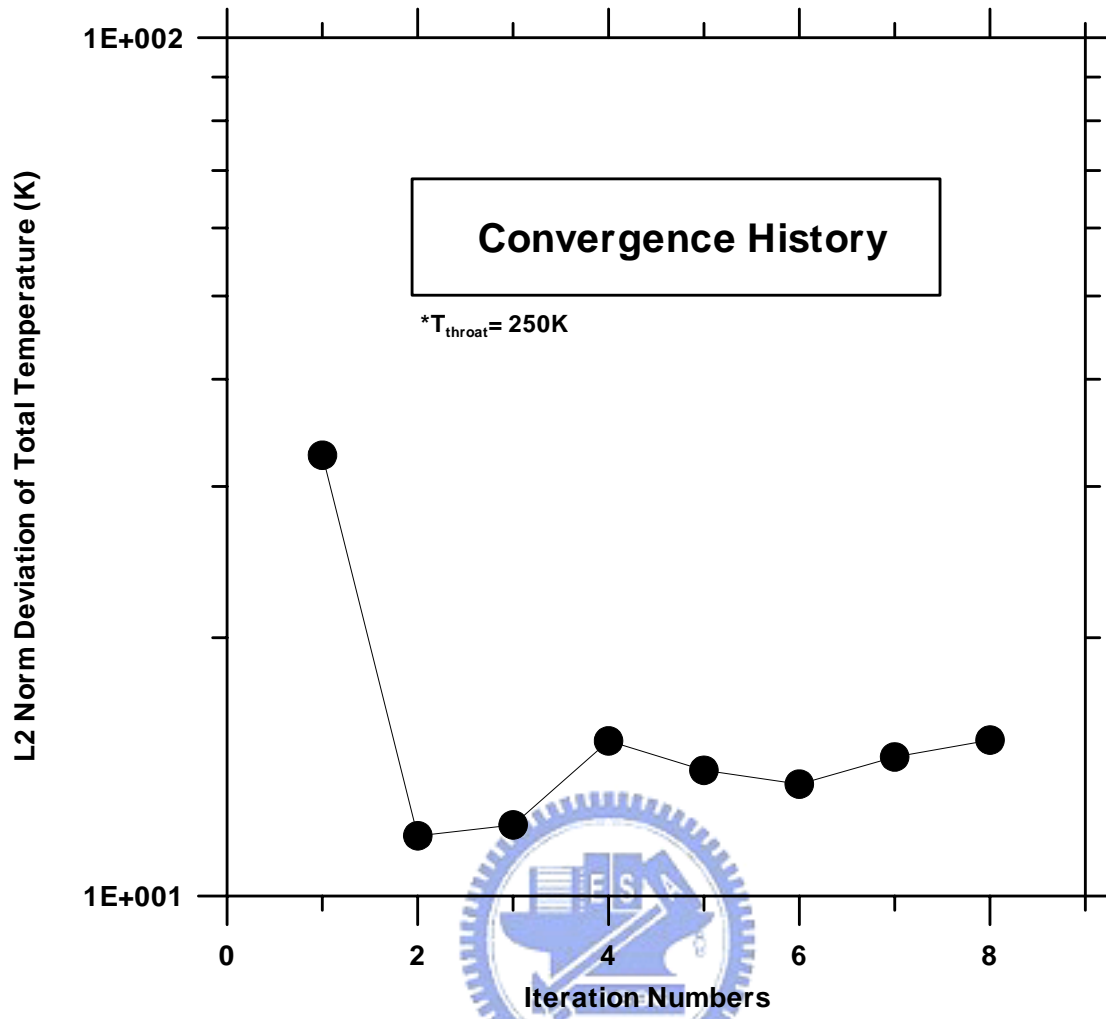
Fig. 3.35 Convergence history of total temperature for the plume simulation issuing from RCS thruster.

Surface Mesh Distribution
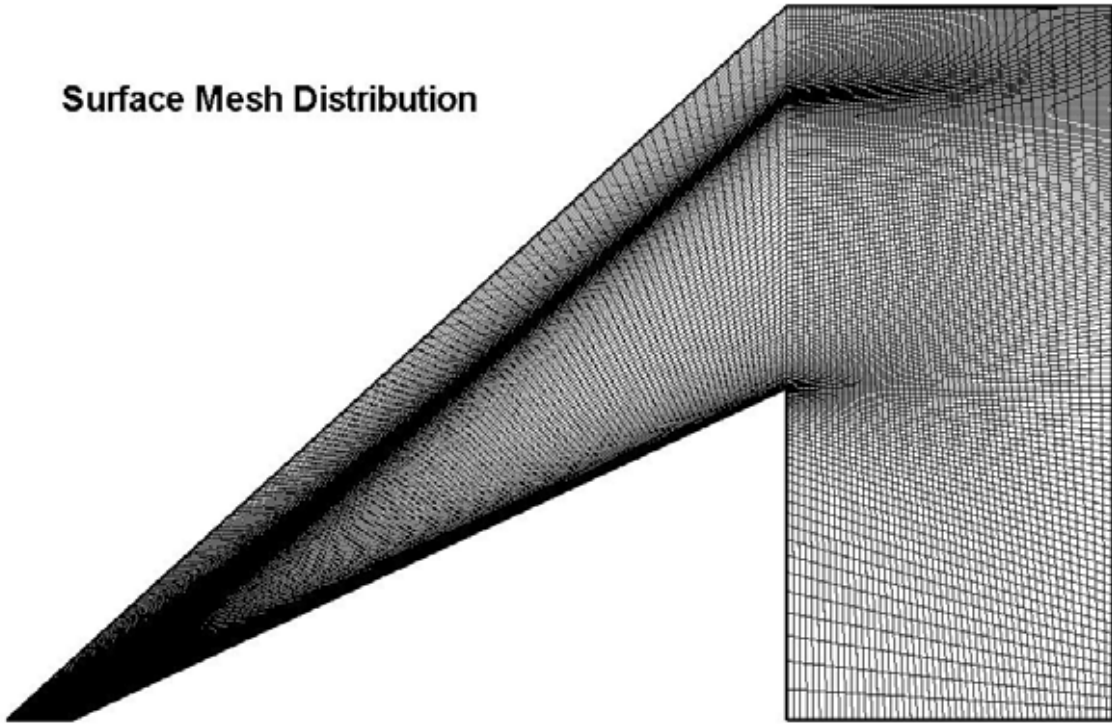
Fig. 4.1   Surface mesh distribution of 2-D wedge flow for the kinetic study of velocity
sampling.
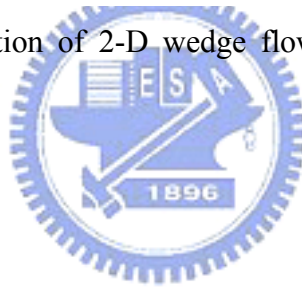
Fig. 4.2   Locations of velocity sampling and continuum breakdown distribution of 2-D wedge flow for the kinetic study of velocity sampling.
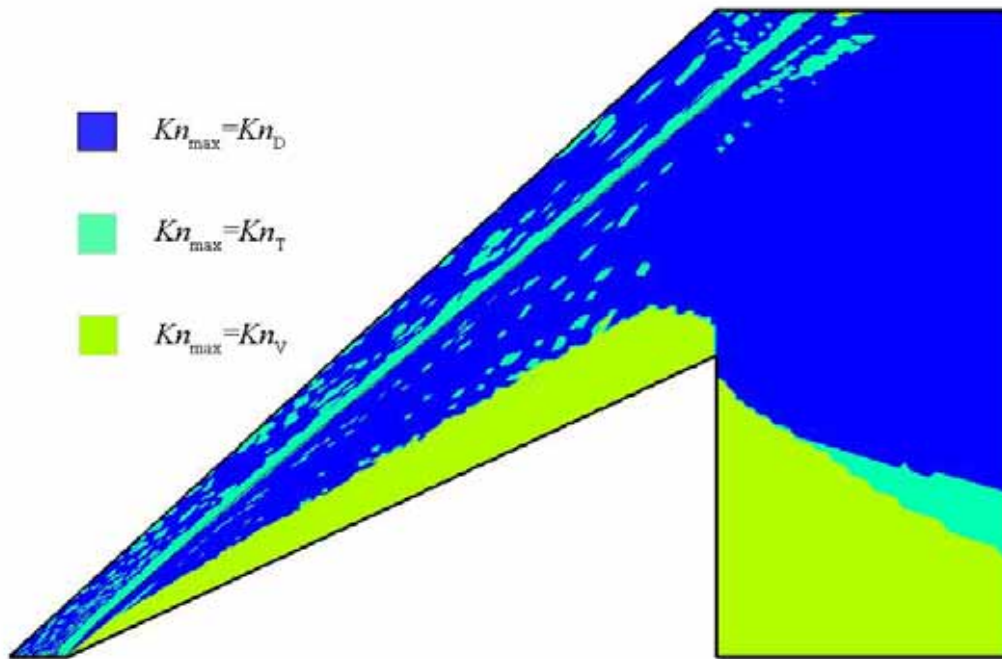
Fig. 4.3　Domain distribution of dominating breakdown parameter of 2-D wedge flow for the kinetic study of velocity sampling.
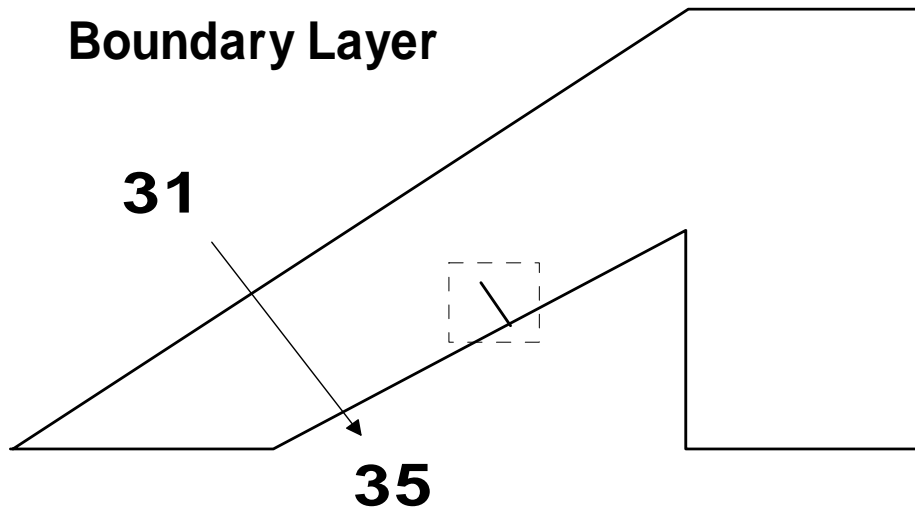
Leading Edge

3 ⟶ 7
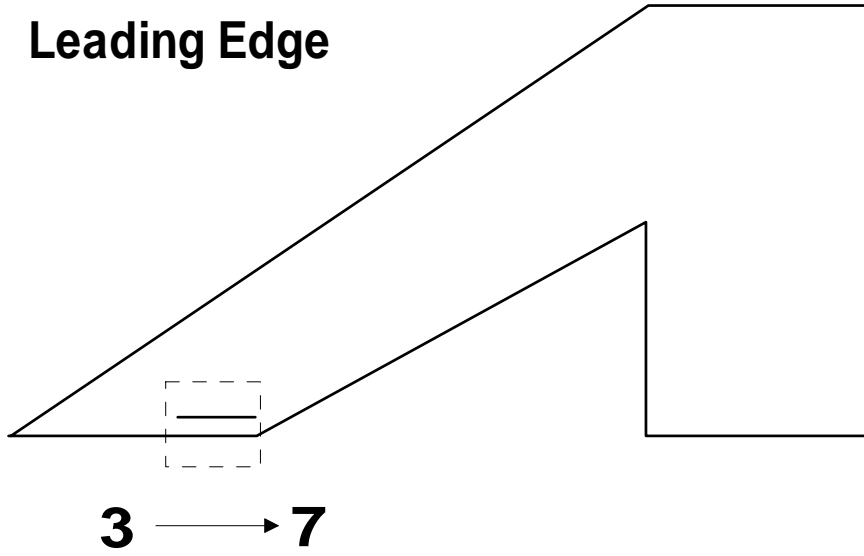
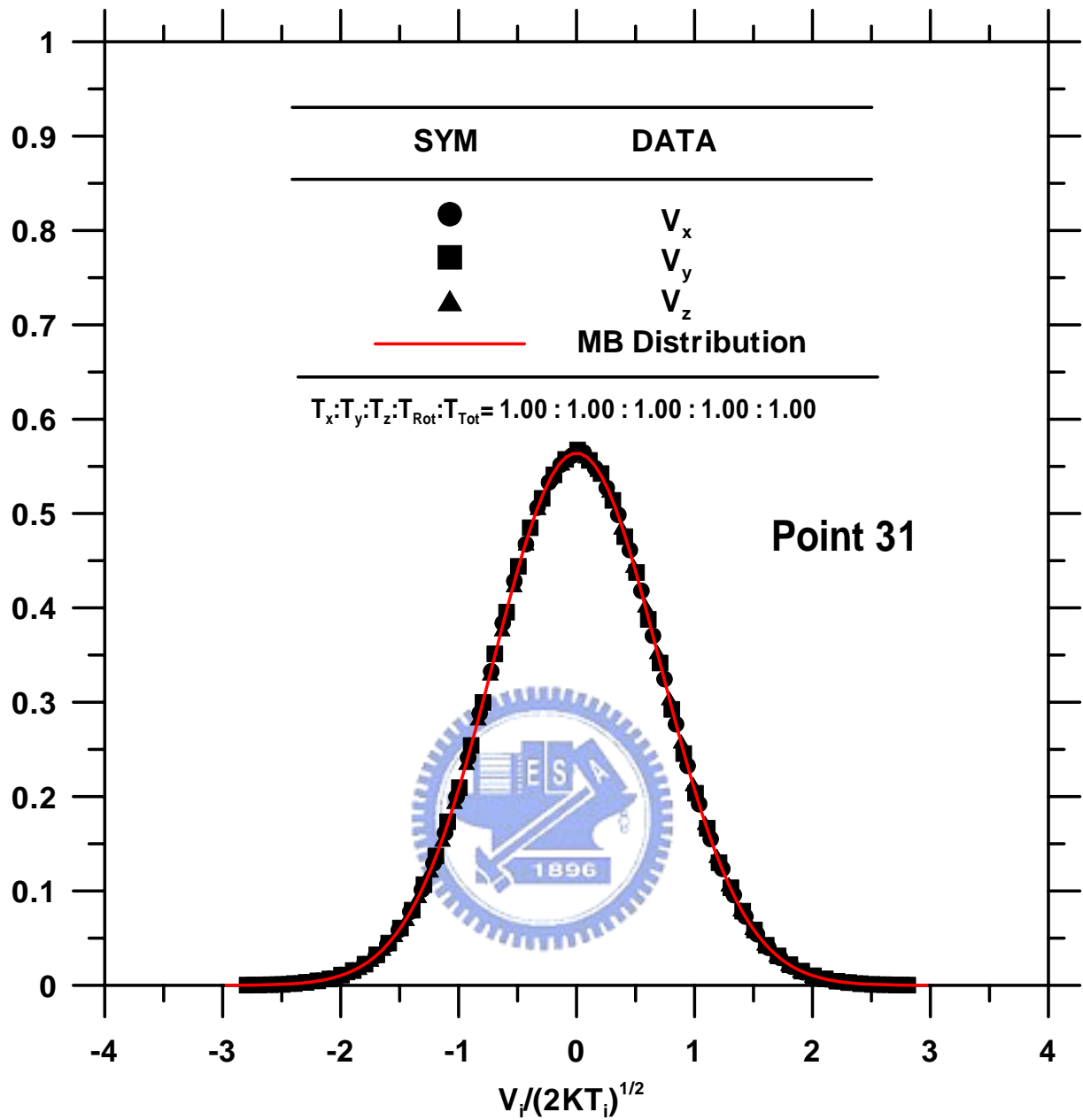Fig. 4.4a   Locations of velocity sampling Point 3-7 (Leading edge region).
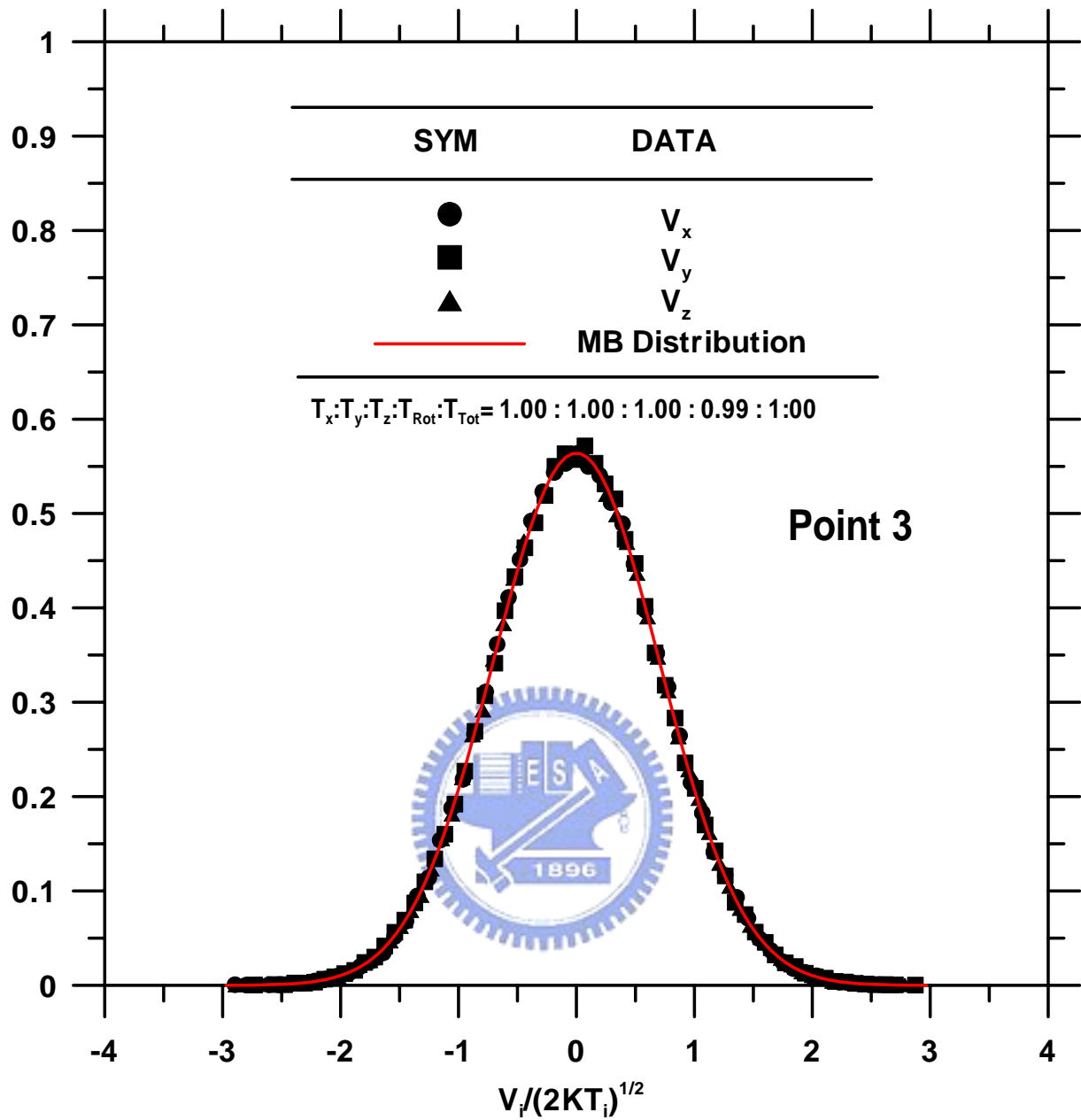
Fig. 4.4b   Random velocity distributions to each direction at Point 3 (Leading edge region).
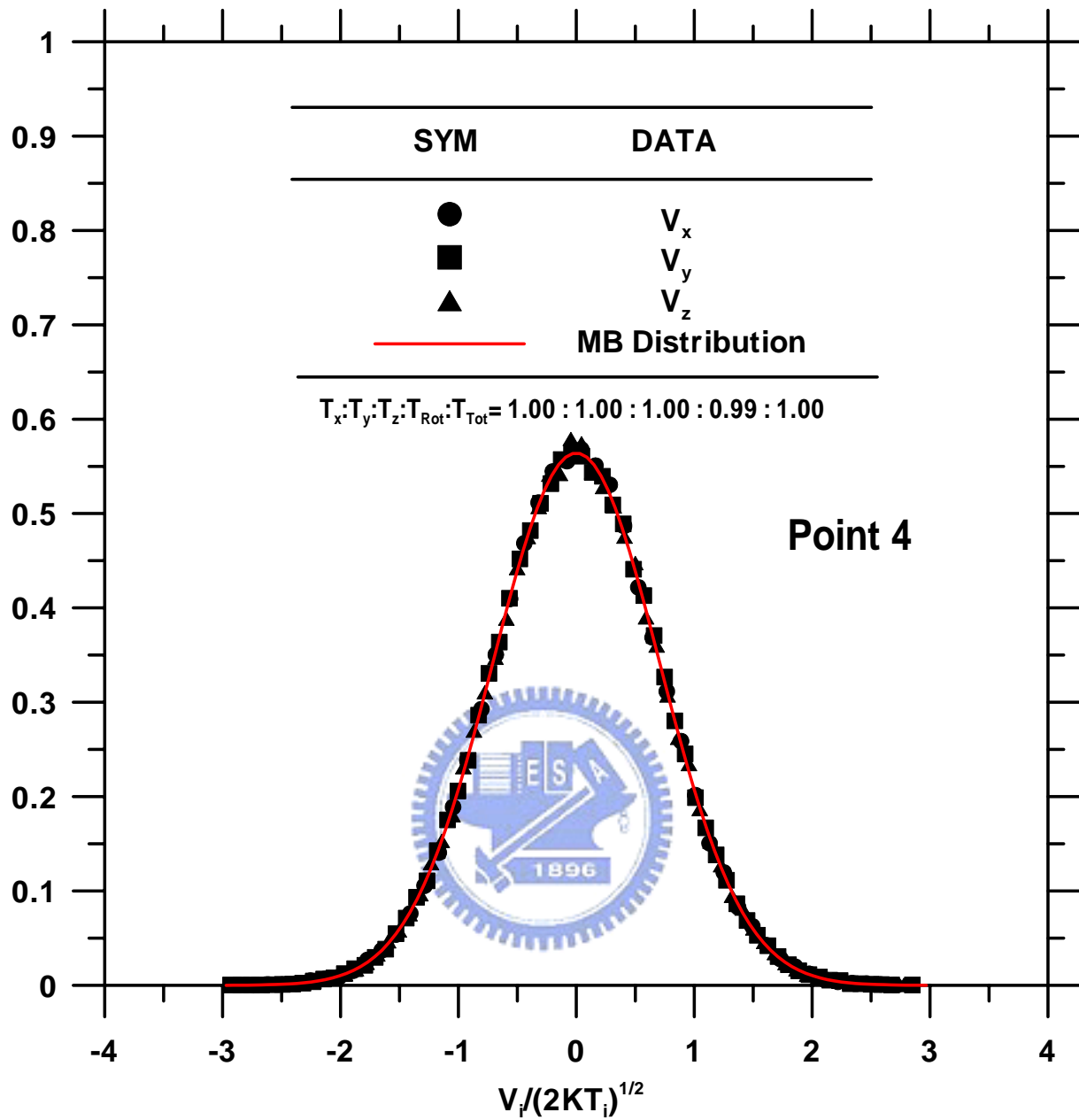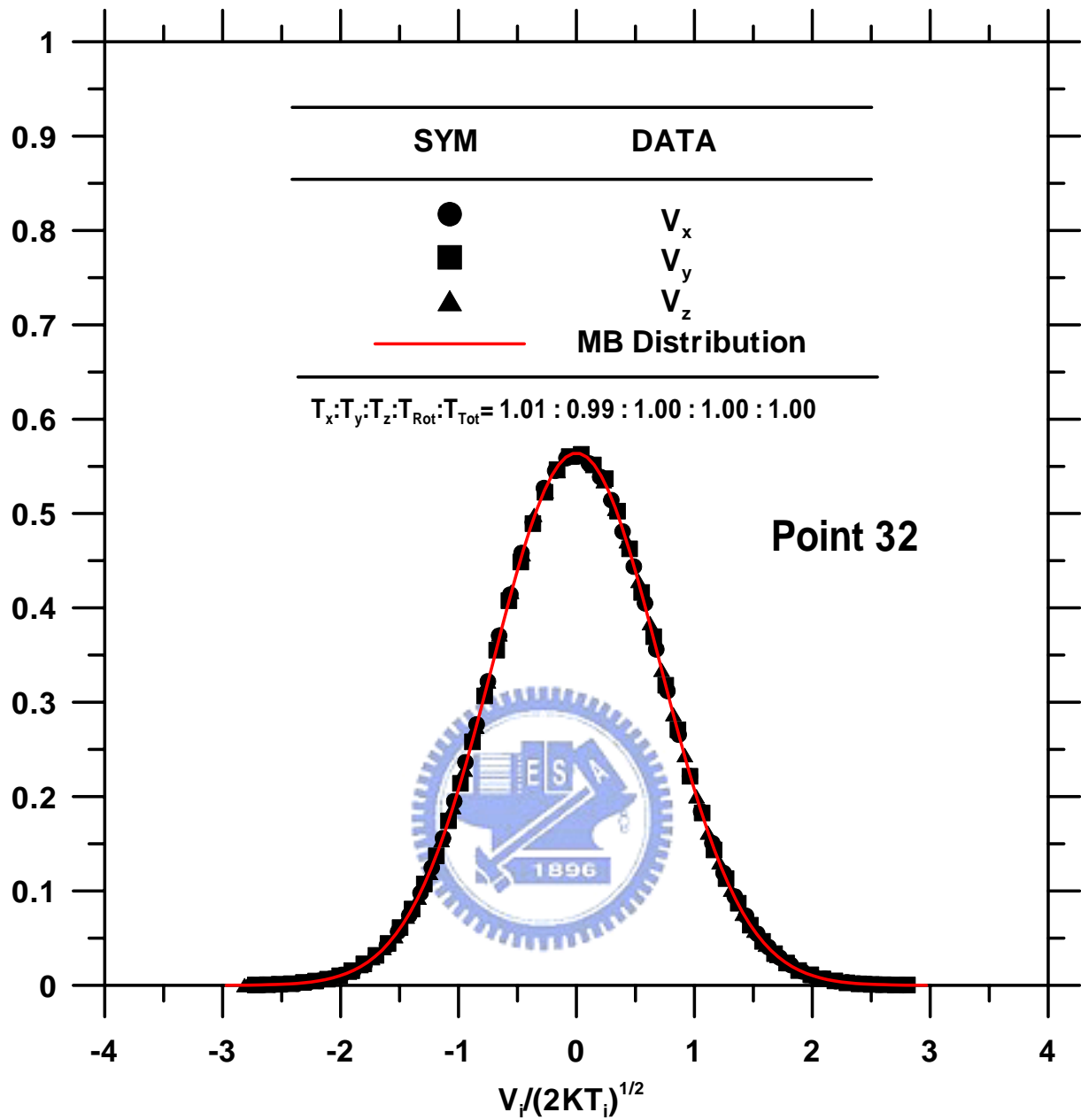
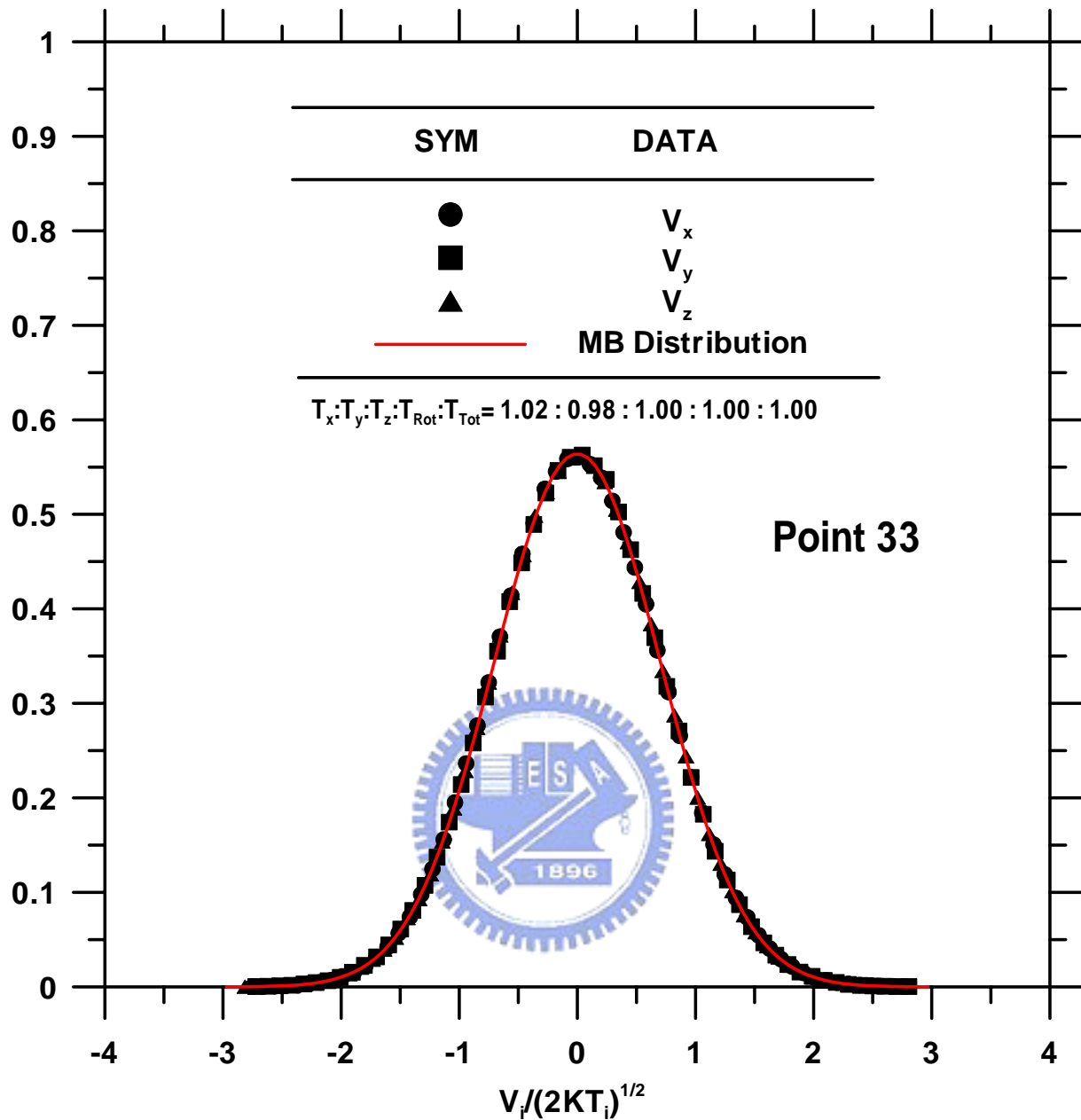Fig. 4.4c   Random velocity distributions to each direction at Point 4 (Leading edge region).
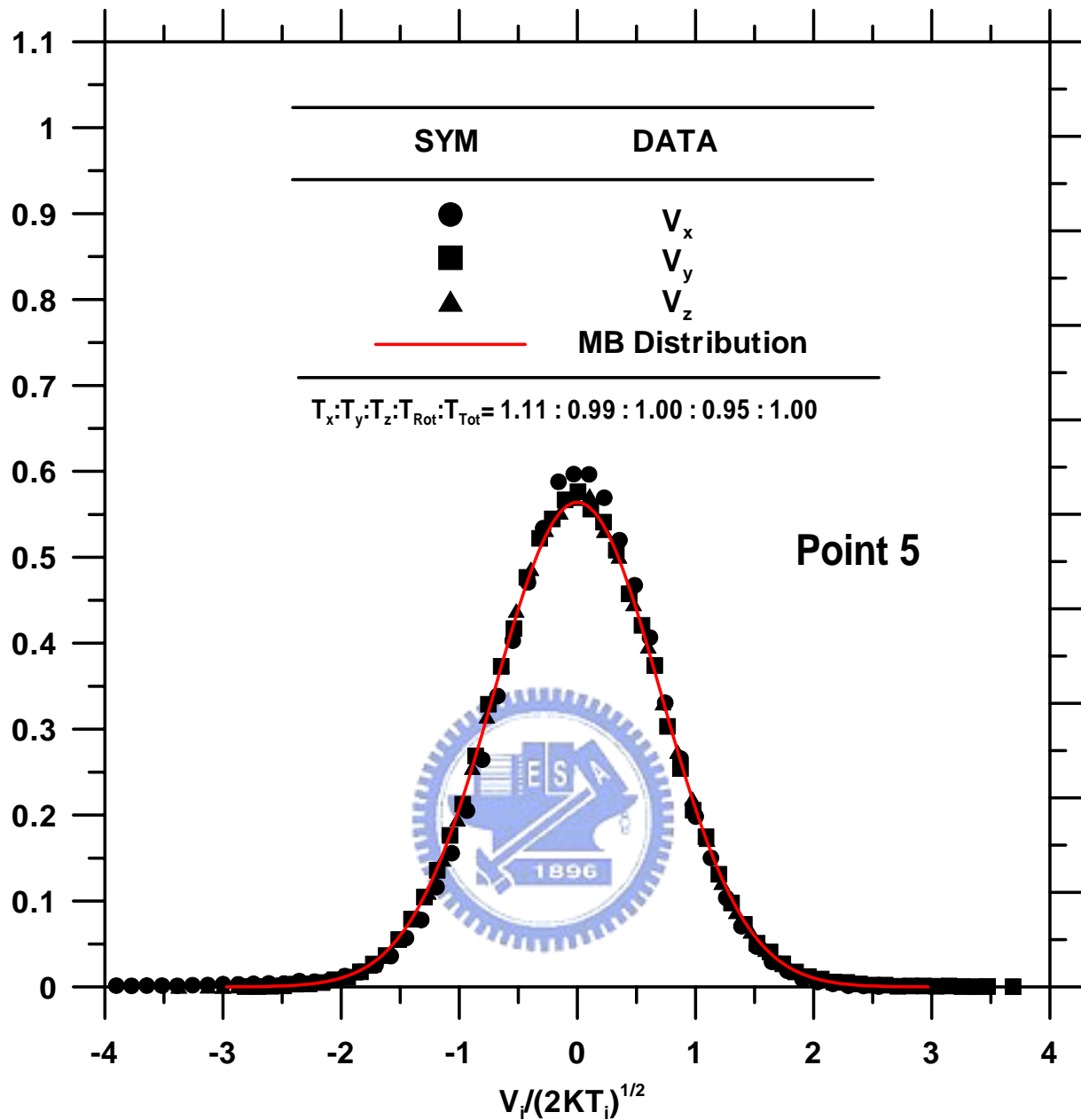
Fig. 4.4d Random velocity distributions to each direction at Point 5 (Leading edge region).
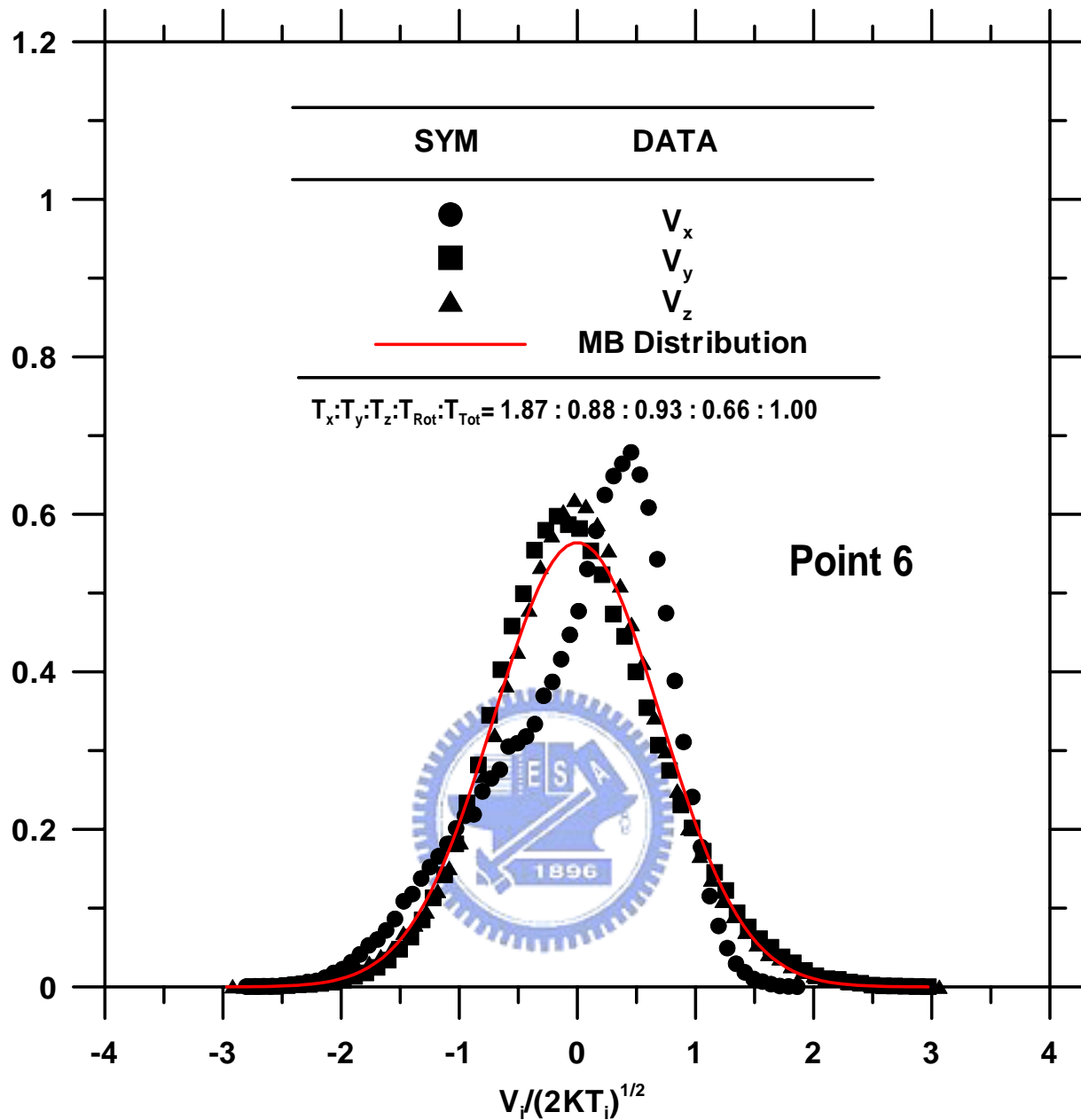
Fig. 4.4e   Random velocity distributions to each direction at Point 6 (Leading edge region).
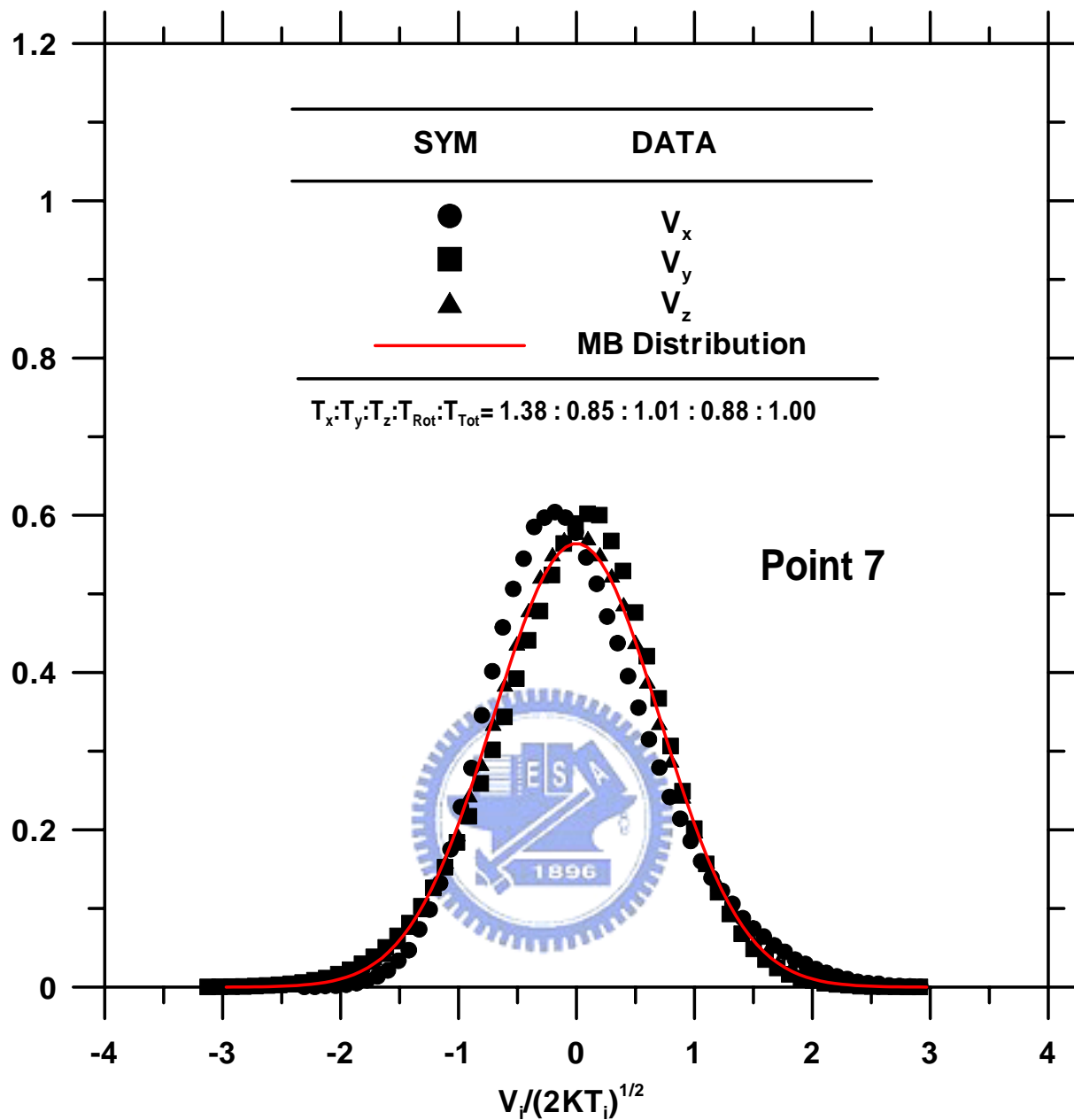
Fig. 4.4f   Random velocity distributions to each direction at Point 7 (Leading edge region).

168

Shock Region

14

19
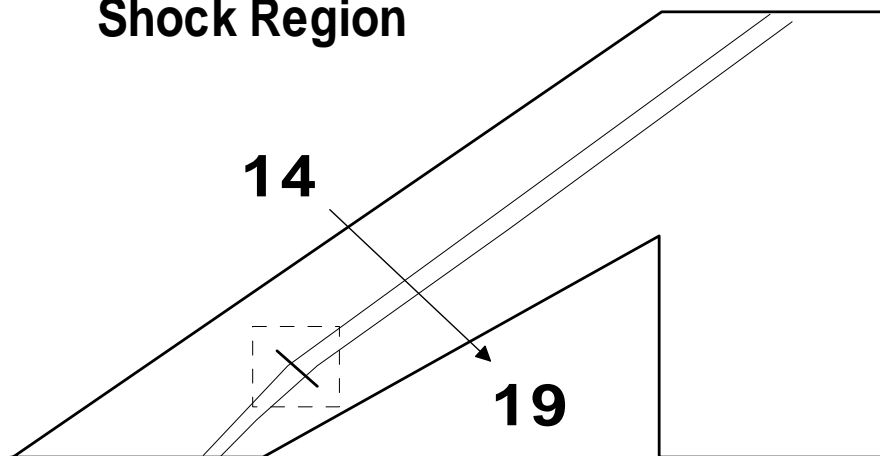
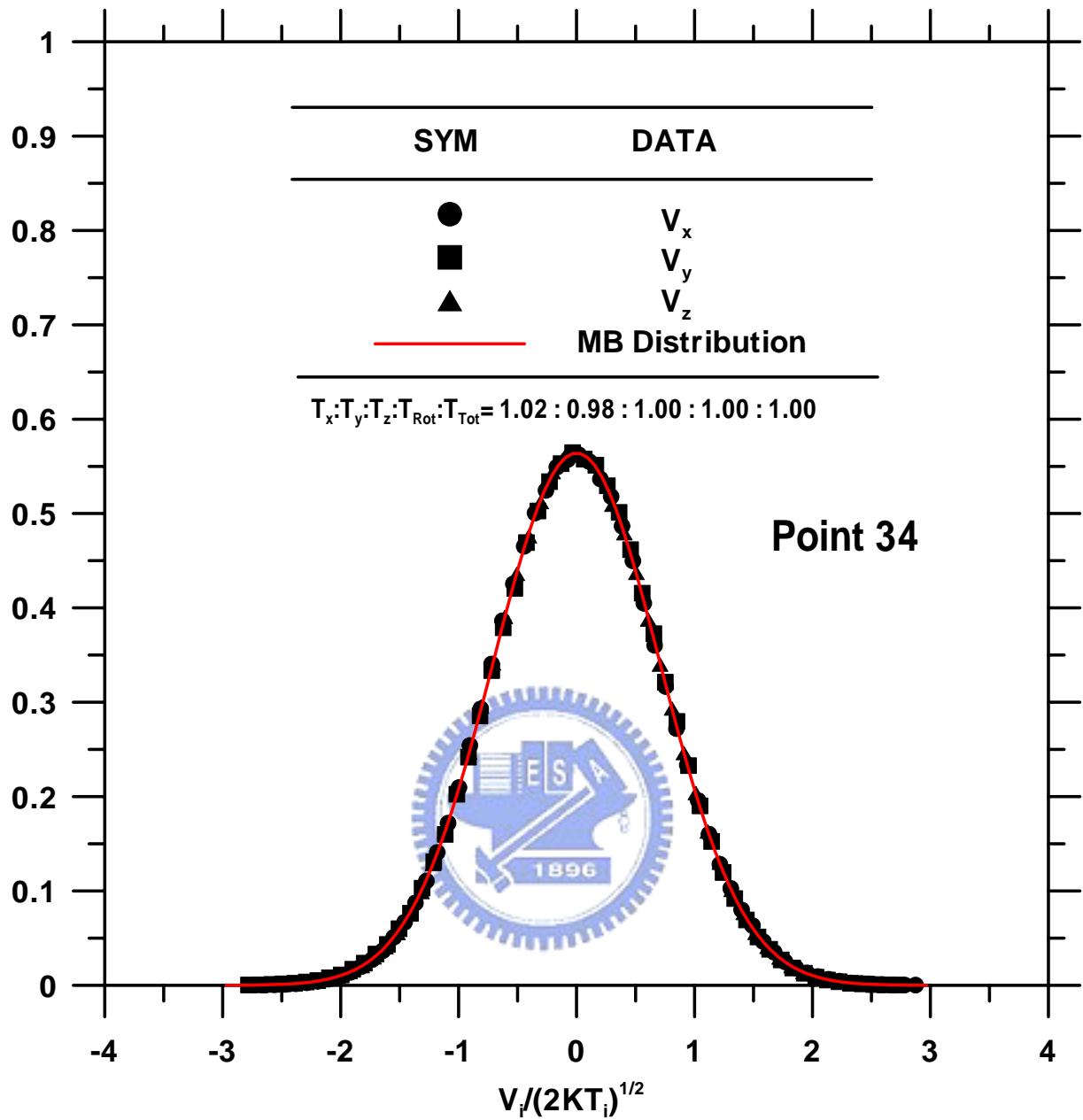Fig. 4.5a   Locations of velocity sampling Point 14-19 (Oblique shock region).
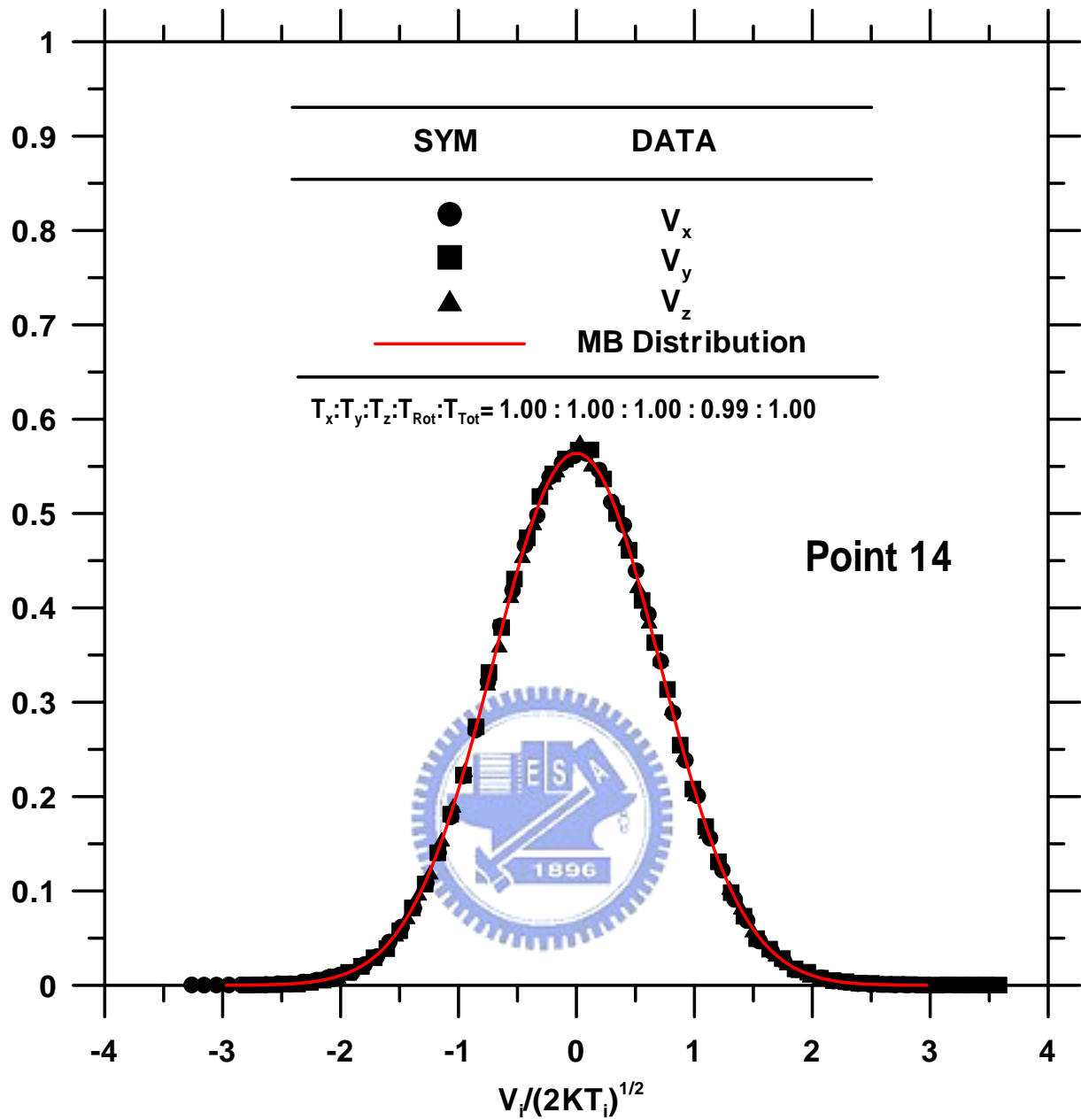
Fig. 4.5b Random velocity distributions to each direction at Point 14 (Oblique shock region).
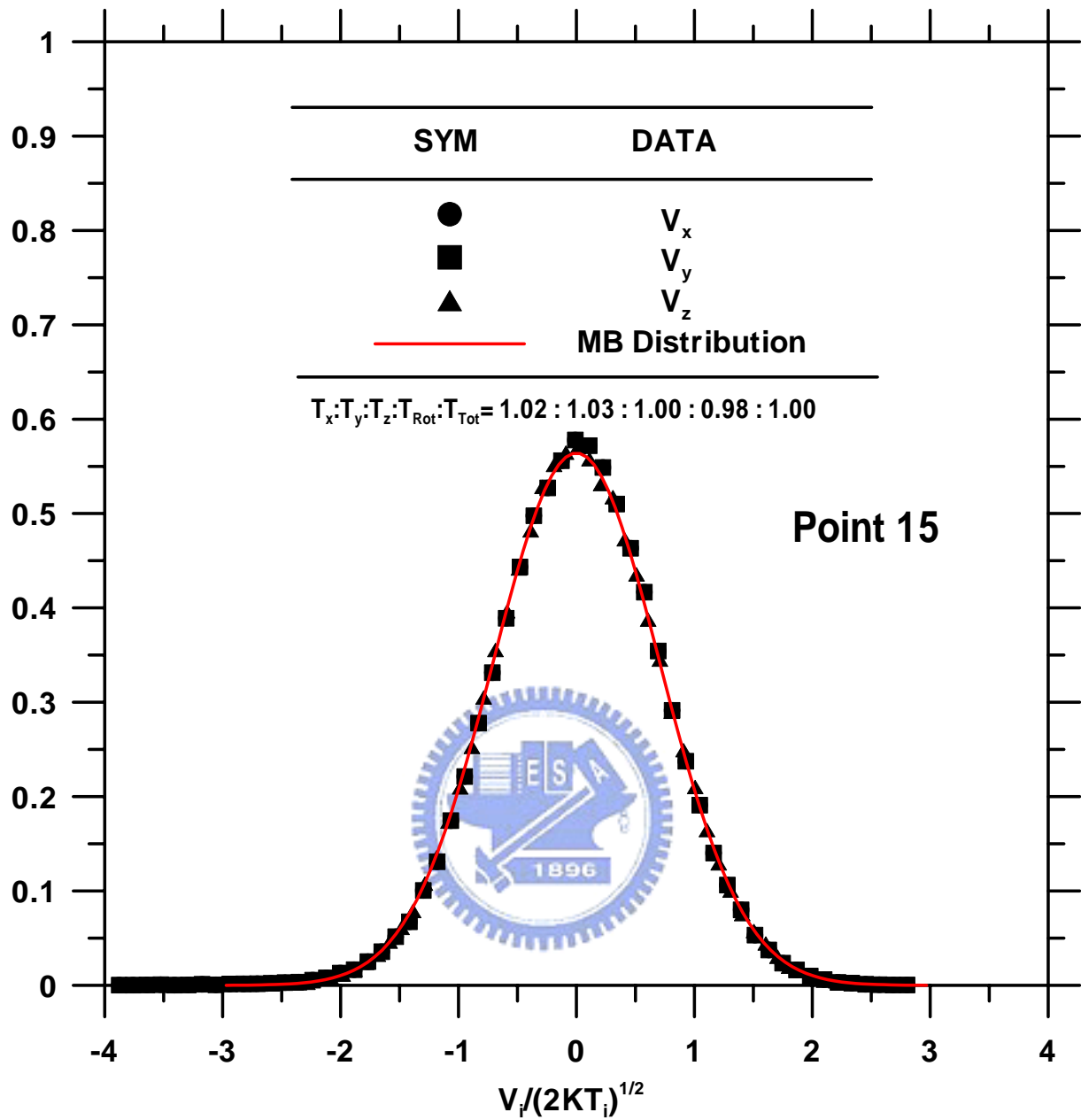
Fig. 4.5c Random velocity distributions to each direction at Point 15 (Oblique shock region).

171
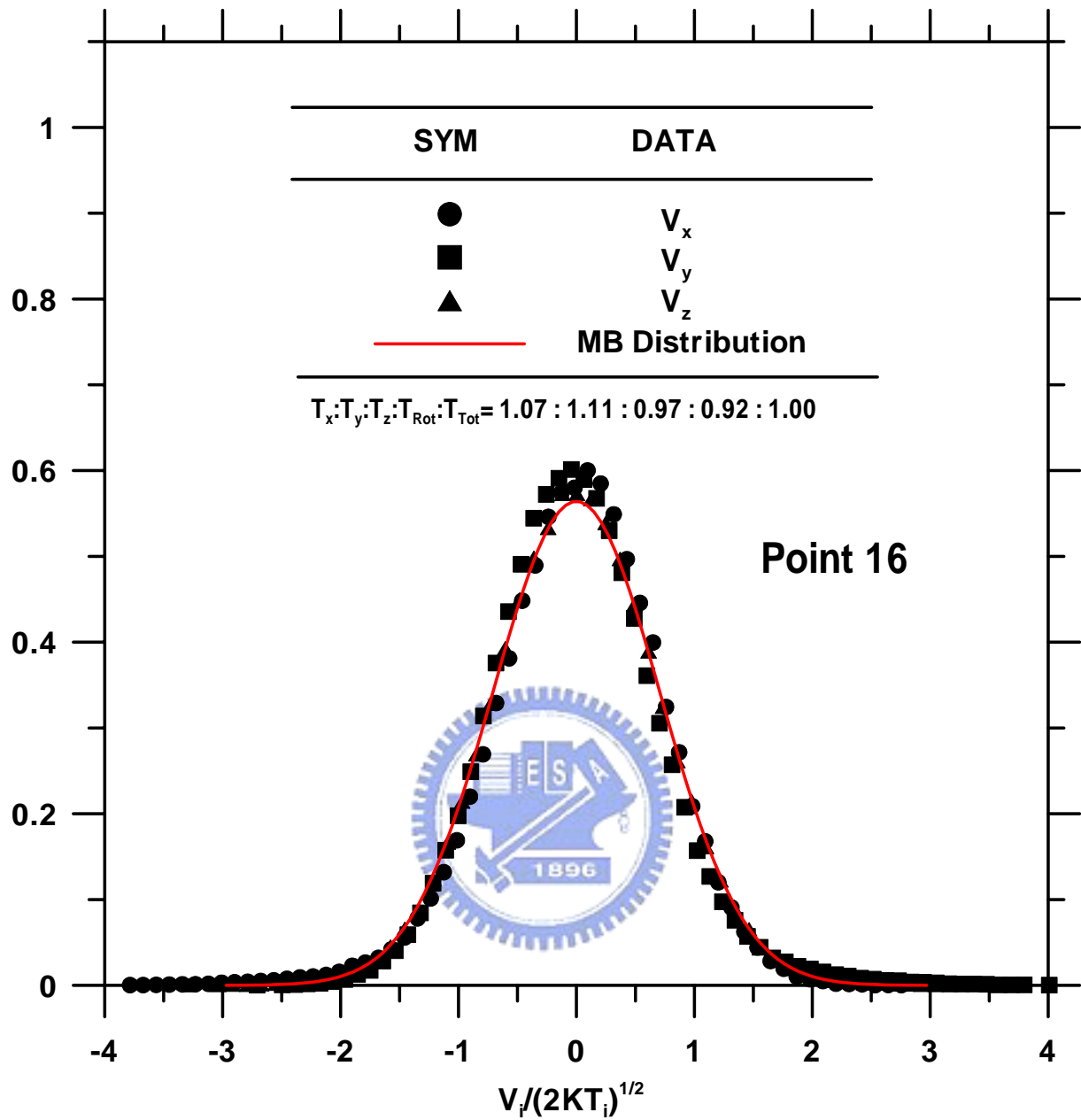
Fig. 4.5d Random velocity distributions to each direction at Point 16 (Oblique shock region).
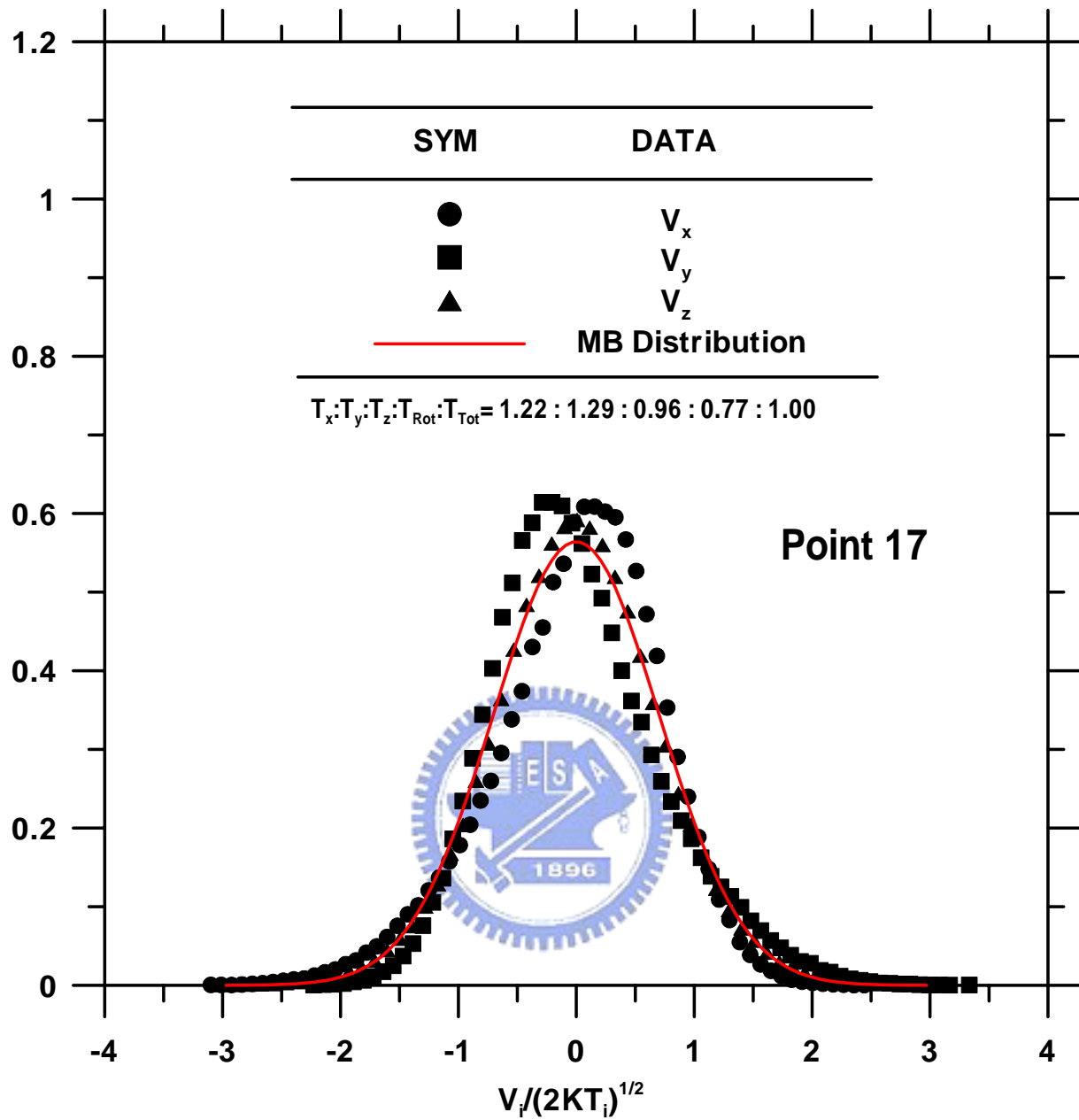
Fig. 4.5e   Random velocity distributions to each direction at Point 17 (Oblique shock region).
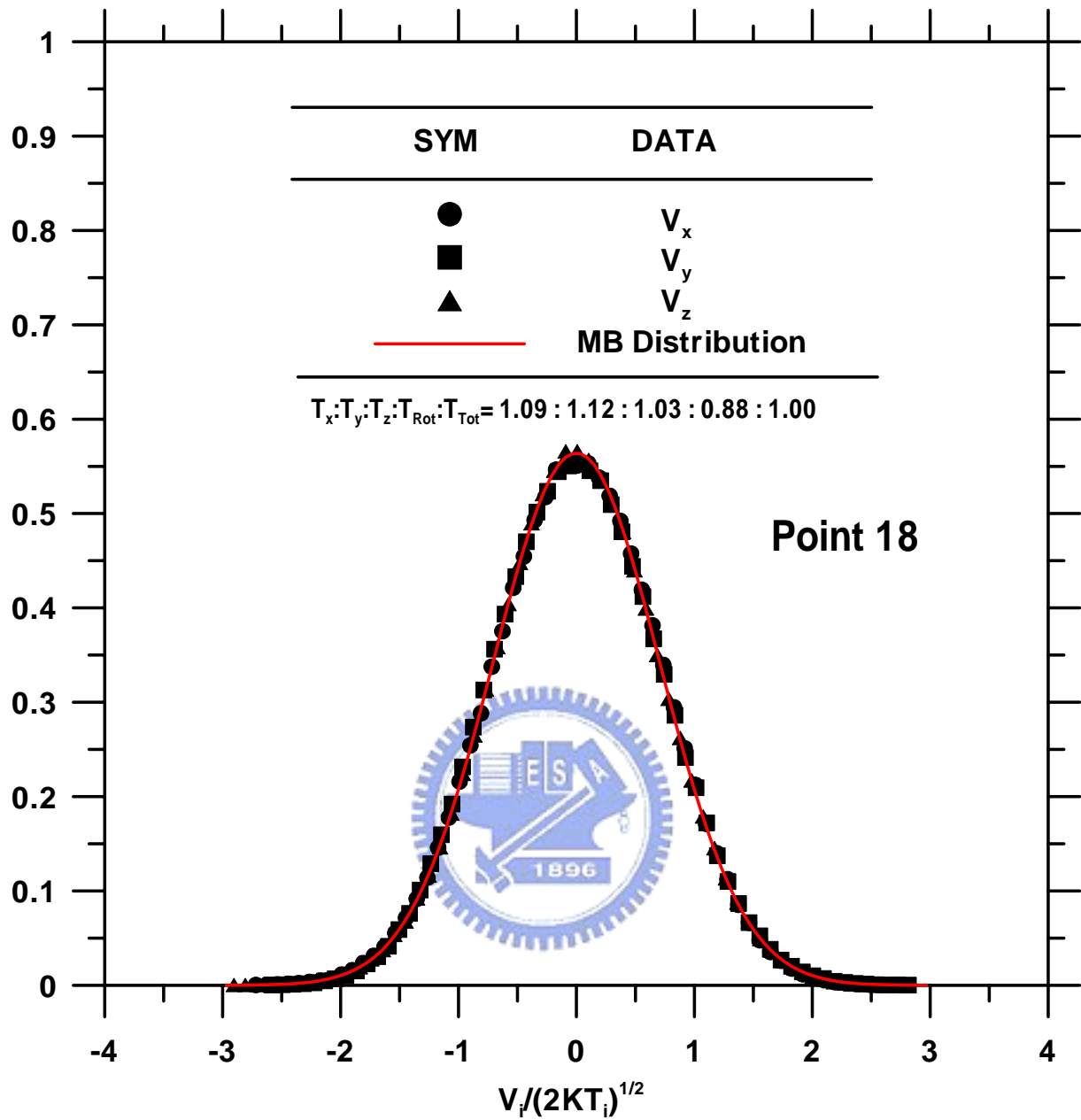
Fig. 4.5f   Random velocity distributions to each direction at Point 18 (Oblique shock region).
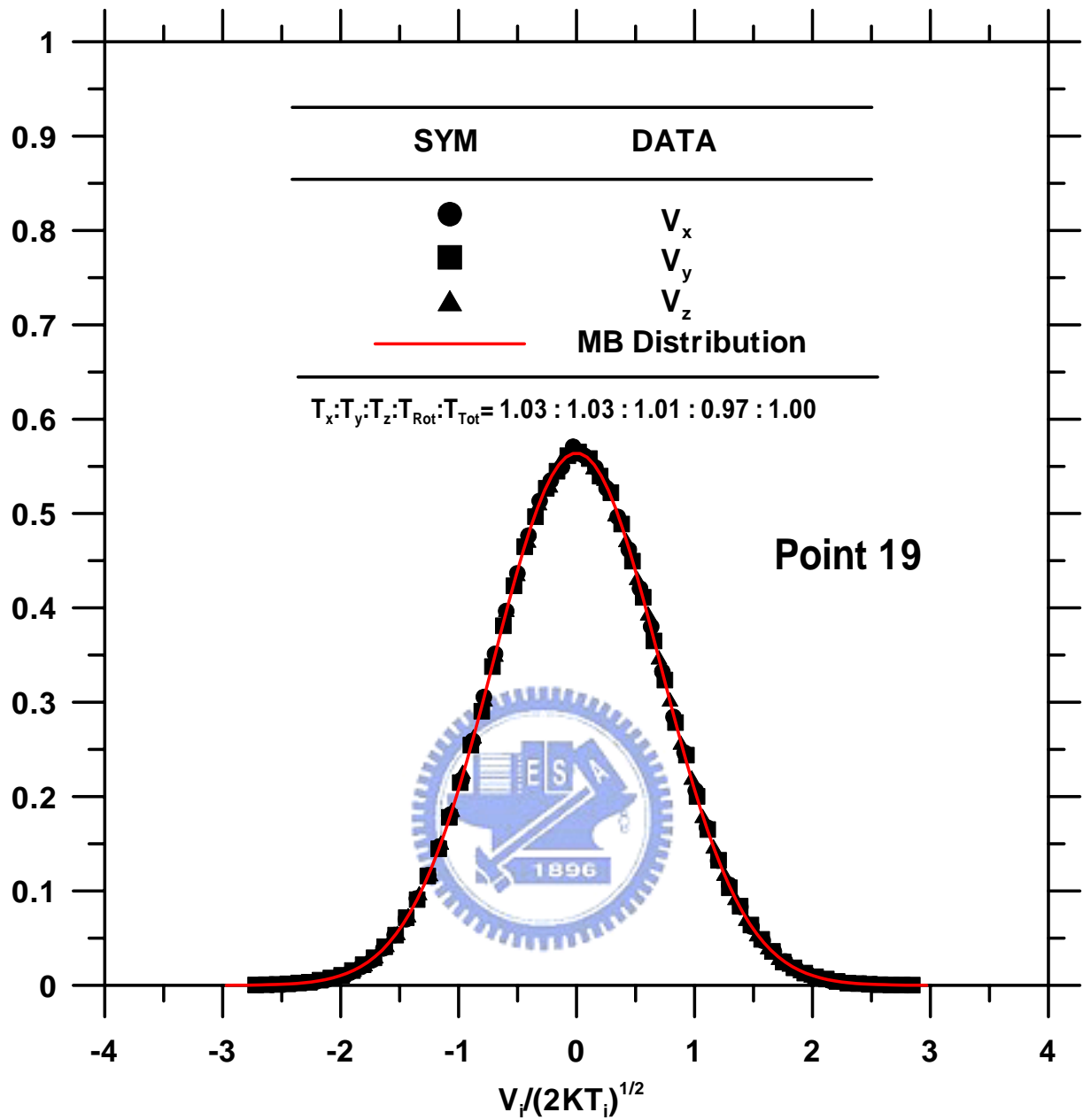
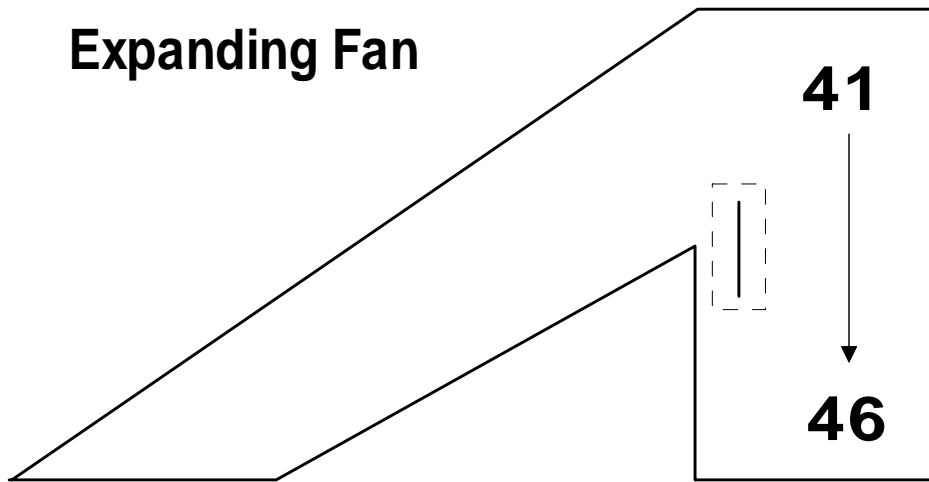Fig. 4.5g Random velocity distributions to each direction at Point 19 (Oblique shock region).
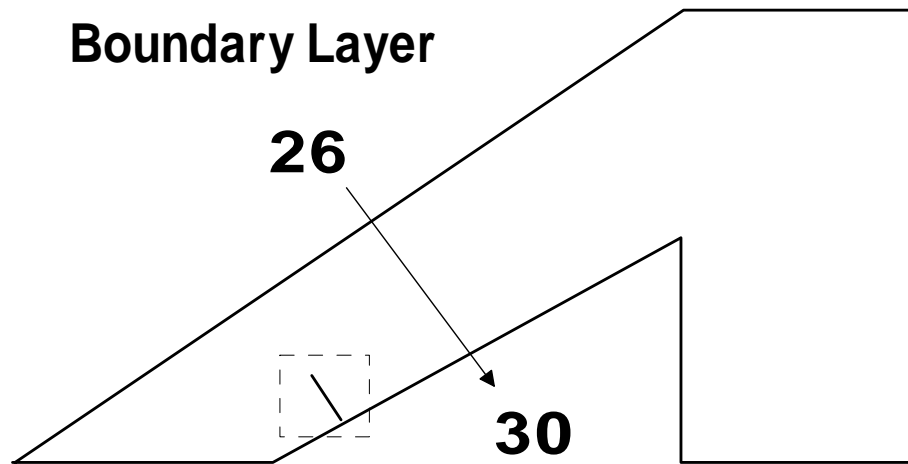
Fig. 4.6b   Locations of velocity sampling Point 26-30 (Boundary layer region).
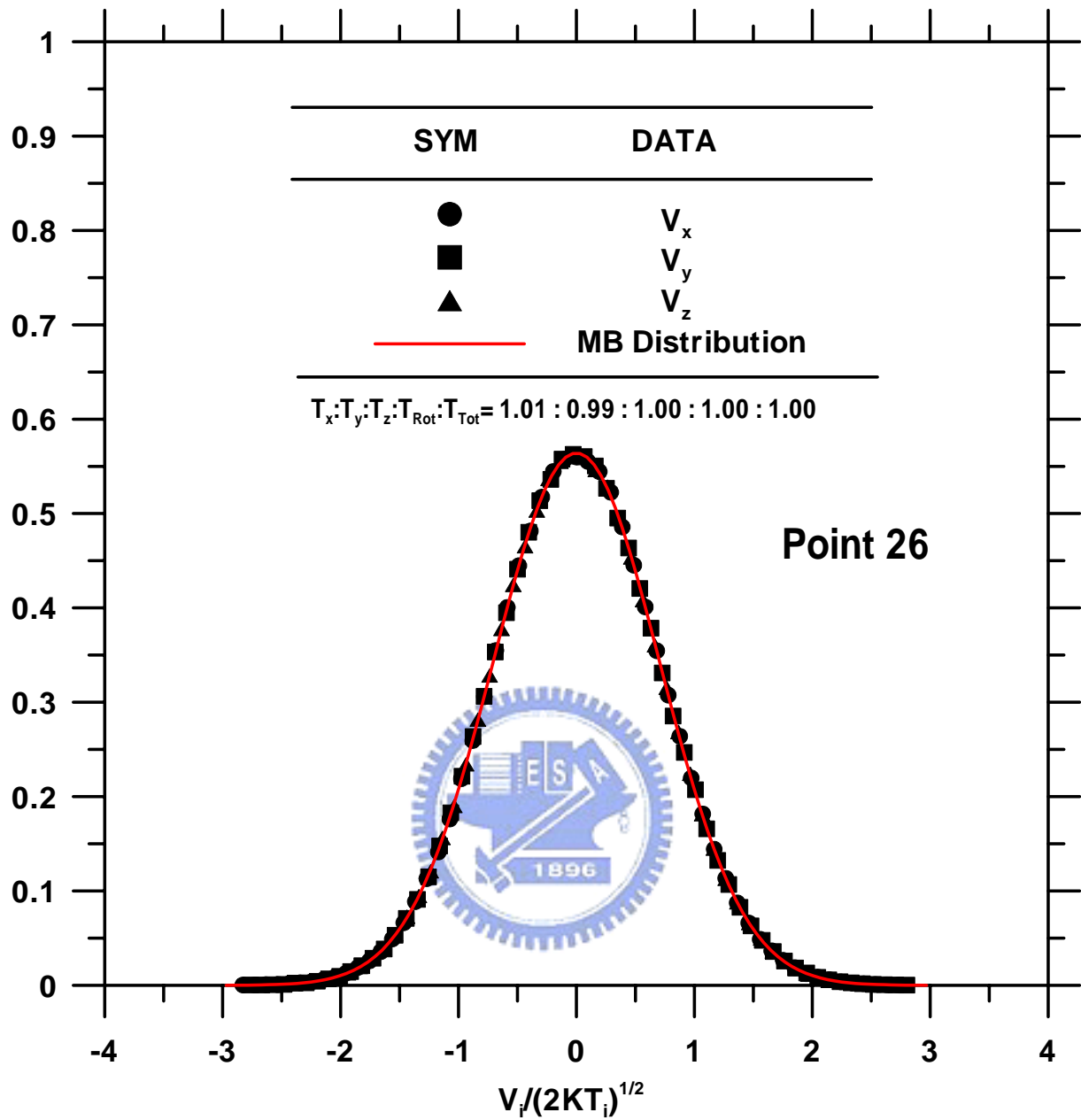
Fig. 4.6b Random velocity distributions to each direction at Point 26 (Boundary layer region).
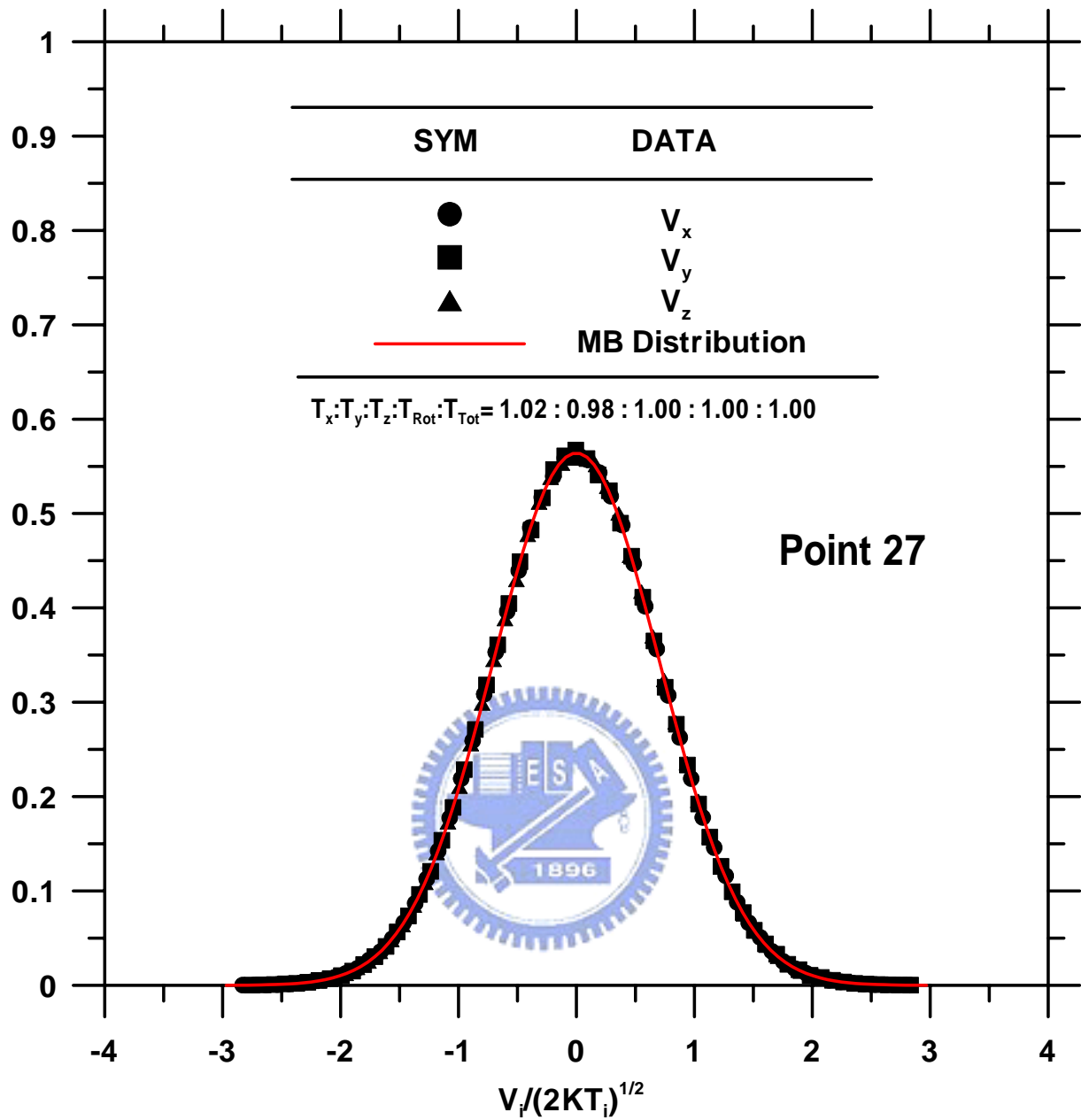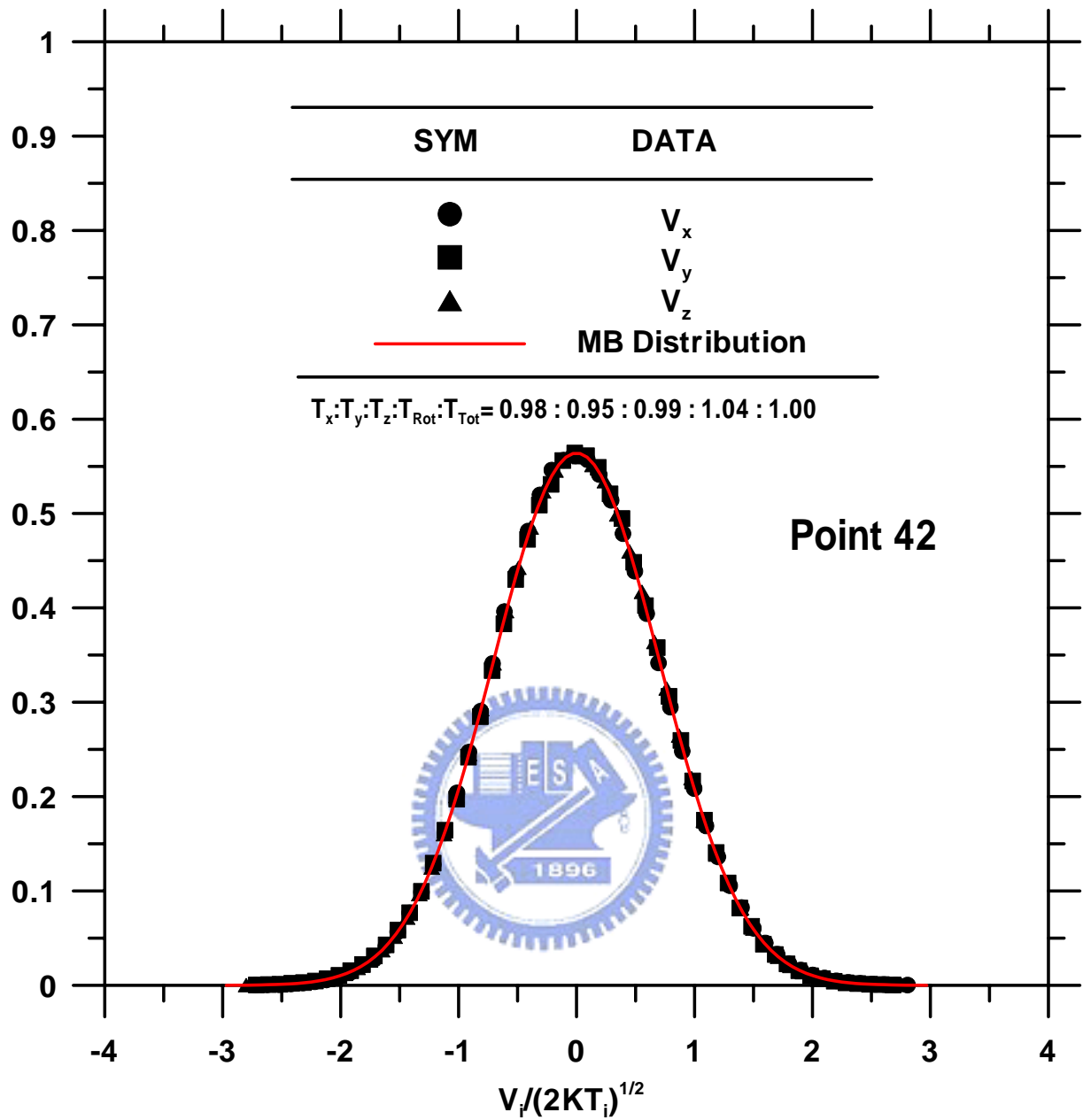
Fig. 4.6c Random velocity distributions to each direction at Point 27 (Boundary layer region).
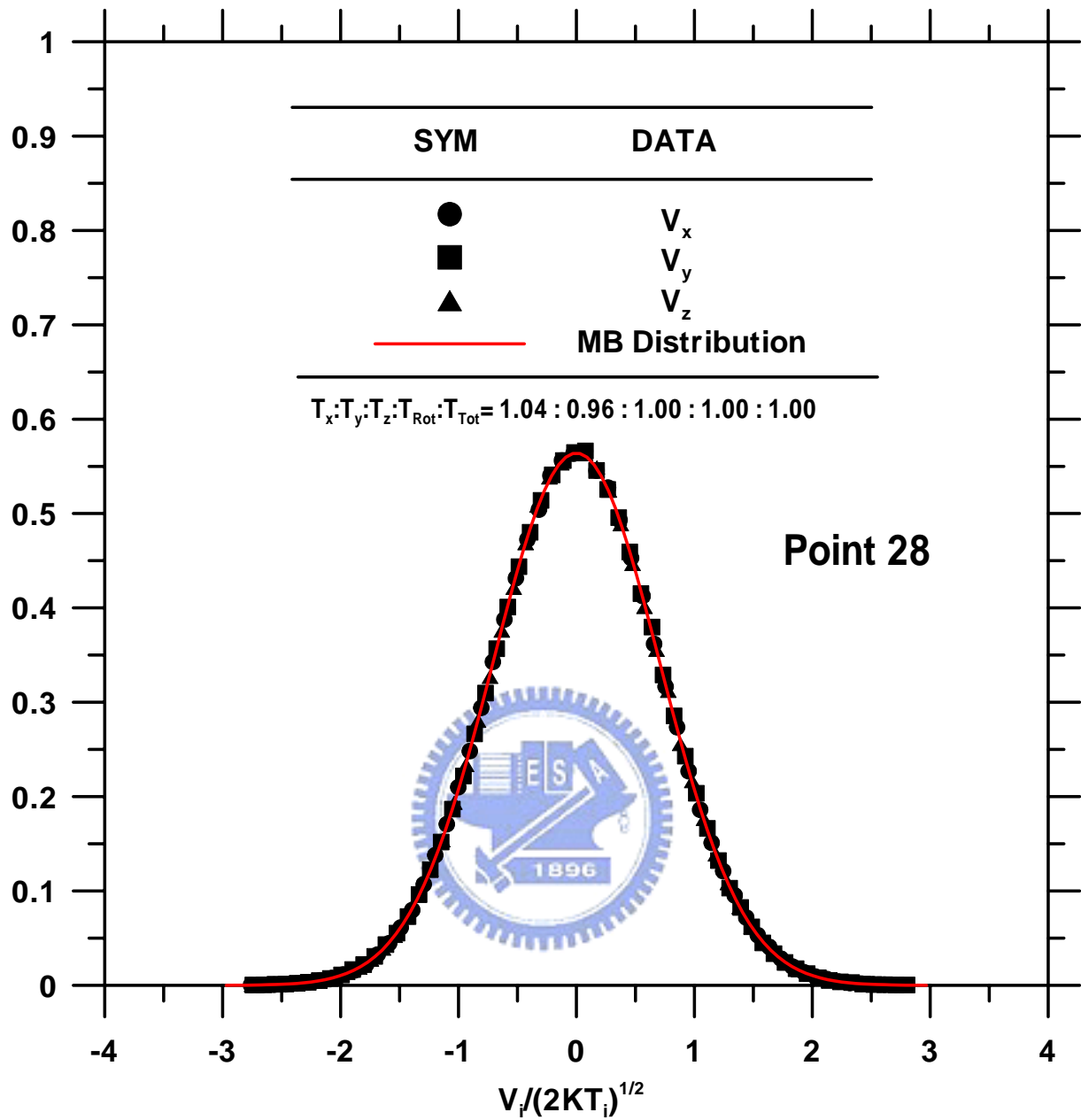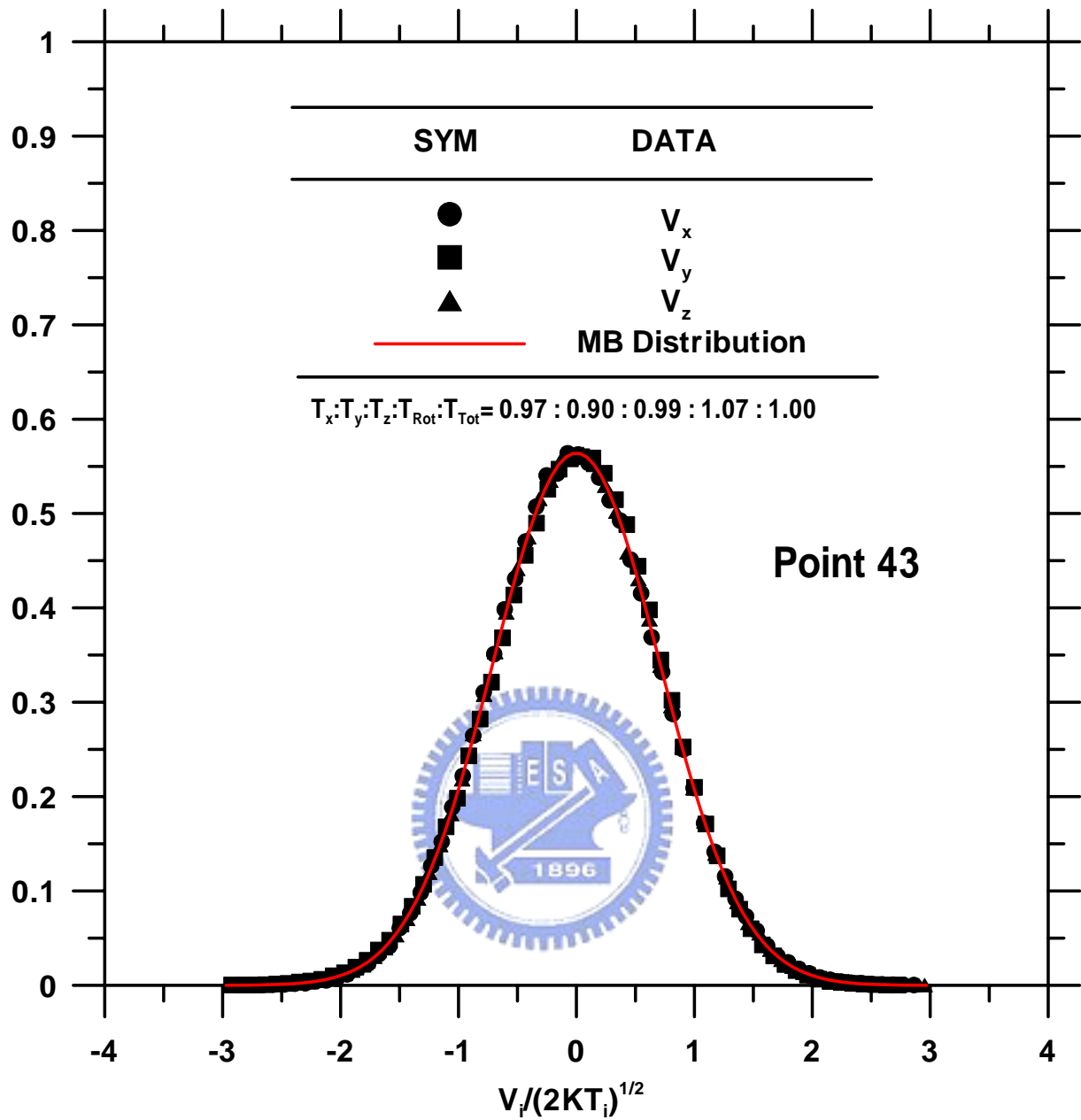
Fig. 4.6d Random velocity distributions to each direction at Point 28 (Boundary layer region).
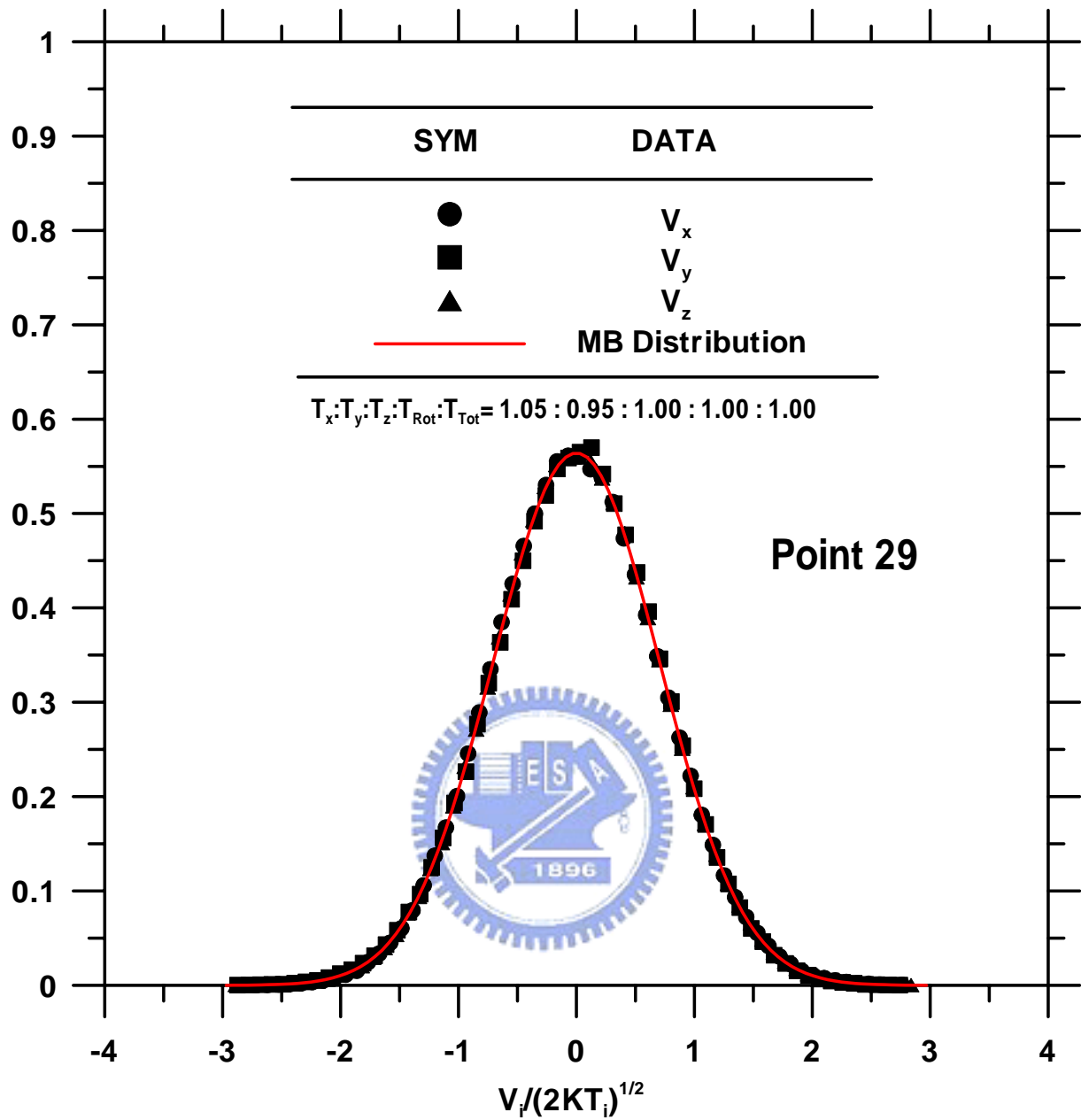
Fig. 4.6e   Random velocity distributions to each direction at Point 29 (Boundary layer region).
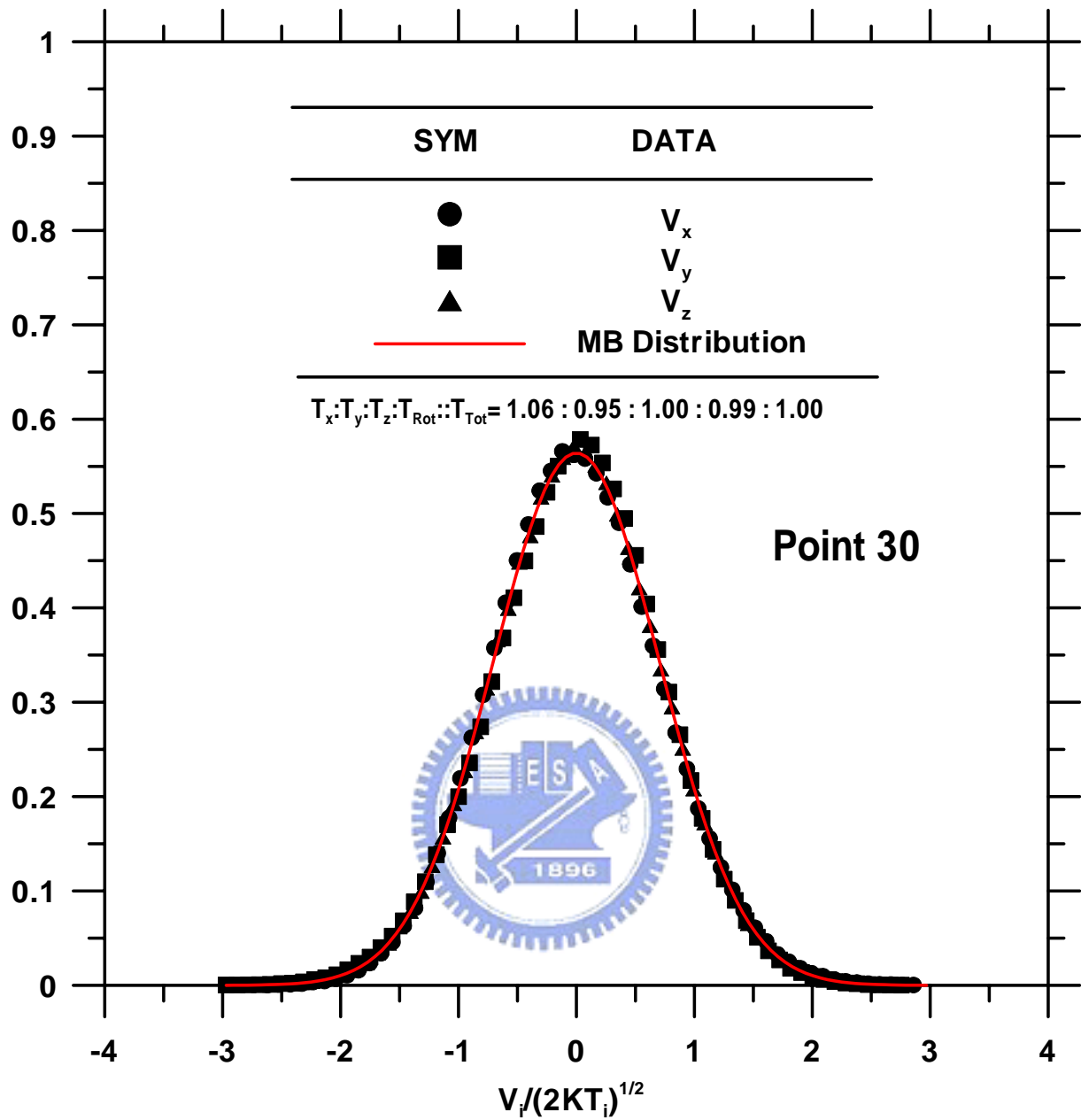
Fig. 4.6f Random velocity distributions to each direction at Point 30 (Boundary layer region).

Boundary Layer

31

35

Fig. 4.7a　Locations of velocity sampling Point 31-35 (Boundary layer region).
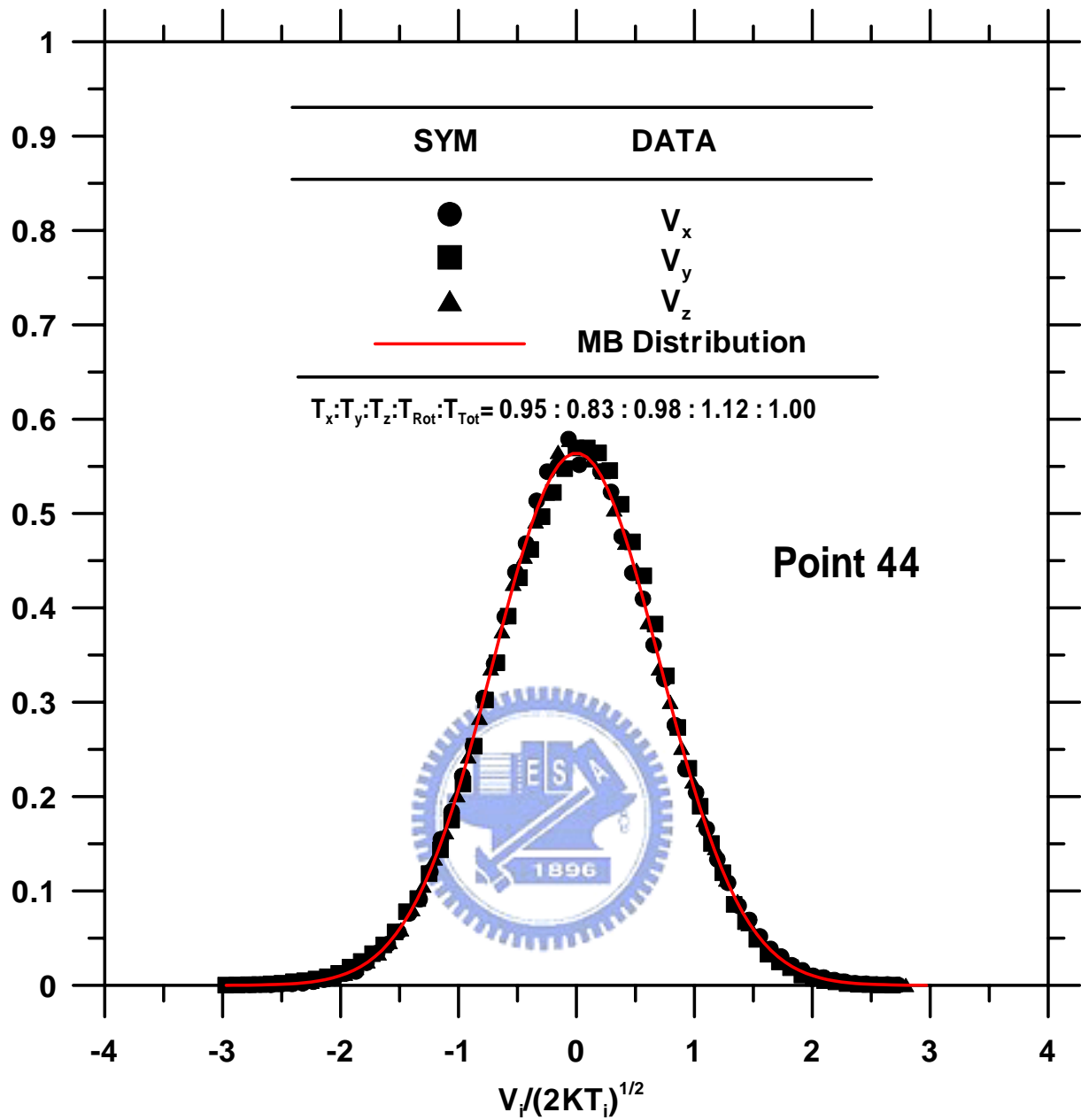
Fig. 4.7b Random velocity distributions to each direction at Point 31 (Boundary layer region).

Fig. 4.7c Random velocity distributions to each direction at Point 32 (Boundary layer region).

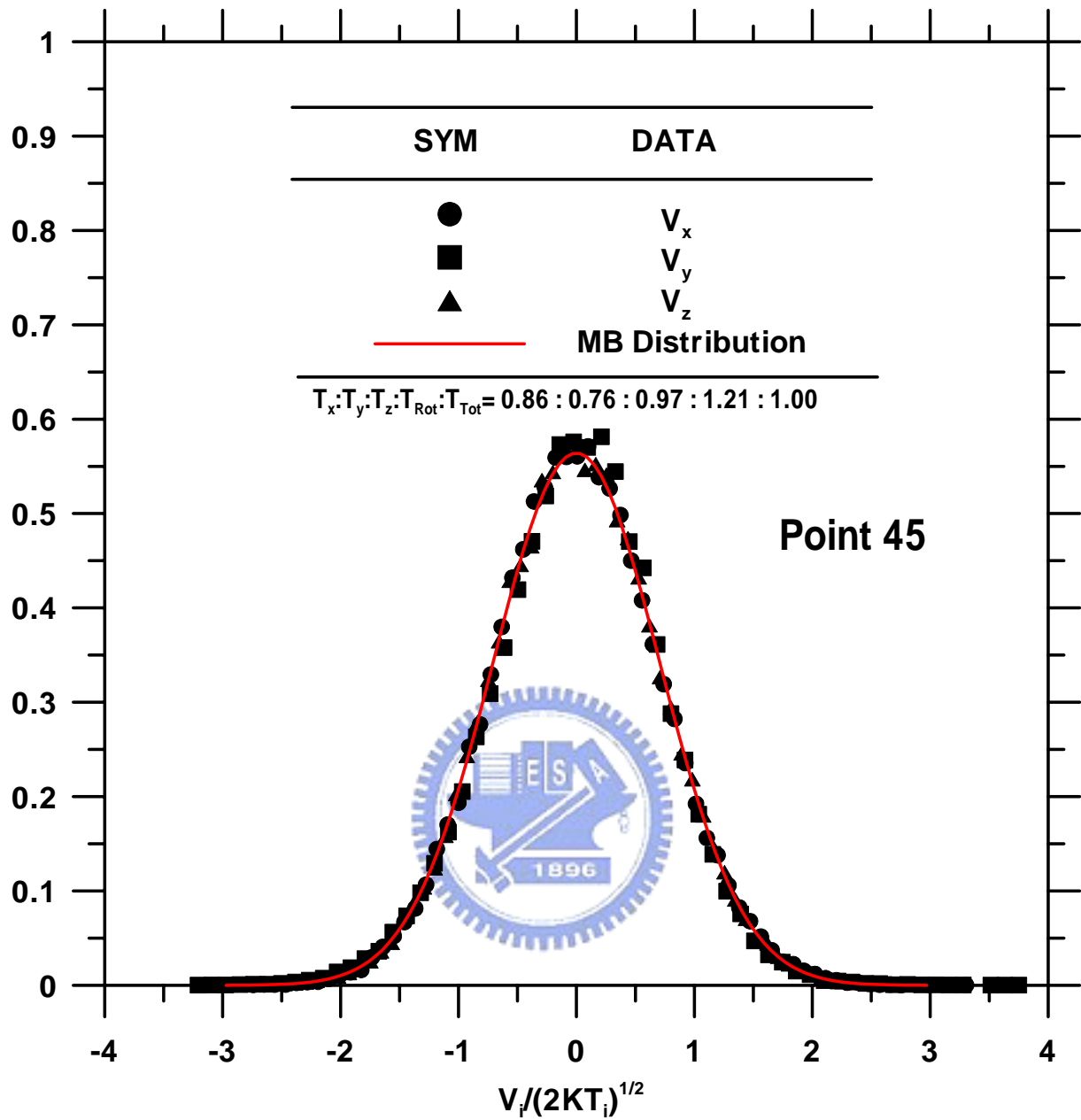Fig. 4.7d Random velocity distributions to each direction at Point 33 (Boundary layer region).

Fig. 4.7e   Random velocity distributions to each direction at Point 34 (Boundary layer region).
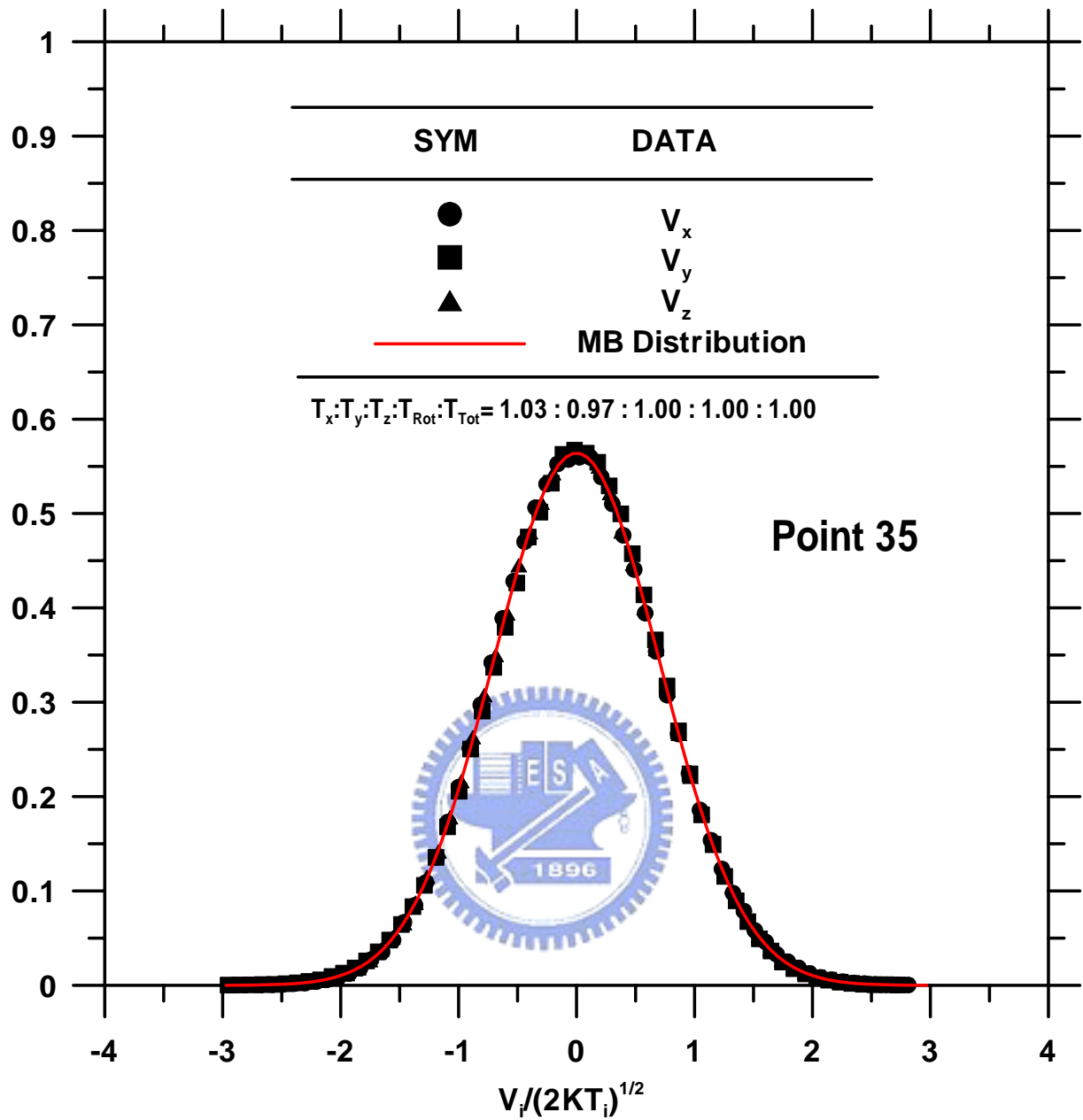
Fig. 4.7f Random velocity distributions to each direction at Point 35 (Boundary layer region).

Expanding Fan

41

46

Fig. 4.8a   Locations of velocity sampling Point 41-16 (Expanding fan region).
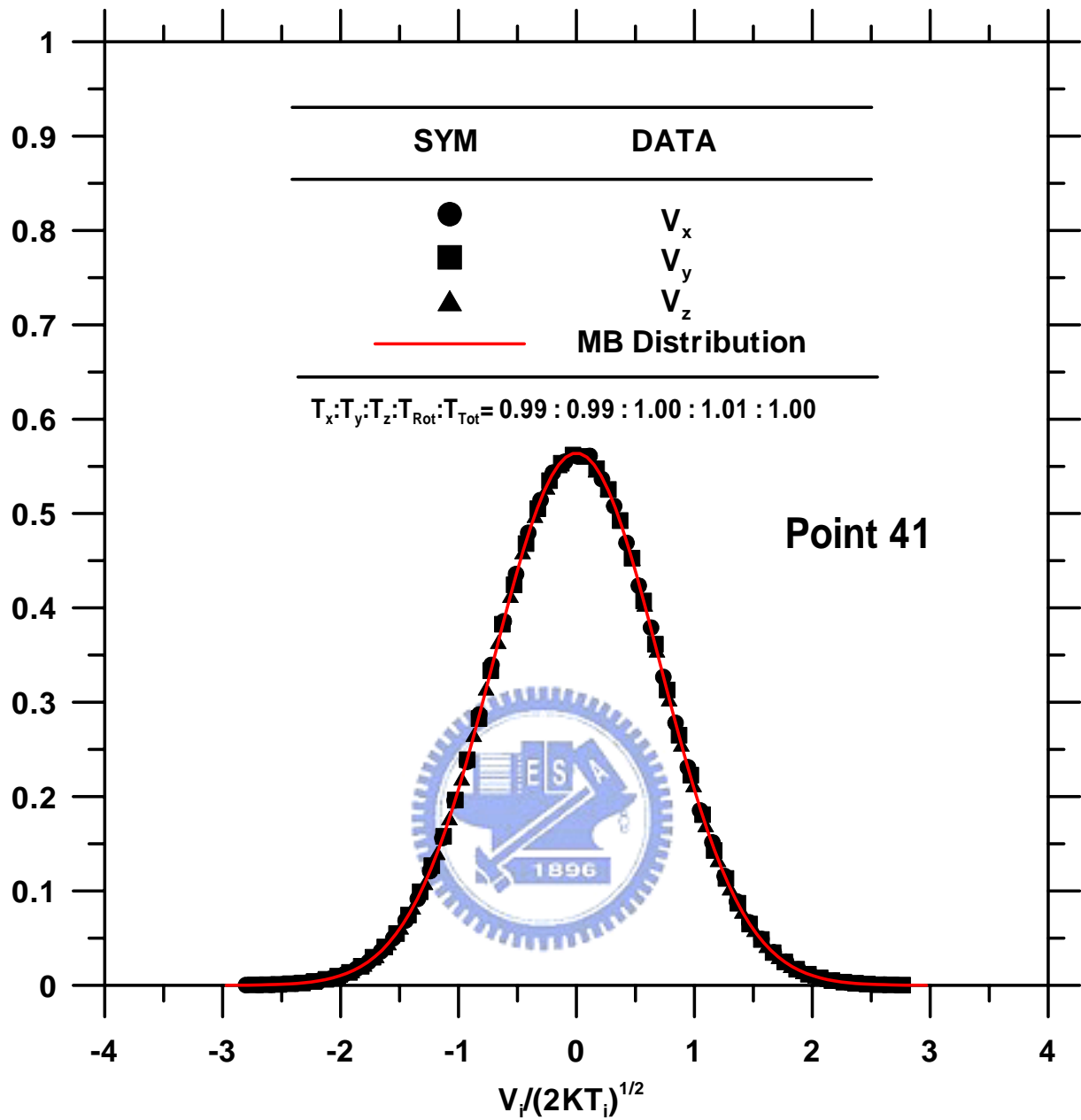
Fig. 4.8b Random velocity distributions to each direction at Point 41 (Expanding fan region).

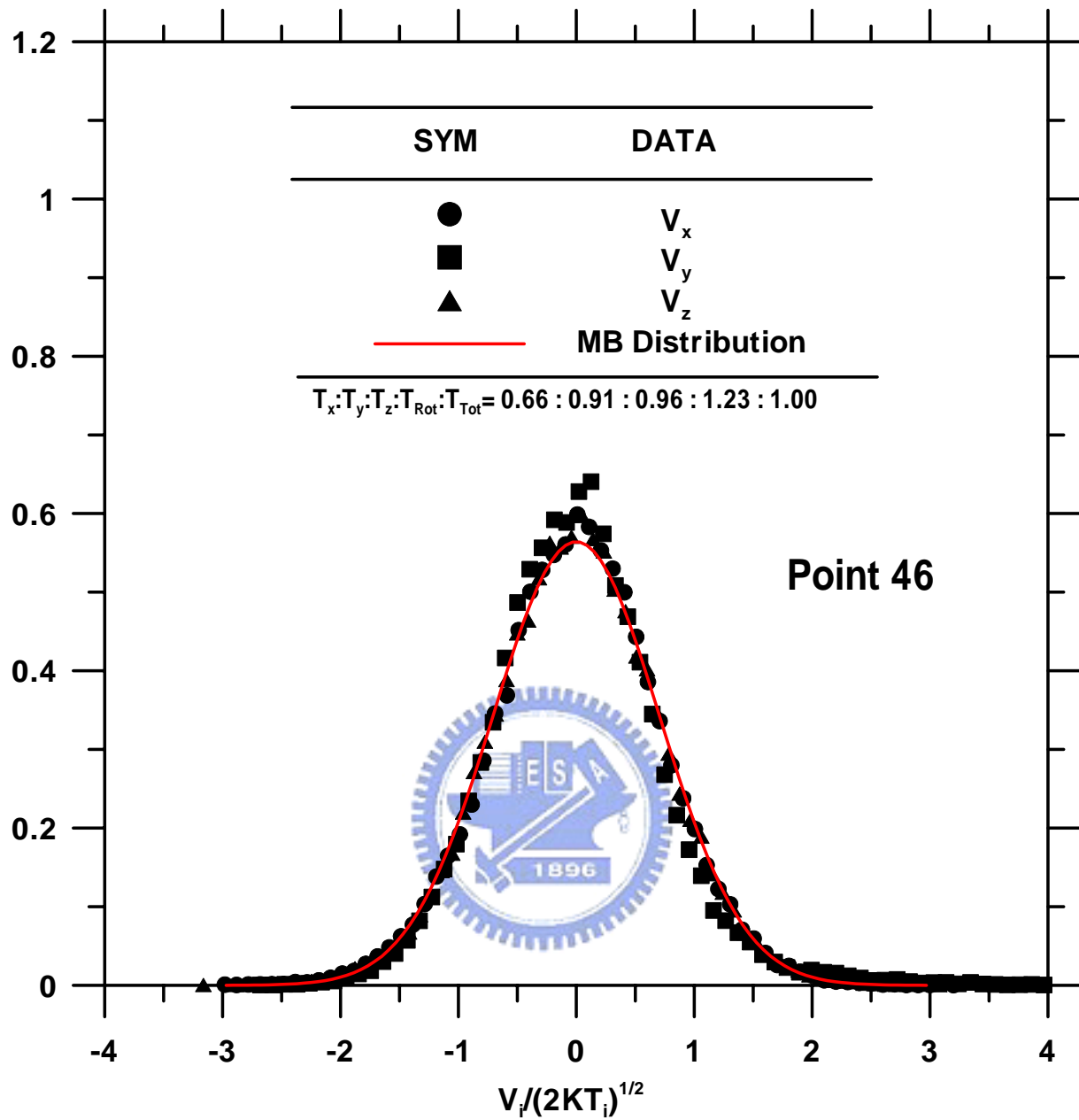Fig. 4.8c Random velocity distributions to each direction at Point 42 (Expanding fan region).
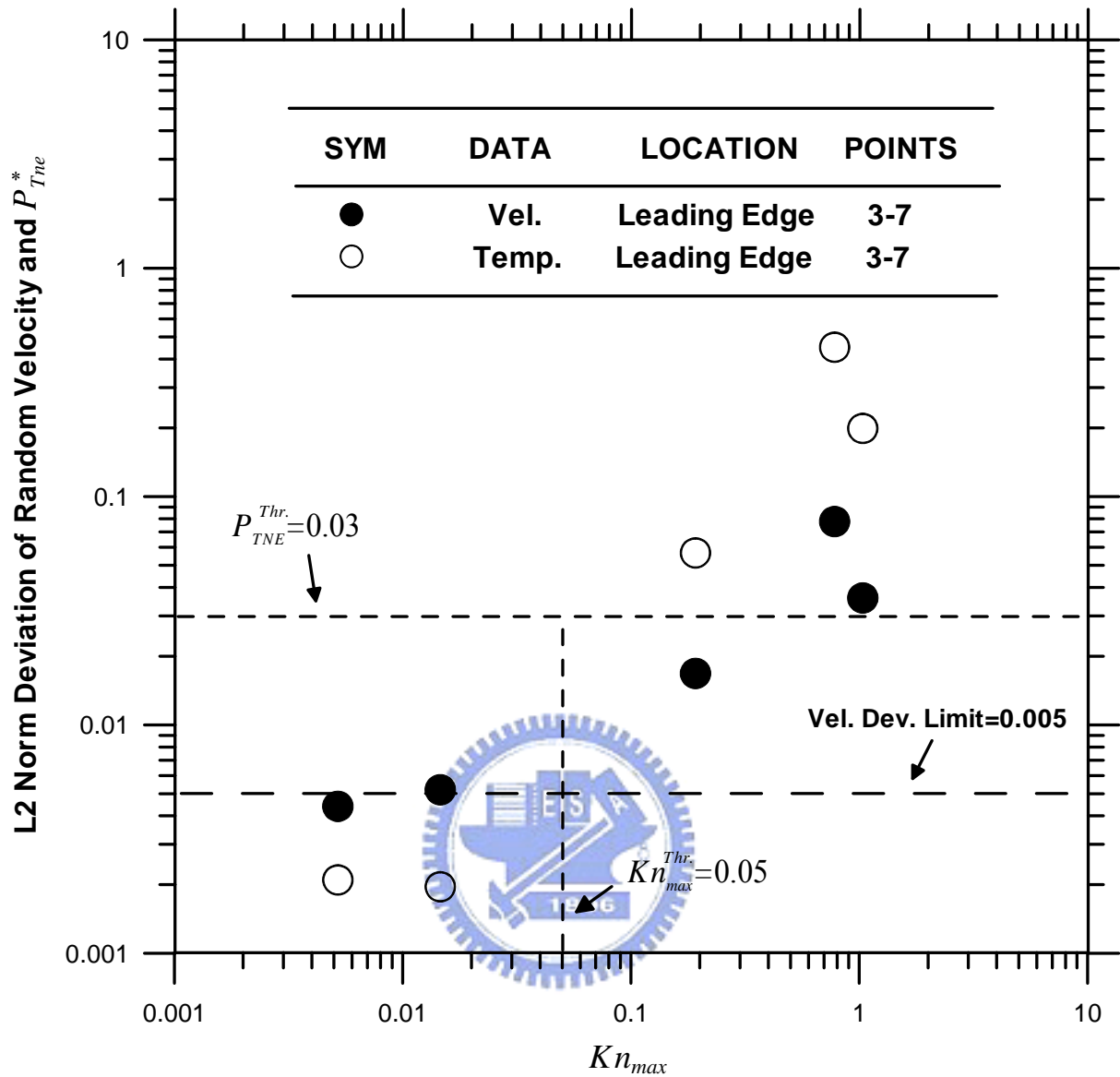
Fig. 4.8d   Random velocity distributions to each direction at Point 43 (Expanding fan region).

Fig. 4.8e   Random velocity distributions to each direction at Point 44 (Expanding fan region).

Fig. 4.8f   Random velocity distributions to each direction at Point 45 (Expanding fan region).

Fig. 4.8g   Random velocity distributions to each direction at Point 46 (Expanding fan region).

Fig. 4.9   L2 norm deviation of random velocity and thermal non-equilibrium indicator as functions of continuum breakdown parameter near the leading edge region.
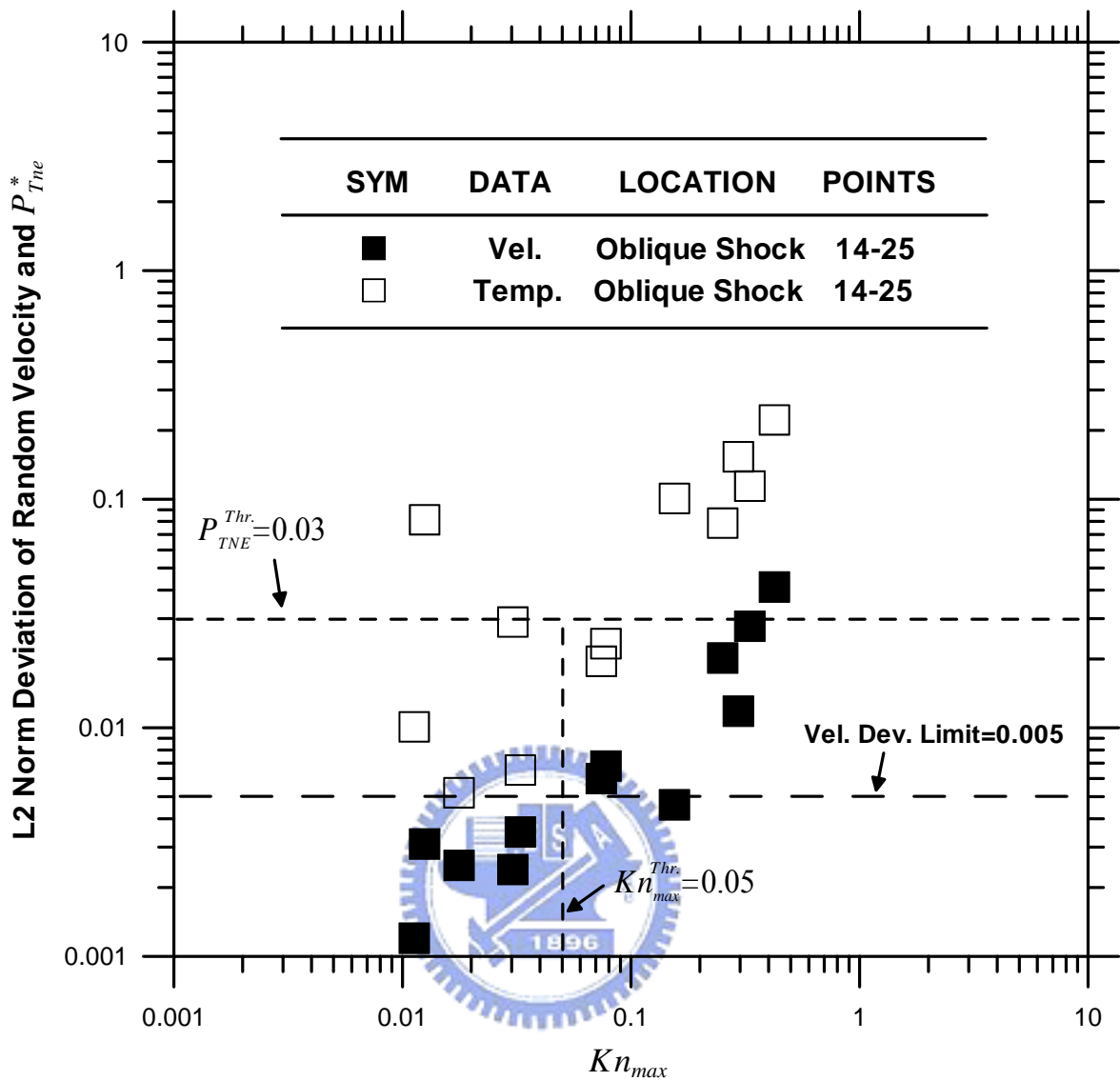
Fig. 4.10 L2 norm deviation of random velocity and thermal non-equilibrium indicator as functions of continuum breakdown parameter near the oblique shock region.
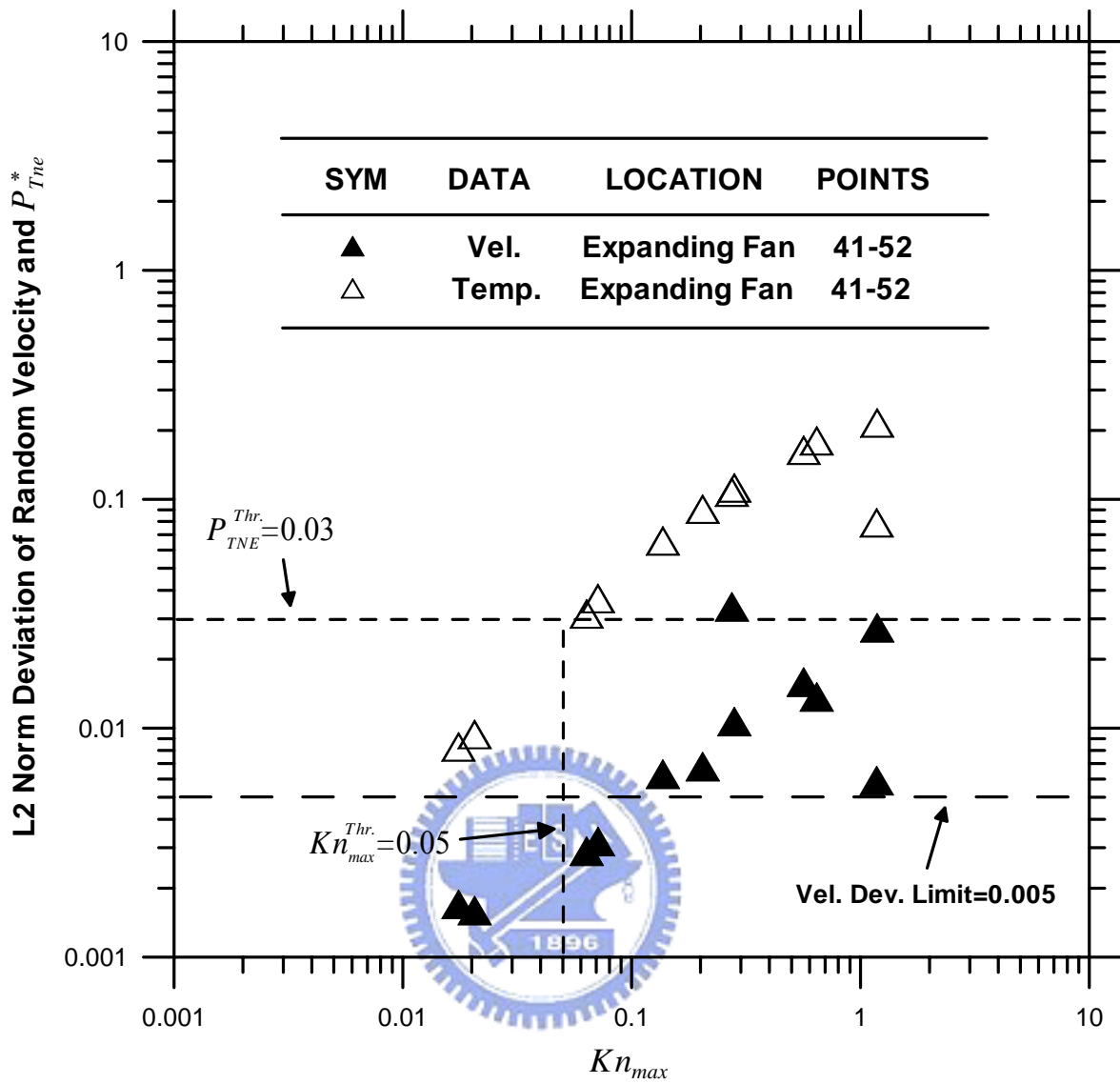
Fig. 4.11 L2 norm deviation of random velocity and thermal non-equilibrium indicator as functions of continuum breakdown parameter near the expanding fan region.
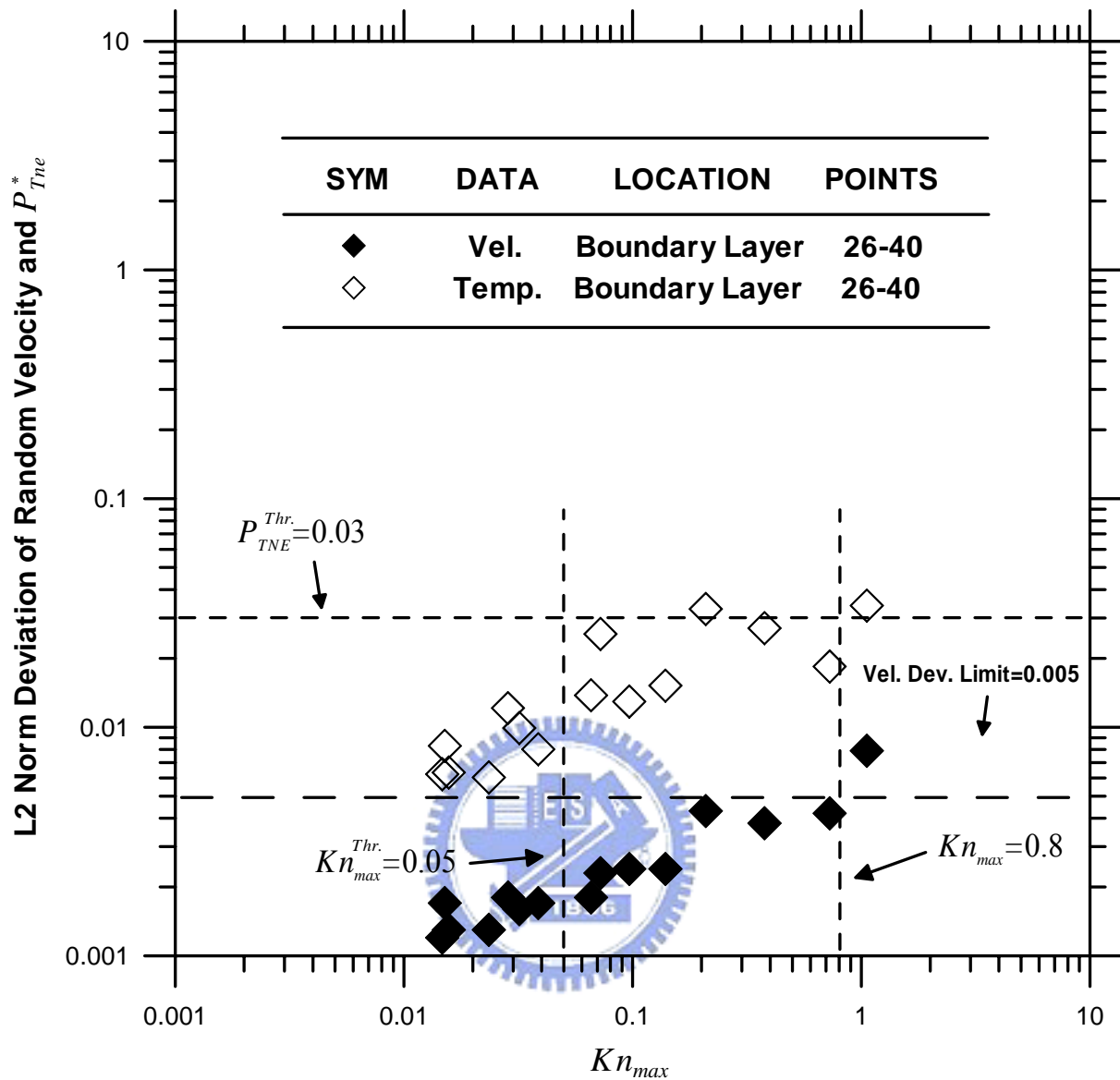
Fig. 4.12   L2 norm deviation of random velocity and thermal non-equilibrium indicator as functions of continuum breakdown parameter near the boundary layer region.
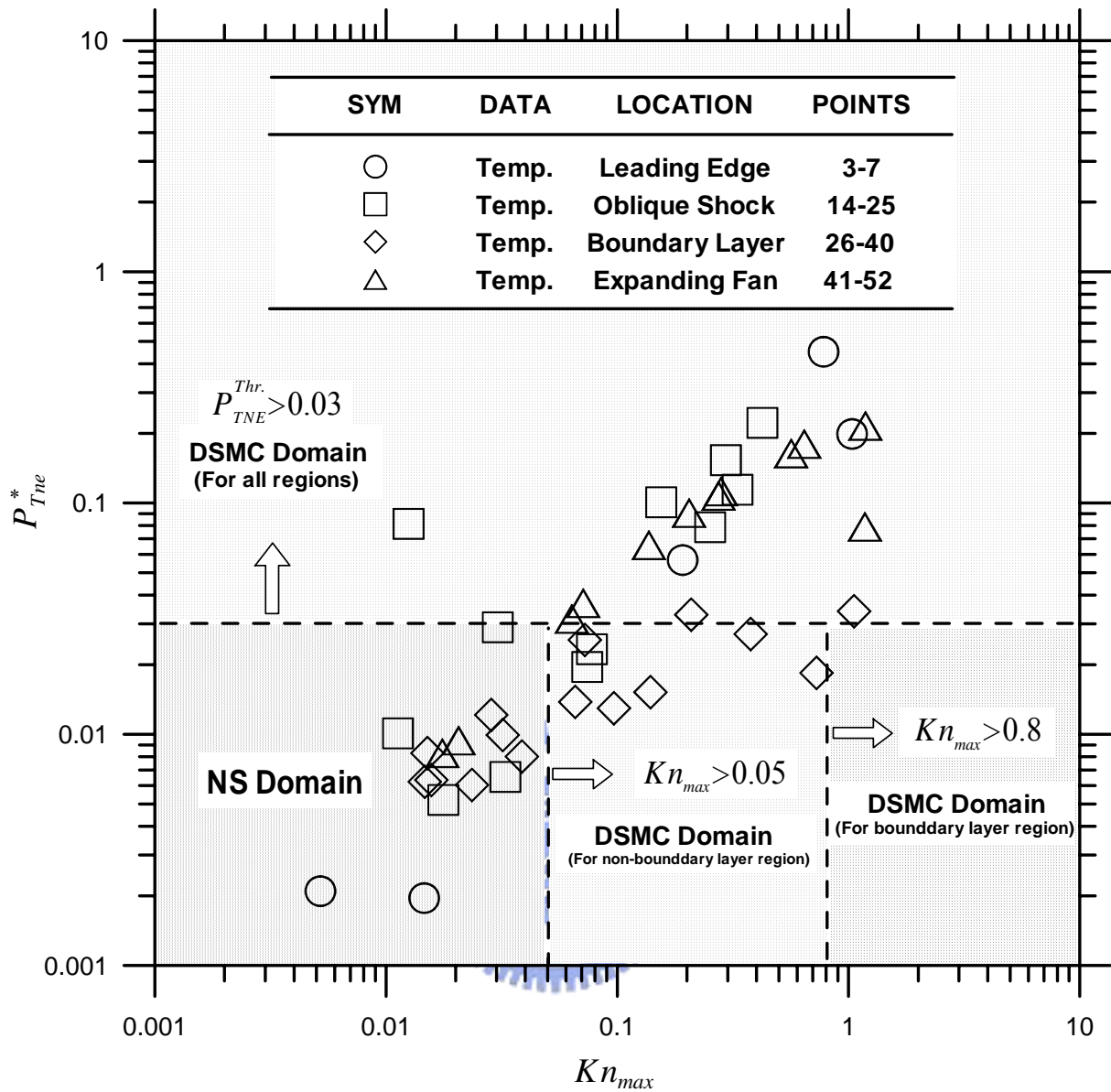
Fig. 4.13 Thermal non-equilibrium indicator as functions of continuum breakdown parameter in different regions.